# A Theoretical and Experimental Study on Biochar as an Adsorbent for Removal of Acid Gases ($CO_2$ and $H_2S$)

By

©Hanieh Bamdad

A thesis submitted to the school of Graduate Studies in partial fulfillment of the requirements for the degree of

Doctor of Philosophy

Faculty of Engineering and Applied Science
Memorial University of Newfoundland

February 2019

St. John's, Newfoundland
Canada

**Abstract**

Biochar, a carbon-rich material that is obtained from forestry wood residues through thermochemical conversion in the absence of oxygen (*i.e.* pyrolysis), is a potential alternative to commercial adsorbents for acid gas treatment. Acid gases ($CO_2$ and $H_2S$) are present in landfill gases, fossil fuel gases, and mining operations. These gases must be treated to improve environmental safety and limit operational issues such as pipeline corrosion. Common processes for removal of acidic gases from landfill, flue, and natural gas streams include amine absorption processes, which are energy and space intensive due to required regeneration, and solid adsorbents (which can be costly to produce and dispose of). In this work, $CO_2$ adsorption using biochar as a solid adsorbent was investigated. Use of biochar as an adsorbent for acid gas removal is relatively novel. The specific objectives included; characterize the biochar structure (*i.e.* chemical, physical, and morphological) through a series of analyses; determine the operating conditions for obtaining maximum adsorption capacity; modify the biochar surface to determine impact on adsorption; and develop a molecular model to simulate the adsorption process to determine if it can be used as a tool in experimental design. Chapter one gives an overview of the conceptual framework of acid gas purification and outlines the objectives, the scopes, and the significance of this study along with a summary of the thesis chapters. Chapter two provides a literature review to identify different types of biochar production methods, reaction conditions (*e.g.* temperature and residence time), and woody biomass as one of possible feedstock materials. The biochar was compared with commercial adsorbents and the results indicated biochar could be used as a feasible

alternative to activated carbon as it is environmentally friendly and a low-cost adsorbent. In addition, the impact of production conditions on biochar properties were investigated and it was found that carbon, hydrogen content, and surface area were significantly affected by pyrolytic temperature. The reported isotherms in the literature were compared and the Freundlich isotherm was the best fit with the biochar. The application of molecular modeling to describe adsorption process and different simulation methods were studied. The biochar for this research was produced from three different woody biomasses: softwood (sawdust and bark (Balsam fir)) and hardwood (Ash wood) through fast pyrolysis at 400-500 ºC and then compared in terms of chemical and physical properties in chapter three. Chapter four looks at the impact of three operating conditions, temperature, inlet feed flow rate, and $CO_2$ concentration, on biochar adsorption capacity and the interaction of these parameters were evaluated using response surface methodology. The operating conditions for maximizing $CO_2$ uptake were determined and the Freundlich isotherm best represented the equilibrium adsorption and the pseudo first-order was selected as a kinetic model. Thermodynamic analysis indicated the adsorption process was spontaneous and exothermic. Further, we found that biochar derived from "waste" materials had better adsorption capacity relative to commercial zeolite. Chapter five describes chemical modification of the biochar using two novel methods of amine functionalization and the maximum adsorption capacity was measured at the conditions obtained in chapter four. The results indicated functionalization decreased the pore volume, surface area, and subsequently the adsorption capacity of the biochar. In order to enhance capacity, the biochars (unmodified and chemically modified) were thermally activated via air diluted with nitrogen at a moderate 560 ºC. Some

nitrogen functionality retained in the biochar structure even after activation. The synthesized N-enriched biochar followed by thermal activation was found to have much higher adsorption capacity as compared with commercially available activated carbon (Norit CA1) and recent carbon based adsorbents in the literature. Chapter six is dedicated to molecular modeling and linking the experimental results with simulations. The effect of various functional groups on adsorption of $CO_2$/$H_2S$ on biochar surface was investigated. It was found that the presence of functional groups promotes $CO_2$ adsorption on the surface with exothermic adsorption energy. As expected, the DFT calculations showed amine functional groups enhanced $CO_2$ adsorption with more exothermic adsorption likely because of stronger bonding compared to other functional groups. The thermodynamic outcomes (Enthalpy and Gibbs free energy) validated that the affinity of the chars for $CO_2$ is on the same order of magnitude as $H_2S$. The simulated thermodynamic parameters and IR vibrational frequencies were calculated and both showed reasonable agreement with experimental results (chapter four and five). The results of this study would be helpful for developing future work, on the scale-up of the adsorption system, further modification of the biochar, $CO_2$ sequestration, regeneration, and atomic-level design of carbon surfaces.

**Acknowledgment**

My overwhelming gratitude goes first to my supervisor, Professor Kelly Hawboldt, who expertly guided me through my research. Her patience, motivation, and in depth knowledge made it possible for me to work on a topic that was of interest to me. It was an enriching experience for me to work under her supervision.

I would also like to express my sincere gratitude to Dr. Stephanie MacQuarrie, who inspired and encouraged me with her kind words and blessing. She provided critical advice and suggested many important additions and improvements especially in the area of chemistry.

I would like to thank my committee member, Dr. Majid Abdi, for valuable comments and suggestions. His expertise in both the academic and industries sectors was invaluable.

I am very thankful to the Faculty of Engineering and Applied Science at Memorial University of Newfoundland, Compute Canada team**,** ACENET consortium, and Gaussian Inc. I am grateful for the funding provided by NSERC (Natural Science and Engineering Research Council of Canada), SGS (School of Graduate Studies of Memorial University), and BioFuelNet Canada.

I would also like to thank the research consultants in the ACENET-compute Canada team, especially Mr. Oliver Stueker (Memorial University) and Mr. Ross Dickson (Dalhousie University), for their constant support during the molecular modeling part of this project.

I would like to express special thanks to my partner, Dr. Sadegh Papari, who helped me spiritually and intellectually throughout this study. Much of my experimental works would have not been completed without guidance from him. His support was essential to my success throughout my doctoral studies.

Finally, I sincerely acknowledge my dearest parents and beloved sister and brother, who have encouraged me to pursue my graduate studies and have been supportive in every way possible.

**Table of Contents**

**List of Tables**

**List of Figures**

# 1. CHAPTER ONE

## Introduction and Overview

The consumption of global energy has risen due to increasing populations globally and higher standards of living [1]. Acid gases, carbon dioxide ($CO_2$) and hydrogen sulfide ($H_2S$), naturally present in produced gases from oil and gas operations [2], landfill gases [3], and mining operations [4] among others. The gases must be removed prior to transport as they are both corrosive and represent a corrosion risk [5]. Further, $H_2S$ is a toxic gas at ppm levels and for safety reasons needs to be mitigated [6]. The most common method for acid gas removal are amine based absorption systems and commercial adsorption. Absorption based systems are energy and space intensive due to required regeneration and use hazardous chemicals [7]. Bio-based adsorbents have been used as an alternative to the existing acid gas removal techniques [8,9]. Bio-based materials are produced from biomass and biomass resources include waste from food processing, agricultural crops and their waste byproducts, wood and wood wastes, municipal solid waste, animal wastes, aquatic plants, and algae. Fig. 1-1 illustrates different source of biomass from industry, agriculture, forestry, and waste as well as their potential final bioenergy applications.

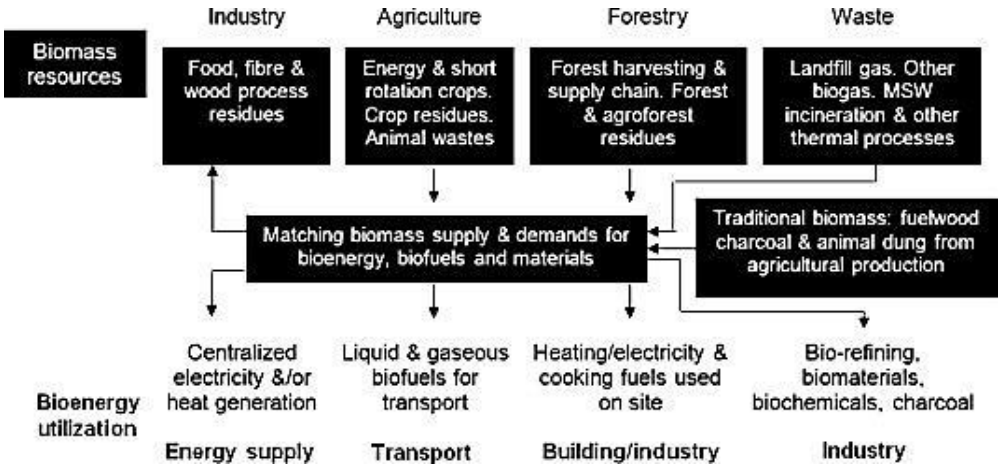

Figure 1-1: Biomass resources converted to bioenergy [1]

Thermo-chemical technologies are established to produce more valuable products through biomass thermal treatment [11]. The different thermal conversion processes of biomass are summarized in Fig. 1-2.

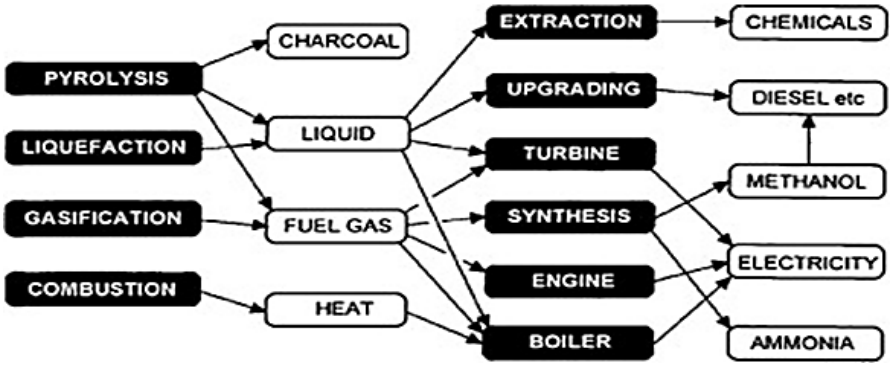


Figure 1-2: Thermo-chemical processes for bioenergy production and the corresponding products [2]

Thermo-chemical conversions are defined based on temperature, duration, and the presence or absence of oxidants and based on these factors classified as pyrolysis, gasification, liquefaction, and combustion [13]. Pyrolysis of biomass is one of the techniques for production of biofuel in the form of char, oil, and gas [14]. This process has been applied by heating the raw biomass at high temperature in the absence of oxygen. Fast, intermediate, and slow are the three main modes of pyrolysis based on temperature and residence time [15]. The three main products of the pyrolysis of biomass are a carbon-rich solid (biochar), a condensed liquid phase (bio-oil), and non-condensable gases. Biochar can be used as a power generator [16], carbon sequester [17], soil

amendment to improve soil quality or fertilizer [18], amendment in concrete [19], adsorbent for pollutants [20], and a raw material for electrodes in microbial fuel cells [21]. In this work, biochar has been used as a bio-based adsorbent and the modified structure makes it ideal for efficient removal of acid gases compared to conventional adsorbents.

Biochar was sourced from forestry residues (softwood and hardwood) that would otherwise be disposed or stockpiled, presenting safety and environmental risk. The feedstock from sawmill residues used in this study was a local biomass obtained from balsam fir and ash wood for production of biochar through fast pyrolysis at lab (semi-batch) and pilot (auger reactor) scale for comparison. Based on the literature, using biochar as an adsorbent for acid gas removal is relatively novel and this type of feedstock for producing biochar is rare [22,23]. The value of this study was producing adsorbent from waste stream and developing market for biochar to maximize the sustainability of the fast pyrolysis process. The lab-scale fixed bed reactor was utilized during this research to study the adsorption capacity of different biochar samples. $CO_2$ has been suggested to test the biochar as an effective indicator of adsorbent performance, because $CO_2$ capacity measurement is less hazardous compared to other gases such as $H_2S$. The preliminary experiments were conducted in order to study the independent and combined interaction effects of adsorption temperature, total inlet flow rate, and % (v/v) $CO_2$ on the adsorption capability of the biochar. The methods used in this study for modifying biochar surface are novel and could improve the $CO_2$ adsorption capacity of the studied biochar remarkably. In each step of the experiment, the biochar sample was compared

with commercial adsorbents (*i.e.* zeolite and activated carbon) and biochar proved superior in both comparisons. Although the molecular modeling of the biochar system was challenging due to restrictions regarding the simulation package and experiments, the molecular simulation was successfully developed and validated with the experimental data obtained from the adsorption system. The results of this study are beneficial for future work, on the scale-up of the adsorption system, further modification of the biochar, $CO_2$ sequestration, and regeneration. In addition, the information obtained in this study will be helpful for atomic-level design of carbon surfaces in order to improve $CO_2/H_2S$ adsorption. This thesis includes a series of manuscripts (paper based) either published, in review processes, or to be submitted for publication. Figure 1-3 illustrates how chapters are integrated.

Chapter two has been published in the *Journal of Renewable and Sustainable Energy Reviews*. The manuscript provided a literature review on common adsorbents for acid gases removal with focus on biochar.

Chapter three has been published in *The Canadian Journal of Chemical Engineering*. The physicochemical properties of three different types of wood-derived biochars (sawdust and bark (Balsam fir) and hardwood (Ash wood)), were characterized and compared with a Metal Organic Framework (MOF) with respect to properties key for adsorbent applications.

Chapter four has been published in the *Journal of Environmental Science and Pollution Research*, and describes the analysis of $CO_2$ adsorption capacity of biochar in a

lab-scale fixed bed reactor. Response surface methodology was applied to determine operating conditions for maximum adsorption and to assess interaction of the adsorption parameters.

Chapter five has been published in the Journal of *Energy & Fuels*, and consists of the modification of the biochar surface via amine functionalizing and thermal treatment. The aim of this chapter was to enhance the adsorption capacity of the biochar and compare it with other synthesized adsorbents.

Chapter six covers molecular modeling of biochar. In this chapter, the impact of various functional groups on the adsorption of $CO_2/H_2S$ on the biochar surface was investigated using the density functional theory (DFT) method. In addition, the simulation results (*i.e.* thermodynamic parameters and FTIR frequencies) were validated by experimental outcomes.

Chapter seven consists of a summary, conclusions, and recommendations.

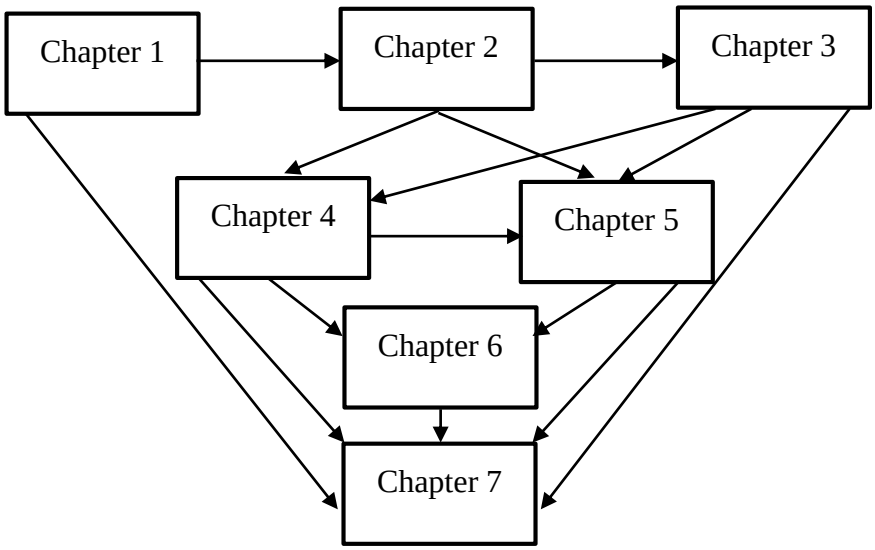


Figure 1-3: Illustration of integration of chapters

## References


[1] B. Petroleum. BP Statistical Review of World Energy. 2016. doi:10.1016/j.egypro.2013.06.172.

[2] Faramawy S, Zaki T, Sakr AAE. Natural gas origin, composition, and processing: A review. J Nat Gas Sci Eng 2016;34:34–54. doi:10.1016/j.jngse.2016.06.030.

[3] Zuberi MJS, Ali SF. Greenhouse effect reduction by recovering energy from waste landfills in Pakistan. Renew Sustain Energy Rev 2015;44:117–31. doi:10.1016/j.rser.2014.12.028.

[4] Pandey B, Gautam M, Agrawal M. Greenhouse Gas Emissions From Coal Mining Activities and Their Possible Mitigation Strategies. Environ. Carbon Footprints, 2018, p. 259–94. doi:10.1016/B978-0-12-812849-7.00010-6.

[5] Pessu F, Barker R, Neville A. Early stages of pitting corrosion of UNS K013014 carbon steel in sour corrosion environments: The influence of CO2, H2S and temperature. NACE Corros 2015 2015;5583:1–17. doi:10.5006/2454.

[6] Reiffenstein RJ, Hulbert WC, Roth SH. Toxicology of Hydrogen Sulfide. Annu Rev Pharmacol Toxicol 1992;32:109–34. doi:10.1146/annurev.pa.32.040192.000545.

[7] Shafeeyan MS, Daud WMAW, Houshmand A, Shamiri A. A review on surface modification of activated carbon for carbon dioxide adsorption. J Anal Appl Pyrolysis 2010;89:143–51. doi:10.1016/j.jaap.2010.07.006.

[8] Heidari A, Younesi H, Rashidi A, Ghoreyshi AA. Evaluation of CO2adsorption with eucalyptus wood based activated carbon modified by ammonia solution through heat treatment. Chem Eng J 2014. doi:10.1016/j.cej.2014.06.004.

[9] Plaza MG, González AS, Pevida C, Rubiera F. Influence of water vapor on CO2 adsorption using a biomass-based carbon. Ind Eng Chem Res 2014;53:15488–99. doi:10.1021/ie500342q.

[10] International Energy Agency. Bioenergy Project Development & Biomass Supply. Good Pract Guidel 2007:66. doi:10.1017/CBO9781107415324.004.

[11] McKendry P. Energy production from biomass (part 1): Overview of biomass. Bioresour Technol 2002;83:37–46. doi:10.1016/S0960-8524(01)00118-3.

[12] Zhang L, Xu C (Charles), Champagne P. Overview of recent advances in thermo-chemical conversion of biomass. Energy Convers Manag 2010;51:969–82. doi:10.1016/j.enconman.2009.11.038.

[13] McKendry P. Energy production from biomass (part 2): Conversion technologies.

Bioresour Technol 2002;83:47–54.

[14] Mohan D, Pittman Charles U., Steele PH. Pyrolysis of Wood/Biomass for Bio-oil: A Critical Review. Energy & Fuels 2006;20:848–89. doi:10.1021/ef0502397.

[15] Bridgwater A V. Review of fast pyrolysis of biomass and product upgrading. Biomass and Bioenergy 2012;38:68–94.

[16] Sophia Ayyappan C, Bhalambaal VM, Kumar S. Effect of biochar on bio-electrochemical dye degradation and energy production. Bioresour Technol 2018;251:165–70. doi:10.1016/j.biortech.2017.12.043.

[17] Mohan D, Abhishek K, Sarswat A, Patel M, Singh P, Pittman CU. Biochar production and applications in soil fertility and carbon sequestration – a sustainable solution to crop-residue burning in India. RSC Adv 2018;8:508–20. doi:10.1039/C7RA10353K.

[18] Palviainen M, Berninger F, Bruckman VJ, Köster K, de Assumpção CRM, Aaltonen H, et al. Effects of biochar on carbon and nitrogen fluxes in boreal forest soil. Plant Soil 2018:1–15. doi:10.1007/s11104-018-3568-y.

[19] Gupta S, Kua HW, Koh HJ. Application of biochar from food and wood waste as green admixture for cement mortar. Sci Total Environ 2018;619–620:419–35. doi:10.1016/j.scitotenv.2017.11.044.

[20] Awasthi MK, Wang M, Chen H, Wang Q, Zhao J, Ren X, et al. Heterogeneity of biochar amendment to improve the carbon and nitrogen sequestration through reduce the greenhouse gases emissions during sewage sludge composting. Bioresour Technol 2017;224:428–38. doi:10.1016/j.biortech.2016.11.014.

[21] Elleuch A, Boussetta A, Yu J, Halouani K, Li Y. Experimental investigation of direct carbon fuel cell fueled by almond shell biochar: Part I. Physico-chemical characterization of the biochar fuel and cell performance examination. Int J Hydrogen Energy 2013;38:16590–604. doi:10.1016/j.ijhydene.2013.08.090.

[22] Gravel V, Dorais M, Ménard C. Organic potted plants amended with biochar: its effect on growth and *Pythium* colonization. Can J Plant Sci 2013;93:1217–27. doi:10.4141/cjps2013-315.

[23] Nemati MR, Simard F, Fortin J-P, Beaudoin J. Potential Use of Biochar in Growing Media. Vadose Zo J 2015;14:0. doi:10.2136/vzj2014.06.0074.

# 2. CHAPTER TWO

## Literature Review

This chapter has been **published**; Bamdad H*, Hawboldt K, MacQuarrie S. A Review on Common Adsorbents for Acid gases Removal: Focus on Biochar. *Renewable and Sustainable Energy Reviews*. 2018;81(P2):1705-20.

**Abstract**

Biochar, a product of pyrolysis of biomass, represents an attractive alternative to non-renewable or unsustainably sourced biomass as an adsorbent material for treating gaseous effluents. Biomass from residues associated with agricultural and forestry operation, otherwise considered waste material or a storage issues, represents a potential sustainable source of adsorbent. There are several adsorbents for removal of contaminants from gases including carbon based, silica based, and metal oxide based adsorbents; however, availability of feedstock, low cost, and potential high adsorption capacity distinguish biochar from other adsorbents. This review includes common sorbents for removal of contaminants from gas, biochar production methods, and compares biochar with activated carbon as one of the most common commercial adsorbents. Adsorption isotherms, mechanisms, and process systems for removal of acid gases such as $CO_2$ and $H_2S$ by biochars have been comprehensively reviewed. The application of molecular modeling to describe adsorption by activated carbons and possible extension to biochar were studied. There is still a lack of published information in the molecular modeling of biochars, and using these models to understand the complex adsorbent mechanisms on the very heterogeneous surfaces of biochar (relative to commercial adsorbent materials such as activated carbons). Therefore, further research needs to fill these gaps to identify all potentials of this promising adsorbent.

Keywords: Acid gases, Adsorbents, Biochar, Molecular Modeling, Gas treatment

## Introduction

Hydrogen sulfide ($H_2S$) and carbon dioxide ($CO_2$) are common contaminants in oil and gas production/processing, wastewater treatment plants, fossil fuel combustion, and landfill gases and can result in corrosion, problematic gaseous emissions, and represent a safety risk [1]. In addition to light hydrocarbons, natural gas can contain variable amounts of carbon dioxide, nitrogen, sulfur compounds, water, aromatics and small amounts of helium (less than 1 vol.%) and mercury (generally 5–300 $\mu gNm^{-3}$) [2]. On offshore platforms, the treatment of any gas or liquid effluent is challenging due to space restrictions and/or manpower on the platform (this limits operator intensive processes). In platforms where the main product is oil, any produced gas is re-injected, used for utilities, and/or flared and must be treated to a level appropriate for these applications. These challenges are not restricted to the offshore, any remote location (e.g. landfills, small wastewater treatment plants etc.) require smaller scale and less operationally intensive alternatives to gas treatment, particularly if the gas is to be used as a fuel. There are a number of processes used to remove $CO_2$ and $H_2S$ (acid gases) from natural gas, including absorption and adsorption. In absorption, the acid gases are removed using solvents such as monoethanolamine (MEA) and diethylamine (DEA). Although the selectivity of this form of separation is relatively high, it is costly due to high energy needs in solvent regeneration and space requirements [3]. An alternative approach to absorption is adsorption in which, the contaminants are removed from the gas mixture by porous solid adsorbents. The most common adsorbents used in natural or produced gas treatment to remove acid gases are carbon based, silica based, and metal organic

frameworks (MOFs) [4–6] adsorbents. The porous solid adsorbents could have amorphous and/or crystalline structure at both the macro and nanoscale. The MOFs and silica are two common representative examples of ordered crystalline structure, while the structure of carbon based adsorbents such as biochar are amorphous but contain some local crystalline structures of aromatic compounds. As the feedstock and processing conditions determine the nature of the biochar, biochars will have different molecular architectures and variable topologies, making them difficult to characterize [5].

Biochar produced from thermochemical conversion of biomass has been used for a number of different applications including structural fill and soil stabilization for construction[4], soil /water decontamination [7] and as adsorbents in gas effluent treatment [8]. The application depends on the properties of the biochars which in turn depend on the feedstock type, pyrolysis temperature, and residence time [9]. Biochar can be generated through thermal treatment of lignocellulose biomass, such as coconut [10], almond [11], palm kernel [12], pistachio nut shell [13], and wood [14] as well as municipal and industrial waste and activated sludge [15,16]. Using biochar as an adsorbent in the gas treatment process could be a sustainable approach if the biomass source is a waste material.

In this article, the application of biochar as an adsorbent for removal of contaminants from gaseous phase has been reviewed. This review includes a summary of the most common sorbents for removal of acid gases from natural or produced gas, processes used to produce biochar and the resulting properties, as well as research related to biochar

adsorption isotherms and mechanisms. Research in process systems and molecular modeling of $H_2S$ and $CO_2$ adsorption by biochar is also reviewed.

### 2.1. Common sorbents for removal of contaminants from gases

There are key criteria that a sorbent material must satisfy, for the sequestration of contaminants to be both economical and operational, including; high adsorption capacity to reduce both adsorbent quantity and equipment size, low friction rate and the ability to tolerate high temperatures, fast adsorption kinetics, stability in oxidizing/reducing environments such as acid gas, steam, and hydrocarbons, and regenerability [17]. Several types of sorbents have been developed over the last two decades which are capable of removing acid gases: (1) carbon based adsorbents (2) microporous and mesoporous silica and (3) metal organic frame works. These three groups are applicable for adsorption of many gaseous compounds, especially hydrogen sulfide and carbon dioxide.

#### 2.1.1. Silica based adsorbents

Silica gels have been used commercially as an adsorbent since World War I. The surface areas range from 200 to 800 $m^2/g$ [18]. Grafting amine functional groups to the pore walls of silica is a strategy for designing new adsorbents and catalysts for treatment of natural gas [19]. This sorbent is similar to aqueous alkaline amine based solvents where the amines covalently linked to the silica chemically bind to the target gaseous components. Amino-functionalized mesoporous silica provides large surface areas, pore volumes and well defined pore structures. Huang et al. [20] studied the feasibility of natural gas desulfurization by amine-grafted silica in 2003. Burwell and Leal [21]

reported selective chemisorption of sulfur dioxide on amine modified silica gel, and Leal et al. [22] investigated carbon dioxide adsorption on amine-grafted silica gel. Table 2-1 illustrates some selected silica based adsorbents' function used in acid gas removal field.

Table 2-1: Silica based sorbents for acid gas removal

| **Silica based adsorbents** | **Adsorbed Gas** | **Uptake (mmol/g) Operating Conditions** | **Refs.** |
|---|---|---|---|
| Silica Xerogel/ 3-aminopropyltriethoxy-silane | $CO_2$ | 1.12<br>25 ºC, 1 bar | [23] |
| MCM-41 Silica/ Dimethyldecylamine | $CO_2$ | 2.5<br>25 ºC, 1.4 bar | [24] |
| MCM-48 Silica/Aminopropyl (3.42 wt%) | $CO_2$ | 0.8<br>25 ºC, ~1 bar | [25] |
| Silica Xerogel | $H_2S$ | 0.01<br>30 ºC, 1 bar | [26] |
| Silica Xerogel/Diethylenetriamine (50 wt%) | $H_2S$ | 0.3<br>30 ºC , 1 bar | [26] |
| MCM-41 Silica/ Dimethyldecylamine | $H_2S$ | 3.5<br>25 ºC , 1.4 bar | [24] |

The above experimental results indicate that the adsorption capacity of pure silica adsorbents is lower than amine functionalized silica. However, grafting amines to silica increases the cost and cannot increase the adsorption capacity notably compared with other adsorbents such as MOFs.

### 2.1.2. Carbon based adsorbents

One of the most important commercial adsorbents is activated carbon, typically derived from sources such as coals (e.g., bituminous coal, lignite), industrial by-products (e.g., scraps of polymeric materials, petroleum), and lignocellulose biomass (e.g., saw

dust, coconut shells, olive stones) [27]. The first step in producing activated carbon (AC) is carbonization in order to produce char. All moisture and volatile compounds are removed thorough this process and physical or a chemical activation follows [67]. Activating agents such as $CO_2$, steam, and air, or a combination of these, at temperatures between 800 to 1250 K are used in physical activation, and alkaline metal and acids are used in chemical activation. Higher porosity increased surface area, and increased pore volume are the main advantages of the activation process [28]. Activated carbon is a widely used adsorbent in gas treatment, water purification, etc. The capacity of activated carbon decreases as the temperature increases; therefore, AC is suitable for low temperature (15-55 °C) application especially for $CO_2$ capture [29].

The industrial application of commercial adsorbents such as zeolite and activated carbon as acid gas adsorbents is restricted because of low selectivity at high temperature, poor adsorption in presence of water vapour, and high cost of regeneration. The regeneration temperature of AC and zeolite is 400-500 ºC and 200 ºC, respectively [30,31].

Several research groups have investigated activated carbon for gaseous sulfur compounds removal. Table 2-2 highlights the impact of activation conditions and source of activated carbon on the sorption properties. For instance, despite the larger surface area in activated wood carbon under acidic conditions, the palm carbon activated under basic conditions with a lower surface areas showed a comparable (although lower) capacity (68 mg/g) for removing acid gases such as $H_2S$.

Table 2-2: Physical and chemical activation conditions and characteristics of activated carbon for removal of $SO_2$ and $H_2S$

| Raw material | Adsorbate | Activation Condition | $S_{BET}$*($m^2$/g) | Sorption capacity (mg/g) | Refs. |
|---|---|---|---|---|---|
| Palm shell | $SO_2$ | $CO_2$, 1100 ºC | 984 | 121.7 | [32] |
| | $H_2S$ | KOH, 30 wt% | 1148 | 68 | [33] |
| Coconut shell | $SO_2$ | Steam, 800 ºC Cu, 3 wt% | 1054 | 24 | [34] |
| | $H_2S$ | Base impregnation | 931 | 215.4 | [35] |
| Wood | $SO_2$ | $H_3PO_4$ activation | 1708 | 120 | [36] |
| | $H_2S$ | $H_3PO_4$ activation | 1470 | 30.9 | [37] |
| Pistachio nut shell | $SO_2$ | $CO_2$, NaOH activation | 1064 | 89.6 | [38] |

* Surface area measurement method: Brunauer-Emmer-Teller (BET)

### 2.1.3. Metal Oxide based adsorbents

Metal oxide based adsorbents can remove sulfur by forming insoluble metal sulfides. Pure metal oxides without a framework have low porosity, surface area, evaporation, and can sinter and mechanically decompose reducing life time and performance [39]. The general reaction between a metal oxide based sorbent and hydrogen sulfde is:

$$M_xO_y(s) + yH_2S \leftrightarrow M_xS_y(s) + yH_2O\ (g) \quad [40–43] \tag{1}$$

where M is the representative metal. Xue et. al studied low temperature removal of $H_2S$ from natural gas using simple oxides of Zn, Ag, Cu, Co, Ni, Ca, Mn and Sn, and mixed oxide of Zn containing Zr, Ti, Al, Cu, Mn, Co, Ni and Fe [44]. Table 2-3 summarizes metal oxides removal of $H_2S$ from natural gas at low temperatures. Mixed metal oxides indicate higher $H_2S$ adsorption capacity compared to single used metal.

Table 2-3: $H_2S$ sorbents at low temperature from selected publications

| Adsorbents | Parameters Tested | $H_2S$ Uptake | Refs. |
|---|---|---|---|
| Zn-O based | Space velocity, Temperature (300-400 °C), Steam concentration, and particle size | 0.1-0.8 (mmol S/g) | [45] |
| Cu-O based | Adsorption Temperature, Space Velocity, and Calcination Temperature | 0.5 (mmol $H_2S$/g) | [46] |
| Fe-Mn–Zn–Ti–O mixed-metal oxides | Temperature (25-100 °C) | 2.5 -7.8 (mmol $H_2S$/g) | [47] |
| Mixed metal oxide Cu-Zn- Al | Temperature (40- 100 ºC) | 2.1-10.8 (mmol S/g) | [48] |

Other groups have investigated moderate (400-600 °C) to high temperatures (600-850 ºC) $H_2S$ removal using various oxides (Table 2-4). This table shows the high stability of metal oxide based adsorbents at high temperature (up to 900 ºC).

Table 2-4: $H_2S$ sorbents at mid to high temperature from selected publications

| Materials | | Sulfidation condition | Refs. |
|---|---|---|---|
| Zinc – Based | Zinc oxide (ZnO) | 375- 800 °C | Sasaoka et al. [49] |
| | | 500 ºC | Sasaoka et al. [50] |
| | Zinc Ferrite (Zn $Fe_3O_4$) | 500- 700 °C | White et al. [51] |
| | Zinc Titanate (Zn-$TiO_2$) | 600- 650 ºC | Lew et al. [52] |
| Copper – Based | CuO – $Al_2O_3$ | 550 - 800 °C | Patrick et al. [53] |
| | Cu - V and Cu - Mo | 300 – 700 ºC | Yaserli et al. [54] |
| Calcium – Based | Uncalcined limestone | 570- 850 °C | Fenouil and Lynn [55] |
| | Limestone, dolomite | 750- 950 ºC | Yrjas et al. [56] |
| Manganese – Based | MnO/$Al_2O_3$ | 600 °C | Atakul et al. [57] |
| | Mn Ore | 550- 850 ºC | Yoon et al. [58] |
| Iron – Based | Ferric Oxide ($Fe_2O_3$) Ferrous Ferric Oxide ($Fe_3O_4$) | 600- 900 °C | Tseng et al. [59] |
| | | 550- 700 ºC | White et al. [60] |

In the area of $CO_2$ adsorbents, Sayyah et al. (2013) studied alkaline metal oxides:

$$MO(s) + CO_2(g) \leftrightarrow MCO_3(s) \text{ [61]} \quad (2)$$

CaO-based metal oxides are attractive due to relatively low cost, abundance, high adsorption capacity, and fast adsorption/ desorption kinetic [62,63] Table 2-5 summarizes some of this work. The mixed metal oxide based adsorbents represent better CO2 adsorption capacity, likewise for capturing $H_2S$.

Table 2-5: $CO_2$ adsorbents at different adsorption temperature

| Materials | Adsorption Temperature (°C) | Adsorption Capacity (mmol/g) | Ref. |
|---|---|---|---|
| CaO | 750 | 2.73 | [64] |
| MgO | 50,75,100 | 0.66,0.59,0.68 | [65] |
| FeO | 25 | 0.031 | [66] |
| $Fe_2O_3$ | 25 | 0.068 | [66] |
| $Fe_3O_4$ | 25 | 0.028 | [66] |
| CaO/MgO | 750 | 3.86 | [64] |
| $CaO/Al_2O_3$ | 650 | 4.32 | [67] |
| $MgO/Al_2O_3$ | 60 | 1.36 | [68] |

### 2.1.3.1. Metal Organic Frameworks (MOFs)

Metal organic frameworks are inorganic–organic hybrid materials comprised of single metal ions or polynuclear metal clusters corners connected by organic ligands formed one, two or three dimensional structure [69]. The metal cations on the surface of these sorbents make it applicable to the desulfurization of natural gas [19]. Highly porous

MOFs featuring high localized charge density, large pore volumes and increased surface areas have the ability to improve the $CO_2$ and $H_2S$ sorption energetics. The targeted design and synthesis of MOFs is in early stages, however several groups have already made significant contributions looking at tailored MOFs for various gaseous compound removal. Fig. 2-1 outlines the synthesis of two common MOFs and Table 2-6 summarizes work in MOFs as adsorbents in acid gas removal.

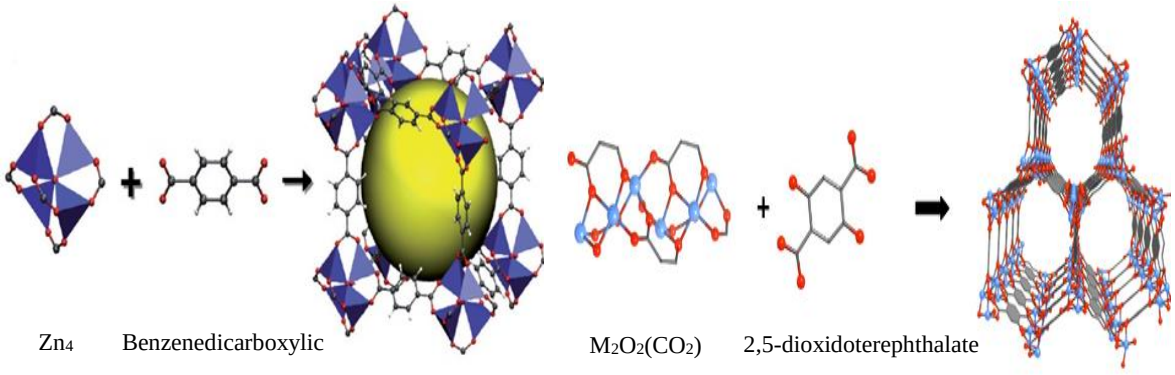


Figure 2-1: Synthesis of (a) MOF-5 [69] and (b) MOF-74 [70]

Table 2-6: Various MOF gas sorbents

| MOFs | Adsorbed Gas | Uptake (mmol/g) Operation Condition | Refs. |
|---|---|---|---|
| MIL-53 (amine functionalized) | $CO_2$ | 6.7 30 ºC, 5 bar | [71] |
| Cu-BTC | $CO_2$ | 16.5 25 ºC , 15 bar | [72] |
| Mg-MOF-74 | $CO_2$ | 14.8 30 ºC , 30 bar | [73] |

| | | | |
|---|---|---|---|
| Mg-MOF-74 | $CO_2$ | 8.9<br>30 ºC , 1 bar | [73] |
| HKUST-1-E | $H_2S$ | 2.1<br>25 ºC , 1 bar | [74] |
| CU-BTC/GOSA (Sulfanilic acid(SA) modified Graphite Oxide (GO)) | $H_2S$ | 3.9<br>25 ºC , 1 bar | [75] |
| MOF-5 | $H_2S$ | 0.5<br>25 ºC , 1 bar | [76] |
| MOF-5/GO (Graphite Oxide (2-7 wt%)) | $H_2S$ | 0.7-3.8<br>25 ºC , 1 bar | [76] |

## 2.2. Production and properties of biochar

### 2.2.1. Woody biomass as feedstock

Typically, woody and agricultural biomass consists of four main components: cellulose, hemicellulose, lignin, and water (Fig. 2-2). Biomass is categorized into wet and dry based on initial moisture content. “Wet” biomass such as freshly cut wood, vegetable/animal waste, and sewage sludge contains additional water resulting in a total water content of more than 30% of the dry weight of the wood, where “dry” biomass contain 12-19% of water stored in the cellulose/lignin structure [77]. Wet and dry biomass can be further classified into two groups: purpose-grown biomass and waste-biomass. Purpose-grown crops have low moisture content (below 10%), a relatively high yield and energy content, and generally need very low maintenance compared to other crops [78]. Waste biomass varies widely and includes agro-forestry waste, animal manure

waste, organic-food wastes, and sewage sludge [79]. The advantages of using waste biomass versus purpose grown or food crops as a feedstock in bioproducts is the utilization of material that would otherwise require disposal and no land requirement to produce the feedstock. Biochar is produced from biomass through a number of different processes outlined in the next section.

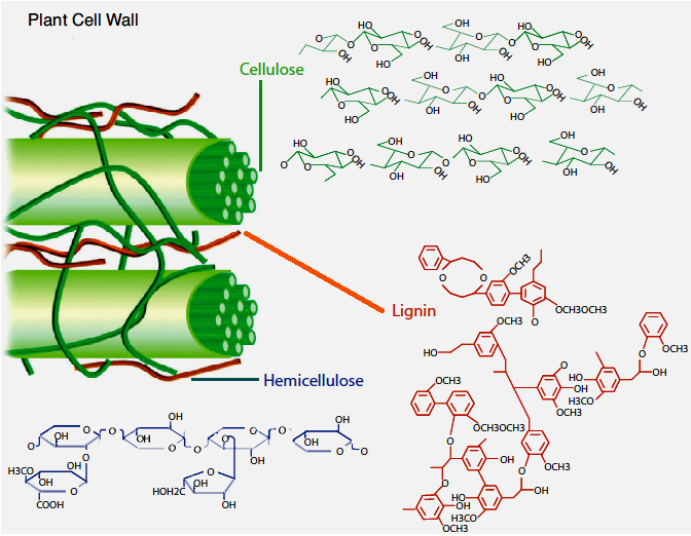


Figure 2-2: Structure of Lignocellulosic biomass [80]

### 2.2.2. Biochar production processes

Pyrolysis, torrefaction, gasification, and hydrothermal carbonization produce biochar. In pyrolysis, biomass is heated between 300 to over 650 ºC (slow to flash pyrolysis) in the absence of oxygen. The three main products are a carbon-rich solid (biochar), a condensed liquid phase (bio-oil), and non-condensable gases such as CO, $CO_2$, $CH_4$, and $H_2$ [81,82]. The types of pyrolysis process (slow, intermediate, fast, and flash) depend on temperature, residence time, and heating rate (see Table 2-7). Table 2-7 is beneficial for

comparison of amount of biochar produced in each process time. Slow pyrolysis is associated with a low peak temperature, slow heating rate, and long residence times. The major product is biochar (25-35%) [83]. In fast pyrolysis, the major product is the condensable liquid, with residence time in seconds to minutes; however, there is also small portions of granular biochar as a product.

Gasification typically refers to the process of partial combustion of biomass at very high temperatures 600-1200 ºC. The main product of this process is a mixture of gases or synthetic gases (CO, $H_2$, and $CO_2$). Most of the organic materials are changed into gases; so, the amount of biochar produced in gasifiers is very small (<10%) [84].

Torrefaction is lower temperature (200-300 ºC) thermal treatment with residence times of 30 min to two hours, also referred to as mild pyrolysis, used to improve biomass properties [85]. The solid product of torrefaction is not truly a "biochar", as the torrefied biomass still contains some volatile organic compounds and therefore has properties between raw biomass and biochar [86].

Hydrothermal carbonization (HTC), referred to as ''wet pyrolysis', occurs at temperatures between 180-250 ºC in a biomass-water mixture under elevated pressure for one to twelve hours [87]. The HTC process results in the formation of three main products: solid particles (hydrochar), liquid (bio-oil mixed with water) and small fractions of gases (mainly $CO_2$) [88].

Table 2-7: Different types of thermochemical reaction

| Processes | Reaction Condition | Biochar | Liqu | Gas |
|---|---|---|---|---|

| | Temperature | Residence time | wt% | id wt% | wt% | Ref. |
|---|---|---|---|---|---|---|
| Slow pyrolysis | 550-950K | 45-550 sec | 35 | 30 | 35 | [89] |
| Fast pyrolysis | 850-1250K | 0.5-10 sec | 12 | 75 | 13 | [89] |
| Flash pyrolysis | 1050-1300K | <0.5 sec | 20 | 50 | 30 | [89] |
| Gasification | ~900-1500K | 10-20 sec | 10 | 5 | 85 | [90] |
| HTC | ~500-600 K | 1-12 h | 50-80 | 5-20 | 2-5 | [91] |

### 2.3. Biochar as a substitute for activated carbon (AC)

As indicated above, activated carbons are widely used as adsorbents in the removal of contaminants from liquids or gases due to large internal surface area (typically 200–2000 $m^2/g$) [92] and pore volumes (0.1-1 $cm^3/g$) [92]. Commercial processes to make activated carbons use degraded and calcified plant matter (e.g. peat, lignite, all ranks of coal) and various lignocellulose materials or agriculture wastes. Activated carbon used in hydrogen sulfide adsorption from gaseous phases, mainly implement impregnated carbon as an adsorbent [93,94]. A well-known side effect of impregnation is that the spontaneous ignition temperature (SIT) of the matrix is reduced. The oxidation of the organic compounds or impregnates, initiates a temperature rise accelerating the reaction rate or self-heating. When the temperature is high enough, the carbon starts to oxidize and contributes to further temperature increases. Ignition occurs when sufficient oxygen is

adsorbed in the form of oxygen complexes [95]. As a result, fire can sometimes occur during bulk shipping or even during its production. Therefore, special packaging is necessary to ensure safe shipment, which increases the costs of the products [96].

Another disadvantage of impregnated carbons is the mechanism of oxidation of hydrogen sulfide, which is mainly converted to elemental sulfur [97]. Sulfur deposited on the surface blocks the pore structure making regenerating in situ difficult utilizing expensive methods such as washing with water [98,99]. The capacity of impregnated carbon is actually lower than unmodified for low concentrations of $H_2S$ [100–102]. AC production requires either physical or chemical activation processes involving high temperatures (up to 950 °C), pressures and often caustic chemicals that produce waste [103]. Additional modifications to improve AC performance, such as surface functionalization with amines and metal oxides, have been used [104,105]. These functionalized activated carbons often perform better, however the process of activation is time consuming and costly and regeneration may be difficult. Waste ACs made from lignite and coals can result in adsorption of moisture leading to oxidation reactions and resulting in desorption of pollutants, thus creating a hazardous environment [106]. Biochar is a plausible alternative to AC as an adsorbent for toxic gases ($CO_2$, $H_2S$) as it is environmentally sustainable, cost-effective (sourced from waste) and more easily remediated. Table 2-8 shows the comparison of biochar with other adsorbents, the uptake amount is corresponded to temperature range. Despite the much lower surface area, Gonzalez et al. [108] showed that biochar by single-step activation with $CO_2$ generated from olive stone and almond shell was just more effective than commercial activated

carbon at uptake of $CO_2$. The adsorption process highly depends on pressure as well as other factors such as temperature and surface area. Ranjani et al. reported the capacity of activated carbon ~9 mmol/g at 25 ºC up to a pressure of 300 psi (~15000 mm Hg) [107], twice that of biochar.

Table 2-8: Comparison of biochar with other adsorbents

| Adsorbents | Surface area ($m^2/g$) | Adsorbate | T (ºC) | P (mm Hg) | Uptake (mmol/g) | Ref. |
|---|---|---|---|---|---|---|
| Biochar | 16.7-1063 | $CO_2$ | 0-50 | 900 | 1.5-4.5 | [108] |
| | | $H_2S$ | 25 | 760 | 0.23 | [8] |
| Zeolite | 924.1 | $CO_2$ | 25-250 | 500 | 0.3-0.2 | [109] |
| | | $H_2S$ | 30 | 30002 | 2.5 | [110] |
| Activated Carbon | 1470 | $CO_2$ | 25-300 | 500 | 2.0-0.2 | [109] |
| | | $H_2S$ | 25 | 760 | 0.9 | [37] |
| Alumina | 128.8 | $CO_2$ | 300 | 500 | 0.3 | [37] |
| | | $H_2S$ | 450 | 760 | 2.9 | [111] |
| Solid Amine | 1389 | $CO_2$ | 75 | 760 | 1.5-0.3 | [43] |

| | | | | | | |
|---|---|---|---|---|---|---|
| | | $H_2S$ | 25 | 760 | 0.67 | [23] |
| MOF | 290-3000 | $CO_2$ | 25 | 0-3000 | 0.6-1 | [112] |
| | | $H_2S$ | 25-100 | 760 | 2.5-7.8 | [47] |

## 2.4. Effect of production condition on biochar properties

The adsorption efficiency of biochar depends on biochar properties, which are in turn a function of pyrolytic temperature, residence time, feedstock, and type of pyrolysis process. The temperature of pyrolysis has more influence on biochar properties than other production conditions [113,114]. Organic compounds in the biomass showed higher carbonization as temperatures increased and produce more ash. In softwoods, the degree of carbonization is greater than hardwood as temperature is increased (Fig. 2-3 and 2-4). In addition, the surface area and pore size increases with increasing temperature. BET results show that the surface area of woody biomass depends on temperature as well as type of feedstock as indicated in Fig 2-5. Oxygen and hydrogen content decreased with increasing pyrolysis temperature generating a hydrophobic biochar surface and effective adsorption of nonpolar molecules such as carbon dioxide (Fig. 2-6). The potential of utilizing biochar for various applications depends on these properties. As such, by changing operating conditions the suitable biochar with specific characteristics can be obtained.

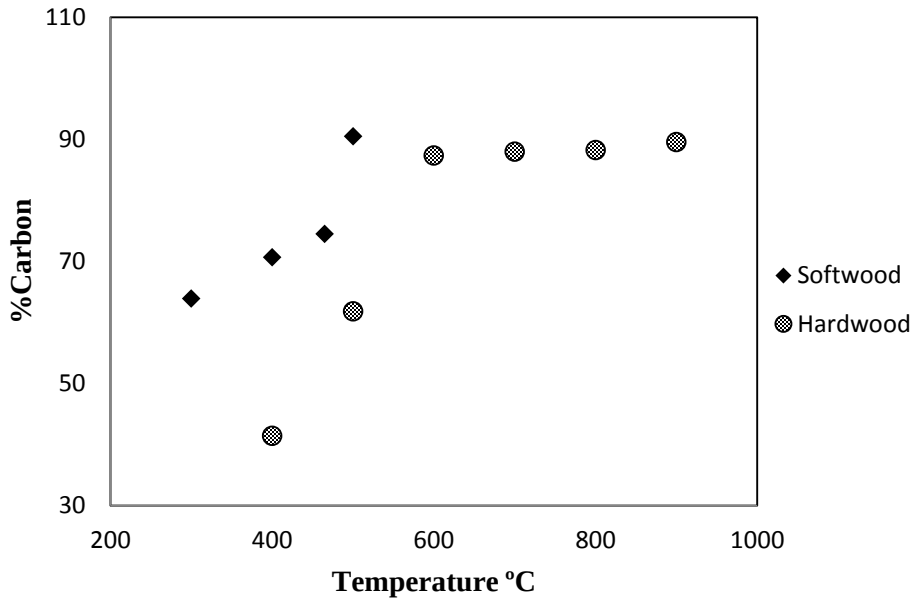


Figure 2-3: Carbon content of softwood [114–116] vs. hardwood [117–119] as a function of pyrolysis temperature in fast pyrolysis process

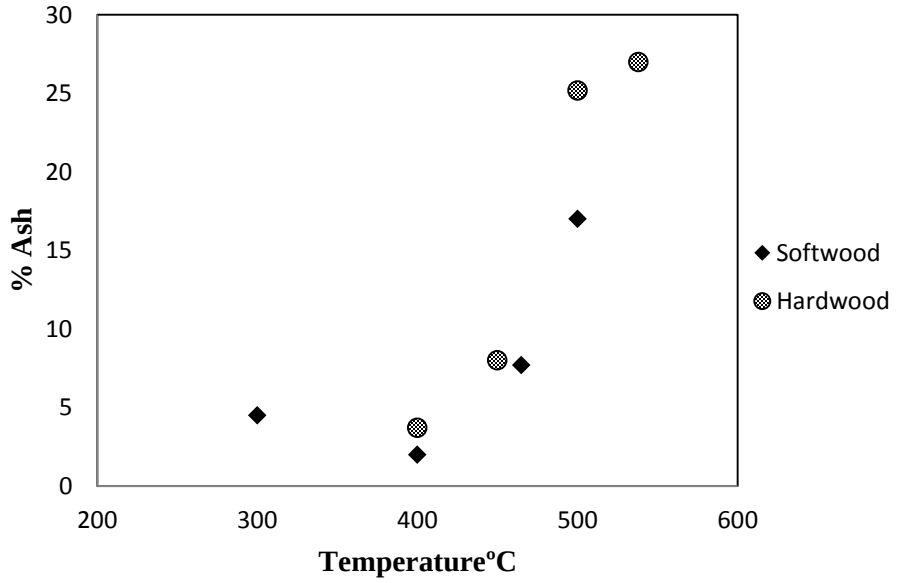


Figure 2-4: Ash content of softwood [114,115] vs. hardwood [116,118,120] as a function of pyrolysis temperature in fast pyrolysis process

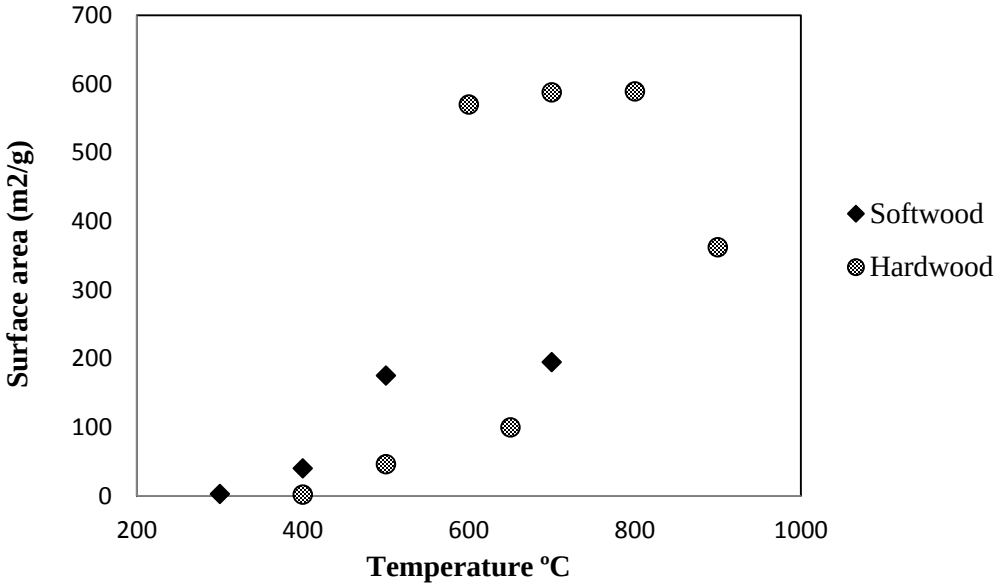


Figure 2-5: Surface area of softwood [114,116] vs. hardwood [116,118,119] as a function of pyrolysis temperature in fast pyrolysis process

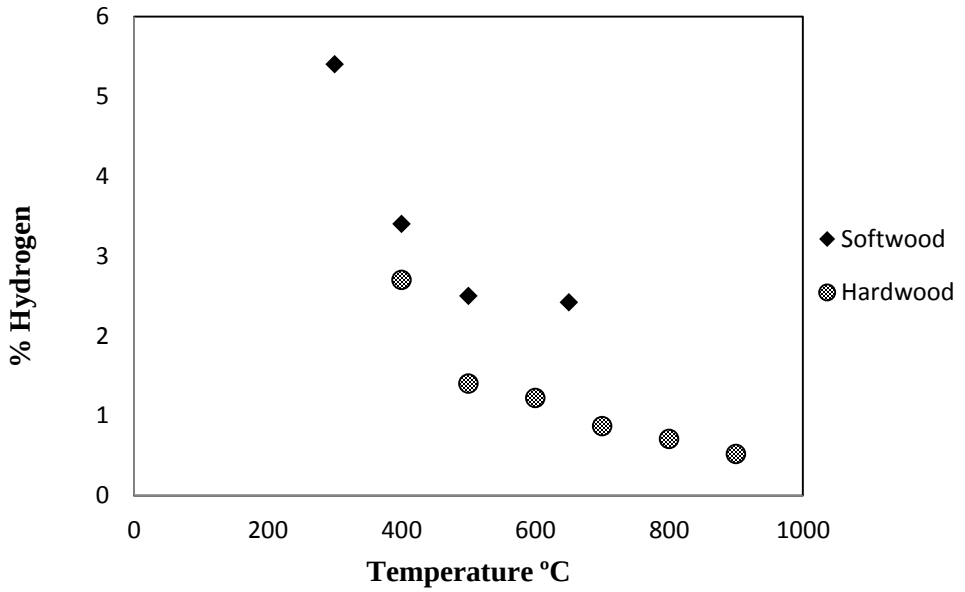


Figure 2-6: Hydrogen content of softwood [114,116] vs. hardwood [117–119]as a function of pyrolysis temperature in fast pyrolysis process

## 2.5. Application of biochar for gas treatment

The most common application of biochar is as a soil amendment to improve soil quality and mitigate greenhouse gas emissions [121]. Specific examples of other application include using biochar as a catalyst for syngas cleaning [122], conversion of syngas to liquid hydrocarbon [123], and sorbent for contaminant reduction in soil, water, and gases [124]. There is a limited research published on the applications of biochar as a gas adsorbent and/or catalyst.

A review of studies on the $H_2S$ and $CO_2$ adsorption mechanisms using biochar and molecular modeling of the adsorption is presented below.

### 2.5.1. $H_2S$ and $CO_2$ adsorption mechanisms on carbon surfaces

Several mechanisms have been proposed for the reaction between hydrogen sulfide and carbon surfaces; however, it is not yet fully understood. Generally, the mechanism of hydrogen sulfide adsorption consists of seven steps as follows [125]; (1) transport of the gas from the bulk of a mixture to a solid particle, (2) transport of the reactants in the pores of the adsorbent particles to an active site, (3) adsorption of the reactants to the active site via Van der Waals forces, (4) reaction of reactants to form an adsorbed product, (5) desorption of the product from the active site, (6) transport of the products in the pores of the catalytic particle out of the particle, (7) and transport of the products from the particle to the bulk of the mixture.

In 2000, Adib et al. [101] proposed a mechanism for $H_2S$ oxidation at low temperature (<100 ºC) and humid conditions on to carbon material. This mechanism consists of four

steps: (3) $H_2S$ adsorption on the carbon surface, (4) dissolution of $H_2S$ in water film, (5) dissociation of $H_2S$, (6) Surface reaction with oxygen.

Physical Adsorption

$$H_2S_{gas} \xrightarrow{K_H} H_2S_{ads} \quad \textbf{(3)}$$

$$H_2S_{ads} \xrightarrow{K_s} H_2S_{ads-liq} \quad \textbf{(4)}$$

$$H_2S_{ads-liq} \xrightarrow{K_a} HS^-_{ads} + H^+ \quad \textbf{(5)}$$

Oxidation

$$2HS^-_{ads} + O^*_{ads} \xrightarrow{K_R} 2S_{ads} + H_2O \quad \textbf{(6)}$$

O*: dissociative adsorbed oxygen

In 2001, Bagreev et al. [126] examined three types of microporous activated carbon as hydrogen sulfide adsorbent as a function of pH. They concluded that moderately low pH in the acidic range promotes the oxidation of $H_2S$ to sulfur oxide and the water regenerate after reaction and the high pH results in $H_2S$ oxidation to elemental sulfur. In 2002, Yan et al. [127] expanded the mechanism proposed by Adib for alkaline carbons. The physical adsorption mechanism was the same however, the oxidation mechanism was expanded and determined the formation of sulfuric acid causes a significant decrease in adsorption capacity of adsorbent.

$$HS^-_{ads} + O^*_{ads} \xrightarrow{K_R} S_{ads} + OH^- \quad \textbf{(7a)}$$

$$HS^-_{ads} + 3O^*_{ads} \xrightarrow{K_R} SO_{2,ads} + OH^- \quad \textbf{(7b)}$$

$$SO_{2,ads} + O^*_{ads} + H_2O_{ads} \xrightarrow{K_R} H_2SO_{4_{ads}} \quad \textbf{(8)}$$

$$H^+ + OH^- \xrightarrow{K_R} H_2O \quad \textbf{(9)}$$

Chiang et al. [128] proposed a conceptual reaction for $H_2S$ adsorption on activated carbon at low temperature. Fig. 2-7 illustrates the steps of adsorption of $H_2S$ on activated carbon. The $H_2S$ is transferred from the bulk phase into the pore of the activated carbon (Fig. 2-7b) $H_2S$ is adsorbed on activated carbon (Fig. 2-7c) The adsorbed-$H_2S$ reacts with the surface oxygen functional groups to dehydrate and form thiol structures on the carbon surface (Fig. 2-7d) Thiols react with each other to form disulfide bonds (Fig. 2-7e) The disulfides further react to form multi-connected sulfur. Finally, a stable crown structure of $S_8$ is formed (Fig. 2-7f).

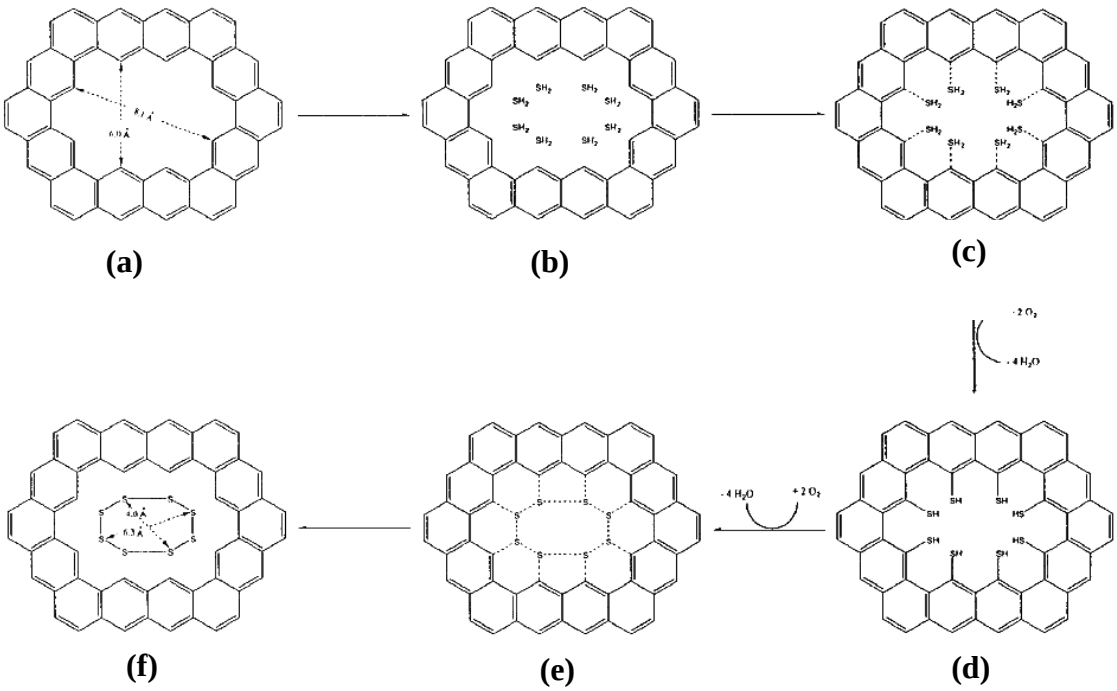


Figure 2-7: Reaction of $H_2S$ adsorption on activated carbon [128]

In 2003, Leuch et al. [129] expanded the primary mechanism proposed by Adib et al. under dry conditions to quantify activated carbon cloth capacities in the removal of hydrogen sulfide present in air. The suggested mechanism is as follows:

$$H_2S_{gas} \overset{K_H}{\rightarrow} H_2S_{ads} \quad \textbf{(1)}$$

$$O_{2,gas} \leftrightarrow O_{2,ads} \quad \textbf{(2)}$$

$$H_2S_{ads} \overset{K_s}{\rightarrow} H_2S_{ads-liq} \quad \textbf{(3)}$$

$$O_{2,ads} \leftrightarrow O_{2,ads-liq} \quad \textbf{(4)}$$

$$H_2S_{ads-liq} \overset{K_a}{\rightarrow} HS^-_{ads} + H^+ \quad \textbf{(5)}$$

$$2C^* + O_2 \overset{K_R}{\rightarrow} 2C(O^*) \quad \textbf{(6)}$$

$$HS^-_{ads} + C(O^*)_{ads} \overset{K_R}{\rightarrow} S_{ads} + OH^- \quad \textbf{(7a)}$$

$$HS^-_{ads} + 3C(O^*)_{ads} \overset{K_R}{\rightarrow} SO_{2,ads} + OH^- \quad \textbf{(7b)}$$

$$SO_{2,ads} + C(O^*)_{ads} \overset{K_R}{\rightarrow} SO_{3_{ads}} \quad \textbf{(8)}$$

$$H^+ + OH^- \overset{K_R}{\rightarrow} H_2O \quad \textbf{(9)}$$

$$SO_{3_{ads}} + H_2O \overset{K_R}{\rightarrow} 2H^+ + SO_4^{2-} \quad \textbf{(10)}$$

where C* is a radical form at the carbon surface.

Bagreev et al. [130] suggested a mechanism for oxidation of hydrogen sulfide by activated carbon and unlike previous mechanisms, hydrogen sulfide does not adsorb on to

carbon surfaces. Instead the carbon surface plays an important role in the oxidation of $H_2S$:

$$C_f + 1/2\ O_2 \overset{K_R}{\rightarrow} C(O) \quad (1)$$

$$C(O) + H_2S \overset{K_R}{\rightarrow} C_f + S + H_2O \quad (2)$$

$$S + xS \overset{K_R}{\rightarrow} S_{x+1} \quad (3)$$

$$S + O_2 \overset{K_R}{\rightarrow} SO_2 \quad (4)$$

where $C_f$ is an active site of carbon

Shang et al. [8] used three different types of biochar sourced from camphor, bamboo, and rice hull as a substitute for activated carbon. Initially it was speculated that the reaction between biochar and hydrogen sulfide is the same as the mechanism proposed by Yan et al. [127] for activated carbon. However, the work indicated $H_2S$ removal by biochars likely differs from the impregnated ACs with caustic (NaOH) due to the presence of caustics in the ACs. Caustics catalyze most of the bases to hydrogen sulfide and cause acidic conditions; therefore, the adsorption capacity of AC decreases significantly. However, the pH of environment of biochar system decreases slightly during reaction and results higher capacity than AC.

Xu et al. [131] proposed a mechanism for hydrogen sulfide removal by biochars derived from pyrolysis of pig manure and sewage sludge.

$$H_2S_{gas} \overset{K_H}{\rightarrow} H_2S_{ads} \overset{K_s}{\rightarrow} H_2S_{ads-liq} \quad (1)$$

$$H_2S_{ads-liq} + OH^- \overset{K_a}{\rightarrow} HS^-_{ads} + H_2O \quad \textbf{(2)}$$

$$HS^-_{ads} + O_2 \overset{K_R}{\rightarrow} S^0 \quad \textbf{(3)}$$

$$HS^-_{ads} + O_2 + H_2O \overset{K_R}{\rightarrow} {SO_4}^{2-} \quad \textbf{(4)}$$

He [132] and Lehmann [133], using SEM-EDS, determined ${SO_4}^{2-}$ was formed on the surface of the biochars while $S^0$ was present in the pores of biochar. It was postulated the excess $O_2$ on the surface oxidized the $H_2S$ to ${SO_4}^{2-}$ but limited $O_2$ in the pores resulted in an incomplete oxidation of $H_2S$ to $S^0$; however, it needs further study.

In contrast to $H_2S$, the adsorption of carbon dioxide onto biochar is mainly controlled by physiosorption. In this type of adsorption, adsorbate adheres to adsorbent by weak interaction like Van der Waals forces. Studies indicate the amount of $CO_2$ adsorbed decreased by increasing the temperature [134,135]. Overall, the heat of adsorption is between 5-800 kJ/mol and predominantly a function of the pore size distribution [136]. Physiosorption is typically 5-40 kJ/mol and the experimental results show that the $CO_2$ adsorption by activated carbon is primarily via physiosorption [11,137,138]. Since biochar is a heterogeneous surface with many different functional groups, predicting a suitable mechanism between surface functional groups and acidic gases is complicated.

### 2.5.2. Application of adsorption isotherms

The adsorption capacity (Qe) of the adsorbent is a function of the temperature, equilibrium concentration of adsorbate (Ce), and adsorption energy (E). At a constant temperature, E is constant and the adsorption capacity varies only with equilibrium

concentration of adsorbate. The relationship between Qe and Ce is characterized by the adsorption isotherm [139]. The equilibrium adsorption isotherm can provide information about the surface properties of adsorbent, the adsorption behaviour, design of adsorption systems, and characterize the adsorbate distribution on adsorbent. The most common adsorption models are Freundlich and Langmuir isotherms. For homogenous adsorptions the most common isotherm is the Langmuir. Assumptions made in developing the Langmuir equation (equation 3) include a fixed number of well-defined localized sites where molecules can adsorb; all sites are equivalent in terms of energy, monolayer adsorption, and no interaction between neighbouring adsorbed molecules [140].

Langmuir Equation: $Q_e = \frac{Q_{max} K_L C_e}{1 + K_L C_e}$ (3)

where Qe is the capacity of adsorption (mg/g), Ce is the equilibrium concentration (mg/L), $Q_{max}$ is the calculated maximum adsorption capacity, and $K_L$ is constant.

The Freundlich isotherm associated with a decrease in binding strength with the increasing degree of site occupation, which means the sites with stronger binding affinities are occupied by adsorbate molecules before weaker sites [141]. In addition, Freundlich isotherms are associated with heterogeneous surfaces.

Freundlich Equation: $Q_f = K_f C_e^{1/n}$ (4)

Where Kf and 1/n are constants related to adsorption capacity and adsorption intensity, respectively.

The Freundlich isotherm is typically a better fit when there is chemisorption compared to the Langmuir due to the non-uniform energy of the surface assumed in the Freundlich versus the uniform surface in the Langmuir [140]. There are a multitude of other isotherm models which have been thoroughly reviewed by Alberti et al. [142]. Other developed isotherm models include Toth and Sips. The Toth isotherm is an empirical model that was developed to improve traditional Langmuir isotherm modeling. It is often useful for describing heterogeneous systems [11]. The energy distribution of Toth isotherm is assumed to be an asymmetric quasi-Gaussian where sites have an adsorption energy lower than the maximum [143]. The Toth isotherm is outlined in equation 5.

Toth Equation: $Q_e = Q_m \frac{C_e}{(K_T + (C_e)^n)^{1/n}}$ (5)

where Qe represents the amount adsorbed (mg/g), Qm is the saturation capacity, Ce is the equilibrium concentration (mg/L), n represents the system heterogeneity ($0<1/n<1$) and $K_T$ is the affinity constant.

Affinity Constant: $K_T = K_0 exp \frac{Q}{RT_0}(\frac{T_0}{T} - 1)$ (6)

where $K_0$ is the affinity constant at standard temperature $T_0$(K), Q is the heat of adsorption, T(K) is the system temperature and R is the universal gas constant.

The Sips isotherm is a combination of the Langmuir and Freundlich isotherms. At low pressure, the Sips reduces to Freundlich isotherm; while at high pressure, it predicts a monolayer adsorption capacity characteristic of the Langmuir isotherm. The Sips isotherm is given in the following general form [144]:

Sips Equation: $Q = Q_m \frac{K_s(C_e)^{1/n}}{1+K_s(C_e)^{1/n}}$ (7)

where Q represents the adsorbed concentration (mg/g), Qm represents the maximum adsorbed concentration, Ks is the affinity constant, Ce is the equilibrium concentration (mg/L), and n is a parameter that characterizes the heterogeneity of the system ($0<1/n<1$).

All four types of isotherms described above have been used for acidic gas adsorption on biochars specifically Toth and Sips. Table 2-9 summarizes isotherms for $CO_2$ and $H_2S$ removal systems. As Table 2-9 illustrates, different types of isotherms have been used up to the present. The Langmuir isotherm is used less than other isotherms, since this isotherm assumes monolayer coverage on a homogeneous surface with identical adsorption sites. These aforementioned simplifications could not reflect the adsorption system behaviour and the experimental data cannot correlate the isotherm appropriately. The Sips and Toth isotherms are the modified version of Freundlich and Langmuir and consequently more adsorption systems can fit with these isotherms.

In addition to isotherms and mechanism, the adsorbent capacity must be determined through a series of experiments.

Table 2-9: Adsorption characteristics of $CO_2$ and $H_2S$ removal systems

| Feedstock | Activating agent | Pyrolytic Temperature (ºC) | Adsorbate | Adsorption Temperature | Adsorption Pressure | Adsorption Capacity | Isotherm | Ref. |
|---|---|---|---|---|---|---|---|---|
| Olive stone | Air at 400-500 ºC | 600 | $CO_2$ | 0, 25, 50 ºC | 1bar | 1.95,1.56,0.4 mmol/g | Toth | [11] |
| Almond shell | Air at 400-500 ºC | 900 | $CO_2$ | 0, 25, 50 ºC | 1bar | 1.43,1.14,0.25 mmol/g | Toth | [11] |
| Olive stones | $CO_2$ and ammonia at 800 ºC | 600 | $CO_2$ | 0, 30 ºC | ~1 bar | 0.77 mmol/g | Sips | [144] |
| Almond shells | $CO_2$ and ammonia at 800 ºC | 900 | $CO_2$ | 0, 30 ºC | ~1 bar | 0.82 mmol/g | Sips | [144] |
| Eucalyptus wood | $H_3PO_4$ and Ammonia at 400 and 800 ºC | 450 | $CO_2$ | 30 ºC | 1 bar | 3.22 mmol/g | Langmuir and Freundlich | [14] |
| Palm kernel shell | $CO_2$at 800 ºC | 700 | $CO_2$ | 30 ºC | 4 bar | 7.32 mmol/g | Langmuir and Freundlich | [12] |

| | | | | | | | | |
|---|---|---|---|---|---|---|---|---|
| Palm shell | $H_2SO_4$ | 700 | $H_2S$ | 25 ºC | 1 bar | 2.24 mg/g | Freundlich | [33] |

## 2.6. Biochar Adsorption Capacity

### 2.6.1. Biochar Adsorption Capacity using Dynamic systems

In this method, a fixed bed reactor (volumetric sorption) or thermo gravimetric analyzer (TGA) (gravimetric sorption) is used to determine capacity. In the fixed bed reactor system, biochars are packed in one or more stainless steel or quartz glass columns (Fig. 2-8). The bed height of biochar in lab scale systems is set at 140-150 mm. Quartz sand or glass balls are packed both on top and on bottom of the biochar to ensure flow distribution. The source gas is passed through the fixed bed at a specific flow rate and inlet and outlet adsorbate gas concentration measured. When inlet and outlet concentrations are equal the experiment is terminated. The adsorption capacity of biochar is calculated by integration of the area below the breakthrough curves (ratio of outlet to inlet adsorbate gas concentration as a function of time plotted is the breakthrough curve). In the TGA method, the samples are dried in situ in airflow, and then allowed to cool down to 25 ºC. The adsorbate gas uptake is then evaluated from the mass gained by the sample when the feed gas is switched to a pure flow of adsorbate gas [8,131,145–148].

### 2.6.2. Biochar Adsorption Capacity using Static systems

The difference between dynamic and static system is that the static system provides sufficient contact time for accumulation of adsorbate gas in the biochar. Therefore, the static tests can determine the maximum adsorption capacity and the corresponding underlying sorption mechanism. In contrast, dynamic tests can provide the useful information regarding the adsorption kinetic and rate equations. In the static method, a

specific amount of biochar is added to an evacuated bottle. The mixture of gas and biochar is shaken for 24 h to ensure equilibrium is reached. The residual concentration of adsorbate gas in the bottle is measured using gas chromatography. The experiment is repeated until the residual concentration of adsorbate gas was equal to the injection concentration [131]. Table 2-10 summarizes different process systems studied for adsorption of $CO_2$ and $H_2S$ by biochar.

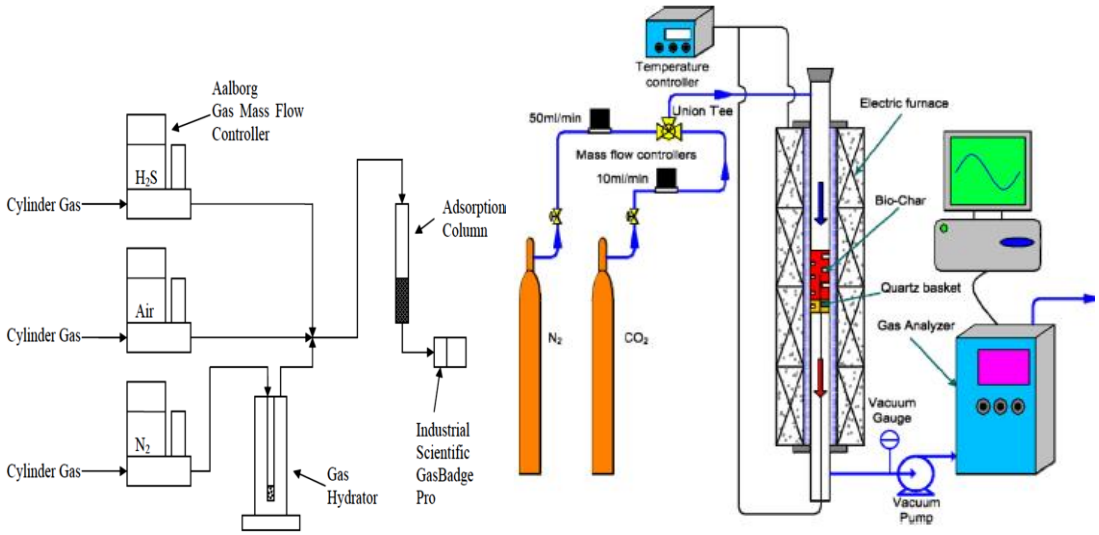


Figure 2-8: The fixed bed adsorption dynamic system for $H_2S$ (left side) [148] and $CO_2$ (right side) [146] capture

Table 2-10: Experimental setup for adsorption

| Adsorbate | Biochar feedstock | Adsorption System | Operating conditions | Factors investigated | Results | Refs. |
|---|---|---|---|---|---|---|
| $CO_2$ | Olive stones (OS) | Dynamic (fixed-bed) *ID:9.2 mm | $T_{ads}$: 25, 27 °C<br>$P_{ads}$:130, | Water vapour | No significant reduction in adso | [145] |

| | | | | | | |
|---|---|---|---|---|---|---|
| | | *LB:147 mm<br>*$W_{char}$:2.8g | 1.5 bar<br>Flow rate : 2.7, 2.8, 15 g/h | | rption of $CO_2$ | |
| | Cotton stalk | Dynamic (fixed-bed) ID:15mm $W_{char}$:5 g | $T_{ads}$: 120 ºC<br>$P_{ads}$: Ambient<br>Flow rate : 10 mL/min | $CO_2$-ammonia modification | Surface area increased significantly | [146] |
| | Almond shells and olive stones | Dynamic (TGA) ID: 20mm LB:45 cm $W_{char}$:3 g | $T_{ads}$: 25-100 ºC<br>$P_{ads}$: Atmospheric<br>Flow rate : 50 $cm^3$/min | Activation (Air at 400–500 ºC) | Narrowed porosity | [11] |
| **$H_2S$** | Camphor, bamboo, and rice hull | Dynamic (fixed-bed) ID:12mm LB:150 mm *LR:300mm | $T_{ads}$: Room temperature<br>$P_{ads}$: Ambient<br>Flow rate : 40 mL/min | Type of feedstock | Rice hull biochar highest capacity | [8] |
| | C. camphora branches | Dynamic (fixed-bed) | $T_{ads}$: room temperature | - Pyrolysis temperature - pH of | Maximum sorption | [147] |

| | | | | | | |
|---|---|---|---|---|---|---|
| | | ID:12mm<br>LB:150 mm<br>LR:300 mm | $P_{ads}$: ambient<br>Flow rate : 40 mL/min | the Surface - Particle size | capacity occurs at 0.3-0.4 mm particle size and 400 ºC | |
| | Sewage sludge and Pig manure waste | Dynamic and Static ID: 9mm LR:550mm<br>$W_{char}$:10 g, 5.5g | $T_{ads}$: Room temperature<br>$P_{ads}$: Ambient<br>Flow rate : 0.5 L/min | Moisture- Type of feedstock | Pig manure biochar had higher capacity-moisture removes $H_2S$ | [131] |

*ID: Inner Diameter, LB: Length of Bed, LR: Length of Reactor, $W_{char}$: Weight of biochar

Experiments are valuable for establishing the capacities and other key operational parameters. However, experiments can be costly and time consuming and therefore development of tools/methods to reduce the number of experiments required are important. One method is to use molecular modeling to simulate the interaction of the surface with the target compound. This type of modeling allows for "testing" the suitability of the surface with and without activation for target compounds. This type of modeling requires complete characterization of the surface and must be combined with experimental data to validate the approach and results.

## 2.7. Molecular modeling simulation of adsorption

Molecular simulations have been widely used to study the fluid adsorption on porous solids. These methods provide a link between the microscopic (molecular) and macroscopic level and simulate large systems with numerous molecules in relatively short times [149–151]. The very first computer simulation of the system consists of hard spheres in gas phase was conducted by Alder and Wainwright in 1960 in order to predict the equilibrium behavior of the system by the equation of state [152]. One of the limitations of simulation is the lack of realistic structure models. In some simulation studies, highly simplified geometric models such as infinite slit or cylindrical pores were used to model surfaces; however, these models did not predict the experimental adsorption isotherms well [153,154]. Adsorbents can be chemically heterogeneous, variable with respect to functional groups, and have finite length pores which play an important role in determining the adsorption mechanism and adsorbed phase equilibrium properties. The edge heterogeneity effect in a slit pore structure named “randomly etched graphite” model (REG) was simulated by Seaton et al. [155]. The REG model was selected because the kinetic selectivity between model and experimental data was in good agreement. Several authors have used heterogeneous surfaces in simulations [156,157], and the results have shown that changes in surfaces lead to varied adsorption isotherms.

### 2.7.1. Potential Models

#### 2.7.1.1. Fluid-Fluid interaction

The interactions between fluid molecules are due to Lennard-Jones and electrostatic interactions. The Lennard-Jones (LJ) potential (U) are described as below [158]:

$$U(r_{ij}) = \begin{cases} 4\varepsilon_{ij}\left[\left(\frac{\sigma_{ij}}{r_{ij}}\right)^{12} - \left(\frac{\sigma_{ij}}{r_{ij}}\right)^{6}\right] & r \le r_c \\ 0 & r > r_c \end{cases} \quad (9)$$

where $\varepsilon_{ij}$ (kJ/mol) is the wall depth and shows how strongly the two particles attract each other, $\sigma_{ij}$ is the diameter (nm), and $r_{ij}$ is the distance between interacting atoms *i* and *j* (nm), and $r_c$ is the cut-off radius.

$CO_2$ is modeled as a three charged center LJ molecule with $\varepsilon_{OO}/k_B$ = 80.507 K, $\sigma_{OO}$ = 0.3033 nm, $\varepsilon_{CC}/k_B$ = 28.129 K, $\sigma_{CC}$ = 0.2757 nm [159]. The O-O and C-O distances are 0.2298 nm and 0.1149 nm respectively. The intermolecular potential $U_{CO2\text{-}CO2}$ is assumed to be a sum of the interatomic potentials between the atoms of the interacting molecules, plus the electrostatic interactions due to $CO_2$ quadruple moment with point partial charges where $q_1 = q_3 = -0.3256e$ and $q_2 = +0.6512e$ [160].

$$U_{CO_2-CO_2} = \sum_{i=1}^{3}\sum_{j=1}^{3}\left[u_{ij} + \frac{q_i q_j}{4\pi\varepsilon_0 r_{ij}}\right] \quad (10)$$

where $\varepsilon_0$ is the permittivity of vacuum. The indices i (j) refer to the sites of the first (second) interacting molecules. All cross interaction potential parameters between two

sites, are calculated according to the Lorentz-Berthelot rules ($\sigma_{ij} = \frac{\sigma_{ii}+\sigma_{jj}}{2}, \varepsilon_{ij} = (\varepsilon_{ii}\varepsilon_{jj})^{1/2}$).

The $H_2S$ and $SO_2$ molecules are modeled as 3-site rigid molecules where a 3-site LJ potential plus a set of partial point charges are distributed at three electrostatic sites. The LJ potential parameters of $CO_2$, $H_2S$, and $SO_2$ are summarized in Table 2-11.

Table 2-11: LJ potential parameters for $CO_2$, $H_2S$, and $SO_2$

| Adsorbate | Site | σ (nm) | ε/$k_B$ (K) | q(e) | Angle (°) | Bond length (nm) | Ref. |
|---|---|---|---|---|---|---|---|
| $CO_2$ | C | 0.2757 | 28.129 | +0.6512 | 180 | 0.1149 | [159] |
| | O | 0.3033 | 80.507 | -0.3256 | | | |
| $H_2S$ | H | 0.098 | 3.9 | +0.124 | 91.5 | 0.1365 | [161] |
| | S | 0.372 | 250.0 | - 0.248 | | | |
| $SO_2$ | S | 0.3585 | 154.4 | +0.470 | 119.5 | 0.14321 | [162] |
| | O | 0.2993 | 62.3 | - 0.235 | | | |

### 2.7.1.2. Solid-Fluid interaction

The solid-fluid interaction is described by the site-to-site method where the solid-fluid interaction is a summation of all LJ and electrostatic interactions of the sites on fluid molecule "i" with the sites on solid atom "j". The interaction between an adsorbate and a single pore solid is described as follows [163],

$$U_{fs}(z) = 2\pi\rho_s\varepsilon_{fs}\sigma_{fs}^2\Delta\left\{0.4\left[\frac{\sigma_{fs}}{z}\right]^{10} - \left[\frac{\sigma_{fs}}{z}\right]^{4} - \left[\frac{\sigma_{fs}^4}{3\Delta(0.61\Delta+z)^3}\right]\right\} \quad (11)$$

where $\rho_s$ is the surface density of carbon atoms in the adsorbent layer, Δ is the separation between layers in adsorbent, Z is the normal distance from the site of an adsorbate molecule to the nuclei of the carbon atoms in the surface adsorbent layer; $\sigma_{fs}$ and $\varepsilon_{fs}$ are the cross interaction parameters determined by the Lorentz-Berthelot mixture rules:

$$\sigma_{fs} = \frac{\sigma_{ff}+\sigma_{ss}}{2} \tag{12}$$

$$\varepsilon_{fs} = (\varepsilon_{ff}\varepsilon_{ss})^{1/2} \tag{13}$$

$\sigma_{ss}$ and $\varepsilon_{ss}$ are the LJ parameters for the carbon surface atoms.

The total external potential ($U_{pore}$) for a fixed slit pore with width *H* (distance between the nuclei of carbon atoms on the opposite wall) can be given by [164]:

$$U_{Pore} = U_{fs}(z) + U_{fs}(H - z) \tag{14}$$

The total energy of N molecules confined in slit pore is [164]:

$$U_{total} = \sum_{i=1}^{N-1}\sum_{i+1}^{N} U_{ij}(r_{ij}) + \sum_{i=1}^{N}\sum_{j=1}^{2} U_{pore} \tag{15}$$

If the adsorbent surface has chemical impurities the total energy would be:

$$U_{total} = \sum_{i,j} U_{ij}(r_{ij}) + \sum_{i,k} U_{ik}(r_{ik}) \tag{16}$$

where *i* and *j* are adsorbate particles and *k* is carbon atom or chemical impurity. The LJ potential parameters for different carbon surfaces are showed in Table 2-12.

Table 2-12: Lennard-Jones parameters used for different carbon surfaces

| Adsorbent | Site | σ (nm) | $\varepsilon/k_B$ (K) | Ref. |
|---|---|---|---|---|
| Activated Carbon | C | 0.34 | 89.44 | [165] |
| Graphene | C | 0.34 | 28.2 | [166] |
| Graphite | C | 0.34 | 28.0 | [167] |
| Graphite, H appended | C | 0.34 | 28.0 | [167] |
| | H | 0.24 | 12.0 | |
| Graphite, OH appended | C | 0.34 | 28.0 | [167] |
| | O | 0.31 | 79.0 | |
| | H | 0.13 | 30.0 | |
| Graphite, COOH appended | C | 0.34 | 28.0 | [167] |
| | C (COOH) | 0.34 | 28.0 | |
| | O (=O) | 0.31 | 79.0 | |
| | O (-O-H) | 0.31 | 79.0 | |
| Single-Walled Carbon Nanotubes(SWNT) | C | 0.34 | 28 | [168] |

### 2.7.2. Simulation Methods

There are two common approaches to performing molecular simulations: stochastic and deterministic. In the stochastic approach, or Monte Carlo (MC), the sample configurations are generated randomly. In the deterministic approach, or Molecular Dynamics (MD), the initial state determines the microstates of the whole system. The information obtained from MD simulation methods can be used to fully characterize the thermodynamic state of the system, the time evolution, and the actual direction of the molecular system [169]. Two simulation packages, VASP and Grande Canonical Monte Carlo, are outlined below to explain each simulation method.

### 2.7.2.1. Vienna Ab-initio Simulation Package (VASP)

The Vienna Ab-initio Simulation Package is used to perform ab-initio quantum-mechanical molecular dynamics (MD) using pseudo potentials and a plane wave basis set. The code uses iterative techniques for the diagonalization of the density-functional theory (DFT). A Hamiltonian matrix calculates the total energy and optimizes the structure of system which contains thousands of atoms [170]. One of the advantages of ab-initio method is they are parameter-free and require no other input than the atomic number [171]. The basic calculation for an ab initio is the Kohn-Sham (KS) energy functional [172]:

$$E_{KS}[\rho(r)] = T_{ni}[\rho(r)] + V_{ne}[\rho(r)] + V_{ee}[\rho(r)] + \Delta T[\rho(r)] + \Delta V_{ee}[\rho(r)] \quad (17)$$

$$\rho(r) = \sum_n f_n |\emptyset_n(r)|^2 \quad (18)$$

where $f_n = 1$ is for occupied bands and $f_n = 0$ for unoccupied bands, the electronic wave functions is $\emptyset_n$, $T_{ni}$, $V_{ne}$, $V_{ee}$, $\Delta T$, $\Delta V_{ee}$ refer to the kinetic energy of non-interacting electrons, the nuclear-electron interaction, the classical electron-electron repulsion, the correction to the kinetic energy deriving from the interacting nature of the electrons, and all non-classical corrections to the electron-electron repulsion energy.

### 2.7.2.2. Grand Canonical Monte Carlo (GCMC)

The GCMC method uses a collection of microscopic systems with fixed volume ($V$), temperature ($T$) and chemical potential ($\mu$) [173]. Each microscopic system (microstate) is an identical simulation box containing a prescribed number of pores and a unique

configuration of adsorbate particles. During the simulations, the adsorbents are treated as a rigid material with atoms frozen. The periodic boundary conditions are imposed in three dimensions to mimic the crystal boundaries associated with the structure. Under these conditions, there is density and energy fluctuation and the averages of the fluctuating quantities are evaluated. The adsorption isotherm is then expressed as the average number of adsorbate molecules (or output density) versus chemical potential ($N=f(\mu)$) at a fixed temperature [160]. In microscopic systems, for single component simulations, three particle actions are possible: attempts to move particles, attempts to delete particles, and attempts to create particles. One particle is chosen at random and given a random displacement. The new configuration of selected particle is accepted with a probability that depends on the energy difference between the new (trial) and the old (current) configuration. The maximum amount of probability for displacing particle is approximately 50% [174].

For a movement attempt:

$$P_{MOV}^{ACC} = \min[1, \exp(-\beta \Delta E_C)] \tag{19}$$

For a creation attempt:

$$P_{CR}^{ACC} = \min\left[1, \frac{Z_i V}{N_i+1} \exp(-\beta \Delta E_C)\right], \; Z_i = \frac{\exp(\beta \mu_i)}{\Lambda_{t,i}^3 \Lambda_{r,i}} \tag{20}$$

For a deletion attempt:

$$P_{DEL}^{ACC} = \min\left[1, \frac{N_i}{Z_i V} \exp(-\beta \Delta E_C)\right] \tag{21}$$

$\Delta E_C$ is the change in configurational energy resulting from the trial, $V$ is the volume of system, $N_i$ is the number of particles of component $i$ in the system, $Z_i$ is the absolute activity, $\Lambda_{r,i}$ is the reciprocal of the translation molecular partition function for $i$, $\Lambda_{t,i}$ is the reciprocal of the translation molecular partition function of $i$.

Common simulation methods such as GCMC and Ab-initio used for adsorption of acidic gases on different carbon surfaces and concluding results are summarized in Table 2-13.

Table 2-13: Simulation methods used for adsorption of acidic gases

| Research area | Adsorbate | Adsorbent | Simulation Method | Results | Ref. |
|---|---|---|---|---|---|
| Adsorption and separation of acidic gases | $H_2S/CH_4$, $CO_2/CH_4$ $H_2S/CO_2$ $CH_4/CO_2/H_2S$ | Nano porous carbon (NPC) | MC | Uptake values and heats of adsorption for pure gases at low pressures in the constricted slit models > simple slit | [175] |
| Adsorption of acidic gases, Comparison between Single Walled Carbon Nano Tube(SWCNT) and Graphene/nanotube hybrid structures (GNHS) | $CO_2$ and $CH_4$ binary mixture | GNHSs | MC | GNHSs show better separation than SWCNT | [176] |
| Influence of specific functional groups on the adsorption selectivity | $CO_2/N_2$ binary mixture | Graphene nanoribbon functionalized with OH, $NH_2$, $NO_2$, $CH_3$ and COOH | MC | Functionalization increases the adsorption of both $CO_2$ and $N_2$ COOH functionalization gives a 28% increase in selectivity compared to H | [177] |
| Adsorption of acidic gases, Selectivity of the different adsorbent surfaces under a | $CO_2/CH_4$ mixtures | Mesoporous carbons, carbon foams, carbon nanotubes (CNTs), and | MC | Foam structures have the highest adsorption capacity because of its special architecture Selectivity enhanced after modification, especially at low | [178] |

| | | | | | |
|---|---|---|---|---|---|
| wide range of temperature and pressure | | nanopore models modified with hydrophilic carboxylic groups | | pressures Modified CNTs have the highest selectivity among the systems tested. | |
| Effect of Fe doping on adsorption of gases | $CO_2/N_2$ mixtures | Single-walled carbon nanotube (CNT) | MD | Combining DFT and van der Waals correction is very effective for describing the long-range interaction between $N_2/CO_2$ and the carbon nanotube (CNT), Doping of Fe atom onto the CNT surface will only affect the adsorption energy of $CO_2$ molecule | [179] |
| Elimination of $H_2S$ Contained in Biogas | $H_2S$ | Metal-supported active carbon | MD | The results of energy calculations suggest that $Cu^0$ and $Cu^+$ species have the highest adsorption affinity with $H_2S$ among various metal and metal ions | [180] |
| Evaluating adsorption energies of the gases | $H_2O$, $CH_4$, CO, $CO_2$, $O_2$, and $H_2$ | Nano porous Graphene | MD | Water represents indeed a particularly interesting case for filtration by Graphene-based membranes | [181] |
| Adsorption of acidic | $CO_2$, $CH_4$ | Defected | MD | The interaction with a defected | [182] |

| | | |
|---|---|---|
| gases, Comparing gas interactions with different surfaces | Graphene surface | Graphene surface with one carbon atom missing (vacancy 0001) yields stronger CO2-surface interactions compared to those of perfect Graphene surface |

Choosing between Monte Carlo (MC) and Molecular Dynamic (MD) largely depends on the phenomenon under investigation. Both simulation methods can provide thermodynamic and structural properties of the systems. However, MC is preferable for simulation of low-density systems. There are a large number of rejected moves in MC calculations as random moves are selected with probability and these random moves cause barrier crossing. In contrast, in MD simulations the molecular collisions transform energy to other molecules and solve the barrier crossing trouble. Some studies compare the specific system with both MD and MC computational methods and found that the results of thermodynamic properties and conformer populations are in accord; however, MC runs are ~2-2.5 times faster than MD to achieve the same level of convergence [183]. The biochar surface and the adsorption of CO2/H2S can be modeled using software (e.g. Gaussian, VASP, and MOPAC). The molecular modeling is being used as a tool to determine target adsorbates, interaction between adsorbates, and relative binding energies. It does not replace experiments but rather informs the adsorption experiments to save time. Further, one is able to better understand the adsorption equilibria and role of functional groups on biochar surface in order to simulate the adsorption process and obtain the thermodynamic parameters.

## 2.8. Conclusion

The authors of this review focused on three types of adsorbent used for purifying gases. The production processes of biochar by diverse source of feedstock under different reaction condition were surveyed. The results of comparing biochar with activated carbon, one of the most prevalent commercial adsorbent, showed that biochar could be used as a feasible alternative to AC as it is environmentally friendly and low-cost adsorbent. The properties of resultant biochars such as carbon, hydrogen content, and surface area were profoundly affected by pyrolytic temperature. The Freundlich isotherm is associated with heterogeneous surfaces and typically has a better fit with biochar due to the non-uniform energy of the surface assumed in the Freundlich model. The adsorption of $H_2S$ on plain carbon surfaces were proposed to occur by the same basic mechanism (Adib et al.) with minor discrepancy. Biochar is a heterogeneous surface with many different functional groups, as such; more study is required in linking surface functionality to the adsorption of acidic gases. Two different process systems dynamic and static tests were used in the literature to determine adsorption capacities and rates. Molecular modeling provides much needed additional information on the properties of different carbon surfaces, acidic gases and common simulation methods for adsorption. As indicated in this work, further investigations are required to the best compounds to target and applications in biochar adsorption.

**Acknowledgment**

The authors are thankful for the great support given by NSERC (Natural Science and Engineering Research Council of Canada), SGS (School of Graduate Studies of Memorial University), and BioFuelNet Canada.

## References


[1] Lebrero R, Bouchy L, Stuetz R, Muñoz R. Odor Assessment and Management in Wastewater Treatment Plants: A Review. Crit Rev Environ Sci Technol 2011;41:915–50. doi:10.1080/10643380903300000.

[2] Tagliabue M, Farrusseng D, Valencia S, Aguado S, Ravon U, Rizzo C, et al. Natural gas treating by selective adsorption: Material science and chemical engineering interplay. Chem Eng J 2009;155:553–66. doi:10.1016/j.cej.2009.09.010.

[3] Yu CH, Huang CH, Tan CS. A review of CO2 capture by absorption and adsorption. Aerosol Air Qual Res 2012;12:745–69. doi:10.4209/aaqr.2012.05.0132.

[4] Abdelhafez A a, Li J, Abbas MHH. Feasibility of biochar manufactured from organic wastes on the stabilization of heavy metals in a metal smelter contaminated soil. Chemosphere 2014;117C:66–71. doi:10.1016/j.chemosphere.2014.05.086.

[5] Hu M. Design, synthesis and applications of Metal Organic Frameworks. Thesis 2011:1–80. doi:10.1007/s10934-015-9910-3.

[6] Khan NA, Hasan Z, Jhung SH. Adsorptive removal of hazardous materials using metal-organic frameworks (MOFs): A review. J Hazard Mater 2013;244–245:444–56. doi:10.1016/j.jhazmat.2012.11.011.

[7] Ahmad M, Rajapaksha AU, Lim JE, Zhang M, Bolan N, Mohan D, et al. Biochar as a sorbent for contaminant management in soil and water: A review. Chemosphere 2014;99:19–23. doi:10.1016/j.chemosphere.2013.10.071.

[8] Shang G, Shen G, Liu L, Chen Q, Xu Z. Kinetics and mechanisms of hydrogen sulfide adsorption by biochars. Bioresour Technol 2013;133:495–9. doi:10.1016/j.biortech.2013.01.114.

[9] Yaman S. Pyrolysis of biomass to produce fuels and chemical feedstocks. Energy Convers Manag 2004;45:651–71. doi:10.1016/S0196-8904(03)00177-8.

[10] Tseng HH, Wey MY. Study of SO2 adsorption and thermal regeneration over activated carbon-supported copper oxide catalysts. Carbon N Y 2004;42:2269–78. doi:10.1016/j.carbon.2004.05.004.

[11] Plaza MG, Gonz??lez AS, Pis JJ, Rubiera F, Pevida C. Production of microporous biochars by single-step oxidation: Effect of activation conditions on CO2 capture. Appl Energy 2014;114:551–62. doi:10.1016/j.apenergy.2013.09.058.

[12] Nasri NS, Hamza UD, Ismail SN, Ahmed MM, Mohsin R. Assessment of porous carbons derived from sustainable palm solid waste for carbon dioxide capture. J. Clean. Prod., vol. 71, 2014, p. 148–57. doi:10.1016/j.jclepro.2013.11.053.

[13] Lua AC, Yang T. Theoretical and experimental SO2 adsorption onto pistachio-nut-shell activated carbon for a fixed-bed column. Chem Eng J 2009;155:175–83.

doi:10.1016/j.cej.2009.07.031.

[14] Heidari A, Younesi H, Rashidi A, Ghoreyshi AA. Evaluation of CO2 adsorption with eucalyptus wood based activated carbon modified by ammonia solution through heat treatment. Chem Eng J 2014;254:503–13. doi:http://dx.doi.org/10.1016/j.cej.2014.06.004.

[15] Dias JM, Alvim-Ferraz MCM, Almeida MF, Rivera-Utrilla J, Sánchez-Polo M. Waste materials for activated carbon preparation and its use in aqueous-phase treatment: A review. J Environ Manage 2007;85:833–46. doi:10.1016/j.jenvman.2007.07.031.

[16] Nasri NS, Ismail SN, Hamza UD, Ahmed MM. Study on the Use and Modification of a Sustainable Solid Waste Material for Carbon Dioxide Capturing 2013:25–7.

[17] Huber GW. Breaking the chemical and engineering barriers to lignocellulosic biofuels. Int Sugar J 2008;110:138+. doi:http://www.ecs.umass.edu/biofuels/.

[18] Ishida H. Characterization of Composite Materials. Elsevier; 2013.

[19] Wang L, Yang RT. New nanostructured sorbents for desulfurization of natural gas. Front Chem Sci Eng 2014;8:8–19. doi:10.1007/s11705-014-1411-4.

[20] Huang HY, Yang RT, Chinn D, Munson CL. Amine-Grafted MCM-48 and Silica Xerogel as Superior Sorbents for Acidic Gas Removal from Natural Gas. Ind Eng Chem Res 2003;42:2427–33. doi:10.1021/ie020440u.

[21] Burwell RL, Leal O. Modified silica gels as selective adsorbents for sulphur dioxide. J Chem Soc Chem Commun 1974:342–3. doi:10.1039/C39740000342.

[22] Leal O, Bolívar C, Ovalles C, García JJ, Espidel Y. Reversible adsorption of carbon dioxide on amine surface-bonded silica gel. Inorganica Chim Acta 1995;240:183–9. doi:10.1016/0020-1693(95)04534-1.

[23] Huang HY, Yang RT, Chinn D, Munson CL. Amine-Grafted MCM-48 and Silica Xerogel as Superior Sorbents for Acidic Gas Removal from Natural Gas. Ind Eng Chem Res 2003;42:2427–33. doi:10.1021/ie020440u.

[24] Belmabkhout Y, De Weireld G, Sayari A. Amine-bearing mesoporous silica for CO2 and H2S removal from natural gas and biogas. Langmuir 2009;25:13275–8. doi:10.1021/la903238y.

[25] Kim S, Ida J, Guliants V V., Lin JYS. Tailoring pore properties of MCM-48 silica for selective adsorption of CO 2. J Phys Chem B 2005;109:6287–93. doi:10.1021/jp045634x.

[26] Jaiboon V, Yoosuk B, Prasassarakich P. Amine modified silica xerogel for H2S removal at low temperature. Fuel Process Technol 2014;128:276–82. doi:10.1016/j.fuproc.2014.07.032.

[27] Yue MB, Sun LB, Cao Y, Wang Y, Wang ZJ, Zhu JH. Efficient CO2 Capturer Derived from As-Synthesized MCM-41 Modified with Amine. Chem – A Eur J 2008;14:3442–51. doi:10.1002/chem.200701467.

[28] Sudaryanto Y, Hartono SB, Irawaty W, Hindarso H, Ismadji S. High surface area activated carbon prepared from cassava peel by chemical activation. Bioresour Technol 2006;97:734–9. doi:10.1016/j.biortech.2005.04.029.

[29] Na B-K, Koo K-K, Eum H-M, Lee H, Song H. CO2 recovery from flue gas by PSA process using activated carbon. Korean J Chem Eng 2001;18:220–7. doi:10.1007/BF02698463.

[30] Hao S, Zhang J, Zhong Y, Zhu W. Selective adsorption of CO2 on amino-functionalized silica spheres with centrosymmetric radial mesopores and high amino loading. Adsorption 2012;18:423–30. doi:10.1007/s10450-012-9428-9.

[31] Koriakin A, Kim YH, Lee CH. Adsorptive desulfurization of natural gas using lithium-modified mesoporous silica. Ind Eng Chem Res 2012;51:14489–95. doi:10.1021/ie301066n.

[32] Sumathi S, Bhatia S, Lee KT, Mohamed AR. Cerium impregnated palm shell activated carbon (Ce/PSAC) sorbent for simultaneous removal of SO2 and NO—Process study. Chem Eng J 2010;162:51–7. doi:10.1016/j.cej.2010.04.056.

[33] Guo J, Luo Y, Lua AC, Chi R, Chen Y, Bao X, et al. Adsorption of hydrogen sulphide (H2S) by activated carbons derived from oil-palm shell. Carbon N Y 2007;45:330–6. doi:10.1016/j.carbon.2006.09.016.

[34] Tseng H-H, Wey M-Y. Study of SO2 adsorption and thermal regeneration over activated carbon-supported copper oxide catalysts. Carbon N Y 2004;42:2269–78. doi:10.1016/j.carbon.2004.05.004.

[35] Elsayed Y, Seredych M, Dallas A, Bandosz TJ. Desulfurization of air at high and low H2S concentrations. Chem Eng J 2009;155:594–602. doi:10.1016/j.cej.2009.08.010.

[36] Macías-Pérez MC, Bueno-López A, Lillo-Ródenas MA, Salinas-Martínez de Lecea C, Linares-Solano A. SO2 retention on CaO/activated carbon sorbents. Part I: Importance of calcium loading and dispersion. Fuel 2007;86:677–83. doi:10.1016/j.fuel.2006.09.004.

[37] Nguyen-Thanh D, Bandosz TJ. Activated carbons with metal containing bentonite binders as adsorbents of hydrogen sulfide. Carbon N Y 2005;43:359–67. doi:10.1016/j.carbon.2004.09.023.

[38] Lua AC, Yang T. Theoretical and experimental SO2 adsorption onto pistachio-nut-shell activated carbon for a fixed-bed column. Chem Eng J 2009;155:175–83. doi:10.1016/j.cej.2009.07.031.

[39] Montes D, Tocuyo E, Gonzaĺez E, Rodriǵuez D, Solano R, Atencio R, et al. Reactive H2S chemisorption on mesoporous silica molecular sieve-supported CuO or ZnO. Microporous Mesoporous Mater 2013;168:111–20. doi:10.1016/j.micromeso.2012.09.018.

[40] Cheah S, Carpenter DL, Magrini-Bair KA. Review of mid- to high-temperature sulfur sorbents for desulfurization of biomass- and coal-derived syngas. Energy

and Fuels 2009;23:5291–307. doi:10.1021/ef900714q.

[41] Ko TH, Chu H, Chaung LK, Tseng TK. High temperature removal of hydrogen sulfide using an N-150 sorbent. J Hazard Mater 2004;114:145–52. doi:10.1016/j.jhazmat.2004.08.023.

[42] Ko TH, Chu H, Liou YJ. A study of Zn-Mn based sorbent for the high-temperature removal of H2S from coal-derived gas. J Hazard Mater 2007;147:334–41. doi:10.1016/j.jhazmat.2007.01.018.

[43] Kim K, Park N. Removal of hydrogen sulfide from a steam-hydrogasifier product gas by zinc oxide sorbent: Effect of non-steam gas components. J Ind Eng Chem 2010;16:967–72. doi:10.1016/j.jiec.2010.04.003.

[44] Xue M, Chitrakar R, Sakane K, Ooi K. Screening of adsorbents for removal of H2S at room temperature. Green Chem 2003;5:529–34. doi:http://dx.doi.org/10.1039/B303167P.

[45] Novochinskii II, Song C, Ma X, Liu X, Shore L, Lampert J, et al. Low-temperature H2S removal from steam-containing gas mixtures with ZnO for fuel cell application. 1. ZnO particles and extrudates. Energy and Fuels 2004;18:576–83. doi:10.1021/ef030137l.

[46] Liu D, Chen S, Fei X, Huang C, Zhang Y. Regenerable CuO-based adsorbents for low temperature desulfurization application. Ind Eng Chem Res 2015;54:3556–62. doi:10.1021/acs.iecr.5b00180.

[47] Polychronopoulou K, Cabello Galisteo F, López Granados M, Fierro JLG, Bakas T, Efstathiou AM. Novel Fe-Mn-Zn-Ti-O mixed-metal oxides for the low-temperature removal of H2S from gas streams in the presence of H2, CO 2, and H2O. J Catal 2005;236:205–20. doi:10.1016/j.jcat.2005.10.001.

[48] Jiang D, Su L, Ma L, Yao N, Xu X, Tang H, et al. Cu-Zn-Al mixed metal oxides derived from hydroxycarbonate precursors for H2S removal at low temperature. Appl Surf Sci 2010;256:3216–23. doi:10.1016/j.apsusc.2009.12.008.

[49] Sasaoka E, Hirano S, Kasaoka S, Sakata Y. Characterization of Reaction between Zinc-Oxide and Hydrogen-Sulfide. Energy & Fuels 1994;8:1100–5.

[50] Sasaoka E, Taniguchi K, Hirano S, Uddin MA, Kasaoka S, Sakata Y. Catalytic Activity of ZnS Formed from Desulfurization Sorbent ZnO for Conversion of COS to H2S. Ind Eng Chem Res 1995;34:1102–6. doi:10.1021/ie00043a011.

[51] Woods MC, Gangwal SK, Harrison DP, Jothimurugesan K. Kinetics of the reactions of a zinc ferrite sorbent in high-temperature coal gas desulfurization. Ind Eng Chem Res 1991;30:100–7. doi:10.1021/ie00049a015.

[52] Lew S, Sarofim a. F, Flytzani-Stephanopoulos M. The reduction of zinc titanate and zinc oxide solids. Chem Eng Sci 1992;47:1421–31. doi:10.1016/0009-2509(92)80287-M.

[53] Patrick V, Gavalas GR, Flytzani-Stephanopoulos M, Jothimurugesan K. High-temperature sulfidation-regeneration of copper(II) oxide-alumina sorbents. Ind Eng

Chem Res 1989;28:931–40. doi:10.1021/ie00091a008.

[54] Yaşyerli S, Dogu G, Irfan AR, Dogu T. Breakthrough Analysis OF H 2 S removal on CU-V-MO, CU-V, and CU-MO mixed oxides. Chem Eng Commun 2003;190:1055–72. doi:10.1080/00986440302101.

[55] Fenouil LA, Lynn S. Study of Calcium-Based Sorbents for High-Temperature H2S Removal. 3. Comparison of Calcium-Based Sorbents for Coal Gas Desulfurization. Ind Eng Chem Res 1995;34:2343–8. doi:10.1021/ie00046a016.

[56] Yrjas KP, Zevenhoven CAP, Hupa MM. Hydrogen Sulfide Capture by Limestone and Dolomite at Elevated Pressure. 1. Sorbent Performance. Ind Eng Chem Res 1996;35:176–83. doi:10.1021/ie9502749.

[57] Atakül H, Wakker JP, Gerritsen AW, van den Berg PJ. Regeneration of MnO/γ-Al2O3 used for high-temperature desulfurization of fuel gases. Fuel 1996;75:373–8. doi:10.1016/0016-2361(95)00237-5.

[58] Yoon Y Il, Chun BH, Yun Y, Kim SH. A Study of a Regeneration Reaction for Desulfurization Sorbents Using Natural Manganese Ore. J Chem Eng JAPAN 2004;37:835–41. doi:10.1252/jcej.37.835.

[59] Tseng SC, Tamhankar SS, Wen CY. Kinetic studies on the reactions involved in the hot gas desulfurization using a regenerable iron oxide sorbent—II. Chem Eng Sci 1981;36:1287–94. doi:10.1016/0009-2509(81)80163-7.

[60] White J., Groves F., Harrison D. Elemental sulfur production during the regeneration of iron oxide high-temperature desulfurization sorbent. Catal Today 1998;40:47–57. doi:10.1016/S0920-5861(97)00120-X.

[61] Sayyah M, Ito BR, Rostam-Abadi M, Lu Y, Suslick KS. CaO-based sorbents for CO2 capture prepared by ultrasonic spray pyrolysis. RSC Adv 2013;3:19872–5. doi:10.1039/C3RA44566F.

[62] Abanades JC, Grasa G, Alonso M, Rodriguez N, Anthony EJ, Romeo LM. Cost Structure of a Postcombustion CO2 Capture System Using CaO. Environ Sci Technol 2007;41:5523–7. doi:10.1021/es070099a.

[63] Abanades JC, Rubin ES, Anthony EJ. Sorbent Cost and Performance in CO2 Capture Systems. Ind Eng Chem Res 2004;43:3462–6. doi:10.1021/ie049962v.

[64] Albrecht KO, Wagenbach KS, Satrio JA, Shanks BH, Wheelock TD. Development of a CaO-based CO2 sorbent with improved cyclic stability. Ind Eng Chem Res 2008;47:7841–8. doi:10.1021/ie8007743.

[65] Ding Y-D, Song G, Liao Q, Zhu X, Chen R. Bench scale study of CO2 adsorption performance of MgO in the presence of water vapor. Energy 2016;112:101–10. doi:http://dx.doi.org/10.1016/j.energy.2016.06.064.

[66] Hakim A, Marliza TS, Abu Tahari NM, Wan Isahak RWN, Yusop RM, Mohamed Hisham WM, et al. Studies on $CO_2$ Adsorption and Desorption Properties from Various Types of Iron Oxides (FeO, $Fe_2O_3$, and $Fe_3O_4$). Ind Eng Chem Res 2016:acs.iecr.5b04091. doi:10.1021/acs.iecr.5b04091.

[67] Wu SF, Li QH, Kim JN, Yi KB. Properties of a nano CaO/Al2O3 CO2 sorbent. Ind Eng Chem Res 2008;47:180–4. doi:10.1021/ie0704748.

[68] Li L, Wen X, Fu X, Wang F, Zhao N, Xiao F, et al. MgO/Al2O3 sorbent for CO2 capture. Energy and Fuels 2010;24:5773–80. doi:10.1021/ef100817f.

[69] Bae YS, Snurr RQ. Development and evaluation of porous materials for carbon dioxide separation and capture. Angew Chemie - Int Ed 2011;50:11586–96. doi:10.1002/anie.201101891.

[70] Grant Glover T, Peterson GW, Schindler BJ, Britt D, Yaghi O. MOF-74 building unit has a direct impact on toxic gas adsorption. Chem Eng Sci 2011;66:163–70. doi:10.1016/j.ces.2010.10.002.

[71] Couck S, Denayer JFM, Baron G V., Rémy T, Gascon J, Kapteijn F. An amine-functionalized MIL-53 metal-organic framework with large separation power for CO2 and CH4. J Am Chem Soc 2009;131:6326–7. doi:10.1021/ja900555r.

[72] Aprea P, Caputo D, Gargiulo N, Iucolano F, Pepe F. Modeling carbon dioxide adsorption on microporous substrates: Comparison between Cu-BTC metal-organic framework and 13X zeolitic molecular sieve. J Chem Eng Data 2010;55:3655–61. doi:10.1021/je1002225.

[73] Remy T, Peter SA, Van Der Perre S, Valvekens P, De Vos DE, Baron G V., et al. Selective dynamic CO2 separations on Mg-MOF-74 at low pressures: A detailed comparison with 13x. J Phys Chem C 2013;117:9301–10. doi:10.1021/jp401923v.

[74] Petit C, Mendoza B, Bandosz TJ. Hydrogen sulfide adsorption on MOFs and MOF/Graphite oxide composites. ChemPhysChem 2010;11:3678–84. doi:10.1002/cphc.201000689.

[75] Ebrahim AM, Jagiello J, Bandosz TJ. Enhanced reactive adsorption of $H_2S$ on Cu–BTC/ S- and N-doped GO composites. J Mater Chem A 2015;3:8194–204. doi:10.1039/C5TA01359C.

[76] Huang ZH, Liu G, Kang F. Glucose-promoted Zn-based metal-organic framework/graphene oxide composites for hydrogen sulfide removal. ACS Appl Mater Interfaces 2012;4:4942–7. doi:10.1021/am3013104.

[77] Kruse a, Karlsruhe F. Hydrothermal Conversion of Biomass . 2010. doi:10.3990/1/9789036528719.

[78] Kludze H, Deen B, Dutta A. Impact of agronomic treatments on fuel characteristics of herbaceous biomass for combustion. Fuel Process Technol 2013;109:96–102. doi:10.1016/j.fuproc.2012.09.043.

[79] Brick S, Lehmann J, Kramer J. Biochar : Assessing the Promise and Risks To Guide U . S . Policy Author 2010.

[80] Alonso DM, Wettstein SG, Dumesic J a. Bimetallic catalysts for upgrading of biomass to fuels and chemicals. Chem Soc Rev 2012;41:8075. doi:10.1039/c2cs35188a.

[81] Papari S, Hawboldt K, Helleur R. Pyrolysis: A theoretical and experimental study on the conversion of softwood sawmill residues to biooil. Ind Eng Chem Res 2015;54:605–11. doi:10.1021/ie5039456.

[82] Papari S, Hawboldt K. A review on the pyrolysis of woody biomass to bio-oil: Focus on kinetic models. Renew Sustain Energy Rev 2015;52:1580–95. doi:10.1016/j.rser.2015.07.191.

[83] Brownsort PA. Biomass pyrolysis processes: performance parameters and their influence on biochar system benefits peter alexander brownsort 2009:83.

[84] Brewer CE, Schmidt-Rohr K, Satrio JA, Brown RC. Characterization of biochar from fast pyrolysis and gasification systems. Environ Prog Sustain Energy 2009;28:386–96. doi:10.1002/ep.10378.

[85] Rousset P, Macedo L, Commandré J-M, Moreira A. Biomass torrefaction under different oxygen concentrations and its effect on the composition of the solid by-product. J Anal Appl Pyrolysis 2012;96:86–91. doi:10.1016/j.jaap.2012.03.009.

[86] Prins MJ, Ptasinski KJ, Janssen FJJG. Torrefaction of wood. J Anal Appl Pyrolysis 2006;77:28–34. doi:10.1016/j.jaap.2006.01.002.

[87] Meyer S, Glaser B, Quicker P. Technical, Economical, and Climate-Related Aspects of Biochar Production Technologies: A Literature Review. Environ Sci Technol 2011;45:9473–83. doi:10.1021/es201792c.

[88] Yan W, Hastings JT, Acharjee TC, Coronella CJ, Vásquez VR. Mass and Energy Balances of Wet Torrefaction of Lignocellulosic Biomass. Energy & Fuels 2010;24:4738–42. doi:10.1021/ef901273n.

[89] Jahirul M, Rasul M, Chowdhury A, Ashwath N. Biofuels Production through Biomass Pyrolysis —A Technological Review. Energies 2012;5:4952–5001. doi:10.3390/en5124952.

[90] Naik SN, Goud V V., Rout PK, Dalai AK. Production of first and second generation biofuels: A comprehensive review. Renew Sustain Energy Rev 2010;14:578–97. doi:10.1016/j.rser.2009.10.003.

[91] Hoekman SK, Broch A, Robbins C. Hydrothermal carbonization (HTC) of lignocellulosic biomass. Energy and Fuels 2011;25:1802–10. doi:10.1021/ef101745n.

[92] Nunes CA, Guerreiro MC. Estimation of surface area and pore volume of activated carbons by methylene blue and iodine numbers. Quim Nova 2011;34:472–6. doi:10.1590/S0100-40422011000300020.

[93] Ghosh TK, Tollefson EL. A continuous process for recovery of sulfur from natural gas containing low concentrations of hydrogen sulfide. Can J Chem Eng 1986;64:960–8. doi:10.1002/cjce.5450640612.

[94] Katoh H, Kuniyoshi I, Hirai M, Shoda M. Studies of the oxidation mechanism of sulphur-containing gases on wet activated carbon fibre. Appl Catal B Environ 1995;6:255–62. doi:10.1016/0926-3373(95)00021-6.

[95] van der Merwe MM, Bandosz TJ. A study of ignition of metal impregnated carbons: the influence of oxygen content in the activated carbon matrix. J Colloid Interface Sci 2005;282:102–8. doi:10.1016/j.jcis.2004.08.056.

[96] Cruz Ceballos DC, Hawboldt K, Hellleur R. Effect of production conditions on self-heating propensity of torrefied sawmill residues. Fuel 2015;160:227–37. doi:10.1016/j.fuel.2015.07.097.

[97] Activated carbon for air purification in New York City's sewage treatment plants. n.d.

[98] Bandosz TJ, Le Q. Evaluation of surface properties of exhausted carbons used as H2S adsorbents in sewage treatment plants. Carbon N Y 1998;36:39–44. doi:10.1016/S0008-6223(97)00148-6.

[99] Bandosz TJ. On the adsorption/oxidation of hydrogen sulfide on activated carbons at ambient temperatures. J Colloid Interface Sci 2002;246:1–20. doi:10.1006/jcis.2001.7952.

[100] Bandosz TJ, Bagreev A, Adib F, Turk A. Unmodified versus Caustics-Impregnated Carbons for Control of Hydrogen Sulfide Emissions from Sewage Treatment Plants. Environ Sci Technol 2000;34:1069–74. doi:10.1021/es9813212.

[101] Adib F, Bagreev A, Bandosz TJ. Analysis of the Relationship between H2S Removal Capacity and Surface Properties of Unimpregnated Activated Carbons. Environ Sci Technol 2000;34:686–92. doi:10.1021/es990341g.

[102] Adib F, Bagreev A, Bandosz T. Effect of pH and Surface Chemistry on the Mechanism of H(2)S Removal by Activated Carbons. J Colloid Interface Sci 1999;216:360–9. doi:10.1006/jcis.1999.6335.

[103] Jonker MTO, Suijkerbuijk MPW, Schmitt H, Sinnige TL. Ecotoxicological Effects of Activated Carbon Addition to Sediments. Environ Sci Technol 2009;43:5959–66. doi:10.1021/es900541p.

[104] Houshmand A, Wan Daud WMA, Shafeeyan MS. Adsorption. Sep Sci Technol 2011;46:1098–112. doi:10.1080/01496395.2010.546383.

[105] Drisko GL, Aquino C, Feron PHM, Caruso RA, Harrisson S, Luca V. One-Pot Preparation and CO2 Adsorption Modeling of Porous Carbon, Metal Oxide, and Hybrid Beads. ACS Appl Mater Interfaces 2013;5:5009–14. doi:10.1021/am4007929.

[106] Shah IK, Pre P, Alappat BJ. Effect of thermal regeneration of spent activated carbon on volatile organic compound adsorption performances. J Taiwan Inst Chem Eng 2014;45:1733–8. doi:10.1016/j.jtice.2014.01.006.

[107] Siriwardane R V., Shen M-S, Fisher EP, Poston JA. Adsorption of CO 2 on Molecular Sieves and Activated Carbon. Energy & Fuels 2001;15:279–84. doi:10.1021/ef000241s.

[108] González AS, Plaza MG, Rubiera F, Pevida C. Sustainable biomass-based carbon adsorbents for post-combustion CO2 capture. Chem Eng J 2013;230:456–65.

doi:10.1016/j.cej.2013.06.118.

[109] Shimekit B, Mukhtar H. Natural Gas Purification Technologies–Major Advances for CO2 Separation and Future Directions. Adv Nat Gas Technol 2012.

[110] Peng X, Cao D. Computational screening of porous carbons, zeolites, and metal organic frameworks for desulfurization and decarburization of biogas, natural gas, and flue gas. AIChE J 2013;59:2928–42. doi:10.1002/aic.14046.

[111] Bakker WJW, Kapteijn F, Moulijn JA. A high capacity manganese-based sorbent for regenerative high temperature desulfurization with direct sulfur production Conceptual process application to coal gas cleaning. Chem Eng J 2003;96:223–35. doi:10.1016/j.cej.2003.08.022.

[112] Zhao Y, Ding H, Zhong Q. Synthesis and characterization of MOF-aminated graphite oxide composites for CO2 capture. Appl Surf Sci 2013;284:138–44. doi:10.1016/j.apsusc.2013.07.068.

[113] Chen B, Zhou D, Zhu L. Transitional Adsorption and Partition of Nonpolar and Polar Aromatic Contaminants by Biochars of Pine Needles with Different Pyrolytic Temperatures. Environ Sci Technol 2008;42:5137–43. doi:10.1021/es8002684.

[114] Kim KH, Kim JY, Cho TS, Choi JW. Influence of pyrolysis temperature on physicochemical properties of biochar obtained from the fast pyrolysis of pitch pine (Pinus rigida). Bioresour Technol 2012;118:158–62. doi:10.1016/j.biortech.2012.04.094.

[115] Spokas K a. K a, Reicosky DCDC. Impacts of sixteen different biochars on soil greenhouse gas production. Ann Environ Sci 2009;3:179–93. doi:IND44486912.

[116] Mukome FND, Zhang X, Silva LCR, Six J, Parikh SJ. Use of chemical and physical characteristics to investigate trends in biochar feedstocks. J Agric Food Chem 2013;61:2196–204. doi:10.1021/jf3049142.

[117] Kim KH, Kim TS, Lee SM, Choi D, Yeo H, Choi IG, et al. Comparison of physicochemical features of biooils and biochars produced from various woody biomasses by fast pyrolysis. Renew Energy 2013;50:188–95. doi:10.1016/j.renene.2012.06.030.

[118] Spokas K a., Novak JM, Stewart CE, Cantrell KB, Uchimiya M, DuSaire MG, et al. Qualitative analysis of volatile organic compounds on biochar. Chemosphere 2011;85:869–82. doi:10.1016/j.chemosphere.2011.06.108.

[119] Guerrero M, Ruiz MP, Alzueta MU, Bilbao R, Millera a. Pyrolysis of eucalyptus at different heating rates: Studies of char characterization and oxidative reactivity. J Anal Appl Pyrolysis 2005;74:307–14. doi:10.1016/j.jaap.2004.12.008.

[120] Jackson MA, Eberhardt TL, Boateng AA, Mullen CA, Groom LH. com Evaluation of Biochars by Temperature Programmed Oxidation/Mass Spectrometry 2013;8:5461–74.

[121] Obia A, Børresen T, Martinsen V, Cornelissen G, Mulder J. Vertical and lateral transport of biochar in light-textured tropical soils. Soil Tillage Res 2017;165:34–

40. doi:http://dx.doi.org/10.1016/j.still.2016.07.016.

[122] Frazier RS, Jin E, Kumar A. Life cycle assessment of biochar versus metal catalysts used in syngas cleaning. Energies 2015;8:621–44. doi:10.3390/en8010621.

[123] Yan Q, Wan C, Liu J, Gao J, Yu F, Zhang J, et al. Iron nanoparticles in situ encapsulated in biochar-based carbon as an effective catalyst for the conversion of biomass-derived syngas to liquid hydrocarbons. Green Chem 2013;15:1631. doi:10.1039/c3gc37107g.

[124] Qian K, Kumar A, Zhang H, Bellmer D, Huhnke R. Recent advances in utilization of biochar. Renew Sustain Energy Rev 2015;42:1055–64. doi:http://dx.doi.org/10.1016/j.rser.2014.10.074.

[125] Scott Fogler H. Elements of chemical reaction engineering. Chem Eng Sci 1987;42:2493. doi:10.1016/0009-2509(87)80130-6.

[126] Bagreev A, Bandosz TJ. H2S adsorption/oxidation on unmodified activated carbons: Importance of prehumidification. Carbon N Y 2001;39:2303–11. doi:10.1016/S0008-6223(01)00049-5.

[127] Yan R, Liang DT, Tsen L, Tay JH. Kinetics and mechanisms of H2S adsorption by alkaline activated carbon. Environ Sci Technol 2002;36:4460–6. doi:10.1021/es0205840.

[128] Chiang HL, Tsai JH, Chang GM, Hsu YC. Adsorption kinetic characteristics of H2S on activated carbon. Adsorption 2002;8:325–40. doi:10.1023/A:1021537530695.

[129] Le Leuch LM, Subrenat A, Le Cloirec P. Hydrogen sulfide adsorption and oxidation onto activated carbon cloths: Applications to odorous gaseous emission treatments. Langmuir 2003;19:10869–77. doi:10.1021/la035163q.

[130] Bagreev A, Bandosz TJ. On the Mechanism of Hydrogen Sulfide Removal from Moist Air on Catalytic Carbonaceous Adsorbents. Ind Eng Chem Res 2005;44:530–8. doi:10.1021/ie049277o.

[131] Xu X, Cao X, Zhao L, Sun T. Comparison of sewage sludge- and pig manure-derived biochars for hydrogen sulfide removal. Chemosphere 2014;111:296–303. doi:10.1016/j.chemosphere.2014.04.014.

[132] He R, Xia FF, Wang J, Pan CL, Fang CR. Characterization of adsorption removal of hydrogen sulfide by waste biocover soil, an alternative landfill cover. J Hazard Mater 2011;186:773–8. doi:10.1016/j.jhazmat.2010.11.062.

[133] Lehmann J, Rillig MC, Thies J, Masiello CA, Hockaday WC, Crowley D. Biochar effects on soil biota – A review. Soil Biol Biochem 2011;43:1812–36. doi:http://dx.doi.org/10.1016/j.soilbio.2011.04.022.

[134] Creamer AE, Gao B, Zhang M. Carbon dioxide capture using biochar produced from sugarcane bagasse and hickory wood. Chem Eng J 2014;249:174–9. doi:10.1016/j.cej.2014.03.105.

[135] Plaza MG, Durán I, Querejeta N, Rubiera F, Pevida C. Experimental and Simulation Study of Adsorption in Postcombustion Conditions Using a Microporous Biochar. 1. CO $_2$ and N $_2$ Adsorption. Ind Eng Chem Res 2016;55:3097–112. doi:10.1021/acs.iecr.5b04856.

[136] Chang Y, Chen D-H. Recovery of gold (III) ions by a chitosancoated magnetic nano-adsorbent. Gold Bull 2006;39:98–102. doi:10.1007/BF03215536.

[137] Chang A, Chuang S, Gray M, Soong Y. In-situ infrared study of CO2 adsorption on SBA-15 grafted with γ-(aminopropyl) triethoxysilane. Energy & Fuels 2003:468–73. doi:10.1021/ef020176h.

[138] Guo B, Chang L, Xie K. Adsorption of Carbon Dioxide on Activated Carbon. J Nat Gas Chem 2006;15:223–9. doi:10.1016/S1003-9953(06)60030-3.

[139] Chen Y, Zhang D. Adsorption kinetics, isotherm and thermodynamics studies of flavones from Vaccinium Bracteatum Thunb leaves on NKA-2 resin. Chem Eng J 2014;254:579–85. doi:10.1016/j.cej.2014.05.120.

[140] Abdullah MA, Chiang L, Nadeem M. Comparative evaluation of adsorption kinetics and isotherms of a natural product removal by Amberlite polymeric adsorbents. Chem Eng J 2009;146:370–6. doi:http://dx.doi.org/10.1016/j.cej.2008.06.018.

[141] Khan TA, Khan EA, Shahjahan. Removal of basic dyes from aqueous solution by adsorption onto binary iron-manganese oxide coated kaolinite: Non-linear isotherm and kinetics modeling. Appl Clay Sci 2015;107:70–7. doi:10.1016/j.clay.2015.01.005.

[142] Alberti G, Amendola V, Pesavento M, Biesuz R. Beyond the synthesis of novel solid phases: Review on modelling of sorption phenomena. Coord Chem Rev 2012;256:28–45. doi:10.1016/j.ccr.2011.08.022.

[143] Foo KY, Hameed BH. Insights into the modeling of adsorption isotherm systems. Chem Eng J 2010;156:2–10. doi:10.1016/j.cej.2009.09.013.

[144] Plaza MG, Garc??a S, Rubiera F, Pis JJ, Pevida C. Evaluation of ammonia modified and conventionally activated biomass based carbons as CO2 adsorbents in postcombustion conditions. Sep Purif Technol 2011;80:96–104. doi:10.1016/j.seppur.2011.04.015.

[145] Plaza MG, González AS, Pevida C, Rubiera F. Influence of water vapor on CO2 adsorption using a biomass-based carbon. Ind Eng Chem Res 2014;53:15488–99. doi:10.1021/ie500342q.

[146] Zhang X, Zhang S, Yang H, Feng Y, Chen Y, Wang X, et al. Nitrogen enriched biochar modified by high temperature CO2-ammonia treatment: Characterization and adsorption of CO2. Chem Eng J 2014;257:20–7. doi:10.1016/j.cej.2014.07.024.

[147] Shang G, Shen G, Wang T, Chen Q. Effectiveness and mechanisms of hydrogen sulfide adsorption by camphor-derived biochar. J Air Waste Manage Assoc

2012;62:873–9. doi:10.1080/10962247.2012.686441.

[148] White AJ. Development of an Activated Carbon from Anaerobic Digestion By-Product to Remove Hydrogen Sulfide from Biogas by Development of an Activated Carbon from Anaerobic Digestion By-Product to Remove Hydrogen Sulfide from Biogas 2010.

[149] Kowalczyk P, Hołyst R, Terzyk AP, Gauden PA. State of hydrogen in idealized carbon slitlike nanopores at 77 K. Langmuir 2006;22:1970–2. doi:10.1021/la053041n.

[150] Gelb LD, Gubbins KE. Pore Size Distributions in Porous Glasses: A Computer Simulation Study. Langmuir 1999;15:305–8. doi:10.1021/la9808418.

[151] Smit B, Maesen TLM. Molecular simulations of zeolites: Adsorption, diffusion, and shape selectivity. Chem Rev 2008;108:4125–84. doi:10.1021/cr8002642.

[152] Alder BJ, Wainwright TE. Studies in Molecular Dynamics. II. Behavior of a Small Number of Elastic Spheres. J Chem Phys 1960;33:1439. doi:10.1063/1.1731425.

[153] Do DD, Do HD. Evaluation of 1-Site and 5-Site Models of Methane on Its Adsorption on Graphite and in Graphitic Slit Pores. J Phys Chem B 2005;109:19288–95. doi:10.1021/jp052448y.

[154] Kanda H, Miyahara M. Freezing of Lennard-Jones fluid in cylindrical nanopores under tensile conditions. Adsorption, vol. 13, 2007, p. 191–5. doi:10.1007/s10450-007-9066-9.

[155] Seaton NA, Friedman SP, Macelroy JMD, Murphy BJ. The Molecular Sieving Mechanism in Carbon Molecular Sieves: A Molecular Dynamics and Critical Path Analysis †. Langmuir 1997;7463:1199–204. doi:10.1021/la9510644.

[156] Kudin KN, Ozbas B, Schniepp HC, Prud'homme RK, Aksay IA, Car R. Raman spectra of graphite oxide and functionalized graphene sheets. Nano Lett 2008;8:36–41. doi:10.1021/nl071822y.

[157] Do DD, Do HD. Modeling of adsorption on nongraphitized carbon surface: GCMC simulation studies and comparison with experimental data. J Phys Chem B 2006;110:17531–8. doi:10.1021/jp062386r.

[158] Lucena SMP, Paiva CAS, Silvino PFG, Azevedo DCS, Cavalcante CL. The effect of heterogeneity in the randomly etched graphite model for carbon pore size characterization. Carbon N Y 2010;48:2554–65. doi:10.1016/j.carbon.2010.03.034.

[159] Harris JG, Yung KH. Carbon Dioxide's Liquid-Vapor Coexistence Curve And Critical Properties as Predicted by a Simple Molecular Model. J Phys Chem 1995;99:12021–4. doi:10.1021/j100031a034.

[160] Konstantakou M, Gotzias A, Kainourgiakis M, Stubos AK, Steriotis T a. GCMC Simulations of Gas Adsorption in Carbon Pore Structures. Simulation 1960. doi:10.5772/15988.

[161] Nath SK. Molecular Simulation of Vapor−Liquid Phase Equilibria of Hydrogen

Sulfide and Its Mixtures with Alkanes. J Phys Chem B 2003;107:9498–504. doi:10.1021/jp034140h.

[162] Ribeiro MCC. Molecular dynamics simulation of liquid sulfur dioxide. J Phys Chem B 2006;110:8789–97. doi:10.1021/jp060518a.

[163] Steele WA. The physical interaction of gases with crystalline solids: I. Gas-solid energies and properties of isolated adsorbed atoms. Surf Sci 1973;36:317–52. doi:http://dx.doi.org/10.1016/0039-6028(73)90264-1.

[164] Yang QY, Zhong CL. Computer simulations of adsorption characteristics of carbon dioxide in slit graphite pores. Can J Chem Eng 2004;82:580–9.

[165] Palmer JC, Brennan JK, Hurley MM, Balboa A, Gubbins KE. Detailed structural models for activated carbons from molecular simulation. Carbon N Y 2009;47:2904–13. doi:10.1016/j.carbon.2009.06.037.

[166] Lithoxoos GP, Peristeras LD, Boulougouris GC, Economou IG. Monte Carlo simulation of carbon monoxide, carbon dioxide and methane adsorption on activated carbon. Mol Phys 2012;110:1153–60. doi:10.1080/00268976.2012.659223.

[167] Tenney CM, Lastoskie CM. Molecular simulation of carbon dioxide adsorption in chemically and structurally heterogeneous porous carbons. Environ Prog 2006;25:343–54. doi:10.1002/ep.10168.

[168] Wang W, Peng X, Cao D. Capture of trace sulfur gases from binary mixtures by single-walled carbon nanotube arrays: A molecular simulation study. Environ Sci Technol 2011;45:4832–8. doi:10.1021/es1043672.

[169] Elliott JA. Novel approaches to multiscale modelling in materials science. Int Mater Rev 2011;56:207–25. doi:10.1179/1743280410Y.0000000002.

[170] Hafner J. Ab-initio simulations of materials using VASP: Density-functional theory and beyond. J Comput Chem 2008;29:2044–78. doi:10.1002/jcc.21057.

[171] Kresse G, Furthmüller J. Efficiency of ab-initio total energy calculations for metals and semiconductors using a plane-wave basis set. Comput Mater Sci 1996;6:15–50. doi:10.1016/0927-0256(96)00008-0.

[172] Kresse G, Hafner J. Ab initio molecular dynamics for liquid metals. Phys Rev B 1993;47:558–61. doi:10.1103/PhysRevB.47.558.

[173] P S, J K. Computer Simulation of Liquids. J Mol Liq 1988;38:267. doi:10.1016/0167-7322(88)80022-9.

[174] Cracknell RF, Nicholson D, Tennison SR, Bromhead J. Adsorption and selectivity of carbon dioxide with methane and nitrogen in slit-shaped carbonaceous micropores: Simulation and experiment. Adsorption 1996;2:193–203. doi:10.1007/BF00128301.

[175] Gholampour F, Yeganegi S. Molecular simulation study on the adsorption and separation of acidic gases in a model nanoporous carbon. Chem Eng Sci

2014;117:426–35. doi:10.1016/j.ces.2014.07.003.

[176] Simulation M, Performances S, Structures NH. Molecular Simulation of Adsorption and Separation Performances for 2015;31:660–6. doi:10.3866/PKU.WHXB201501291.

[177] Dasgupta T, Punnathanam SN, Ayappa KG. Effect of functional groups on separating carbon dioxide from CO 2 / N 2 gas mixtures using edge functionalized graphene nanoribbons 2015;121:279–91.

[178] Lu L, Wang S, Müller EA, Cao W, Zhu Y, Lu X, et al. Adsorption and separation of CO2/CH4 mixtures using nanoporous adsorbents by molecular simulation. Fluid Phase Equilib 2014;362:227–34. doi:10.1016/j.fluid.2013.10.013.

[179] Du a J, Sun CH, Zhu ZH, Lu GQ, Rudolph V, Smith SC. The effect of Fe doping on adsorption of CO2/N2 within carbon nanotubes: a density functional theory study with dispersion corrections. Nanotechnology 2009;20:375701. doi:10.1088/0957-4484/20/37/375701.

[180] Palma V, Barba D, Ciambelli P. H 2 S Removal in Biogas by Direct Catalytic Oxidation to Sulphur on V 2 O 5 / CeO 2 Catalysts 2012;29:631–6. doi:10.3303/CET1229106.

[181] Ambrosetti A, Silvestrelli PL. Gas Separation in Nanoporous Graphene from First Principle Calculations. J Phys Chem C 2014;118:19172–9. doi:10.1021/jp504914u.

[182] Liu Y, Wilcox J. First-principles studies of CO2/CH4 adsorption on the defected graphene surface. Abstr. Pap. Am. Chem. Soc., vol. 239, AMER CHEMICAL SOC 1155 16TH ST, NW, WASHINGTON, DC 20036 USA; 2010.

[183] Ulmschneider JP, Ulmschneider MB, De Nola A. Monte carlo vs molecular dynamics for all-atom polypeptide folding simulations. J Phys Chem B 2006;110:16733–42. doi:10.1021/jp061619b.

# 3. CHAPTER THREE

## Chemical, Physical, and Morphological Characterization of Biochar as Gas Adsorbent

This chapter has been **published**; Bamdad H*, Hawboldt K. Comparative study between physiochemical characterization of biochar and Metal Organic Frameworks (MOFs) as gas adsorbents. The *Canadian Journal of Chemical Engineering*. 2016 Nov 1;94(11):2114-20.

## Abstract

The literature review indicated that the characterizations of biochar were profoundly affected by pyrolysis conditions and feedstock. As such, in this study, biochar produced from three different woody biomasses softwood (sawdust and bark (Balsam fir)) and hardwood (Ash wood), were compared in terms of chemical and physical properties. The biochar was produced via fast pyrolysis at 400-500 ºC in a 4 kg/h capacity auger reactor. The produced biochars were characterized for elemental composition, surface area, morphology, proximate analysis, crystalline structure, and thermal properties. These biochars were then compared with a Metal Organic Framework (MOF) with respect to properties key for adsorbent applications. All biochars were basic (pH 8.9-10.7), while MOFs were acidic. Based on TGA results, biochars are less resistant to heat compared to MOFs. The morphology of biochar and MOF-5 differ in pore size, chemistry, and structure. Biochar has higher carbon content and more aromatic functional groups than MOFs, which could play an important role in the adsorption of acidic gases from natural/produced gas.

Keywords: Biochars, Metal Organic Frameworks (MOFs), Physiochemical characterization tests, Gas adsorbents

## Introduction

Hydrogen sulfide ($H_2S$) and carbon dioxide ($CO_2$) are common contaminants in oil and gas production/processing, wastewater treatment plants, fossil fuel combustion, and landfill gases, which can all result in corrosion, negative environmental effects, and

represent a safety risk [1]. In addition to light hydrocarbons, natural gas can contain variable amounts of carbon dioxide, nitrogen, sulfur compounds, water, and small amounts of helium (less than 1 vol.%) and mercury (generally 5–300 $\mu gNm^{-3}$) [2]. On offshore platforms, the treatment of any gas or liquid effluent is challenging due to space restrictions on the platform and/or manpower on the platform. In platforms where the main product is oil, any produced gas is re-injected, used for utilities, and/or flared, and must be treated to an appropriate level for these applications. These challenges are not restricted to offshore and any remote location (e.g. landfills, small wastewater treatment plants etc.) require smaller scale, less operationally intensive alternatives to gas treatment, particularly if the gas is to be used as a fuel. There are a number of processes used to remove $CO_2$ and $H_2S$ (acid gases) from natural gas, including absorption and adsorption. In absorption, the acid gases are removed using solvents such as monoethanolamine (MEA) and diethylamine (DEA). Although the selectivity of this form of separation is relatively high, it is costly due to high energy needs in solvent regeneration and space requirements [3]. An alternative approach to absorption is adsorption, in which the contaminants are removed from the gas mixture by porous solid adsorbents. The most common adsorbents used in natural or produced gas treatment to remove acid gases are metal organic framework adsorbents, commercial adsorbents such as biochars, and silica.

Biochar produced from thermochemical conversion of biomass has been used for a number of different applications, including structural fill for construction and soil stabilization [4], soil/water decontamination [5], and as adsorbents in gas effluent treatment [6,7].The application depends on the properties of the biochars, which in turn

depend on the feedstock type, pyrolysis temperature, and residence time [8]. Biochar can be generated through thermal treatment of lignocellulosic biomass, such as coconut, almond, hazelnut, palm kernel shells, rice husk and wood [9,10], as well as municipal and industrial waste, and activated sludge [11,12]. Using biochar as an adsorbent in the gas treatment process could be a sustainable approach if the biomass source is a waste material.

Metal Organic Frameworks (MOF) are an emerging class of inorganic–organic hybrid materials comprised of single metal ions or polynuclear metal cluster corners connected by organic ligands that formed one, two or three dimensional structures [13]. MOFs are particularly effective for the removal of $H_2S$ from natural gas due to the chemical affinity of $H_2S$ to metal cations on the surface of these sorbents [14]. There are a number of studies in MOF applied to carbon dioxide capture [15–17]. MOF exhibit properties advantageous for gas purification, such as high selectivity, uniform micropores, high surface areas, and thermal and chemical stability [18], however there are high synthesis costs, time consuming production, low hydrothermal stability, and high regeneration costs [19]. Biochar, as a by-product of an existing process, is less intensive to produce, more environmentally friendly, and the surface area properties can be enhanced.

One of the key aspects in determining adsorbents' application to gas treatment is to characterize the structural properties of the adsorbents. The objective of this study is to investigate the physiochemical properties of biochars sourced from different woody biomasses and compare them with metal based adsorbent (Metal Organic Frameworks

(MOF)), one of the adsorbents in gas industries, to determine the potency of acid gas removal form natural or produced gas.

## 3.1. Experimental Methodology

### 3.1.1. Feedstock

Biochar was sourced from feedstock that would otherwise be stockpiled and the action of microorganism convert it to landfill gases (mainly consist of $CH_4$ and $CO_2$). Three types of feedstocks including softwood sawdust and bark (Balsam fir) and hardwood sawdust (Ash wood) were obtained from Sexton Lumber sawmill (Bloom- field, Newfoundland, and Labrador) and ABRI-tech, Quebec. The feedstocks were dried for 2 days at ambient temperature to decrease the moisture to ~12%. The samples were ground through a cutter mill to produce an average particle size of less than 2 mm. After grinding, biomasses were dried in the oven at 70 ºC overnight to about 2% moisture content prior to fast pyrolysis.

### 3.1.2. Biochar Production

The feedstocks were pyrolyzed at different pyrolysis temperatures in an auger reactor (Fig. 3-1).

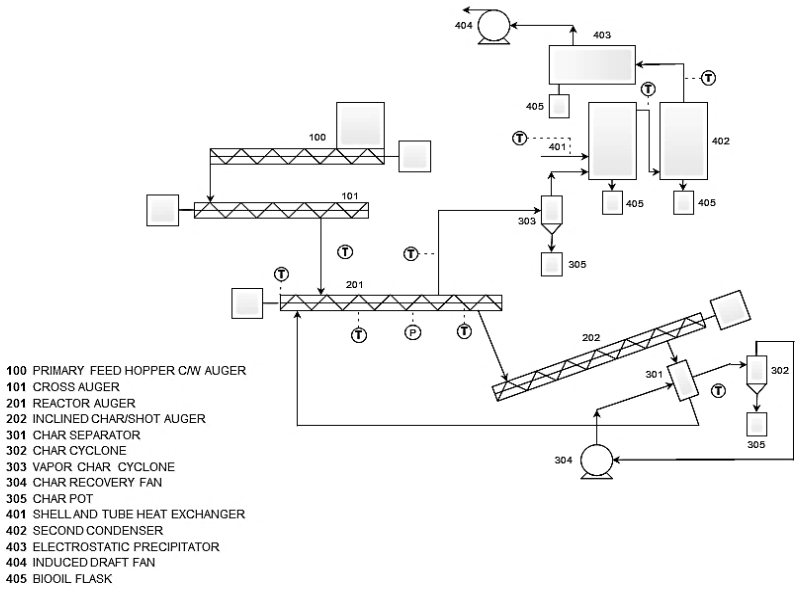


Figure 3-1: Process flow diagram (PFD) of pyrolysis system

Biooil, char, and gas are the pyrolysis products, with biooil as the main product, which has a highest yield at 450 ºC. In this study, we focused on producing biochar by fast pyrolysis method because the primary objective was producing biooil, and then the biochar market was developed in order to maximize the sustainability of the process. This process includes a feeder consisting of two augers (100 and 101), an auger reactor (201) for converting biomass to products, an incline reactor for feeding the heat carrier steel shot (202), a cyclone for char separation (303), followed by two condensers (401 and 402) and an electrostatic precipitator (403) for biooil collection. The biochar is collected (305) at the back of the system. Two vacuum fans are used (304 and 404) to recover char and gas respectively. The biochar from sawdust, hardwood, and bark are called SW biochar, HW biochar, and BK biochar followed by produced temperature hereafter. The changes in feedstock after pyrolysis can be observed by product appearance in Fig. 3-2.

The final form of all biochars looks the same because the auger reactor act as grinder and crush all feedstocks.

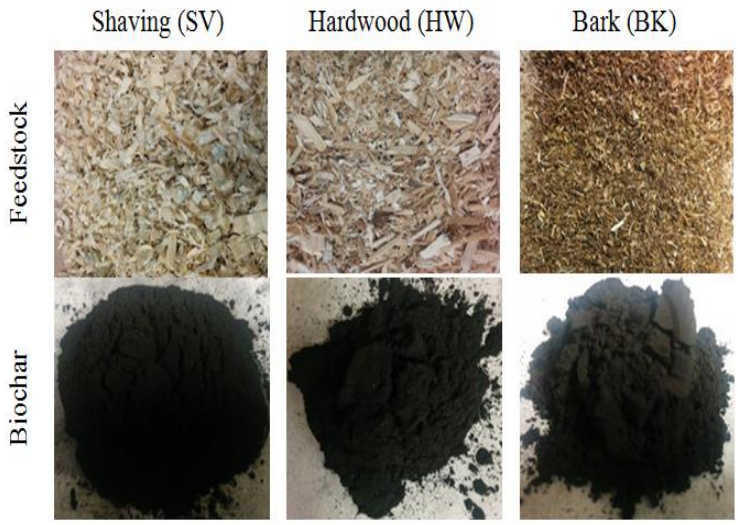


Figure 3-2: The appearance of feedstocks and biochars

### 3.2. Analytical Methods

The pH of the biochars was measured with a ratio of 1:5 (wt/wt), 1 g of produced char and 5 g of distilled water weighed into a 20 mL glass scintillation vial and shaken for 30 minutes using a solution mixer (Thermo Scientific Vortex Maxi Mix II). The solution was then measured using a pH meter (SympHony B10P), which was calibrated using an alkaline buffer. The elemental analysis of the biochar was performed using a CHN/O Analyzer (Perkin Elmer Series II 2400) and the oxygen content was determined by the difference of total elements and wt.% of C, H, and N.

The ash content of the biochar was determined as follows: 2 g of char was placed into a porcelain crucible. The crucible was transferred to a muffle furnace set at 600 ºC and

left overnight. The mass remaining was ash, and percentage ash was calculated as (wt. ash/wt. char) * 100.

The surface morphology of biochar was studied using a Scanning Electron Microscope or SEM (FEI 650F). In the SEM analysis, samples were mounted on carbon adhesive tabs of 12 mm diameter, which were put on aluminum stubs using carbon tape to avoid the formation of electric charge on the surface during scanning. Images were taken at low vacuum, with a pressure of 0.7 torr.

The average pore size, pore volume, and surface area of biochar were measured by $N_2$ adsorption at 77K (Micrometrics Tristar II Plus), and the BET (Brunauer–Emmett–Teller) equation was used to calculate the surface area of the biochar. The bulk densities of the biochars were computed based on the weight of biochar compacted into the mold over the volume of the mold by using the Wilson (1970) [20] test method.

The thermogravimetric Analysis (TA Instruments model Q500) method was used to measure percent moisture, volatiles, ash, and fixed carbon of the biochar produced. For the Thermogravimetric Analysis (TGA) experiment, 5-10 mg sample of biochar was prepared and heated from room temperature to 750 $^0$C, under a steady 50 mL/min flow of nitrogen. At 750 $^0$C, the gas was switched to air at 50 mL/min and held isothermally for 15 minutes in order to fully oxidize the sample.

Infrared spectra were obtained by using a FTIR (Bruker Alpha FTIR spectrometer) with a range of 400 to 4000 $cm^{-1}$, a resolution of 4 $cm^{-1}$, and a total of 24 scans for both background and sample measurement. X-Ray Diffraction (XRD) analysis (Rigaku

Ultima-IV at 40 kV and 44 mA using Cu-Kα energy source) were also performed to measure XRD patterns within an angular range of 5–100º (2θ).

Fig. 3-3 summarizes the characterization tests used in this work. In order to compare biochars with metal organic frameworks, the physiochemical properties of MOFs including SEM, BET, TGA, FTIR and XRD were obtained from the literature.

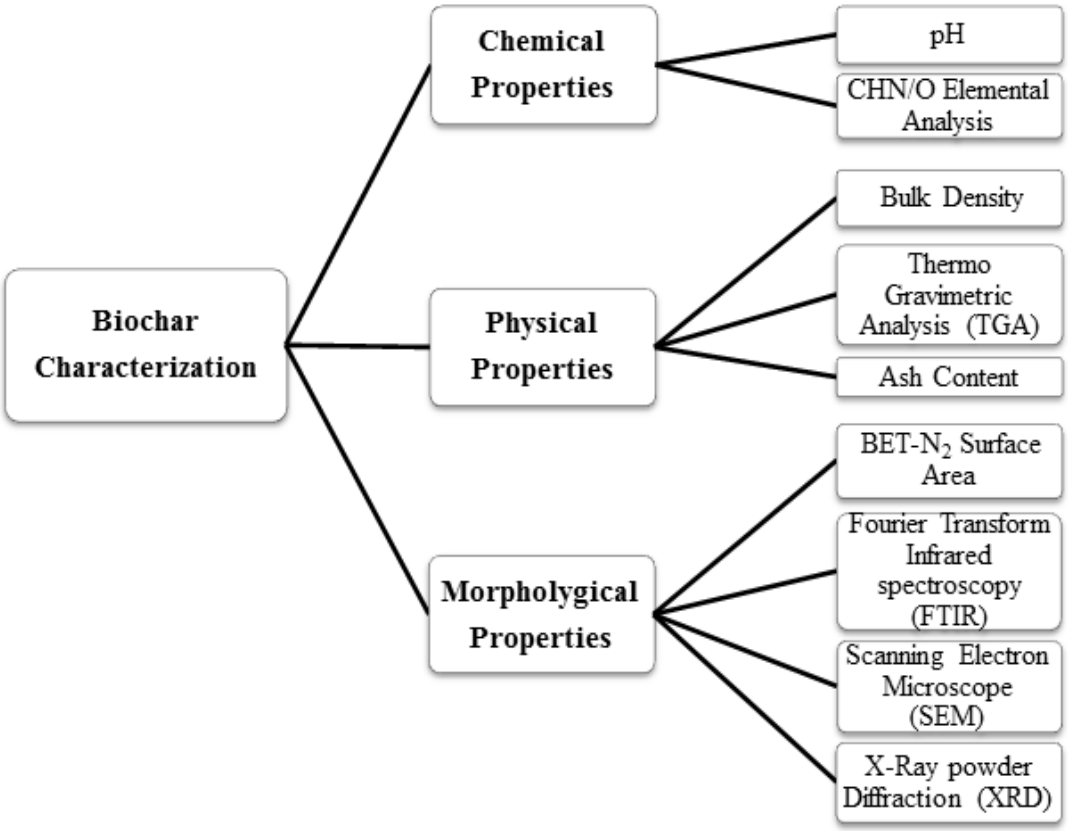


Figure 3-3: Flowchart of applied characterization tests on biochars

## 3.3. Results and discussion

### 3.3.1. Characterization

#### 3.3.1.1. Chemical properties

The elemental composition and pH of the biochars are presented in Table 3-1 and 3-2, respectively. All biochars were basic (8.9-10.7), whereas MOFs are mostly acidic due to the synthesis process [21]. Surfaces with higher pH could be more favourable to adsorb acidic gases [22], however other factors impact the adsorption process. C, H, N elementals for all of the three feedstock were in a similar range, as carbon content was from 48% to 49.6%. The H and N contents ranged between 5.7% to 6% and 0.01 to 0.3 %, respectively. The C content of bark as feedstock was the highest between all feedstock, which is consistent with the TGA results. Hardwood (feedstock) showed the highest H and N content and sawdust contained the most O content amongst feedstock. As seen in Table 1, the biochar samples have higher carbon contents and less hydrogen and oxygen contents compared to raw feedstock. The atomic H:C and O:C ratios of biochars decreased with an increase in pyrolysis temperature, which may be due to dehydration, decarboxylation, and decarbonylation [23]. These structural alterations induce more carbonization process [24]. Biochars with lower H:C ratios produced under higher thermal transformation results in greater loss of H and N relative to C [25]. Based on the H:C results, it is evident that highest carbonization with the lowest H:C ratio occurred in sawdust at 500 °C biochar. The (O+N):C ratios (polarity index) were decreased by increasing pyrolysis temperature [26]. More polar surfaces have the potential to adsorb polar molecules such as hydrogen sulfide more readily [27].

Table 3-1: Elemental analysis of feedstock and biochar samples (wt%, dry basis)

| | Samples | C | H | N | O | H:C | O:C | (O+N):C |
|---|---|---|---|---|---|---|---|---|
| Feedstock | Sawdust | 47.70 | 5.68 | 0.01 | 46.62 | 0.12 | 0.98 | 0.98 |
| | Hardwood | 48.70 | 6.05 | 0.35 | 44.90 | 0.12 | 0.92 | 0.93 |
| | Bark | 49.63 | 6.00 | 0.19 | 44.18 | 0.12 | 0.89 | 0.89 |
| Biochar | SW450-labscale | 79.40 | 3.40 | 0.05 | 12.90 | 0.04 | 0.16 | 0.16 |
| | SW400 | 70.90 | 3.10 | 0.07 | 25.93 | 0.04 | 0.37 | 0.37 |
| | SW450 | 74.79 | 3.51 | 0.24 | 21.46 | 0.05 | 0.29 | 0.29 |
| | SW500 | 76.37 | 2.36 | 0.15 | 19.12 | 0.03 | 0.25 | 0.25 |
| | HW400 | 72.53 | 3.12 | 0.15 | 24.21 | 0.04 | 0.33 | 0.34 |
| | HW450 | 73.25 | 3.64 | 0.16 | 22.95 | 0.05 | 0.31 | 0.315 |
| | HW500 | 74.84 | 2.34 | 0.22 | 22.60 | 0.03 | 0.30 | 0.30 |
| | BK450 | 67.67 | 3.11 | 0.42 | 28.61 | 0.05 | 0.42 | 0.43 |
| | Mix BK-SW450 | 69.88 | 2.45 | 0.20 | 27.46 | 0.04 | 0.39 | 0.40 |
| | AC (Norit) | 81.34 | 2.10 | 0.28 | 16.28 | 0.02 | 0.20 | 0.20 |

### 3.3.1.2. Physical properties

The bulk densities of all dry biochars were less than 1 g/cm$^{-3}$ (Table 3-2), which is consistent with the results proposed by Byrne and Nagle [28]. The observed low density of biochars may be due to high internal porosity [25].

Thermo Gravimetric Analysis (TGA) was carried out to determine the structure [24] and thermal stability of the feedstock and biochar samples. The feedstock and biochar TGA curves are shown in Fig. 3-4. The biochar source (woody biomass) is made up of four main components: water, cellulose, hemicellulose, and lignin. The ratio of these components is a function of the wood type and is reflected in the produced char. The first stage of mass loss (~7%) was due to moisture evaporation up to 135 °C in all three feedstocks. The decomposition of hemicellulose occurs much quicker than cellulose or lignin at a relatively low temperature range (200 °C to 300 °C) [29]. Hemicellulose is a mixture of various polymerized monosaccharaides (xylose, glucose, arabinose, mannose etc.) with a lower degree of polymerizing. Due to its amorphous structure and large number of branches, the thermal stability is lower than that of cellulose [30]. The temperature range for hemicellulose degradation in the feedstock partially overlaps the cellulose degradation (300 °C-400 °C) as seen in our study [31]. The decomposition of lignin occurs in a broader range of temperature between 300 °C and 700 °C due to a three dimensional heterogeneous aromatic structure and subsequently higher thermal stability [29]. In all three cases, bark feedstock exhibited higher lignin content than sawdust and hardwood. The compositions of the three biomasses are summarized in Table 3-3.

In the biochar samples, the first weight loss on the TGA curve is related to moisture loss (up to 150 ºC) and medium volatiles, the second and third is attributed to fixed carbon and ash, respectively. The type of feedstock used to obtain biochars influenced the moisture and the volatile-matter content [32]. Fig. 3-4 shows there is a significant change in the thermal degradation profiles as pyrolysis temperature increased. The TGA curves

of biochar show the fixed Carbon content increased with pyrolysis temperature due to increasing concentrations of volatile matter being released. Biochar produced from sawdust at 500 °C exhibited the highest fixed carbon content in comparison to the other biochar samples. The ash concentration of the biochar was impacted mainly by feedstock type [33]. Comparing these findings with related literature also revealed the ash content was increased by increasing the pyrolysis temperature [34]. The increase in ash content is the result of a progressive concentration of minerals and destructive volatilization of lignocellulosic matters as temperature increased [34,35]. The weight loss curve of bark char differs from sawdust and hardwood char because the lignin content (and resulting pyrolysis products) in bark is higher than sawdust and hardwood [36]. The decomposition initiates at 300-400 ºC for biochar and 400-500 ºC for MOF-5 [21]. Therefore, MOF-5 is more resistant to thermal degradation compared to biochars. Table 3-3 exemplifies the proximate analysis results of the three samples. Fixed carbon ranged from 62–65%, volatile matter from 26–34%, and ash contents from 3–7.55%, depending on the biochar type. The ash percentage analyzed by TGA (Table 3-3) is different from the ash percentage found with a muffle furnace (Table 3-2). In general, the muffle furnace is a more precise method to determine ash content.

Table 3-2: Physiochemical characteristics of obtained biochars

| | SW biochar | HW biochar | BK biochar |
|---|---|---|---|
| pH | 9.982 | 10.740 | 8.977 |
| Ash (wt.%, dry basis) | 10.960 | 8.247 | 9.734 |
| Bulk Density (g $cm^{-3}$) | 0.323 | 0.342 | 0.356 |

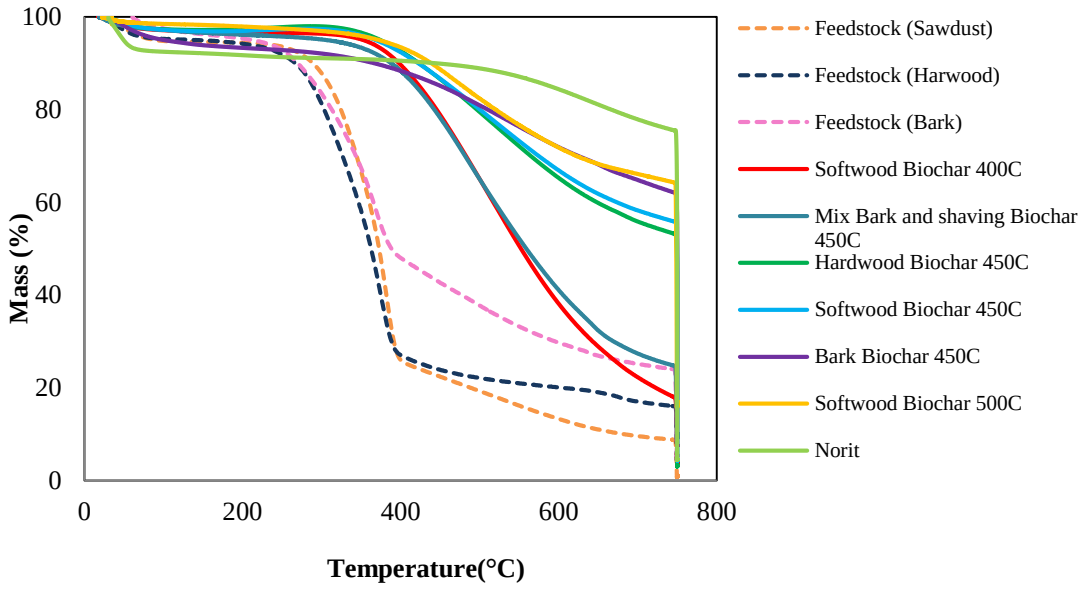


Figure 3-4: TGA curves of biomasses and biochars

Table 3-3: Proximate analysis of the feedstocks and samples

| Compositions (wt%) | Sawdust | Hardwood | Bark | SW450 biochar | HW450 biochar | BK450 biochar |
|---|---|---|---|---|---|---|
| Volatile matter | 89.87 | 82.44 | 75.97 | 32.74 | 34.61 | 26.97 |
| Fixed carbon | 7.81 | 12.5 | 18.73 | 62.94 | 62.32 | 65.48 |
| Ash | 2.32 | 5.06 | 5.3 | 4.32 | 3.07 | 7.55 |

### 3.3.1.3. Morphological properties

SEM images (Fig. 3-5) illustrate the amorphous and heterogeneous structure of the biochars. A comparison between SEM micrographs of all chars and MOF-5 highlight the difference between the heterogeneous unstructured biochars and the developed structure

of the MOFs (Fig. 3-5). Among the biochars sourced from different feedstock, hardwood char has a distinctive honey comb structure and is more porous than the other two biochar samples, with the pore diameters in the range of μm to nm. By increasing the pyrolysis temperature (SW and HW 400-500 °C), low molecular-weight volatiles released more from the matrix structure, resulting in the development of rudimentary pores in the biochar [37]. The BET surface area experiments were duplicated and the average was reported in the Table 3-4. The BET results (Table 3-4) indicate the specific surface areas for softwood and hardwood at 450 °C were 2.8$m^2$/g and 15.3$m^2$/g, respectively. From the above results, it can be seen that the BET surface area of biochar from hardwood was five times higher than of softwood. At this temperature, the BET surface area for bark char was calculated to be 8.69 $m^2$/g. This difference could be attributed to the compositional compounds such as lignin, cellulose, and hemicellulose in the original feedstock [38]. The average pore size of hardwood char is lower than the other biochar samples at 450 °C. This may be advantageous in gas adsorption as studies have concluded that small and narrow pores absorb fluids faster than larger ones due to driving pressure [39,40]. Table 3-4 demonstrates that an increase in pyrolysis temperature considerably promotes porosity development, since both surface area and pore volume were higher for materials prepared at higher pyrolysis temperatures. This is because with the increase in charring temperature, the size of volatile molecules evolved micropores in biochar leading to an increase in BET surface area [41]. The surface area drastically rose for the char produced from mixing two different feedstocks (bark and sawdust) at 450 °C. Overall, the highest BET surface area seen among biochars produced from woody biomass was for sawdust pyrolyzed at 500°C, 95.6 $m^2$/g due to releasing more volatile matters at high temperature.

The BET surface area of MOFs is reported as 290-3000 $m^2/g$ [19,39] in the literatures, depending on the materials and methods of synthesis.

**HW450 Biochar 16000x**

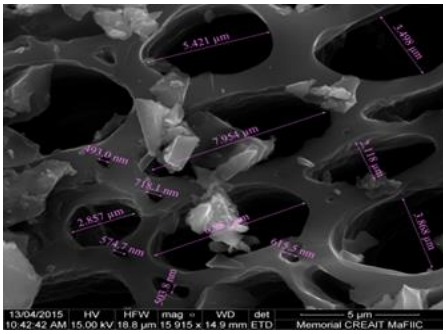


**HW450 Biochar 2000x**

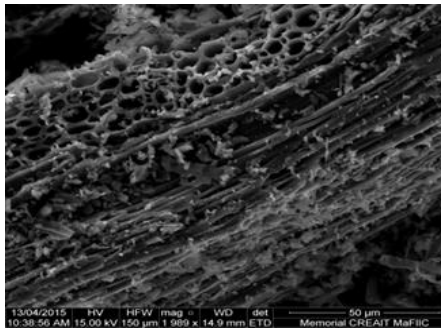


**BK450 Biochar 14000x**

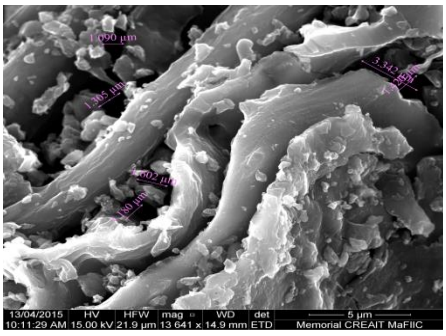


**BK450 Biochar 7000x**

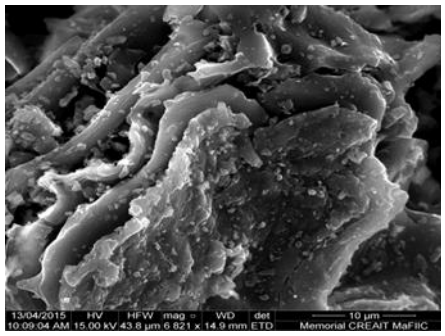


**SW450 Biochar 15000x**

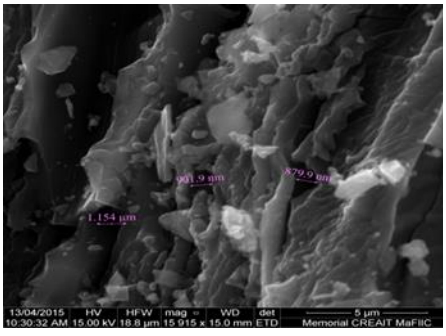


**SW450 Biochar 2000x**

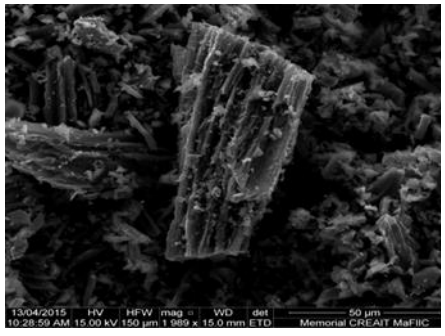

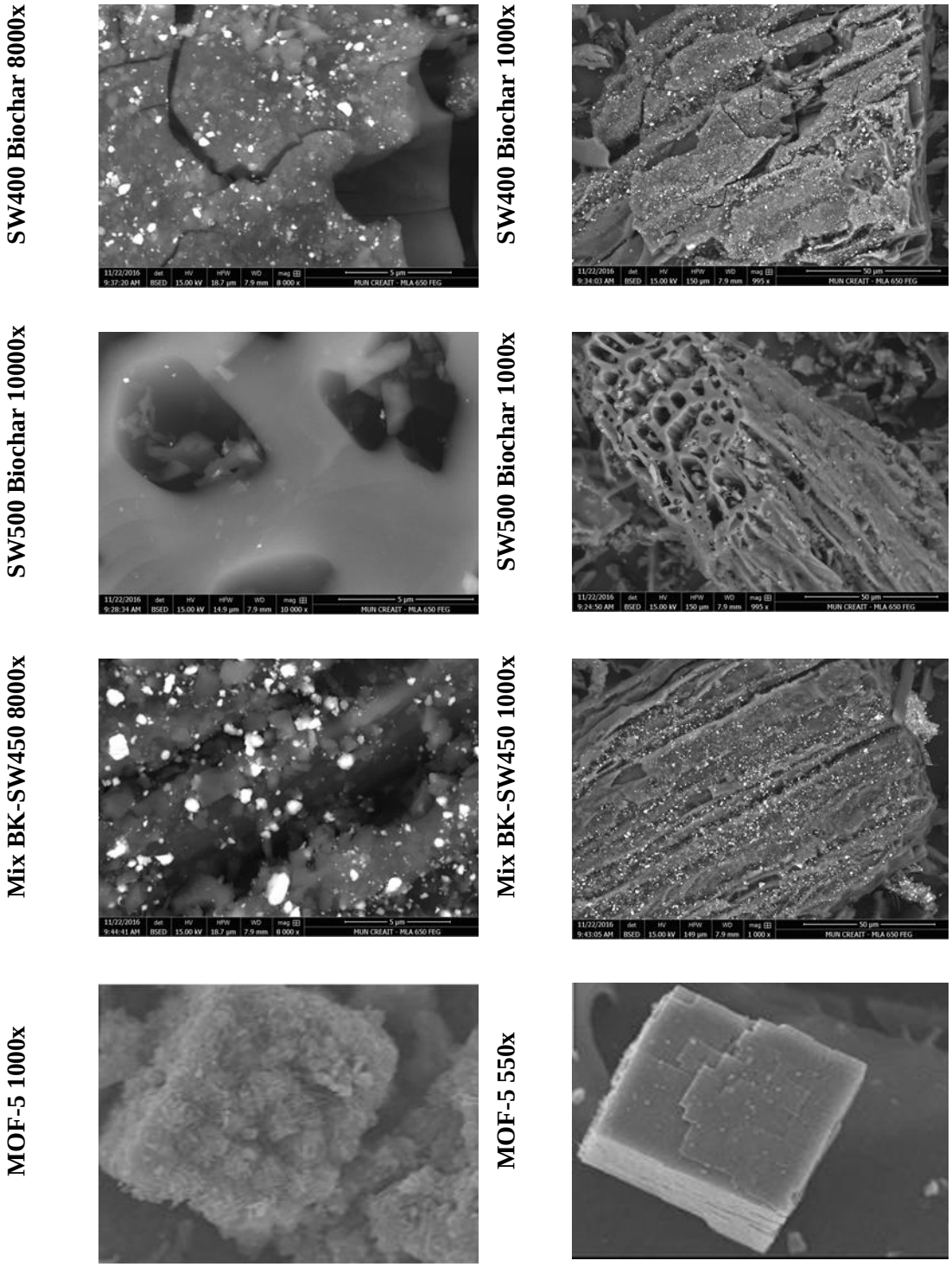


Figure 3-5: SEM micrographs: first row: hardwood biochar produced at 450 ºC-16000x (left) and 2000x (right); second row: bark biochar produced at 450 ºC-14000x (left) and 7000x (right); third row: sawdust biochar produced at 450 ºC-15000x (left) and

2000x (right); fourth row: sawdust biochar produced at 400 ºC-10000x (left) and 1000x (right); fifth row: sawdust biochar produced at 500 ºC-8000x (left) and 1000x (right); sixth row: mix of sawdust and bark biochar produced at 450 ºC-8000x (left) and 1000x (right); seventh row: MOF-5 1000x (left) MOF-5 550x (right) [27]

Table 3-4: Morphological properties of biochar samples and activated carbon

| Samples | SA (BET)($m^2$/g) | Avg. Pore size (nm) | Micropore volume ($cm^3$/g) |
|---|---|---|---|
| SW450-labscale | 2.47 | 6.62 | N/A |
| SW450 | 2.76 | 7.23 | N/A |
| SW400 | 7.15 | 7.18 | N/A |
| HW400 | 7.35 | 7.08 | 0.0004 |
| BK450 | 8.68 | 9.09 | 0.0007 |
| HW450 | 15.30 | 6.80 | 0.0039 |
| Mix BK-SW450 | 30.52 | 6.99 | 0.009 |
| HW500 | 50.91 | 5.79 | 0.0171 |
| SW500 | 95.58 | 4.36 | 0.0328 |
| AC (Norit) | 1166.49 | 3.63 | 0.3246 |

In the FTIR spectra of all biomasses (Fig. 3-6), there is a broad band at 3400-3200 $cm^{-1}$ indicating O-H stretching which may be attributed to the presence of moisture, phenol or hydroxyl groups. The disappearance of the O-H group in the char samples could be due to the moisture evaporation during pyrolysis process [42]. Previous studies [43,44] indicated hemicellulose begins to decompose at 160 °C; however, some parts of cellulose and lignin will be remaining in the biochar structure after the pyrolysis process [45]. The peaks in the range of 700 to 1800 $cm^{-1}$ and 2800 to 3500 $cm^{-1}$ suggest the presence of lignin and cellulose, respectively. The absorption peak at 900-700 and 1600-1500 $cm^{-1}$

found in the lignin spectra of all char and biomass, correspond to aromatic C-H stretch, and C=C in the aromatic ring, respectively [46]. The bands attributed to aliphatic and aromatic $CH_n$ decreased in sawdust char samples as the temperature increased, possibly due to the breaking of the weak bonds between the C and H of the groups [47]. All of the biomass samples showed a strong and broad peak around 1000 $cm^{-1}$, which could correspond to aliphatic C-O-C stretching [48]. These peaks were much weaker in char samples because of decomposition of cellulose and hemicellulose during conversion process [49]. The peak at 1700-1600 $cm^{-1}$ was related to C=O stretching attributed to the carbonyl group [50] while the small peak in the 3000-2700 $cm^{-1}$ region illustrates the aliphatic C-H stretch vibration and/or C-C chains in the biochar spectrum [51]. However, in all types of biomasses, the C-H stretching was more noticeable, suggesting the thermochemical conversion may destroy some of the C-H groups in biochar samples [48]. The phenol functional group peaks (O-H) were observed (3300-3900 $cm^{-1}$) as well, with lost intensity by increasing temperature in char samples [52]. The FTIR spectra of biochars and MOF-5 [21] are almost identical, however, the C=O functional group peaks in biochars intensify more than MOF-5. This outcome is consistent with thermogravimetric analysis results in that the carbon content (aromaticity) of biochar samples is higher than MOFs.

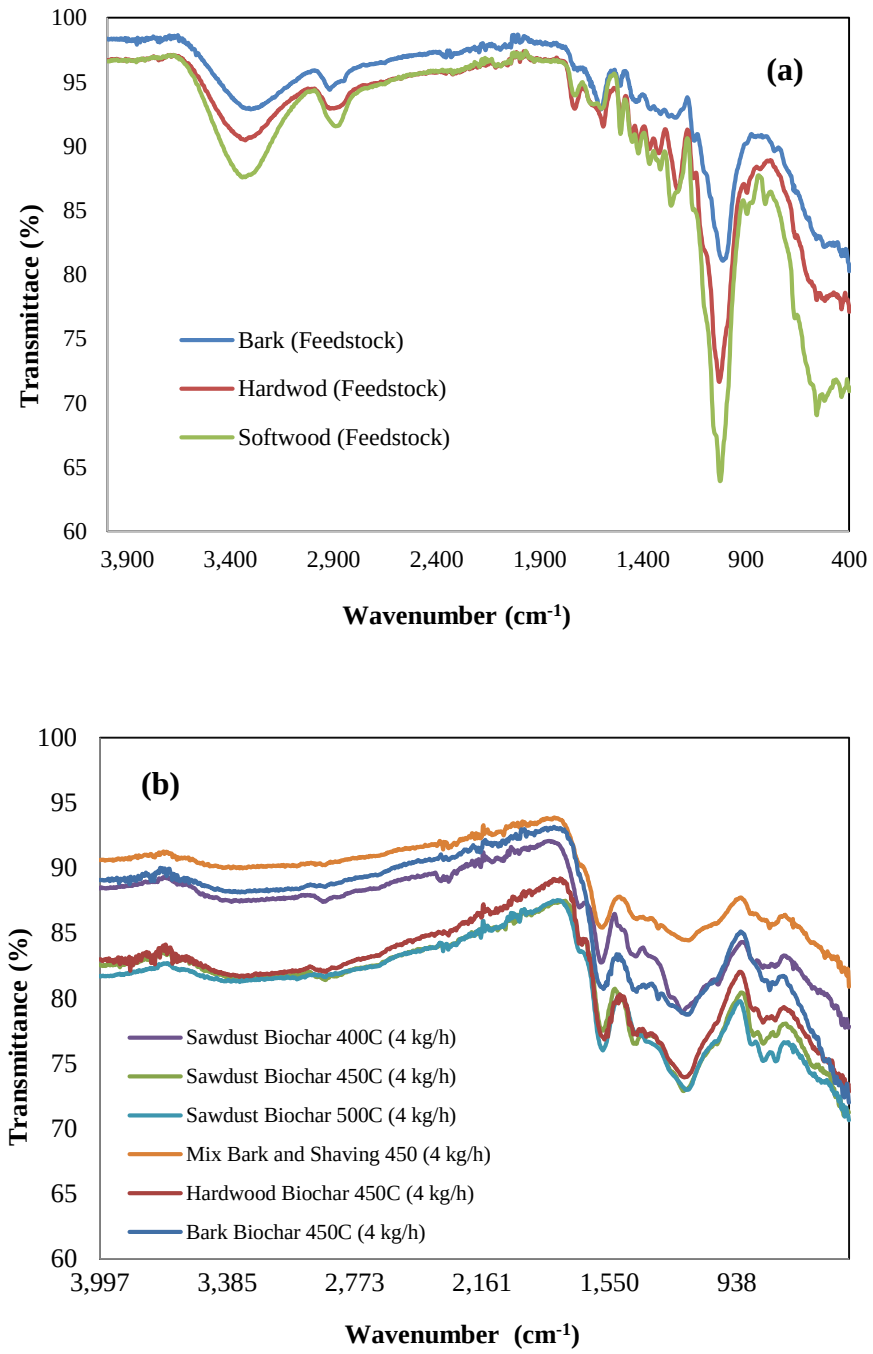


Figure 3-6: FTIR spectra of feedstocks (a) and biochar samples (b)

XRD analysis indicates the crystalline salts, inorganic phase (minerals) [52] of biochars and MOF-5 (Fig. 3-7). Two narrow, sharp peaks in MOF-5 around 12º and 17º

were attributed to zinc hydroxide ($Zn(OH)_2$) [21]. In biochar samples, the peaks are almost the same. The profiles at 16º and 20º were assigned to the cellulose crystalline region of wood. These results are in agreement with previous studies [53,54]. Peaks at 27º, 30º, 32º, 36º, and 43º confirmed the formation of Quartz ($SiO_2$), Calcite ($CaCO_3$), Dolomite ($CaMg(CO_3)_2$), Magnetite ($Fe_3O_4$), and $C_{70}$(Carbon) during pyrolysis, respectively (Table 3-5). The type and amount of inorganic crystalline phase depend on the biomass and produced temperature [49].

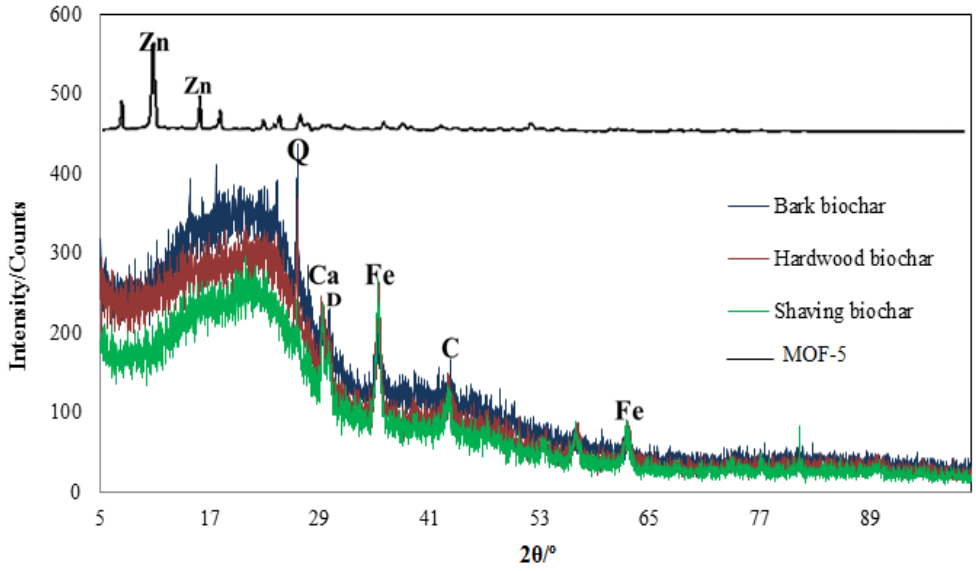


Figure 3-7: X-ray diffraction profiles of MOF-5[27] and biochars; Q: Quartz ($SiO_2$), Ca: Calcite ($CaCO_3$), Dolomite ($CaMg(CO_3)_2$), Magnetite ($Fe_3O_4$), $C_{70}$ (Carbon), Zn: ($Zn(OH)_2$)

Table 3-5: XRD results for biochars and MOF-5

| Mineral list | Formula |
|---|---|

| | | |
|---|---|---|
| **Biochars** | Quartz | $SiO_2$ |
| | Calcite | $CaCO_3$ |
| | Dolomite | $CaMg(CO_3)_2$ |
| | Magnetite | $Fe_3O_4$ |
| | Carbon | $C_{70}$ |
| **MOF-5** | Zinc Hydroxide | $Zn(OH)_2$ |

### 3.4. Conclusion

In this study, physical and chemical properties of three different types of wood-derived biochars were characterized, and results were compared with those of MOFs reported in the literature. The experimental results of pH tests showed that the biochar samples were basic which may indicate possible better acidic gas adsorption. The elemental analysis showed polarity of bark biochar (BK biochar) possibly favourable for polar gas adsorption. Based on FTIR and TGA results, biochar has higher carbon content and more aromatic functional groups in compare with MOFs. The thermal stability and surface area of MOFs are higher than the biochars. The SEM and XRD results showed the differences in the morphology, pore size, mineral content, and structure of biochar and MOF-5. The MOFs had uniform micropore structure while biochars had honey comb structure with variable pore diameters. Although all the biochar samples almost had the

same physiochemical properties, sawdust biochar 500 °C had the highest surface area, which can be chosen as the best biochar for adsorption.

Overall, the results comparing biochar with MOFs showed that MOFs have high surface area, uniform porosity and high thermal stability. It is difficult to predict if the heterogeneous nature of the surface morphology and chemical content of the biochars will be beneficial or a limitation to use as an adsorbent. Typically, this is determined through experiments. However, with this characterization data it is possible to use molecular modeling as a tool for the "best" application and/or treatment of the biochar to enhance adsorbency. These characteristics make MOFs attractive for high selectivity adsorption applications. However, the analysis of biochars showed they have good adsorption properties and may be more desirable, due to cost and environmental sustainability, when applied to bulk gas removal applications. In these applications, such as gas injection on offshore platforms, the gas quality standards are far less stringent than domestic utility or pipeline specifications. There are still some important challenges to consider for practical application of biochars for removing acid gases from produced and natural gas such as capacities, effect of impurities (*e.g*. water) and regeneration. As such, further research is required to identify all potentials of this promising adsorbent.

**Acknowledgement**

The authors are thankful for the great support given by NSERC (Natural Science and Engineering Research Council of Canada), SGS (School of Graduate Studies of Memorial University), and BioFuelNet Canada.

## References


[1] Lebrero R, Bouchy L, Stuetz R, Muñoz R. Odor Assessment and Management in Wastewater Treatment Plants: A Review. Crit Rev Environ Sci Technol 2011;41:915–50. doi:10.1080/10643380903300000.

[2] Tagliabue M, Farrusseng D, Valencia S, Aguado S, Ravon U, Rizzo C, et al. Natural gas treating by selective adsorption: Material science and chemical engineering interplay. Chem Eng J 2009;155:553–66. doi:https://doi.org/10.1016/j.cej.2009.09.010.

[3] Yu CH, Huang CH, Tan CS. A review of CO2 capture by absorption and adsorption. Aerosol Air Qual Res 2012;12:745–69. doi:10.4209/aaqr.2012.05.0132.

[4] Abdelhafez A a, Li J, Abbas MHH. Feasibility of biochar manufactured from organic wastes on the stabilization of heavy metals in a metal smelter contaminated soil. Chemosphere 2014;117C:66–71. doi:10.1016/j.chemosphere.2014.05.086.

[5] Ahmad M, Rajapaksha AU, Lim JE, Zhang M, Bolan N, Mohan D, et al. Biochar as a sorbent for contaminant management in soil and water: A review. Chemosphere 2014;99:19–23. doi:10.1016/j.chemosphere.2013.10.071.

[6] Plaza MG, Gonz??lez AS, Pis JJ, Rubiera F, Pevida C. Production of microporous biochars by single-step oxidation: Effect of activation conditions on CO2 capture. Appl Energy 2014;114:551–62. doi:10.1016/j.apenergy.2013.09.058.

[7] Ghosh TK, Tollefson EL. A continuous process for recovery of sulfur from natural gas containing low concentrations of hydrogen sulfide. Can J Chem Eng 1986;64:960–8. doi:10.1002/cjce.5450640612.

[8] Yaman S. Pyrolysis of biomass to produce fuels and chemical feedstocks. Energy Convers Manag 2004;45:651–71. doi:10.1016/S0196-8904(03)00177-8.

[9] Lua AC, Yang T. Theoretical and experimental SO2 adsorption onto pistachio-nut-shell activated carbon for a fixed-bed column. Chem Eng J 2009;155:175–83. doi:10.1016/j.cej.2009.07.031.

[10] Tseng H-H, Wey M-Y. Study of SO2 adsorption and thermal regeneration over activated carbon-supported copper oxide catalysts. Carbon N Y 2004;42:2269–78. doi:10.1016/j.carbon.2004.05.004.

[11] Dias JM, Alvim-Ferraz MCM, Almeida MF, Rivera-Utrilla J, Sánchez-Polo M. Waste materials for activated carbon preparation and its use in aqueous-phase treatment: A review. J Environ Manage 2007;85:833–46. doi:10.1016/j.jenvman.2007.07.031.

[12] Siti Noraishah I, MM H. Study on the Use and Modification of a Sustainable Solid Waste Material for Carbon Dioxide Capturing 2013.

[13] Bae YS, Snurr RQ. Development and evaluation of porous materials for carbon dioxide separation and capture. Angew Chemie - Int Ed 2011;50:11586–96. doi:10.1002/anie.201101891.

[14] Wang L, Yang RT. New nanostructured sorbents for desulfurization of natural gas. Front Chem Sci Eng 2014;8:8–19. doi:10.1007/s11705-014-1411-4.

[15] Song C, Ling Y, Jin L, Zhang M, Chen D-L, He Y. CO 2 adsorption of three isostructural metal–organic frameworks depending on the incorporated highly polarized heterocyclic moieties. Dalt Trans 2016;45:190–7.

[16] Salah M, Marakchi K, Dalbouha S, Senent ML, Kabbaj OK, Komiha N. Influence of the functionalization of imidazole on its CO 2 uptake efficiency. A theoretical contribution. Comput Theor Chem 2015;1073:1–8.

[17] Wu H, Thibault CG, Wang H, Cychosz KA, Thommes M, Li J. Effect of temperature on hydrogen and carbon dioxide adsorption hysteresis in an ultramicroporous MOF. Microporous Mesoporous Mater 2016;219:186–9.

[18] Venna SR, Carreon MA. Metal organic framework membranes for carbon dioxide separation. Chem Eng Sci 2015;124:3–19.

[19] Andirova D, Cogswell CF, Lei Y, Choi S. Effect of the structural constituents of metal organic frameworks on carbon dioxide capture. Microporous Mesoporous Mater 2016;219:276–305.

[20] Wilson SD. Suggested method of test for moisture-density relations of soils using Harvard compaction apparatus. Spec. Proced. Test. Soil Rock Eng. Purp. Fifth Ed., ASTM International; 1970.

[21] Zhao Y, Ding H, Zhong Q. Synthesis and characterization of MOF-aminated graphite oxide composites for CO2 capture. Appl Surf Sci 2013;284:138–44. doi:10.1016/j.apsusc.2013.07.068.

[22] Shang G, Shen G, Liu L, Chen Q, Xu Z. Kinetics and mechanisms of hydrogen sulfide adsorption by biochars. Bioresour Technol 2013;133:495–9. doi:10.1016/j.biortech.2013.01.114.

[23] Saikia R, Chutia RS, Kataki R, Pant KK. Perennial grass (arundo donax l.) as a feedstock for thermo-chemical conversion to energy and materials. Bioresour Technol 2015;188:265–72. doi:10.1016/j.biortech.2015.01.089.

[24] Mimmo T, Panzacchi P, Baratieri M, Davies CA, Tonon G. Effect of pyrolysis temperature on miscanthus (Miscanthus ?? giganteus) biochar physical, chemical and functional properties. Biomass and Bioenergy 2014;62:149–57.

doi:10.1016/j.biombioe.2014.01.004.

[25] Yargicoglu EN, Sadasivam BY, Reddy KR, Spokas K. Physical and chemical characterization of waste wood derived biochars. Waste Manag 2015;36:256–68. doi:10.1016/j.wasman.2014.10.029.

[26] Zhang P, Sun H, Yu L, Sun T. Adsorption and catalytic hydrolysis of carbaryl and atrazine on pig manure-derived biochars: Impact of structural properties of biochars. J Hazard Mater 2013;244–245:217–24. doi:10.1016/j.jhazmat.2012.11.046.

[27] Bockris J, Klerer J. Environmental chemistry. J Electrochem Soc 1979;126:64C–64C.

[28] Byrne CE, Nagle DC. Carbonization of wood for advanced materials applications. Carbon N Y 1997;35:259–66.

[29] Cao X, Zhong L, Peng X, Sun S, Li S, Liu S, et al. Comparative study of the pyrolysis of lignocellulose and its major components: Characterization and overall distribution of their biochars and volatiles. Bioresour Technol 2014;155:21–7. doi:10.1016/j.biortech.2013.12.006.

[30] Ma Z, Chen D, Gu J, Bao B, Zhang Q. Determination of pyrolysis characteristics and kinetics of palm kernel shell using TGA-FTIR and model-free integral methods. Energy Convers Manag 2015;89:251–9. doi:10.1016/j.enconman.2014.09.074.

[31] Kim KH, Kim JY, Cho TS, Choi JW. Influence of pyrolysis temperature on physicochemical properties of biochar obtained from the fast pyrolysis of pitch pine (Pinus rigida). Bioresour Technol 2012;118:158–62. doi:10.1016/j.biortech.2012.04.094.

[32] Jindo K, Mizumoto H, Sawada Y, Sanchez-Monedero M a., Sonoki T. Physical and chemical characterizations of biochars derived from different agricultural residues. Biogeosciences Discuss 2014;11:11727–46. doi:10.5194/bgd-11-11727-2014.

[33] Crombie K, Mašek O, Sohi SP, Brownsort P, Cross A. The effect of pyrolysis conditions on biochar stability as determined by three methods. GCB Bioenergy 2013;5:122–31. doi:10.1111/gcbb.12030.

[34] Tsai WT, Liu SC, Chen HR, Chang YM, Tsai YL. Textural and chemical properties of swine-manure-derived biochar pertinent to its potential use as a soil amendment. Chemosphere 2012;89:198–203. doi:10.1016/j.chemosphere.2012.05.085.

[35] Cao X, Harris W. Properties of dairy-manure-derived biochar pertinent to its potential use in remediation. Bioresour Technol 2010;101:5222–8.

doi:10.1016/j.biortech.2010.02.052.

[36] Harkin JM, Rowe JW. Bark and its possible uses. US Dep Agric For Serv For Prod Lab 1971:60.

[37] Lua AC, Lau FY, Guo J. Influence of pyrolysis conditions on pore development of oil-palm-shell activated carbons. J Anal Appl Pyrolysis 2006;76:96–102. doi:10.1016/j.jaap.2005.08.001.

[38] Manyà JJ. Pyrolysis for biochar purposes: A review to establish current knowledge gaps and research needs. Environ Sci Technol 2012;46:7939–54. doi:10.1021/es301029g.

[39] Polychronopoulou K, Cabello Galisteo F, López Granados M, Fierro JLG, Bakas T, Efstathiou AM. Novel Fe-Mn-Zn-Ti-O mixed-metal oxides for the low-temperature removal of H2S from gas streams in the presence of H2, CO 2, and H2O. J Catal 2005;236:205–20. doi:10.1016/j.jcat.2005.10.001.

[40] Schoelkopf J, Gane PAC, Ridgway CJ. A comparison of the various liquid interaction radii derived from experiment and network modelling of porous pigmented structures. Colloids Surfaces A Physicochem Eng Asp 2004;251:149–59. doi:http://dx.doi.org/10.1016/j.colsurfa.2004.09.001.

[41] Li J, Dai J, Liu G, Zhang H, Gao Z, Fu J, et al. Biochar from microwave pyrolysis of biomass: A review. Biomass and Bioenergy 2016;94:228–44. doi:10.1016/j.biombioe.2016.09.010.

[42] Chaiwat W, Hasegawa I, Tani T, Sunagawa K, Mae K. Analysis of Cross-Linking Behavior during Pyrolysis of Cellulose for Elucidating Reaction Pathway. Energy & Fuels 2009;23:5765–72. doi:10.1021/ef900674b.

[43] Jouiad M, Al-Nofeli N, Khalifa N, Benyettou F, Yousef LF. Characteristics of slow pyrolysis biochars produced from rhodes grass and fronds of edible date palm. J Anal Appl Pyrolysis 2015;111:183–90. doi:10.1016/j.jaap.2014.10.024.

[44] Yang H, Yan R, Chen H, Lee DH, Zheng C. Characteristics of hemicellulose, cellulose and lignin pyrolysis. Fuel 2007;86:1781–8. doi:10.1016/j.fuel.2006.12.013.

[45] Mitra S, Singh P, Manzoor S, Bhattacharyya P, Bera T, Kumar Patra A, et al. Can rice and wheat biochar amendment protect the carbon loss from tropical soils - An experimental study. Environ Prog Sustain Energy 2016;35:183–8. doi:10.1002/ep.12193.

[46] Wang L, Butterly CR, Wang Y, Herath HMSK, Xi YG, Xiao XJ. Effect of crop residue biochar on soil acidity amelioration in strongly acidic tea garden soils. Soil Use Manag 2014;30:119–28. doi:10.1111/sum.12096.

[47] Yang H, Yan R, Chen H, Lee DH, Liang DT, Zheng C. Mechanism of Palm Oil Waste Pyrolysis in a Packed Bed. Energy & Fuels 2006;20:1321–8. doi:10.1021/ef0600311.

[48] Qian K, Kumar A, Patil K, Bellmer D, Wang D, Yuan W, et al. Effects of Biomass Feedstocks and Gasification Conditions on the Physiochemical Properties of Char. Energies 2013;6. doi:10.3390/en6083972.

[49] Li J, Liang N, Jin X, Zhou D, Li H, Wu M, et al. The role of ash content on bisphenol A sorption to biochars derived from different agricultural wastes. Chemosphere 2017;171:66–73. doi:https://doi.org/10.1016/j.chemosphere.2016.12.041.

[50] Gunes A, Inal A, Sahin O, Taskin MB, Atakol O, Yilmaz N. Variations in mineral element concentrations of poultry manure biochar obtained at different pyrolysis temperatures, and their effects on crop growth and mineral nutrition. Soil Use Manag 2015;31:429–37.

[51] Chen WY, Mattern DL, Okinedo E, Senter JC, Mattei AA, Redwine CW. Photochemical and acoustic interactions of biochar with CO2 and H2O: Applications in power generation and CO2 capture. AIChE J 2014;60:1054–65. doi:10.1002/aic.14347.

[52] Prakongkep N, Gilkes RJ, Wiriyakitnateekul W. Forms and solubility of plant nutrient elements in tropical plant waste biochars. J Plant Nutr Soil Sci 2015;178:732–40. doi:10.1002/jpln.201500001.

[53] Jiang ZH, Yang Z, So CL, Hse CY. Rapid prediction of wood crystallinity in Pinus elliotii plantation wood by near-infrared spectroscopy. J Wood Sci 2007;53:449–53. doi:10.1007/s10086-007-0883-y.

[54] Liu Y, Yao S, Wang Y, Lu H, Brar SK, Yang S. Bio- and hydrochars from rice straw and pig manure: Inter-comparison. Bioresour Technol 2017;235:332–7. doi:10.1016/j.biortech.2017.03.103.

# 4. CHAPTER FOUR

## Application of biochar for acid gas removal: Experimental and statistical analysis using $CO_2$

This chapter has been **published**; Bamdad H*, Hawboldt K, MacQuarrie S, Papari S. Application of biochar for acid gas removal: Experimental and statistical analysis using $CO_2$. *Journal of Environmental Science and Pollution Research.* ESPR-D-18-08271.

## Co-authorship Statement

Hanieh Bamdad is the corresponding author of the paper presented in this chapter. Her contribution was preforming analysis on all samples, interpreting data, and writing the manuscript. Dr. Kelly Hawboldt and Dr. Stephanie MacQuarrie supervised development of work, helped in data interpretation and manuscript editing. Dr. Sadegh Papari helped to evaluate and edit the manuscript.

## Abstract

Acid gases such as carbon dioxide and hydrogen sulphide are common contaminants in oil and gas operations, landfill gases, and exhaust stacks from power plants. While there are a processes currently used to treat these effluents (e.g. amine absorption and adsorption using zeolite), many of these processes require high energy, space and hazardous chemicals. Removal using biochar derived from the fast pyrolysis of forestry residues represents a more sustainable option. In addition to the biochar properties determined through various characterization tests in chapter three, the significant adsorption parameters have an impact on the adsorption capacity of the biochar and must be optimized. In this chapter, adsorption using $CO_2$ as a surrogate for acid gases was investigated using various biochars produced from fast pyrolysis of sawmill residues. Response surface methodology was used to determine operating conditions for maximum adsorption and assess interaction of the adsorption parameters, *i.e.*, temperature, inlet feed flow rate, and $CO_2$ concentration, on biochar adsorption capacity. The Freundlich isotherm best represented the equilibrium adsorption and the kinetic model was pseudo

first-order. Thermodynamic analysis indicated the adsorption process was spontaneous and exothermic. The biochar had better adsorption capacity relative to commercial zeolite. Our results suggested that biochar could be used as a sustainable and cost-effective option for contaminant removal from acid gases produced in landfill gas treatment, fossil fuel extraction and/or combustion.

Keywords: Acid gases; carbon dioxide; adsorption; biochar; RSM

## Introduction

Acid gases ($CO_2$ and $H_2S$) are present in landfill gases (due to anaerobic digestion of organic matter), fossil fuel extraction, production and combustion gases, and exhaust from power plants among other gas streams. $H_2S$ is a toxic, corrosive gas and produces $SO_2$ on combustion, resulting in acid rain. The control of carbon dioxide ($CO_2$) is critical not only from a global warming and climate change perspective, but also from issues related to corrosion. Absorption has practical limitations in the removal of carbon dioxide and other acidic gases (*e.g.* $H_2S$) in operations such as offshore oil and gas platforms or remote regions (e.g. landfills). The most common method for acid gas removal ($CO_2$ and $H_2S$) from flue/produced/natural gas is gas-liquid amine-based absorption columns. In remote operations such as offshore oil and gas platforms, these processes have practical challenges including equipment space footprint (e.g. column plus regenerator), chemical storage, motion issues, and solvent regeneration energy requirements (Shafeeyan et al. 2010). An alternative approach to absorption processes is adsorption using porous solids. A review of common adsorbents used in natural/produced gas treatment were previously

reported (Bamdad et al. 2016). Among adsorbents, biochar is a low-cost sustainable option with excellent adsorbent properties that can be enhanced by further activation and/or surface functionalization (Wang et al. 2011). Biochar surface properties are a function of production conditions and feedstock, which in turn determines the capacity to adsorb various contaminants from aqueous or gaseous phases (Rajapaksha et al. 2014). In fast pyrolysis, the main product is bio-oil, as such biochar is a by-product. However, the biochar from fast pyrolysis contains functional groups which make it ideal for acid gas capture.

There have been several studies on biochar production (Guerrero et al. 2005; Kim et al. 2012, 2013), characterization (Spokas et al. 2011; Abnisa et al. 2013), and application as a gas adsorbent (Heidari et al. 2014; Plaza et al. 2014a). To the best of our knowledge, there is only limited research focused on statistical optimization of carbon-based adsorbents, specifically biochar, related to acid gas/$CO_2$ sorption. Pevida et al. (García et al. 2011) optimized commercial activated carbon (Norit R2030) using response surface methodology (RSM) to evaluate the combined effect of the $CO_2$ partial pressure and temperature (independent variables) on $CO_2$ capture capacity and breakthrough time (response variables). They found no interaction effect between the two independent variables on the responses and maximum adsorption was obtained at 25 ºC and a $CO_2$ partial pressure of 3 bar. There are limited data on the adsorption isotherm and kinetic models associated with this process. These are critical first steps in determining feasibility of process and designing larger scale systems.

In this work, the biochar capacity (from wood residues) for $CO_2$ removal is determined using "fast" pyrolysis biochars. $CO_2$ has been suggested to test the biochar as an effective indicator of adsorbent performance for other gases such as $H_2S$ and measuring $CO_2$ capacity is less hazardous. The pyrolysis conditions were at temperatures from 400–500 ºC, with vapour residence times in 10 seconds. Biochar was sourced from sawmill residues (softwood (balsam fir) and hardwood (ash wood)) and produced at lab (semi-batch) and pilot (auger reactor) scale for comparison. Details of these systems are described elsewhere (Papari et al. 2015, 2017). The impact of three significant variables, *i.e.*, adsorption temperature, total inlet flow rate, and % (v/v) $CO_2$, and combined interactions on the adsorption capacity were investigated. After determining the adsorption operating conditions where maximum adsorption occurred, sample screening among chars was performed to select the adsorbent with the highest capacity and compared with commercial adsorbent. The thermodynamic parameters, isotherm, and adsorption kinetics were obtained.

## 4.1. Materials and Methods

### 4.1.1. Materials

To validate our experimental apparatus a commercial chemically activated wood-based carbon supplied by Sigma Aldrich (Norit CA1) was tested. Once the system was validated, two sets of experiments were performed: one studying the impact of adsorption process parameters on capacity of a selected biochar (softwood bark feedstock pyrolyzed at 450 ºC), and a second comparing biochars produced from different feedstocks and

pyrolysis temperatures. The other biochars were also randomly tested with respect to the impact of adsorption parameters to confirm the RSM results. The experiments and feedstock are summarized in Table 4-1.

Table 4-1: List of samples and production conditions

| **Sample** | **Feedstock** | **Type of pyrolysis** | **Scale** | **Operating temperature (°C)** | **Application** | **Abbreviated names** |
|---|---|---|---|---|---|---|
| Activated Carbon (Norit CA1) | Wood | N/A | N/A | N/A | Validation, Optimization | AC |
| Biochar | Softwood Bark | Fast | Pilot | 450 | Maximum adsorption, Comparison | F-P-BK450 |
| Biochar | Softwood Sawdust | Fast | Lab | 450 | Comparison | F-L-SW450 |
| Biochar | Softwood Sawdust | Fast | Pilot | 400, 450, 500 | Comparison | F-P-SW400, F-P-SW450, F-P-SW500 |
| Biochar | Hardwood | Fast | Pilot | 400, 450, 500 | Comparison | F-P-HW400, F-P-HW450, F-P-HW500 |
| Biochar | Softwood Bark and Sawdust | Fast | Pilot | 450 | Comparison | F-P-Mix BK-SW450 |

Adsorbents were dried in the oven at 60 ºC overnight before each experiment. A detailed description of production process and physiochemical properties of fast pyrolysis biochar have been reported elsewhere (Bamdad and Hawboldt 2016).

### 4.1.2. Characterizations

Textural properties of all samples were measured by $N_2$ adsorption isotherms obtained at 77 K with a Micrometrics Tristar II Plus, USA. The average pore size and micropore volume were measured by the pore size distribution techniques, BJH (Barrett-Joyner-Halenda), and t-plot method, respectively. The BET (Brunauer–Emmett–Teller) equation was used to calculate the surface area of the biochar. Prior to the gas adsorption measurement, the samples were degassed at 200 ºC, overnight. Elemental analysis of the biochar was performed using a CHN elemental analyzer (Perkin Elmer Series II 2400).

## 4.2. Adsorption-desorption experiments

Three parameters (pressure, mass, and gas flow) can be measured to determine equilibrium gas adsorption capacity (Rouquerol et al. 2013). The experimental procedures generally classified into static (using mass and pressure) and dynamic (using gas flow) systems. In static or batch experiments, the closed system is loaded with adsorbent and followed by loading with the adsorbate and the pressure monitored. Once the system pressure equilibrates, equilibrium adsorption capacity is calculated. The static set up allows for accurate equilibrium measurements. However, the process is time consuming, is not representative of fixed bed flow systems, and the accuracy decreases dramatically at low adsorbate partial pressure (Schaefer 1991). In dynamic experiments, the adsorbate

gas continuously flows through a column packed with adsorbent. The true equilibrium is potentially difficult to reach in this method, due to mass and heat transfer resistances (Valenciano et al. 2015, Schaefer 1991). However, this method is reliable for equilibrium predications where the bed is isothermal and there is negligible pressure drop across the bed (Wu et al. 2007). In our design system, the temperature was held constant and no measurable pressure drop was observed (see supplementary-Table S2).

A single-bed adsorption-desorption unit (Length: 300 mm, i.d.: 15 mm) was constructed from borosilicate glass for conducting the dynamic adsorption-desorption experiments. Figure 4-1 shows the process flow of the adsorption-desorption setup.

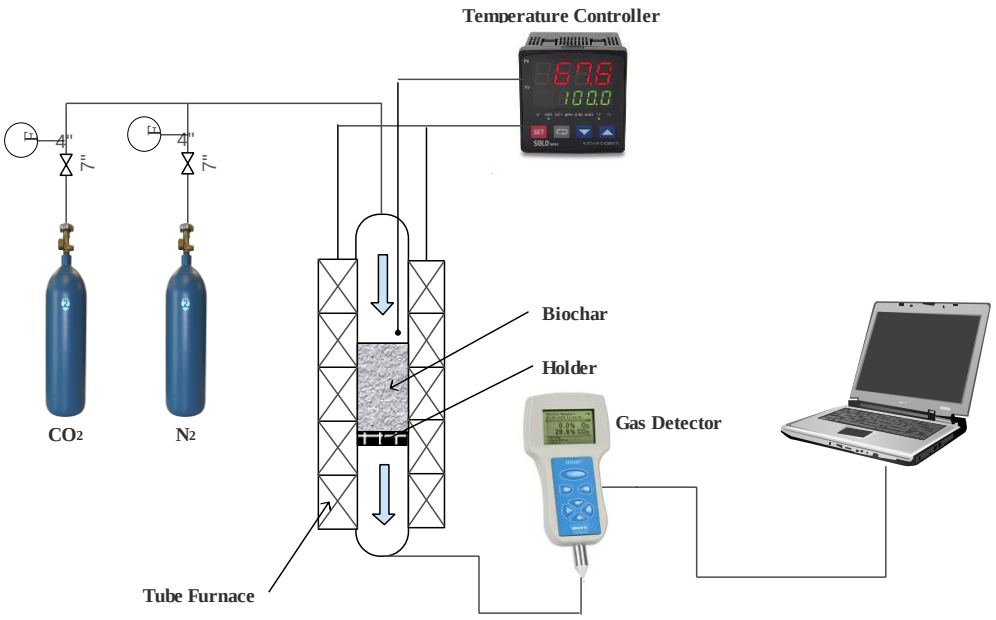


Figure 4-1: Schematic of lab-scale adsorption system

Adsorbents were dried in the oven at 60 ºC overnight before each experiment. Prior to the analysis, the samples were degassed at 150 °C by purging $N_2$ flow through the

adsorption column for 1 hour and then cooled to room/desired temperature. The drying and degassing steps are sufficient to remove water and subsequent impact on the adsorption. A mixture of $CO_2/N_2$ was used as an inlet gas stream for the adsorption process. The adsorption bed temperature was controlled with a tube furnace connected to the temperature controller (OMEGA®). The temperature probe was located directly above the adsorbent bed. The composition of the outlet gas stream was continuously monitored as a function of time with a gas analyzer (OXYBABY® M+). Each experiment was terminated when $CO_2$ broke through the bed, *i.e.*, bed saturation time was reached. The adsorption capacity of biochar was calculated through the integration of the area below the breakthrough curves (Wang et al. 2014) (Equation 1), which is determined by the ratio of outlet to inlet adsorbate gas concentration as a function of time.

$$Q = \frac{F \int_0^t (C_0 - C) dt}{m} \quad (1)$$

where $Q$ is adsorption capacity (mmol $g^{-1}$), $F$ is the inlet $CO_2$ flow rate (mL $min^{-1}$), $C_0$ is inlet $CO_2$ concentration (mmol $L^{-1}$), $C$ is outlet $CO_2$ concentration (mmol $L^{-1}$), and $m$ is adsorbent mass (g). To verify our dynamic system, data from the flow system compared to data from a static system at the same temperature, pressure, and $CO_2$ concentration. The static experiments were conducted in a 3Flex surface characterization analyzer (MicroMeritics). The equilibrium adsorption capacity from the static system and the flow system agreed within less than 8%. Based on this, we continued with our system.

The desorption experiment was done using $N_2$ at 100 mL/min and ambient temperature. Nitrogen was flowed through the dynamic system and again $CO_2$ measured

at the exit. The spent biochar after regeneration was then reused in the $CO_2$ adsorption experiment ($CO_2$ at 60 mL/min).

The adsorption column was packed with 1.53 g of Norit activated carbon to validate the experimental setup and compare the obtained result (adsorption capacity) with the literature (Gil et al. 2015). The adsorption process was performed at 20 ºC and 1 bar. A total flow rate of 30 mL $min^{-1}$ (STP) was maintained during adsorption with an inlet $CO_2$ concentration of 70% (v/v). One of the key factors in gas adsorption processes is determining an optimum adsorbent loading range. 1, 2, and 2.5 g of Norit AC were loaded into the adsorption column to investigate the effect of loading. These experiments were performed with pure carbon dioxide as an inlet gas at ambient temperature and pressure in the flow range of 60–200 mL $min^{-1}$ (STP).

### 4.3. Response surface Methodology

Design of experiment software (Design-Expert 9.0.0) is a tool for management and optimization of a set of experiments. In this work, RSM was coupled with central composite design (CCD) (Box and Wilson 1951) to investigate the influence of independent variables on the response. Three significant variables were identified based on our experience and literature review (Thouchprasitchai et al. 2017): temperature (A), total inlet gas flow rate (B), and $CO_2$ concentration (C). (A) was studied between 20–80 ºC, (B) between 60–200 mL $min^{-1}$, and (C) between 20–100% (v/v). The responses, or dependent variables, are those which were measured during the experiments. In this study, the dependent variable was the $CO_2$ adsorbent capacity. Overall, 20 experiments were performed, including eight factorial points ($2^3$ full factorial design), six axial points,

and six replicates of the centre of the design. Each run was carried out in duplicate. As indicated above, the conditions where maximum adsorption occurred were determined by an experimental design methodology using bark biochar produced in a fast pyrolysis auger reactor at 450 °C (F-P-BK450).

### 4.3.1. Statistical Analysis

A polynomial function was fitted to the data set collected from the CCD. A quadratic model was used to study the $CO_2$ adsorbent capacity (Q) as a function of A, B, and C:

$$Y_k = \beta_0 + \sum_{i=1}^{3} \beta_i X_i + \sum_{i=1}^{3} \sum_{j=1}^{3} \beta_{ij} X_i X_j + \sum_{i=1}^{3} \beta_{ii} X_i^2 \qquad \text{k=1} \tag{2}$$

where $Y_1$ represents $CO_2$ capture capacity (Q). The coefficients $\beta_0$, $\beta_i$ $\beta_{ij}$, and $\beta_{ii}$ were obtained from fitting the model, and $X_i$ and $X_j$ are the factors being studied, *i.e.*, temperature, total inlet flow rate, and $\%CO_2$. This model only applies to F-P-BK450; however, the same interactions and impacts were observed in all chars studied.

The above equation describes the behaviour of the response in the defined experimental boundary as a function of the independent variables. The factors were normalized to vary between +1 and −1(Papari et al. 2015), to compare variables with different units and affect the response evenly.

$$X_i = \frac{x_i - x_i^0}{\Delta x_i} \tag{3}$$

where $x_i^0$ is the midpoint, $x_i$ is the real value, $\Delta x_i$ is the half range, and $X_i$ is the coded value which varies from −1 to +1. The model coefficients ($\beta_0$, $\beta_i$, $\beta_{ij}$, and $\beta_{ii}$) were calculated using the following equations:

$$\beta_0 = a_1 \sum_{u=1}^{n} Y_u + a_2 \sum_{i=1}^{k} \sum_{u=1}^{n} Y_u X_{iu}^2 \tag{4}$$

$$\beta_i = a_3 \sum_{u=1}^{n} X_{iu} Y_u \tag{5}$$

$$\beta_{ij} = a_4 \sum_{u=1}^{n} X_{iu} X_{ju} Y_u \tag{6}$$

$$\beta_{ii} = a_5 \sum_{u=1}^{n} Y_u X_{iu}^2 + a_6 \sum_{i=1}^{k} \sum_{u=1}^{n} Y_u X_{iu}^2 - a_7 \sum_{u=1}^{n} Y_u \tag{7}$$

where $a_1$, $a_2$, $a_3$, $a_4$, $a_5$, $a_6$, and $a_7$ were determined by design expert software (Draper and Smith 1998).

The model was statistically evaluated using analysis of variance (ANOVA) and a lack of fit test. The main objective of using ANOVA was to determine which of the proposed models, factors, and interactions were statistically significant. The derived model can be a polynomial type, *e.g.*, quadratic, cubic, etc., or factorial type with n-factor interaction, *e.g.*, 2FI, 3FI, etc. (Morero et al. 2016). The P-value (or probability value) is a parameter related to the probability of matching a result as extreme as the observed value (Bruce 2016). The P-value will help us determine whether a parameter is significant with respect to impact on response if P-value < 0.05. The predicted model equation is illustrated through response surface and contour plots. The three-dimensional plot, the response

surface plot, shows the response(s) as a function of independent variables. In the contour plot the lines of constant response are plotted on the plane of the two independent variables(Baş et al. 2007). It should be noted, this model is specific to this system and only used to evaluate the impact of the variables, not to be used directly as a scale up tool.

### 4.4. Adsorption Isotherm and Thermodynamics

As indicated previously, adsorption isotherms and kinetics can be determined by static and dynamic methods each with their own limitations (Schaefer 1991). Dynamic systems are particularly appropriate when the proposed application is fixed bed adsorption design. There are numerous examples in the literature where dynamic systems have been used to determine isotherms and kinetic models (e.g. Pseudo-first and second order models). The $CO_2$ adsorption isotherm on the biochar with the highest adsorption capability after sample screening was obtained to gain insight into the adsorption equilibrium, adsorbent surface properties, and to characterize the adsorbate distribution on the adsorbent (Bamdad et al. 2016). The most common adsorption isotherms are the Freundlich and Langmuir isotherms. For homogenous adsorptions, the most common isotherm is the Langmuir isotherm. Assumptions inherent in this model include a fixed number of well-defined localized sites where molecules can adsorb, all sites are equivalent in terms of energy, monolayer adsorption, and no interaction between neighbouring adsorbed molecule (Langmuir 1916):

$$Q_e = \frac{Q_{max} K_L P}{1 + K_L P} \quad (8)$$

where $Q_e$ is the adsorption capacity (mmol $g^{-1}$), P is the adsorbate's partial pressure or equilibrium pressure (bar), $Q_{max}$ is the maximum amount of $CO_2$ adsorbed, and $K_L$ is a constant.

The Freundlich isotherm is an empirical equation applied to multilayer adsorption with non-uniform distribution of heat of adsorption and affinity over the heterogeneous surface (Freundlich 1926). Freundlich isotherms predict a decrease in binding strength with the increasing degree of site occupation, which means the sites with stronger binding affinities are occupied by adsorbate molecules before weaker sites (Khan et al. 2015).

$$Q_e = K_f P^{1/n} \tag{9}$$

where $K_f$ and 1/n are constants related to adsorption capacity and adsorption intensity (heterogeneity factor), respectively.

Thermodynamic parameters, including ΔG (Gibbs free energy change), ΔH (Enthalpy change), and ΔS (Entropy change) can provide the information regarding adsorption mechanism and behaviour (Chen and Zhang 2014). The degree of spontaneity of an adsorption process can be assessed by the Gibbs free-energy change, and a higher negative value reflects a more energetically favourable adsorption (Liu 2009). According to the laws of thermodynamic, ΔG can be calculated as follows:

$$\Delta G = -RTln\frac{P}{P_s} \tag{10}$$

The heat of adsorption at a selected adsorbed amount (Q) can be determined by the Clausius–Clapeyron equation:

$$\Delta H = R\left(\frac{dlnP}{d\frac{1}{T}}\right)_Q \tag{11}$$

Entropy change can be obtained from the definition of Gibbs energy (Equation 12).

$$\Delta S = \frac{\Delta H - \Delta G}{T} \tag{12}$$

where P is the $CO_2$ equilibrium pressure, $P_s$ is the standard pressure, T is the absolute temperature in K, and R is the gas constant with a value of 8.314 J $mol^{-1}$ $K^{-1}$.

### 4.5. Adsorption Kinetics

Adsorption kinetics can provide useful information on adsorption rate and mechanism of the process at specific initial adsorbate pressure and constant temperature. Two different kinetic models, including pseudo-first order and pseudo-second order, were studied to assess the $CO_2$ adsorption rate. The differential and integral form of pseudo-first order can be written as below (Liu et al. 2011):

$$\frac{dq_t}{dt} = k(q_e - q_t) \tag{13}$$

$$\ln(q_e - q_t) = \ln q_e - kt \tag{14}$$

The pseudo-second order rate equations is shown as below (Ho and McKay 1999):

$$\frac{dq_t}{dt} = k(q_e - q_t)^2 \quad (15)$$

$$\frac{t}{q_t} = \left(\frac{1}{kq_e^2}\right) + \frac{t}{q_e} \quad (16)$$

where $q_e$ and $q_t$ are the adsorption capacity at equilibrium and at time t, respectively, (mmol $g^{-1}$), k is the rate constant of the adsorption. If each of the above kinetic models is applicable for the system, then the plot of the integral form of the model should be linear (correlation coefficient $R^2$ near to 1).

### 4.6. Results and Discussion

#### 4.6.1. Biochar Properties

The physiochemical characteristics of the studied biochars are summarized in Table 4-2 (data presented is mean of the observed results). Pyrolysis temperature and feedstock type significantly affect the biochar properties. The BET surface areas for the biochars produced in this study ranged from 2–96 $m^2$ $g^{-1}$. An increase in fast pyrolysis temperature promotes porosity development, because both surface area and pore volume are increased. This is a result of the release of smaller molecules enhancing pore development and BET surface area of biochars (Lua et al. 2004; Li et al. 2016). Increasing pyrolysis temperature influences not only textural properties, but also chemical make-up. Based on

the elemental analysis results, the highest carbonization with the lowest H:C ratio occurred for F-P-SW500 among chars.

Table 4-2: Properties of biochar samples

| Samples | SA* ($m^2$ $g^{-1}$) | Avg. pore size (nm) | Micropore volume ($cm^3$ $g^{-1}$) | C (%) | H (%) | N (%) | H:C |
|---|---|---|---|---|---|---|---|
| F-L-SW450 | 2.47 | 6.62 | N/A | 79.40 | 3.40 | 0.05 | 0.04 |
| F-P-SW450 | 2.76 | 7.23 | N/A | 74.79 | 3.51 | 0.24 | 0.05 |
| F-P-SW400 | 7.15 | 7.18 | N/A | 70.90 | 3.10 | 0.07 | 0.04 |
| F-P-HW400 | 7.35 | 7.08 | 0.0004 | 72.53 | 3.12 | 0.15 | 0.04 |
| F-P-BK450 | 8.68 | 9.09 | 0.0007 | 67.67 | 3.11 | 0.42 | 0.05 |
| F-P-HW450 | 15.30 | 6.80 | 0.0039 | 73.25 | 3.64 | 0.16 | 0.05 |
| F-P-Mix BK-SW450 | 30.52 | 6.99 | 0.009 | 69.88 | 2.45 | 0.20 | 0.04 |
| F-P-HW500 | 50.91 | 5.79 | 0.0171 | 74.84 | 2.34 | 0.22 | 0.03 |
| F-P-SW500 | 95.58 | 4.36 | 0.0328 | 78.37 | 2.36 | 0.15 | 0.03 |

*****BET

### 4.6.2. Validation

The reference material used for validation was activated carbon (Norit CA1). The AC adsorption capacity was measured to be 1.03 mmol $g^{-1}$ (Equation 1), which is in good agreement with the work conducted by Gil et al. (1.02 mmol $g^{-1}$) (Gil et al. 2015) under the same operating conditions. The experiments indicate the system cannot handle an amount of adsorbent higher than 2 grams due to back pressure. Figures 4-2a and b summarize the breakthrough curves of the adsorption system at inlet gas flow rates of 60

and 200 mL $min^{-1}$ with 1 and 2 g of AC, respectively. The adsorption capacity varied from 3.12-3.4 (mmol $g^{-1}$) at 60 mL $min^{-1}$ and 2.97-3.29 (mmol $g^{-1}$) at 200 mL $min^{-1}$ for 1 and 2 g adsorbent loading, respectively. The adsorbate uptake increased with an increase in the adsorbent mass, and could be due to the higher number of binding sites with increasing adsorbent bed height, resulting in high removal efficiency (Geethakarthi and Phanikumar 2011). The optimum adsorbent loading in our lab scale system was taken as 2 g for the operating gas flow rate of our system (60–200 mL $min^{-1}$).

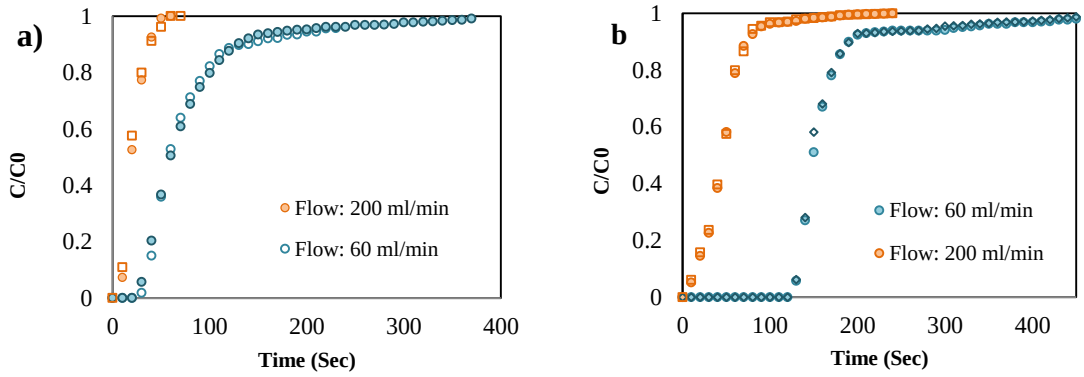


Figure 4-2: The AC breakthrough curves at total inlet flow rates of 60 and 200 mL $min^{-1}$, adsorbent mass: (a) 1 and (b) 2 g

### 4.6.3. Dynamic Adsorption Experiments

The impact of adsorption process parameters was investigated on the adsorption capacity of a selected biochar (F-P-BK450). To verify these results held, regardless of the biochar used, additional experiments were performed to ensure the same trends were observed. In the dynamic experiments, the temperature was varied from 20–80 ºC, total inlet flow rates from 60–200 mL $min^{-1}$, and inlet carbon dioxide concentrations from 20–100% (v/v) $CO_2$. The $CO_2$ outlet concentration was recorded over time, and the breakthrough curves were obtained (Figure 4-3). In a fixed bed adsorption system,

maximum mass transfer occurs at the start of the experiment. The adsorption zone moves further up the adsorbent bed as time passes and the front part of the adsorption bed becomes saturated. This process continues until the adsorbate concentration at the exit becomes equal to the inlet concentration and the adsorbent column becomes entirely saturated (Ghorai and Pant 2005). The general shape of breakthrough curves along the column is determined by adsorption capacity of the adsorbent with respect to the inlet flow rate, feed concentration, and adsorbent temperature (García et al. 2011). It was observed that (Figure 4-3a–d, and f) higher feed flow rates showed shorter breakthrough time (steeper curve) since the bed became saturated more quickly due to the higher mass of $CO_2$ flowing into the column per unit time compared to a lower flow rate (Monazam et al. 2013). At high flow rates, the mass transfer zone becomes narrower and the mass transfer coefficient increases because of a higher Reynold's number (Mulgundmath et al. 2012). In contrast, the equilibrium adsorbent capacity was higher at lower flow rates due to longer residence time, resulting slow transport of the adsorbate molecules with a large diffusion coefficient (Auta and Hameed 2014). At the flow rates and $CO_2$ concentrations studied, increasing temperature results in a shorter breakthrough time (Figure 4-3a, c, and g). These observations are in accordance with other studies (Gallucci and Van Sint Annaland 2015; Shafeeyan et al. 2015). A slightly longer breakthrough time can be seen (Figure 3e) by decreasing the concentration of $CO_2$ in the inlet feed. The plausible interpretation of this result is that the binding sites became more quickly saturated in the system with high $CO_2$ inlet concentration. Conversely, the lower concentration gradient at low initial $CO_2$ concentrations resulted in slower transport in the dynamic adsorption process (Tamez Uddin et al. 2009).

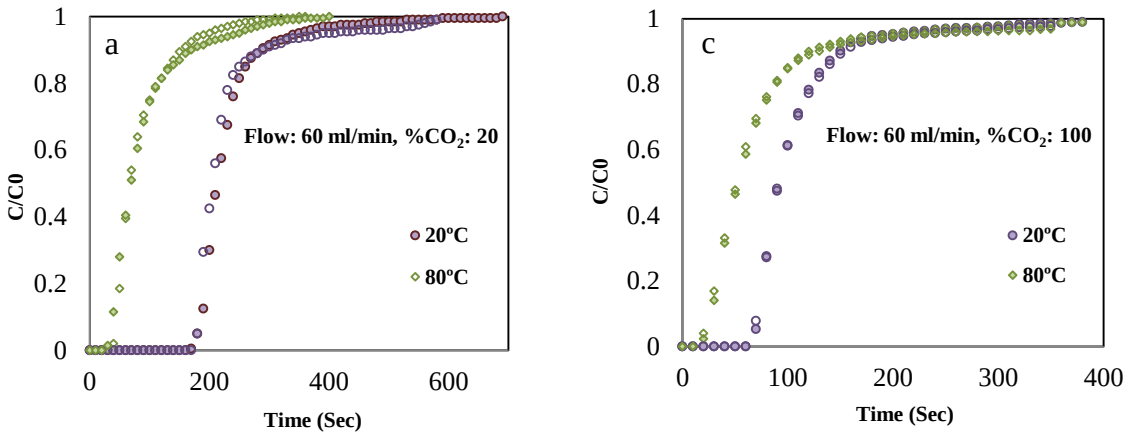


Figure 4-3: Breakthrough curves for 20% (v/v) of $CO_2$ at varying adsorption temperatures and flow rates (The rest is in supplementary material)

### 4.6.4. ANOVA Analysis

A quadratic mathematical model was developed based on the backward elimination method using the analysis of important combinations of variables, fitting experimental data, and evaluating the model errors. The adsorption performance of the biochar was obtained by the analysis of $CO_2$ adsorption capacity (Q) as a response parameter. The adsorption capacity (Q) varied from 0.07–2.21 mmol $g^{-1}$.

The ANOVA test (Table 4-S1) determines the statistically significant terms (P-value < 0.05) in the model at 95% confidence interval. The quadratic terms represent the interaction between temperature–total flow rate (AB), temperature–%$CO_2$ (AC), temperature (A), and %$CO_2$ (C) have a significant effect on adsorption capacity of biochar. The F-value (46.88) is adequately large and the P-value is small (<less than 0.05) which indicates the mathematical model is in good agreement with the experimental data (Chen et al. 2009a). The values of $R^2$ (0.9558) and adjusted-$R^2$ (0.9354) are close to one,

and predicted $R^2$ (0.8189) and the adjusted $R^2$ are within 0.20 of each other, indicating that the adopted model is appropriate (Baroutaji et al. 2015). The achieved adequate precision (Adeq=23.352), which measures the signal-to-noise ratio, is greater than 4, which demonstrates good model discrimination (Zhu et al. 2010). Adeq precision compares the range of predicted values at design points to the average prediction error (Anderson and Whitcomb 2013).

Response surface and contour plots for adsorption capacity of $CO_2$ as a function of temperature (°C) and total flow rate are presented in Figure 4-4. Total flow rate (B) has insignificant influence on adsorption capacity compared to other variables. However, a slight decrease of adsorption capacity can be seen by increasing the flow rate from 60 to 130 mL $min^{-1}$. This decrease may be because of the lower contact time between adsorbent and adsorbate gas ($CO_2$). In contrast, the adsorption capacity increased by increasing the flow rate from 130 to 200 mL $min^{-1}$. This could be due to a higher convective mass transfer rate which dominates over contact time in high flow regions. The $Q_{CO2}$ decreases as adsorption temperature (A) increases because of the exothermic nature of the adsorption process (Lua and Yang 2009; González et al. 2013). At low flow rates, i.e., 60 mL min-1, the impact of temperature is less pronounced than at higher flow rates, i.e., 200 mL min-1. Since $B^2$ is a significant term according to ANOVA, the trend for factor B in the contour plot exhibits a noticeable curvature compared to $A^2$ and $C^2$.

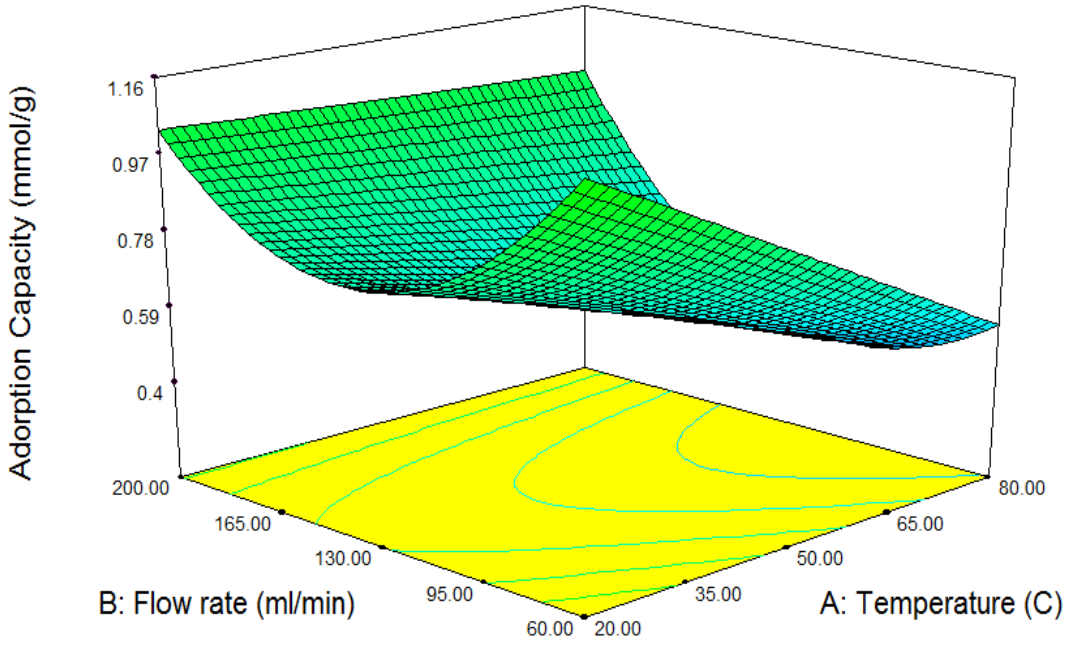


Figure 4-4: Effect of temperature and total inlet flow rate on $CO_2$ adsorption capacity of biochar; 60% $CO_2$

Figure 4-5 shows the effect of two significant parameters, temperature and %$CO_2$, on adsorption capacity simultaneously. Adsorption capacity decreased as $CO_2$ concentrations decreased. At higher adsorbate concentration, the concentration difference results in a higher driving force and hence higher adsorbent capacities (O'Mahony et al. 2002). At low temperatures, the $CO_2$ adsorbent capacity increased as the CO2 concentration in the inlet increased. At higher temperatures, this effect was negligible. The highest $CO_2$ capture capacity (2.21 mmol $g^{-1}$) was obtained at an adsorption temperature of 20 ºC, 100% $CO_2$, and an inlet flow rate of 60 mL $min^{-1}$. The equation was obtained by using the above statistical parameters and eliminating non-significant coefficients (Table 4-3). Although the developed equation is specific to our system, the parameter interactions and trends would apply to scale up.

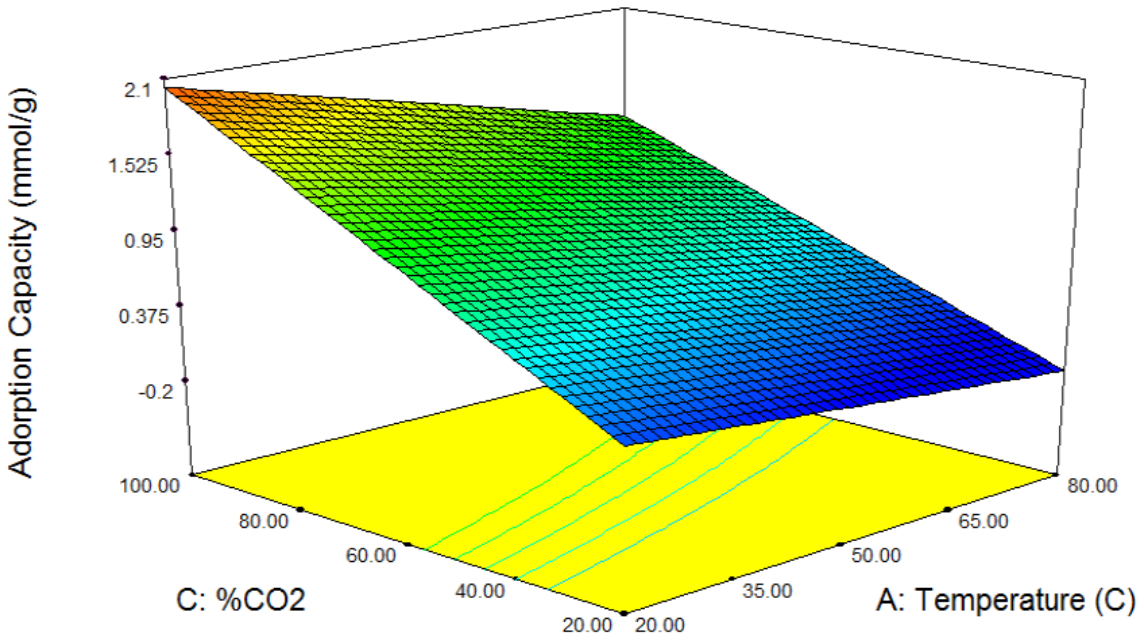


Figure 4-5: Response surface and contour plots for $CO_2$ capture capacity as a function of temperature (A) and $\%CO_2$ (C), Total inlet flow rate: 60 mL $min^{-1}$

Table 4-3: Quadratic model (QM) for bark biochar (F-P-BK450) adsorption capacity in terms of coded factors

| | | |
|---|---|---|
| QM with interactions | $0.61 - 0.16A + 0.083B + 0.78C + 0.14A \times B - 0.11A \times C + 0.32B^2$ | (8) |
| Code | A: Temperature, B: total flow rate, C: $\%CO_2$ | |

### 4.6.5. Sample Screening: $CO_2$ uptake

The $CO_2$ adsorption capacity of the biochar samples was compared at 20 °C, 60 mL $min^{-1}$, and pure $CO_2$ (Figure 4-6). The $CO_2$ uptake of all of the biochars was between 1.4–2.4 mmol $g^{-1}$. Softwood sawdust biochar (sample F-P-SW500) produced in the auger reactor at 500 ºC showed the highest capacity, reflected in the highest surface area and

total micropore volume of the series, and the average pore width was significantly narrower compared to other samples (95.58 $m^2 g^{-1}$, 0.03 $cm^3 g^{-1}$, and 4.36 nm, respectively). Future work will incorporate modifying the surface and structure of SW500 that are capable of increasing the surface area and promoting $CO_2$ capture performance.

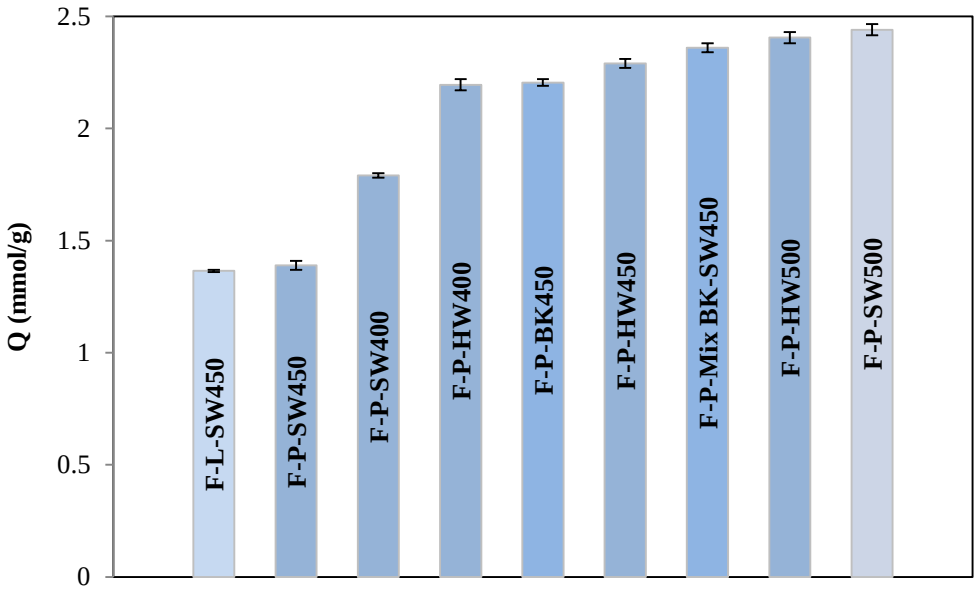


Figure 4-6: Adsorption capacity of different biochar samples at maximum adsorption condition

The results showed a range of $CO_2$ adsorption capacity of biochar from 1.5 to 2.4 mmol $g^{-1}$. This compares very well with a commercial adsorbent, Zeolite-13X, with an adsorption capacity of 1.7 mmol $g^{-1}$ for pure $CO_2$ at atmospheric pressure and room temperature. Tests of $CO_2$ adsorption for zeolite were carried out in a BelCat equipment (BEL-Japan) with a quartz reactor (Espejel-Ayala et al. 2014).

### 4.6.6. Isotherm and Thermodynamic Analysis

The char which demonstrated the highest capacity (F-P-SW500) was used to study isotherm behaviour. Results for the Langmuir and Freundlich models are summarized in Figure 4-7. The calculated values of both equations' constants are listed in Table 4-4. The regression coefficient ($R^2$) of Freundlich model (0.99) was higher than that of the Langmuir model (0.86), which suggested that the model was more suitable to predict the experimental data. The Freundlich model is a better fit because of the non-homogeneous nature of the surface of the biochar and possible multilayer adsorption (Halsey 1948). Based on Giles (Giles et al. 1974) and Sing et al. (Sing et al. 1985) classifications, a 1/n value greater than 1 corresponds to sigmoidal-shaped (S) or type III isotherm classes, respectively. The type III isotherm indicates weak adsorbate-adsorbent and relatively strong adsorbate-adsorbate interactions (Ryu et al. 1999).

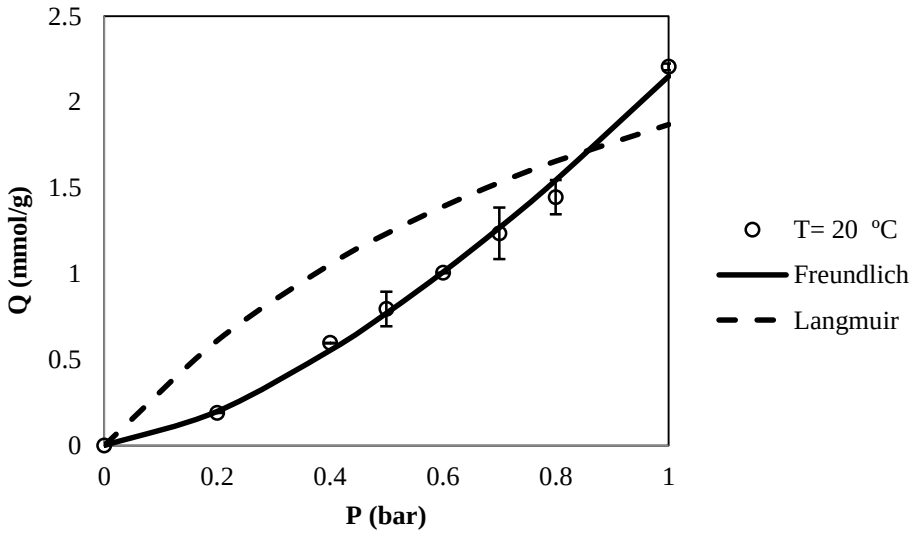


Figure. 4-7: Adsorption isotherms of $CO_2$ on biochar (F-P-SW-500 ºC) at 20 ºC, 60 mL $min^{-1}$, Q: adsorption capacity, P: equilibrium $CO_2$ pressure

Table 4-4: Langmuir and Freundlich model constants

| Langmuir model | | | Freundlich model | | |
|---|---|---|---|---|---|
| $K_L$ | $q_{max}$ | $R^2$ | $K_F$ | 1/n | $R^2$ |
| 3.86 | 0.94 | 0.86 | 2.15 | 1.47 | 0.99 |

To analyze the thermodynamic properties, adsorption tests were performed at various temperatures, 293–353 K. At each temperature, the corresponding $CO_2$ equilibrium pressure was obtained and the Gibbs free energy was calculated according to Equation 10. The values of the thermodynamic parameters of $CO_2$ adsorption on F-P-SW-500 ºC are summarized in Table 4-5.

Table 4-5: Thermodynamic parameters of $CO_2$ adsorption on biochar

| Sample | $Q_e$ (mmol $g^{-1}$) | ΔH (kJ $mol^{-1}$) | ΔG (kJ $mol^{-1}$) | | | | ΔS (J $mol^{-1}$ $K^{-1}$) |
|---|---|---|---|---|---|---|---|
| | | | 293K | 313K | 333K | 353K | |
| F-P-SW-500 | 0.1 | -15.39 | -5.61 | -4.94 | -4.46 | -2.93 | -33.7 |
| | 0.5 | -5.64 | -2.23 | -2.08 | -1.92 | -1.25 | -11.66 |
| | 1.2 | -3.49 | -0.87 | -0.55 | -0.45 | -0.26 | -9.16 |

The negative values of ΔG at each temperature indicate the adsorption take place spontaneously. The decreasing absolute values of ΔG with increasing the temperature show that the adsorption process is in favoured at lower temperatures (Seyhi et al. 2011). The heat of adsorption (ΔH) was calculated from the slope of plot of ln P *vs*. 1/T at surface loadings of 0.1, 0.5, and 1.2 mmol $g^{-1}$ (Figure 4-8). The negative value of ΔH illustrates the adsorption process is exothermic in nature, which is in agreement with other studies (Creamer et al. 2014; Plaza et al. 2014b). Physical adsorption typically produces a heat of adsorption between 0-20 kJ $mol^{-1}$; whereas chemisorption is typically

between 80–400 kJ $mol^{-1}$ (Gereli et al. 2006). Based on the values in Table 5, the $CO_2$ adsorption on unmodified biochar was dominated by physisorption (Heidari et al. 2014). The heat of adsorption (absolute value) decreased with increasing surface coverage ($Q_e$), which can be attributed to surface heterogeneity and adsorbate–adsorbate interaction, followed by adsorbate–adsorbent interaction (Srivastava et al. 2007). The negative entropy of adsorption (ΔS) reflects the randomness reduction and the affinity of the adsorbate material toward biochar surface (Chen et al. 2009b).

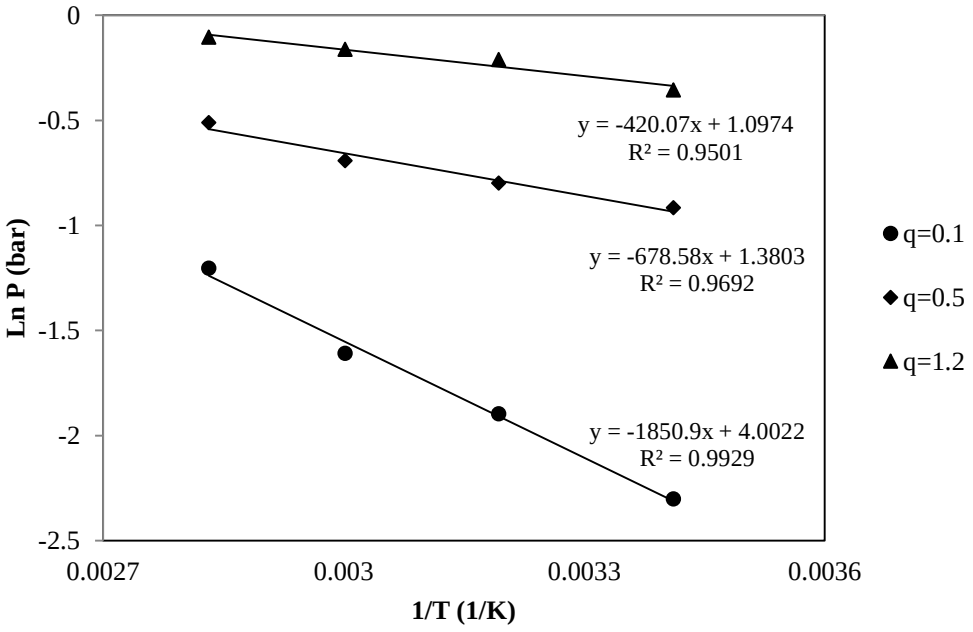


Figure 4-8: Enthalpy determination at different temperatures (293–353 K), P: equilibrium $CO_2$ pressure, q: surface loading (mmol $g^{-1}$)

### 4.6.7. Kinetic Analysis

Pseudo first-order and pseudo second-order, two widely used kinetic models, were assessed with obtained experimental data at maximum adsorbency (Figure 4-9).

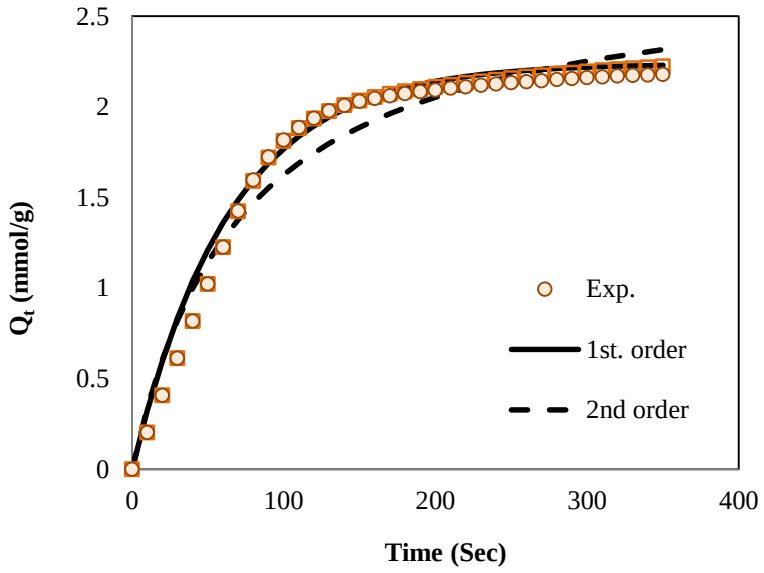


Figure 4-9: Kinetic model fittings of $CO_2$ adsorption on biochar (F-P-SW-500ºC) at maximum adsorbency, Experiments were performed in duplicate (circle and square symbols)

Table 4-6: Obtained parameters of kinetic models for $CO_2$ adsorption on biochar

| Initial %$CO_2$ (v/v) | $Q_e$ (Exp.) | Pseudo first-order | | Pseudo second-order | |
|---|---|---|---|---|---|
| | | $Q_e$ (mmol $g^{-1}$) | k ($min^{-1}$) | $Q_e$ (mmol $g^{-1}$) | k (g $mmol^{-1}$ $min^{-1}$) |
| 20 | 0.19 | 0.27 | 0.01 | 0.28 | 0.016 |
| 40 | 0.60 | 0.55 | 0.007 | 0.82 | 0.007 |
| 60 | 1.01 | 0.9 | 0.01 | 1.23 | 0.009 |
| 80 | 1.45 | 1.94 | 0.02 | 1.84 | 0.007 |
| 100 | 2.21 | 2.24 | 0.02 | 2.79 | 0.005 |

Table 4-6 summarizes the experimental values and calculated kinetic model constants. The results show the pseudo first-order model is a better fit to the experimental data (the correlation coefficient is close to 1). The pseudo-first order model applied to processes that involve physical adsorption or reversible interaction between adsorbent and

adsorbate, such as $CO_2$ adsorption on activated carbon or zeolite sorbents (Ammendola et al. 2017). This agrees with the thermodynamics, which indicate a physisorption process. Previous studies also proposed likewise the pseudo-first order kinetic model in $CO_2$ adsorption at low initial partial pressure (Wang et al. 2015; Goel et al. 2016), which is consistent with our results.

### 4.6.8. Regeneration of biochar

Key to any adsorbent large-scale application is determining if the adsorbent can be regenerated and if not how well the adsorbent binds the target contaminant (to determine re-use in other applications). As such, a preliminary set of experiments was performed to evaluate the performance of the loaded biochar. Regeneration experiments are typically conducted at high temperature (ranging from 100-500 °C), as these temperatures accelerate the desorption process (Chatterjee et al. 2018). However, these temperatures could degrade the biochar and are energy and cost intensive. Given these factors and that this is a screening study, we choose to study desorption at the same temperatures used for adsorption. This temperature also fits well given one of the longer term application of the spent char is as a soil amendment. $CO_2$ adsorption-desorption tests were carried out in three consequent cycles at ambient temperature.

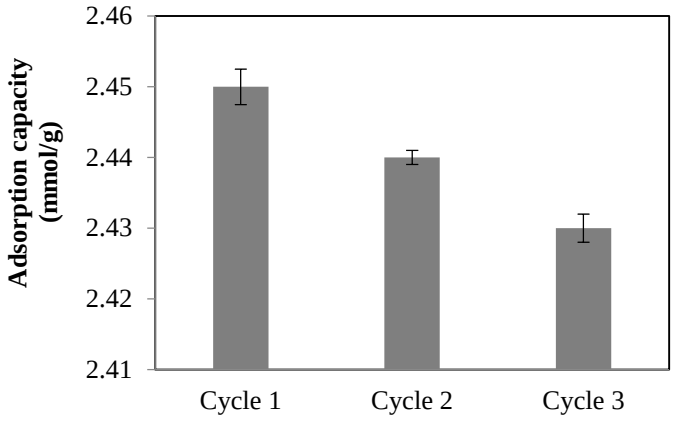


Figure 4-10: Adsorption capacity of biochar (F-P-SW-500ºC) for three cycles

The results in Figure 4-10 indicate that the adsorption capacity slightly decreased after each cycle. After three cycles, the adsorption capacity was reduced by 0.8%, which shows the high stability of biochar with no significant loss compared to fresh adsorbent. The BET surface area of the spent biochar (after single-step adsorption) with and without regeneration was 83.9 (avg. pore size: 4.78 nm, pore volume: 0.029 cm3/g) and 76.6 m2/g (avg. pore size: 4.8 nm, pore volume: 0.026 cm3/g), respectively, while the original biochar surface area was 95.6 m2/g (avg. pore size: 4.36 nm, pore volume: 0.033 cm3/g). The results demonstrate the 12% reduction in surface area after the 1st cycle of adsorption-desorption led to slightly decrease the adsorption capacity. In another study (Plaza et al. 2007), where three cycles were done on nitrogen enriched carbons for CO2 capture, the decrease in capacity was 5-20% depending on the nature of the nitrogen groups. The regeneration in this case was done under vacuum and 25 ºC.

The TGA analysis results of spent biochar with and without regeneration are shown in Figures 4-11.

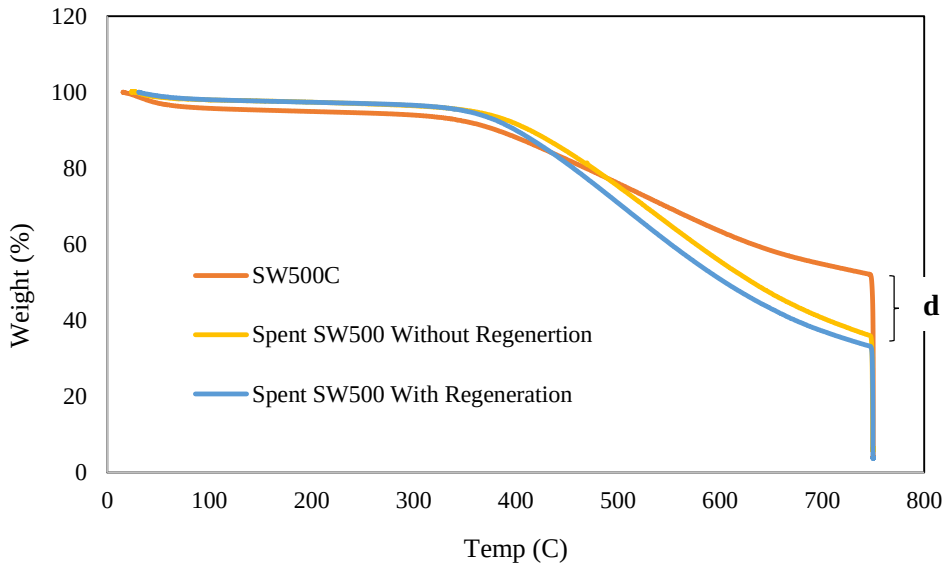


Fig. 4-11: TGA curves for original and spent biochar

In the TGA graphs, the specified difference (d) between original biochar and spent biochar without regeneration could indicates the amount of $CO_2$ adsorbed by biochar.

$$d = \frac{(50.21 - 35.96)g}{100\ g} \times \frac{1000}{44\ g/mol} = 3.2\ mmol/g$$

The adsorption capacity of the SW500 ºC biochar obtained 2.4 mmol/g experimentally. The calculated amount (d) is higher than the experimental result because "d" shows the accumulative volatile matters released during the approximate analysis and the volatile matters such as moisture content of the two samples may be different initially. Figure 4-12 illustrates the IR frequencies of original and spent biochars.

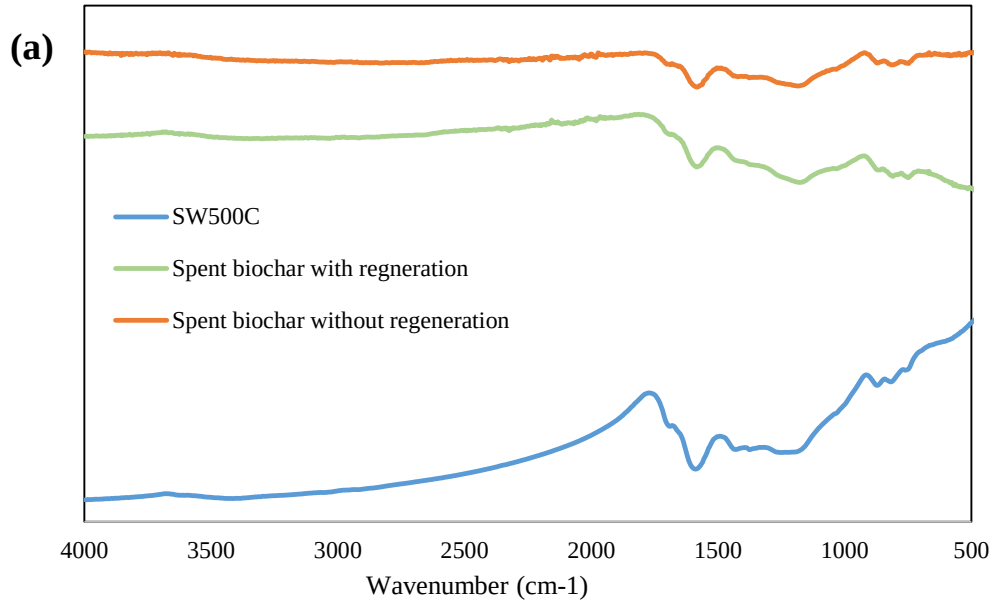


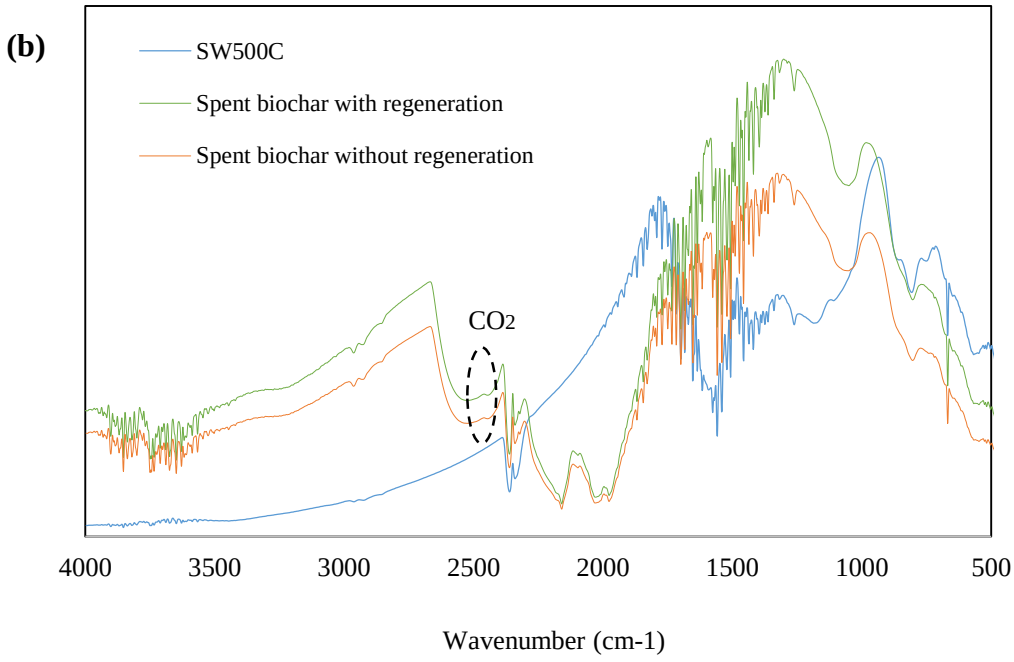


Fig. 4-12: IR vibrations of biochars (F-P-SW-500ºC), (a) with background, (b) without background

The IR frequencies of original and spent biochars with background did not show any $CO_2$ peaks due to presence of background $CO_2$ (Figure 4-12a). When the background was removed for both regenerated and spent biochar, $CO_2$ peaks were observed (Figure 4-12b). This indicates $CO_2$ remains in the biochar sample even after desorption with nitrogen. This was corroborated by desorption tests in 3Flex surface characterization analyzer –MicroMeritics, which showed some $CO_2$ remains on the structure after regeneration. This is potentially another reason for the decrease in adsorption capacity as in this experimental system the outlet $CO_2$ is measured. This also observed elsewhere (Plaza et al. 2007). Our work shows that the biochar shows good regeneration potential however, more studies are required to determine the strength of the $CO_2$ binding (e.g. higher temperatures and/or lower pressures in desorption).

## 4.7. Conclusion

A fixed bed adsorption system was designed, validated, and used to study biochars derived from different feedstock, in the adsorption of $CO_2$. Response surface methodology was used to evaluate the combined effect of temperatures (20–60 ºC), total inlet flow rates (60–200 mL $min^{-1}$), and $CO_2$ concentrations (20–100 (v/v) %) on the $CO_2$ adsorbent capacity of a number of biochars derived at different fast pyrolysis temperatures. The breakthrough time decreased with increasing temperature, inlet feed flow rate, and $CO_2$ concentration. The interactions between temperature–total flow rate and temperature–%$CO_2$ were significant and the $CO_2$ inlet concentration was the most influential variable in the adsorbent capacity of the biochar. The operating conditions for maximizing $CO_2$ uptake in this system were 20 °C, 60 mL $min^{-1}$ flow rate, and pure $CO_2$.

Softwood biochar produced at 500 °C (F-P-SW500) resulted in the highest adsorption capacity (2.4 mmol $g^{-1}$) compared to the other studied chars while a commercial zeolite has 1.7 mmol $g^{-1}$ $CO_2$ uptake capacity. The Freundlich isotherm best predicts the isotherm behaviour of the studied chars. The calculated thermodynamic properties indicate the $CO_2$ adsorption is a spontaneous process, involving physical adsorption, and is exothermic in nature. A pseudo first-order model showed an excellent fit with the data. The regeneration tests demonstrated that biochar is a good option for $CO_2$ sequestration. This work shows that biochar derived from "waste" materials, *e.g.*, softwood residues, is a viable sustainable alternative to existing adsorbents. Next steps include determining the characteristics of the char for instance further experiments for maximizing regeneration, and if the char can be further optimized through activation or functionalization to increase adsorption capacity and/or binding strength. In addition, other gases (e.g. $H_2S$, trace hydrocarbons) will be introduced to determine interference/competition effects.

**Acknowledgment**

We would like to express our gratitude to Dr. Andrew Carrier, Postdoctoral Fellow in Cape Breton University for productive comments and discussion.

## Supplementary

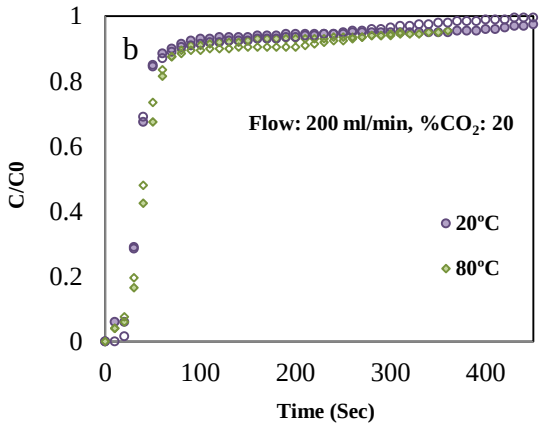


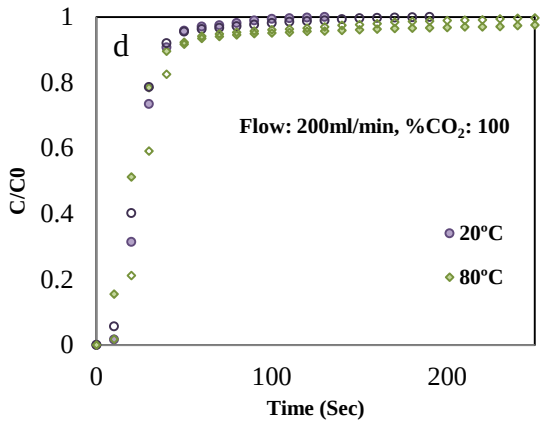


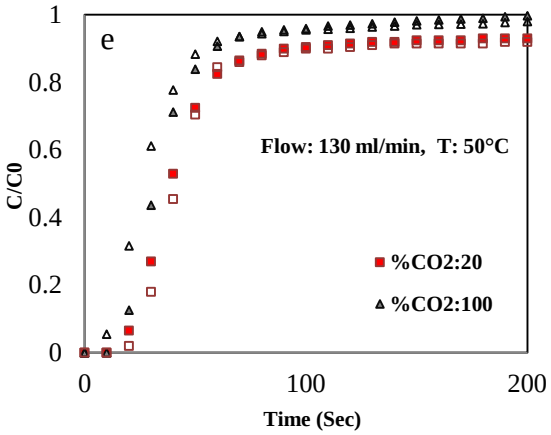


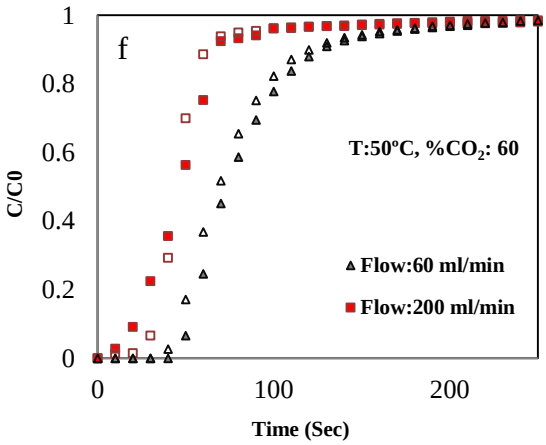


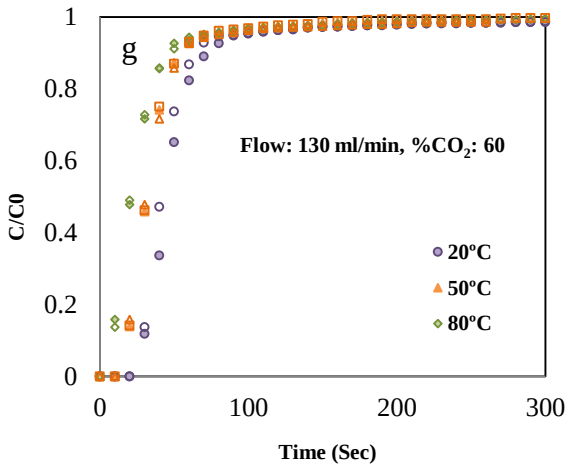

Figure 4-3-rest: Breakthrough curves for different % of $CO_2$ at varying adsorption temperatures and flow rates

Table 4-S1: Results of multiple regression analysis and ANOVA for response surface reduced quadratic model

| Source | $Q_{CO2}$ (mmol/g) | | | | | |
|---|---|---|---|---|---|---|
| | SS[a] | DF[b] | MS[c] | F-value | P-value | Mark |
| Quadratic Model | 7.19 | 6 | 1.20 | 46.88 | < 0.0001 | Significant |
| A, Temperature | 0.25 | 1 | 0.25 | 9.95 | 0.0076 | |
| B, Flow rate | 0.068 | 1 | 0.068 | 2.66 | 0.1268 | |
| C, $\%CO_2$ | 6.11 | 1 | 6.11 | 238.84 | < 0.0001 | |
| AB | 0.15 | 1 | 0.15 | 5.86 | 0.0308 | |
| AC | 0.10 | 1 | 0.10 | 3.92 | 0.0694 | |
| $B^2$ | 0.51 | 1 | 0.51 | 20.08 | 0.0006 | |
| Residual | 0.33 | 13 | 0.026 | | | |
| Lack of fit | 0.33 | 8 | 0.042 | | | Not Significant |
| Pure error | 0.000 | 5 | 0.000 | | | |
| Cor total | 7.53 | 19 | | | | |

[a] Sum of Square

[b] Degree of Freedom

[c] Mean Square

Ergun's law is used to estimate the bed pressure drop (Chahbani and Tondeur 2001).

$$\frac{-\Delta P}{L} = 150\frac{\mu u(1-\varepsilon)^2}{{d_p}^2\varepsilon^3} + 1.75\frac{\rho_f u^2(1-\varepsilon)}{d_p\varepsilon^3}$$

where $-\Delta P$ is the Pressure drop through the packed bed (Pa), u is the interstitial fluid velocity, (m/s), dp is the particle diameter (m), ε is the bed porosity, $\rho_f$ is the fluid density

(kg/m3), μ is the viscosity of the fluid flowing through the packed bed (Pa.s), and L is the length of column (m).

The adsorbent porosity can be defined as below (Brewer et al. 2014).

$$\varepsilon = 1 - \frac{\rho_e}{\rho_s} = 1 - \frac{0.5}{1.5} = 0.67$$

Table 4-S2: All the properties for the fixed bed setup

| Property | Value | Unit |
|---|---|---|
| Temperature | 20 | ºC |
| Fluid density | 1.84 | kg/m$^3$ |
| Fluid dynamic Viscosity | 1.47*10$^{-5}$ | Pa.s |
| Fluid velocity | 0.006 | m/s |
| Bed porosity | 0.67 | - |
| Particle diameter | 45*10$^{-6}$ | m |
| Column length | 0.03 | m |
| Envelope density of adsorbent | 0.5 (Brewer et al. 2014) | g/cm$^3$ |
| Skeletal density of adsorbent | 1.5 (Brewer et al. 2014) | g/cm$^3$ |

$$-\Delta P = \left[150\frac{1.47 * 10^{-5} * 0.006 * (1-0.67)^2}{(45 * 10^{-6})^2 * 0.67^3} + 1.75\frac{1.84 * (0.006)^2(1-0.67)}{45 * 10^{-6} * 0.67^3}\right]$$

$$* (0.03m) = 67\ pa = 0.0007\ bar$$

## References

Abnisa F, Arami-Niya A, Daud WMAW, Sahu JN (2013) Characterization of Bio-oil and Bio-char from Pyrolysis of Palm Oil Wastes. Bioenergy Res 6:830–840. doi: 10.1007/s12155-013-9313-8

Ammendola P, Raganati F, Chirone R (2017) CO2 adsorption on a fine activated carbon in a sound assisted fluidized bed: Thermodynamics and kinetics. Chem Eng J 322:302–313. doi: https://doi.org/10.1016/j.cej.2017.04.037

Anderson MJ, Whitcomb PJ (2013) DOE Simplified: Practical Tools for Effective Experimentation

Auta M, Hameed BH (2014) Adsorption of carbon dioxide by diethanolamine activated alumina beads in a fixed bed. Chem Eng J 253:350–355. doi: http://dx.doi.org/10.1016/j.cej.2014.05.018

Bamdad H, Hawboldt K (2016) Comparative study between physicochemical characterization of biochar and metal organic frameworks (MOFs) as gas adsorbents. Can J Chem Eng 9999:1–7. doi: 10.1002/cjce.22595

Bamdad H, Hawboldt K, MacQuarrie S (2016) A review on common adsorbents for acid gases removal: Focus on biochar. Renew. Sustain. Energy Rev.

Baroutaji A, Gilchrist MD, Smyth D, Olabi AG (2015) Crush analysis and multi-objective optimization design for circular tube under quasi-static lateral loading. Thin-Walled Struct 86:121–131. doi: 10.1016/j.tws.2014.08.018

Baş D, Boyacı İH, Bas D, et al (2007) Modeling and optimization I: Usability of response surface methodology. J Food Eng 78:836–845. doi: 10.1016/j.jfoodeng.2005.11.024

Box GEP, Wilson KB (1951) On the experimental attainment of optimum conditions. J R Stat Soc 13:1–45. doi: 10.1007/978-1-4612-4380-9_23

Bruce PC (2016) Introductory Statistics and Analytics: A Resampling Perspective

Chen CP, Chuang MT, Hsiao YH, et al (2009a) Simulation and experimental study in determining injection molding process parameters for thin-shell plastic parts via design of experiments analysis. Expert Syst Appl 36:10752–10759. doi: 10.1016/j.eswa.2009.02.017

Chen S, Shen W, Yu F, Wang H (2009b) Kinetic and thermodynamic studies of adsorption of Cu2+ and Pb2+ onto amidoximated bacterial cellulose. Polym Bull 63:283–297. doi: 10.1007/s00289-009-0088-1

Chen Y, Zhang D (2014) Adsorption kinetics, isotherm and thermodynamics studies of flavones from Vaccinium Bracteatum Thunb leaves on NKA-2 resin. Chem Eng J 254:579–585. doi: 10.1016/j.cej.2014.05.120

Creamer AE, Gao B, Zhang M (2014) Carbon dioxide capture using biochar produced from sugarcane bagasse and hickory wood. Chem Eng J 249:174–179. doi: 10.1016/j.cej.2014.03.105

Draper NR, Smith H (1998) Applied Regression Analysis. Technometrics 47:706. doi: 10.1198/tech.2005.s303

Espejel-Ayala F, Corella RC, Pérez a M, et al (2014) Carbon dioxide capture utilizing zeolites synthesized with paper sludge and scrap-glass. Waste Manag Res 32:1219–26. doi: 10.1177/0734242X14554643

Foo KY, Hameed BH (2012) Textural porosity, surface chemistry and adsorptive properties of durian shell derived activated carbon prepared by microwave assisted NaOH activation. Chem Eng J 187:53–62. doi: 10.1016/j.cej.2012.01.079

Gallucci F, Van Sint Annaland M (2015) Process Intensification for Sustainable Energy Conversion

García S, Gil M V, Martín CF, et al (2011) Breakthrough adsorption study of a commercial activated carbon for pre-combustion CO2 capture. Chem Eng J 171:549–556. doi: http://dx.doi.org/10.1016/j.cej.2011.04.027

Geethakarthi a., Phanikumar BR (2011) Adsorption of reactive dyes from aqueous solutions by tannery sludge developed activated carbon: Kinetic and equilibrium studies. Int J Environ Sci Technol 8:561–570. doi: 10.1007/BF03326242

Gereli G, Seki Y, Murat Kuşoğlu I, Yurdakoç K (2006) Equilibrium and kinetics for the sorption of promethazine hydrochloride onto K10 montmorillonite. J Colloid Interface Sci 299:155–162. doi: 10.1016/j.jcis.2006.02.012

Ghorai S, Pant KK (2005) Equilibrium, kinetics and breakthrough studies for adsorption of fluoride on activated alumina. Sep Purif Technol 42:265–271. doi: http://dx.doi.org/10.1016/j.seppur.2004.09.001

Gil M V., Álvarez-Gutiérrez N, Martínez M, et al (2015) Carbon adsorbents for CO2 capture from bio-hydrogen and biogas streams: Breakthrough adsorption study. Chem Eng J 269:148–158. doi: 10.1016/j.cej.2015.01.100

Giles CH, Smith D, Huitson A (1974) A general treatment and classification of the solute adsorption isotherm. I. Theoretical. J Colloid Interface Sci 47:755–765. doi: 10.1016/0021-9797(74)90252-5

Goel C, Kaur H, Bhunia H, Bajpai PK (2016) Carbon dioxide adsorption on nitrogen enriched carbon adsorbents: Experimental, kinetics, isothermal and thermodynamic studies. J CO2 Util 16:50–63. doi: 10.1016/j.jcou.2016.06.002

González AS, Plaza MG, Rubiera F, Pevida C (2013) Sustainable biomass-based carbon adsorbents for post-combustion CO2 capture. Chem Eng J 230:456–465. doi: 10.1016/j.cej.2013.06.118

Guerrero M, Ruiz MP, Alzueta MU, et al (2005) Pyrolysis of eucalyptus at different heating rates: Studies of char characterization and oxidative reactivity. J Anal Appl Pyrolysis 74:307–314. doi: 10.1016/j.jaap.2004.12.008

Halsey G (1948) Physical Adsorption on Non Uniform Surfaces. J Chem Phys 16:931–937. doi: 10.1063/1.1747042

Heidari A, Younesi H, Rashidi A, Ghoreyshi AA (2014) Evaluation of CO2 adsorption with eucalyptus wood based activated carbon modified by ammonia solution through heat treatment. Chem Eng J 254:503–513. doi: 10.1016/j.cej.2014.06.004

Ho YS, McKay G (1999) Pseudo-second order model for sorption processes. Process Biochem 34:451–465. doi: 10.1016/S0032-9592(98)00112-5

Khan TA, Khan EA, Shahjahan (2015) Removal of basic dyes from aqueous solution by adsorption onto binary iron-manganese oxide coated kaolinite: Non-linear isotherm and kinetics modeling. Appl Clay Sci 107:70–77. doi: 10.1016/j.clay.2015.01.005

Kim KH, Kim JY, Cho TS, Choi JW (2012) Influence of pyrolysis temperature on physicochemical properties of biochar obtained from the fast pyrolysis of pitch pine (Pinus rigida). Bioresour Technol 118:158–162. doi: 10.1016/j.biortech.2012.04.094

Kim KH, Kim TS, Lee SM, et al (2013) Comparison of physicochemical features of biooils and biochars produced from various woody biomasses by fast pyrolysis. Renew Energy 50:188–195. doi: 10.1016/j.renene.2012.06.030

Li J, Dai J, Liu G, et al (2016) Biochar from microwave pyrolysis of biomass: A review. Biomass and Bioenergy 94:228–244

Liu H, Cai X, Wang Y, Chen J (2011) Adsorption mechanism-based screening of cyclodextrin polymers for adsorption and separation of pesticides from water. Water Res 45:3499–3511. doi: 10.1016/j.watres.2011.04.004

Liu Y (2009) Is the free energy change of adsorption correctly calculated? J Chem Eng Data 54:1981–1985. doi: 10.1021/je800661q

Lua AC, Yang T (2009) Theoretical and experimental SO2 adsorption onto pistachio-nut-shell activated carbon for a fixed-bed column. Chem Eng J 155:175–183. doi: 10.1016/j.cej.2009.07.031

Lua AC, Yang T, Guo J (2004) Effects of pyrolysis conditions on the properties of activated carbons prepared from pistachio-nut shells. J Anal Appl Pyrolysis 72:279–287. doi: 10.1016/j.jaap.2004.08.001

Monazam ER, Spenik J, Shadle LJ (2013) Fluid bed adsorption of carbon dioxide on immobilized polyethylenimine (PEI): Kinetic analysis and breakthrough behavior. Chem Eng J 223:795–805. doi: 10.1016/j.cej.2013.02.041

Morero B, Groppelli ES, Campanella EA (2016) Evaluation of biogas upgrading technologies using a response surface methodology for process simulation. J Clean Prod. doi: 10.1016/j.jclepro.2016.09.167

Mulgundmath VP, Jones RA, Tezel FH, Thibault J (2012) Fixed bed adsorption for the removal of carbon dioxide from nitrogen: Breakthrough behaviour and modelling for heat and mass transfer. Sep Purif Technol 85:17–27. doi: 10.1016/j.seppur.2011.07.038

O'Mahony T, Guibal E, Tobin JM (2002) Reactive dye biosorption by Rhizopus arrhizus biomass. Enzyme Microb Technol 31:456–463. doi: 10.1016/S0141-0229(02)00110-2

Papari S, Hawboldt K, Helleur R (2015) Pyrolysis: A theoretical and experimental study on the conversion of softwood sawmill residues to biooil. Ind Eng Chem Res 54:605–611. doi: 10.1021/ie5039456

Papari S, Hawboldt K, Helleur R (2017) Production and Characterization of Pyrolysis Oil from Sawmill Residues in an Auger Reactor. Ind Eng Chem Res. doi: 10.1021/acs.iecr.6b04405

Plaza MG, González AS, Pevida C, Rubiera F (2014a) Influence of water vapor on CO2 adsorption using a biomass-based carbon. Ind Eng Chem Res 53:15488–15499. doi: 10.1021/ie500342q

Plaza MG, González AS, Pis JJ, et al (2014b) Production of microporous biochars by single-step oxidation: Effect of activation conditions on CO2 capture. Appl Energy 114:551–562. doi: 10.1016/j.apenergy.2013.09.058

Rajapaksha AU, Vithanage M, Zhang M, et al (2014) Pyrolysis condition affected sulfamethazine sorption by tea waste biochars. Bioresour Technol 166:303–308. doi: 10.1016/j.biortech.2014.05.029

Rouquerol J, Rouquerol F, Llewellyn P, Maurin G, Sing KSW. Adsorption by Powders and Porous Solids: Principles, Methodology and Applications: Second Edition. 2013. doi:10.1016/C2010-0-66232-8.

Ryu Z, Zheng J, Wang M, Zhang B (1999) Characterization of pore size distributions on carbonaceous adsorbents by DFT. Carbon N Y 37:1257–1264. doi: 10.1016/S0008-6223(98)00322-4

Schaefer M (1991) Measurement of Adsorption-Isotherms by Means of Gas Chromatography

Seyhi B, Drogui P, Buelna G, Blais JF (2011) Modeling of sorption of bisphenol A in sludge obtained from a membrane bioreactor process. Chem Eng J 172:61–67. doi: 10.1016/j.cej.2011.05.065

Shafeeyan MS, Daud WMAW, Houshmand A, Shamiri A (2010) A review on surface modification of activated carbon for carbon dioxide adsorption. J Anal Appl Pyrolysis 89:143–151. doi: https://doi.org/10.1016/j.jaap.2010.07.006

Shafeeyan MS, Daud WMAW, Shamiri A, Aghamohammadi N (2015) Modeling of Carbon Dioxide Adsorption onto Ammonia-Modified Activated Carbon: Kinetic Analysis and Breakthrough Behavior. Energy and Fuels 29:6565–6577. doi: 10.1021/acs.energyfuels.5b00653

Sing KSW, Everett DH, Haul R a. W, et al (1985) REPORTING PHYSISORPTION DATA FOR GAS / SOLID SYSTEMS with Special Reference to the Determination of

Surface Area and Porosity (Recommendations 1984). Pure Appl Chem 57:603–619. doi: 10.1351/pac198557040603

Spokas K a., Novak JM, Stewart CE, et al (2011) Qualitative analysis of volatile organic compounds on biochar. Chemosphere 85:869–882. doi: 10.1016/j.chemosphere.2011.06.108

Srivastava VC, Mall ID, Mishra IM (2007) Adsorption thermodynamics and isosteric heat of adsorption of toxic metal ions onto bagasse fly ash (BFA) and rice husk ash (RHA). Chem Eng J 132:267–278. doi: http://doi.org/10.1016/j.cej.2007.01.007

Tamez Uddin M, Rukanuzzaman M, Maksudur Rahman Khan M, Akhtarul Islam M (2009) Adsorption of methylene blue from aqueous solution by jackfruit (Artocarpus heteropyllus) leaf powder: A fixed-bed column study. J Environ Manage 90:3443–3450. doi: 10.1016/j.jenvman.2009.05.030

Thouchprasitchai N, Pintuyothin N, Pongstabodee S (2017) Optimization of CO2 adsorption capacity and cyclical adsorption/desorption on tetraethylenepentamine-supported surface-modified hydrotalcite. J Environ Sci. doi: https://doi.org/10.1016/j.jes.2017.02.015

Valenciano R, Aylón E, Izquierdo MT (2015) A Critical Short Review of Equilibrium and Kinetic Adsorption Models for VOCs Breakthrough Curves Modelling. Adsorpt Sci Technol 33:851–869. doi: 10.1260/0263-6174.33.10.851

Wang J, Huang H, Wang M, et al (2015) Direct capture of low-concentration CO2 on mesoporous carbon-supported solid amine adsorbents at ambient temperature. Ind Eng Chem Res 54:5319–5327. doi: 10.1021/acs.iecr.5b01060

Wang Q, Luo J, Zhong Z, Borgna A (2011) CO2 capture by solid adsorbents and their applications: current status and new trends. Energy Environ Sci 4:42–55. Wang X, Chen L, Guo Q (2014) Development of hybrid amine-functionalized MCM-41 sorbents for CO2 capture. Chem Eng J 260:573–581. doi: 10.1016/j.cej.2014.08.107

Zhu T, Heo HJ, Row KH (2010) Optimization of crude polysaccharides extraction from Hizikia fusiformis using response surface methodology. Carbohydr Polym 82:106–110

# 5. CHAPTER FIVE

## Nitrogen functionalized biochar as a renewable adsorbent for efficient $CO_2$ removal

This chapter has been **published**; Bamdad H*, Hawboldt K, MacQuarrie S. Nitrogen functionalized biochar as a renewable adsorbent for efficient $CO_2$ removal. *Energy & Fuels*. 2018, 32, 11742−11748

## Co-authorship Statement

Hanieh Bamdad is the corresponding author of the paper presented in this chapter. Her contribution was preforming analysis on all samples, interpreting data, and writing the manuscript. Dr. Kelly Hawboldt and Dr. Stephanie MacQuarrie supervised development of work, helped in producing samples and manuscript editing.

## Graphical abstract

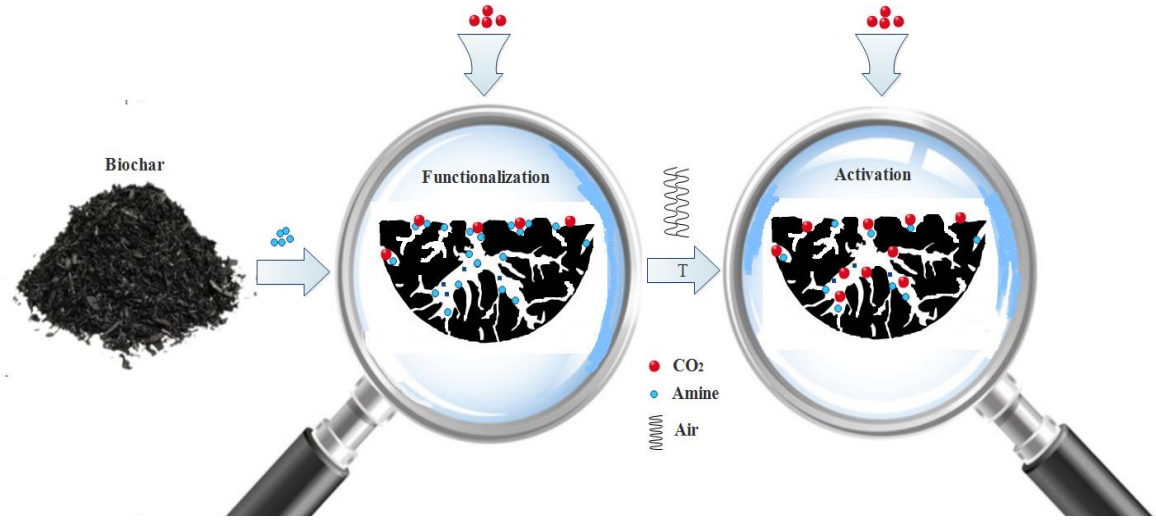


## Abstract

In the previous chapter, the operating conditions for maximizing $CO_2$ uptake was obtained. In addition, it was found that biochar can be used as a sustainable and cost-effective option for removal of acid gases; however, further modifications still required to enhance adsorption capacity of biochar aimed at this chapter. In this study, biochar was thermally and chemically (thermo-chemically) modified and compared to the unmodified parent char in carbon dioxide adsorption. The biochars were sourced from sawmill

residues and produced via fast pyrolysis in an auger reactor. The biochar was chemically functionalized using two novel methods of amine functionalization: i) nitration followed by reduction and ii) condensation of aminopropyl triethoxysilane on the surface. The obtained outcomes indicated functionalization resulted in a reduction in the pore volume and surface area of the biochar. The biochars (unmodified and chemically modified) were thermally activated via air diluted with nitrogen at moderate 560 ºC to determine if the adsorption properties could be enhanced. The thermally treated functionalized chars had a lower H:C ratio, higher surface area, micropore volume, and sufficient amount of nitrogen compared to the unmodified char. The thermally treated aminopropyl triethoxysilane char had the highest adsorption capacity of 3.7 mmol/g with 0.24 wt% nitrogen. Biochars sourced from residues demonstrated high efficiency of carbon dioxide removal, comparable to some synthesized adsorbents reported in the literature.

**Keywords:** Biochar; Adsorption; Functionalizing; Thermal activation; $CO_2$

## Introduction

Sawmill residues in the form of bark, sawdust and saw chips are currently stockpiled and represent a safety and environmental liability; this is particularly problematic in remote regions where transport of this material offsite is costly. Thermal conversion of this biomass via pyrolysis [1], to bio-oil [2] and/or biochar, is one method of monetizing these residues. Biochar can be used as a soil amendment, adsorbent for contaminants in water, wastewaters [3], and gas [4,5], among others. The removal of acid gases such as $H_2S$ and $CO_2$ from gas streams (such as vent/flare gases) is one such application. Traditional methods

to remove these gases can be energy and space intensive, may require expensive and/or toxic chemical, and complex infrastructure [6]. In offshore and any other remote locations (e.g. landfills, small wastewater treatment plants etc.), small scale and less operationally intensive method for gas treatment are required. The common method for acid gas removal is absorption; the acid gases are removed using solvents such as monoethanolamine (MEA) and diethylamine (DEA). Although the selectivity of this form of separation is relatively high, amines are corrosive and highly volatile and the method is cost-intensive due to high energy needs for solvent regeneration (around 85 kJ/mol $CO_2$) [7] and space requirements (separate column for regeneration). Adsorbent systems using porous solids are an attractive alternative to traditional gas-liquid contacting systems. Adsorbents sourced from waste biomass is potentially a more sustainable approach to gas treatment, however factors such as adsorption efficiency, needs of the operator (e.g. bulk removal vs. high purity gas products), regeneration and disposal options must be considered. In order to assess these factors experiments are required to determine adsorption capacities, regeneration potential, and stability of the spent adsorbent. In previous chapter, we have demonstrated that biochar based adsorbents, sourced from forestry residues and produced via fast pyrolysis, are a feasible alternative to traditional solid $CO_2$ adsorbent systems. $CO_2$ was chosen as target since it is often associated with $H_2S$ in petroleum and landfill gases, and can serve as a surrogate for $H_2S$ (a safety and environmentally problematic gas). However, there is potential to improve the adsorbent characteristics by chemically and/or thermally activating the biochar. Incorporating nitrogen functional groups into carbon-based adsorbents enhances surface basicity and could improve adsorption of particular compounds (e.g. $H_2S$ and $CO_2$) and/or the added

nitrogen can chemically interact with these acidic gases, i.e. dipole–dipole, hydrogen bond, covalent bond, etc. [8]. Another motivation for selecting biochar as an adsorbent was low cost/availability even after additional functionalization steps relative to other adsorbents. The biochar price is only 1/6 of that of commerce activated carbon [9].

There are several methods for functionalizing carbon surfaces with nitrogen groups. Ammonia is commonly used [10] where adsorbent particles are placed in a tube furnace. The adsorbent is gradually heated up to the specified temperature typically with $N_2$ purging. Once the set point temperature is reached, the $N_2$ is replaced with $NH_3$ or $NH_3$ mixture. Zhang et al. [11] modified soybean straw biochar by $NH_3$ over a temperature range of 500-900 ºC. This not only enhances the surface area (from 1.5 to as high as 496 $m^2/g$), but also increased the $CO_2$ adsorption capacity up to 1.8 mmol/g. Other methods of introducing nitrogen include addition of nitrogen rich proteins and amino acids. Jayshri et al. [12] synthesized nitrogen enriched carbon using local soybean as the nitrogen source (soy protein) followed by chemical activation using zinc chloride and physical activation using $CO_2$ . The surface area of synthesized nitrogen enriched carbon increased to 811 $m^2/g$ and the breakthrough adsorption capacity to 0.5 mmol/g at 120 °C. Pevida et al. [13] applied different alkylamines to activated carbon (Norit CGP) through a wet impregnation method to increase the basicity and nitrogen content. The impregnation decreased the surface area (from 1762 to 90 $m^2/g$) and there was no increase in adsorption capacity. In fact, the raw activated carbon showed the highest $CO_2$ adsorption capacity. It was proposed the amine might block a fraction of the pores, reducing the surface area for adsorption. In order to enhance $CO_2$ adsorption capacity, Zhang et al. [11] used $CO_2$

activation at high temperatures (500-900 ºC) on the soybean straw based biochar. The surface area of the aminated modified chars increased from 5.5 to 397 $m^2/g$ and the $CO_2$ adsorption capacity at 30 ºC increased from 1 to 1.7 mmol/g with increasing activation temperature (500 to 800 ºC). Further increasing activation temperature to 900 ºC resulted in a decrease in adsorption capacity to 1.5 mmol/g. The decrease could be a result of thermal degradation of some amine functional groups, indicating an optimum activation temperature(s) to maximize adsorption.

Thermal activation of biochar has focussed on high temperatures (up to 900 ºC), however at high temperatures the role of the nitrogen functional groups in adsorption is partially or completely lost. As such, in this work we focussed on activating the biochars in an air or oxygen environment at moderate temperature (below 600 °C) in order to both achieve higher surface area while minimizing functionalization loss. The biochar was produced from fast pyrolysis of local softwood residues in an auger reactor. Two novel methods to introduce nitrogen functionality to the biochars were used. A subset of the biochars was thermally activated using a diluted air-nitrogen mixture at a moderate temperature (560 ºC) and compared with non-activated chars. The relationship between the impact of porous structures and nitrogen-containing group on upgrading $CO_2$ adsorption capacity of biochar was assessed. Further investigation on functionalizing of these biochars can enhance the adsorption and allow the chars to be “tailored” to a target gas (such as other acid gases, $H_2S$).

## 5.1. Materials and Methods

### 5.1.1. Materials

A commercial chemically activated wood-based carbon (Norit CA1) from Sigma-Aldrich was used to compare against the biochars. Sexton Lumber sawmill (Bloomfield, Newfoundland and Labrador) supplied the softwood sawmill sawdust (balsam fir) feedstock. All chemicals utilized in the functionalizing sector were reagent grade chemicals purchased from Sigma-Aldrich and Fischer Scientific. The chemicals used for functionalizing were sulphuric acid, nitric acid, 2-propanol, ammonium hydroxide, sodium hydrosulfite, acetic acid, aminopropyl triethoxysilane, hydrochloric acid, and ethanol.

### 5.1.2. Adsorbent Preparation

The sawdust was dried for 2 days at ambient temperature to decrease the moisture to ~0.12 g/g (12 %). The average particle size of the samples was reduced to less than 2 mm after grinding and then dried again at 70 °C overnight to further decrease the moisture content to 2 % prior to pyrolysis. Fast pyrolysis (at 500$^{o}$C) was used to produce the biochar in an auger reactor. Details on the fast pyrolysis reactor is reported elsewhere [14]. The biochar samples are labelled according to the type of activation/functionalization, temperature of pyrolysis and, when required, temperature of activation.

The biochars were aminated based on a modified literature method [15] comprised of two steps. The first step is nitration of the biochar. Concentrated sulphuric acid (18 M, 50 mL) was added slowly to concentrated nitric acid (15.7 M, 50 mL) at 0 $^{o}$C. A 9 g sample of

washed biochar was added to the acid mixture and stirred for 50 min. The mixture was filtered and washed with distilled water and 2-propanol. The residue was then air-dried at ambient temperature resulting in the introduction of nitro groups to the surface of the biochar. The nitrated biochar was then reduced by addition of 50 mL distilled water and 20 mL of ammonium hydroxide (3 M) and stirred for 10 min without heating. Sodium hydrosulfite (28 g) was added to the solution and allowed to mix overnight under a reflux condenser to avoid solvent evaporation. 20 mL of glacial acetic acid (17.5 M) was diluted in 100 mL water and added to the solution and stirred for 5 h. The solution was then cooled to room temperature, filtered, washed with distilled water and 2-propanol, and air-dried. The final product is aminated biochar and the samples' name was prefixed with "AM" in the text. Figure 5-1 outlines the synthesis.

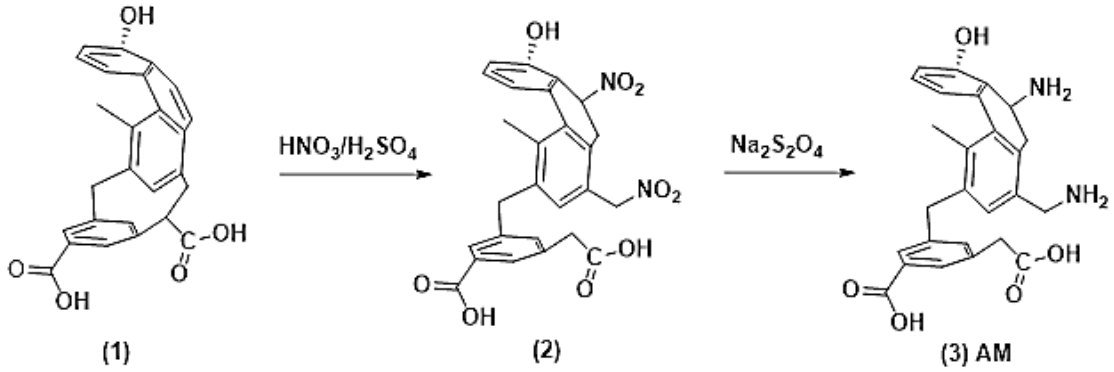


Figure 5-1: Schematic example of the nitration and reduction of biochar [15] under reflux (exothermic)

Aminopropyl triethoxysilane (APTES) was grafted to the surface of the biochar by suspending biochar in distilled water in a 10:1 ratio (char/water) and slowly adding APTES (20% by weight). The APTES-biochar solution was sonicated for 10 min. To

promote the condensation reaction, the pH of the suspension was then adjusted between 3 and 4 using concentrated hydrochloric acid (11.7 M) and allowed to sit for 1 h at ambient temperature, and condensed (refluxed) over 6 h at 70 $^0$C. The resulting biochar was filtered and washed with ethanol followed by distilled water, and dried under vacuum at 40 $^0$C overnight. The biochar produced is labeled with "AP" (Figure 5-2).

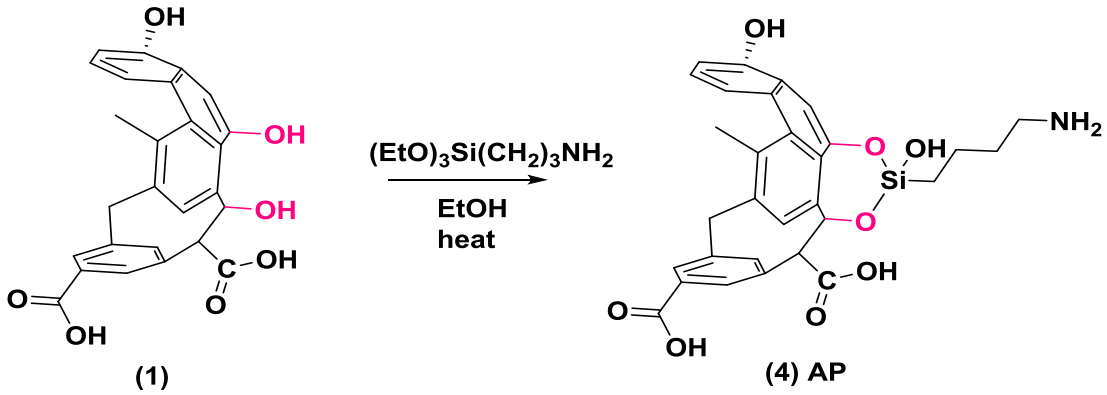


Figure 5-2: Surface modification of biochar with APTES [16–18] under reflux at 70 °C

Samples of the biochars were thermally activated at 560 °C using air flow diluted with nitrogen (5% oxygen) for two hours at a 100 mL/min flow rate and labeled as "A-560". The biochar samples were heated up gradually to the specified temperature in the tube furnace with $N_2$ purging and once the set point temperature is reached, the $N_2$ is replaced with air-nitrogen mixture.

### 5.1.3. Adsorbent Properties

The microstructure of the biochars was obtained using a scanning electron microscope (SEM) (FEI 650F). Samples were mounted on carbon adhesive 12 mm diameter tabs,

which were put on aluminum stubs using carbon tape to avoid the formation of an electric charge on the surface during scanning. Images were taken at low vacuum, with a pressure of 93.3 Pa. The instrument has a secondary-electron (SE), a backscattered-electron (BSE), and a mix of (SE) and (BSE) imaging modes for morphological analyses of the samples. Textural properties of all samples were determined by $N_2$ adsorption-desorption isotherms obtained at 77 K with automatic equipment (Micrometrics Tristar II Plus, USA). Prior to measurement, the flowing-gas degassing was employed at 200°C over night which removes adsorbed contaminants from the surface and pores of the samples. The average pore size and micropore volume were measured via the pore size distribution technique, BJH (Barrett-Joyner-Halenda) and the t-plot method, respectively. The BET (Brunauer–Emmett–Teller) was used to calculate the surface area of the biochar. The bulk elemental analysis of the biochar was performed using a CHN elementary analyzer (Perkin Elmer Series II 2400). Infrared spectra were determined by using a FTIR (Bruker Alpha FTIR spectrometer, accessory type: Single-bounce diamond crystal ATR) with a range of 400 to 4000 $cm^{-1}$ and a total of 24 scans for both background and sample measurement.

### 5.1.4. Adsorption-desorption experiments in a fixed bed reactor

A single-bed adsorption unit was made from borosilicate glass for conducting the adsorption experiments. Figure 5-3 illustrates the schematic of the adsorption-desorption setup.

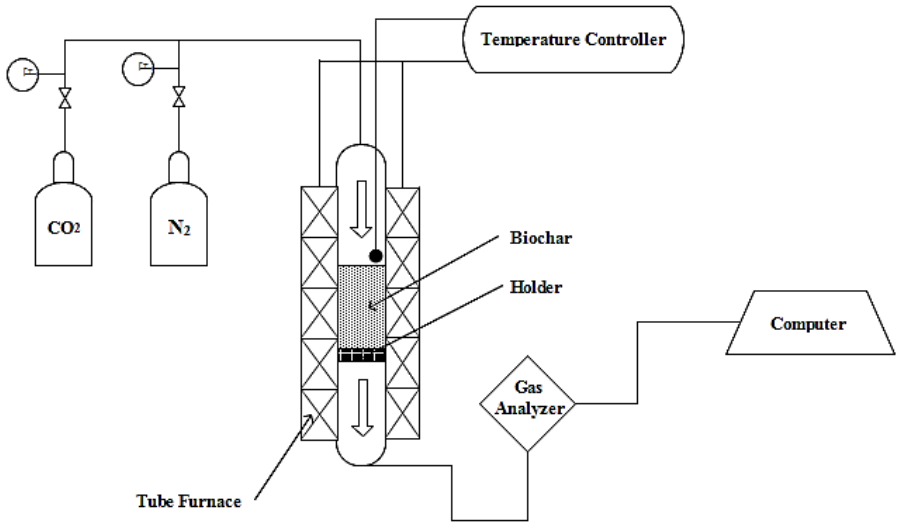


Figure 5-3: Schematic of lab-scale adsorption-desorption system

Before each experiment, the adsorbent was dried in the oven at 60 ºC overnight. Approximately 2.0 g of biochar was placed in the fixed bed reactor (length: 300mm, ID: 15mm), and pure $CO_2$ at 60 mL/min was introduced into the reactor. The adsorption experiments were conducted at room temperature (20 °C). The flow rate of $CO_2$ was controlled with mass flow controller and the composition of the outlet gas stream was continuously monitored with a gas analyzer (OXYBABY® M+). The process was terminated when the bed was saturated as measured by $CO_2$ detected at exit (break through). The adsorption capacity was calculated by integration of the area below the breakthrough curves [19] (equation 1) which is determined by the ratio of outlet to inlet adsorbate gas concentration as a function of time.

$$Q = \frac{F \int_0^t (C_0 - C) dt}{m} \quad (1)$$

where $Q$ is adsorption capacity (mmol/g), $F$ is flow rate of inlet $CO_2$ (mL/min), $C_0$ is concentration of inlet $CO_2$ (mmol/L), $C$ is concentration of outlet $CO_2$ (mmol/L), and $m$ is weight of the biochar (g).

The desorption experiment was done using $N_2$ at 100 mL/min and ambient temperature. Nitrogen was flowed through the system and again $CO_2$ measured at the exit. The spent biochar after regeneration was then reused in the $CO_2$ adsorption experiment ($CO_2$ at 60 mL/min).

## 5.2. Results and Discussion

### 5.2.1. Characterizations

Physical, chemical, and morphological properties of raw and modified biochars are summarized in Table 5-1.

Table 5-1: Properties of biochar samples and activated carbon

| Samples | Surface Area (BET) ($m^2/g$) | Avg. Pore size (nm) | Micropore volume ($cm^3/g$) | C (wt%) | H (wt%) | N (wt%) | H:C | N:C |
|---|---|---|---|---|---|---|---|---|
| AM-SW500 | 3.22 | 7.20 | N/A | 61.99 | 2.56 | 3.90 | 0.04 | 0.063 |
| AP-SW500 | 59.18 | 3.89 | 0.026 | 74.58 | 2.55 | 0.30 | 0.03 | 0.004 |
| SW500 | 95.58 | 4.36 | 0.033 | 76.37 | 2.36 | 0.15 | 0.03 | 0.002 |
| SW500-A-560 | 391.76 | 3.12 | 0.159 | 77.24 | 1.90 | 0.12 | 0.025 | 0.002 |
| AM-SW500-A-560 | 343.32 | 2.97 | 0.133 | 68.37 | 1.46 | 3.17 | 0.021 | 0.046 |
| AP-SW500-A- | 394.12 | 3.08 | 0.160 | 80.15 | 1.63 | 0.24 | 0.020 | 0.003 |

| | | | | | | | | |
|---|---|---|---|---|---|---|---|---|
| 560 | | | | | | | | |
| AC (Norit) | 1166.49 | 3.63 | 0.325 | 81.34 | 2.10 | 0.28 | 0.026 | 0.003 |

The BET surface areas for the biochars produced in this study ranged from 3 (aminated char) to 394.1 (thermally activated modified biochar) $m^2/g$. The commercial activated carbon (Norit) has the highest surface area at 1166.5 $m^2/g$. The pore volume of the functionalized samples (Table 5-1- row 1 and 2) decreased compared to the other chars. This indicates the amine molecules may be "blocking" smaller pores, thereby reducing surface area, which has been reported by others during functionalization of porous materials [20,21]. The textural properties of the samples were further developed by thermal activation, which increased the surface area (~3 times) and pore volume of the product (Table 5-1- row 4-6). This occurred due to thermal degradation and volatilization processes [21]. The impact of activation on the functional groups is discussed below through FTIR analyses.

The nitrogen content increased following amine functionalization for both methods (Table 5-1). In biochar without addition of nitrogen groups, lower H:C ratio indicates a hydrophobic char that can favour adsorption of nonpolar molecules (such as $CO_2$). However, this trend was not noted in the aminated chars as will be discussed in more detail in subsequent sections. The carbon content increased, while the nitrogen and hydrogen decreased during the activation process for both functionalized samples, indicating the degradation of some functional groups [22,23]. The reduction of the H:C ratio after heat treatment has the potential to increase the adsorption capability of the biochar.

The highest surface area with the lowest H:C was in the activated aminated char, AP-SW500-A-560.

To determine the impact of functionality, the FTIR spectra of all samples were analyzed in Figure 5-4.

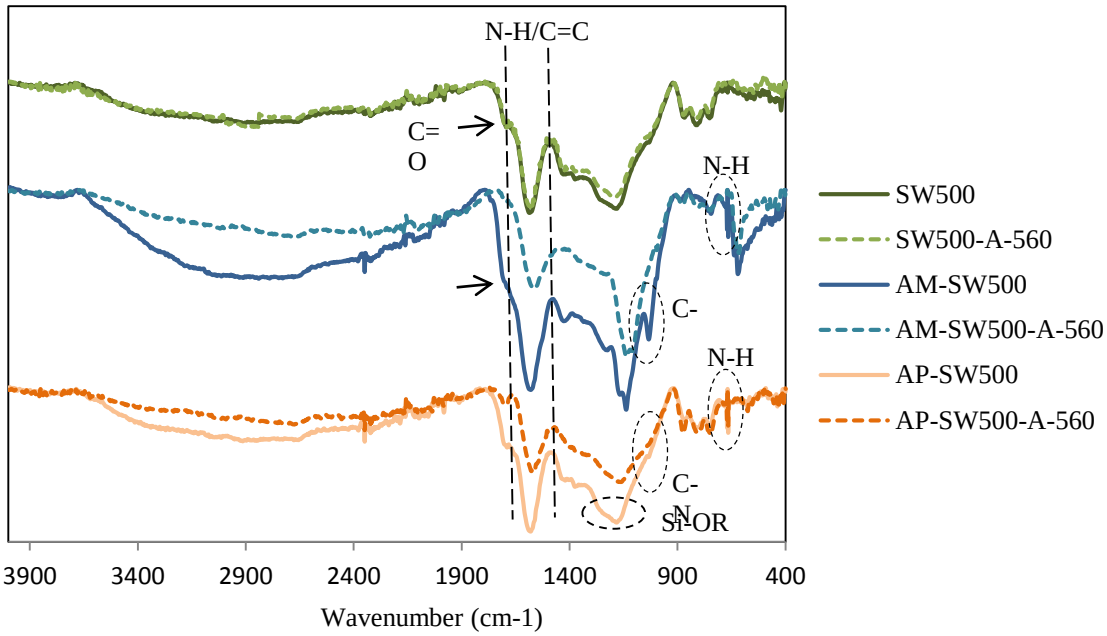


Figure 5-4: FTIR analysis of different biochar samples

The identification of nitrogen functional groups in IR diagrams can be challenging, as they are present in the same wavelength as other functional groups and can be masked. The absorption peak at 900-660 $cm^{-1}$ is likely N-H bending, as it was found in all N-functionalized biochar samples and are visible in nitrogen functionalized chars but not in the unmodified biochar samples. C-N groups were observed at 1250-1000 $cm^{-1}$, more predominantly in amine functionalized samples due to higher nitrogen content. The peaks in the range of 1000 to 1200 $cm^{-1}$ were present only in the APTES chars (AP-SW500,

AP-SW500-A-560), could indicate Si-OR. This was expected due the $(EtO)_3Si(CH_2)_3NH_2$ used in the ATPES process (Figure 5-2). All chars showed identical peaks at 1650-1550 $cm^{-1}$ likely corresponding to C=C and/or N-H bending. The C-N and N-H peak intensities for aminated samples (AM-SW500, AM-SW500-A-560) were strongest due to higher loadings of nitrogen. The peak appeared in the range of 1700 $cm^{-1}$ could be related to C=O (Carboxyl group). The carboxyl group could be displaced by amide after functionalizing and therefore, the C=O peak was less prominent for aminated samples (Figure 5-5). Phenol functional groups (O-H) were observed as small peaks in the range of 1390-1310 and 3900-3300 $cm^{-1}$. The absorption peak intensities decreased for activated samples (dashed lines) likely due to loss of some functional groups. For instance, the intensity of C-N functional group in AM-SW500 reduced after activation. The impact of N-functional groups and decomposition after activation on $CO_2$ adsorption process will be outlined in subsequent sections.

SEM analyses on the fresh (SW500), aminated, and activated surfaces are shown in Figure 5-5 in order to study the appearance effects of functionalizing and activation on biochar samples.

SW500

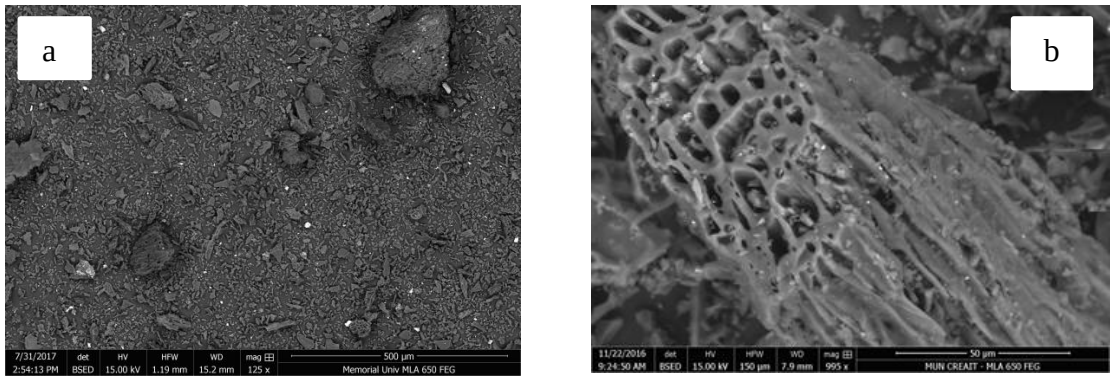

AM-SW500

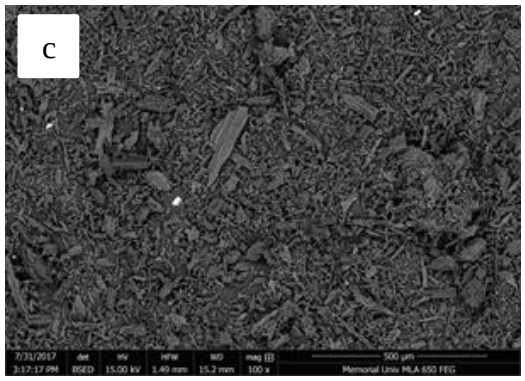


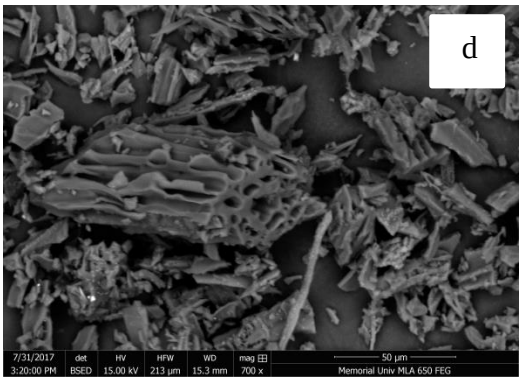


AP-SW500

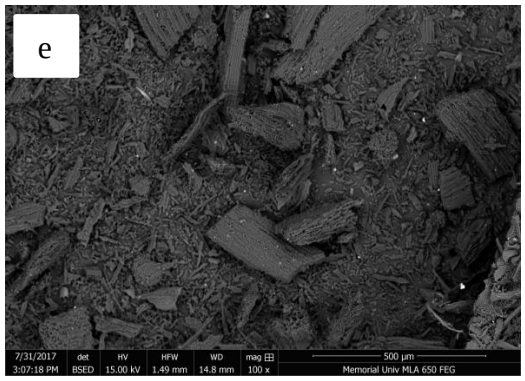


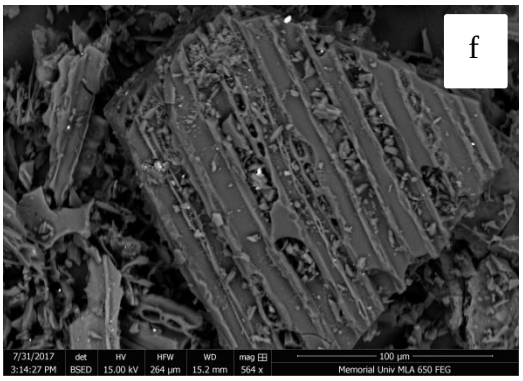


SW500-A-560

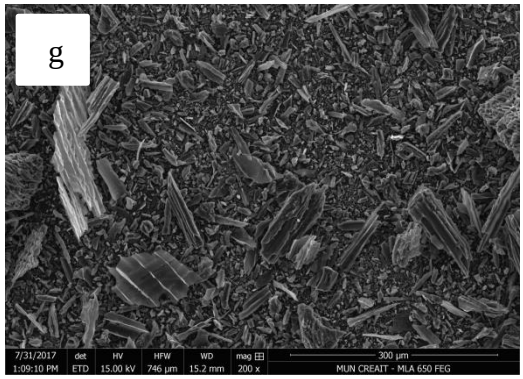


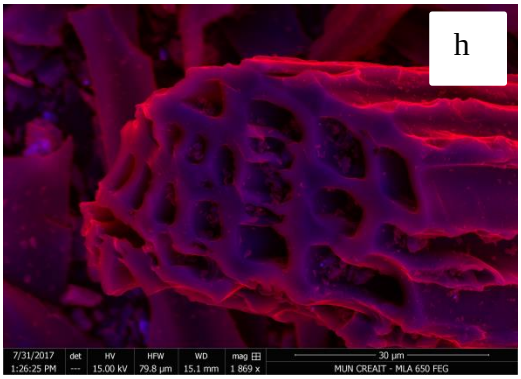


AM-SW500-A-560

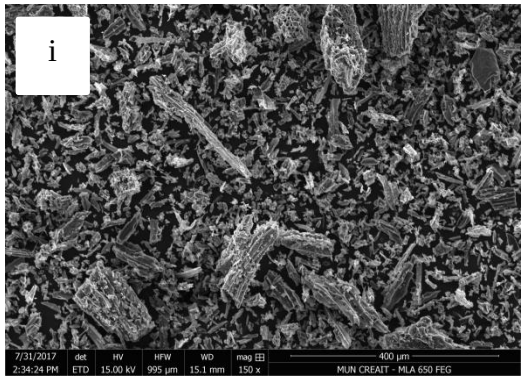


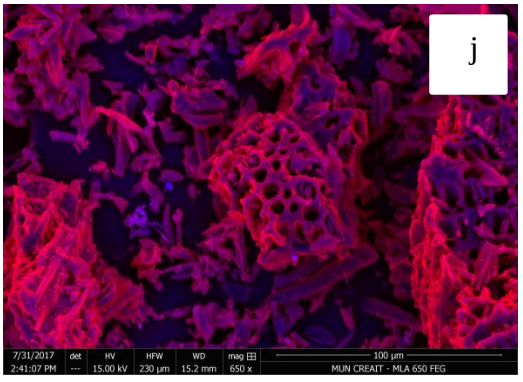

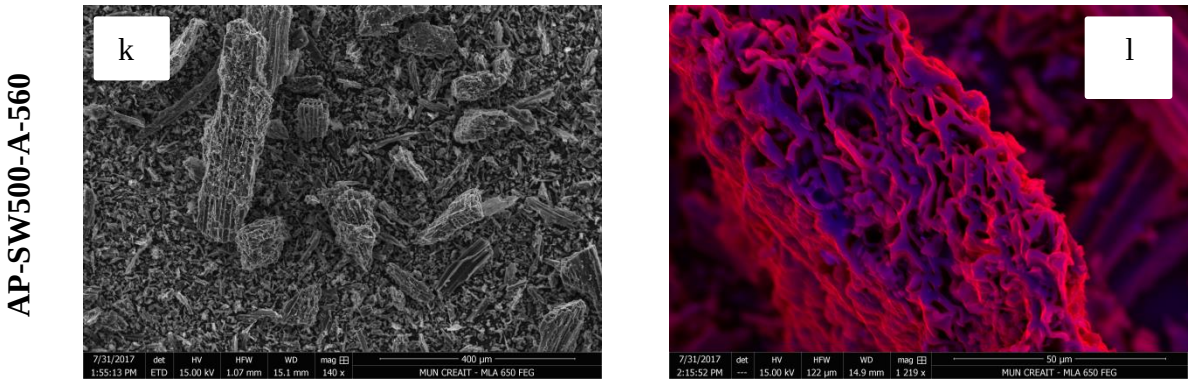


Figure 5-5: SEM images at different resolutions (Best mode was selected for each), left column (low resolution: 300-500µm), right column (high resolution: 30-100µm)

The overall morphology of the samples (Fig. 5-5a,c,e) at low resolution instrument (i.e., at large length scales) reveals no marked differences between samples. At high resolution (Fig. 5-5d,f), the porous structure of the samples is partly diminished after functionalizing, indicating the amine groups were distributed unevenly and occluding some of the pores. The reduction in the surface area and pore volume of functionalized chars validates the SEM results [24]. After one step physical activation, the carbon framework was observed more clearly and the pores became developed and broadened in both low and high resolutions (Fig. 5-5g,h,i,j,k,l). The etching action between the walls and the activating agent (oxygen diluted with nitrogen) at a high temperature as a result of pore skeleton development which leads to more large-volume pores [25].

### 5.2.2. $CO_2$ Adsorption-desorption

As indicated above, our ultimate goal is to study the adsorption of acidic/sour gases ($H_2S$ and $CO_2$). $CO_2$ is used as a surrogate for both in these screening experiments, as it does not have the safety issues associated with $H_2S$. We have also shown through

molecular modeling that the affinity of the chars for $CO_2$ is on the same order of magnitude as $H_2S$. The impact of amine modification on $CO_2$ adsorption capacity was studied at maximum adsorption capacity conditions (20 °C, 60 mL/min, pure $CO_2$). These conditions were determined from previous work (Chapter four). The adsorption performance for all samples and breakthrough curves of two samples (original and modified) are presented in Figure 5-6.

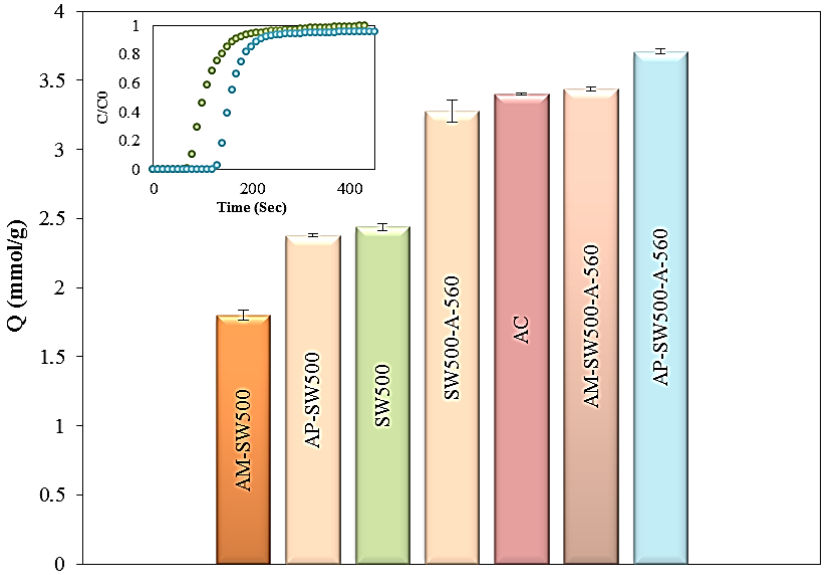


Figure 5-6: Comparison of maximum adsorption capacity of biochars at 20 °C, inlet feed flow rate of 60 mL/min, and pure $CO_2$; breakthrough curves: green for SW500 and blue for AP-SW500-A-560

As the nitrogen loading increases, the adsorption capacity decreases likely due to blocking of pores and/or coating the adsorbent surface by the larger amine groups, preventing $CO_2$ diffusion on to the pores [26,27] particularly at low temperature [28]. For instance, among functionalized samples, AP-SW500 showed a higher adsorption capacity in spite of the lower nitrogen loading relative to the AM chars. This result is consistent

with the characterization tests such as BET surface area and elemental analysis as discussed in the previous section. To further increase the surface area and promote $CO_2$ adsorption, the samples were activated by diluted airflow for two hours. The $CO_2$ adsorption was lower for the two sets of functionalized samples compared to non-functionalized char, but higher after the activation step. For AM-SW500, the adsorption after functionalization with nitrogen is 1.8 mmol/g with 39 mg N/g; while, after activation, the $CO_2$ adsorption capacity rose to 3.4 mmol/g. This indicates there is a balance between functionality and surface area when adding groups (such as amine) to enhance $CO_2$ adsorption [29]. Further testing is required to determine the optimum(s) nitrogen loading and assess the impact of the thermal treatment on the nature of the nitrogen and other functional groups. The nitrogen amounts decreased from 18-20% in the activation process of the biochars (Table 5-1). In addition to nitrogen loss, there was a decrease in the nitrogen functional peaks in the FTIR. The nitrogen loss through volatization and decomposition of the nitrogen functionality is likely the reason for the peak reduction.

Comparing the activated N-loaded biochars (AP-SW500-A-560 and AM-SW500-A-560) to the commercial carbon (Norit), the overall SA is lower, but they demonstrate enhanced adsorption. The reason could be due to a trade-off between the textural and chemical properties; that is, even at lower SA and pore volume the added functionality enhances the adsorption via chemical interaction between the adsorbate and the amines [30] and the more hydrophobic surface. After activation, the adsorption for the N-functionalized chars is almost the same, while the non-functionalized char is lower. As

there was no loss of inherent functional groups for the non-functionalized chars and an almost equivalent increase in SA for all chars, this shows that the nitrogen groups are playing a role in adsorption. The activated material, AP-SW500-A-560, with a surface area of 394 $m^2/g$ and 0.24 wt% N, was the best adsorbent tested (3.7 mmol $CO_2/g$). The adsorption capacity of this type of biochar was higher (30-40%) compared to original biochar (SW500). Table 5-2 summarizes the prepared biochar and other carbon based adsorbents in the literature including templated carbons and chemical activated adsorbents.

Table 5-2: Summary of comparison between prepared sample and other adsorbents

| Sorbents | Feedstock | Activation agent, Temp.(°C) | $CO_2$ Capacity (mmol/g) | Experimental Conditions (T,P,%$CO_2$,F) | Process Scale | Ref. |
|---|---|---|---|---|---|---|
| N-doped Microporous Carbon | Urea formaldehyde resin | KOH, 500-800 | 1.8-3.76 | 25 °C, 1atm,100, 30mL/min | Lab | [23] |
| N-doped Activated Carbon | Bean dreg | KOH, 600-800 | 3-4 | 25 °C, 1 atm, 100, N/A | Lab | [24] |
| N-doped template carbon | Zeolite | N/A | 4 | 25 °C, 1 atm, 100, 50mL/min | Lab | [25] |
| N-doped porous carbons | Polyimine | KOH, 600-750 | 2-3.1 | 25 °C, 1 atm, 100, N/A | Lab | [26] |
| Ultra- | Cyanopyridiniu | N/A | 3.68 | 25 °C, 1 atm, | Lab | [27] |

| | | | | | | |
|---|---|---|---|---|---|---|
| Microporous Carbons | m dicationic salt | | | 100, N/A | | |
| ***AP-SW500-A-560*** | ***Sawdust softwood*** | ***Air, 560*** | ***3.2-3.7*** | ***25 °C, 1 atm, 100, 60mL/min*** | ***Lab*** | ***This work*** |

The functionalized, activated char showed adsorbent capacities on par with or exceeding those of other commercial or synthetic adsorbents. The advantage with this char is in addition to producing the char; fast pyrolysis of forestry residues produces oil with energy and high value chemical potential applications [31].

The stability of the samples AP-SW500-A-560 and AM-SW500-A-560 was studied by a series of adsorption and subsequent regeneration (using $N_2$ at room temperature) cycles. Regeneration experiments are typically conducted at high temperature (ranging from 100-500 °C), since these temperatures accelerate the desorption process [32]. At this stage of the study, we used room temperature to regenerate the char in an effort to assess the binding of $CO_2$ at these conditions. The reasons were two fold, *i)* to assess the spent biochars use in soils and understanding the $CO_2$ sequestration capacity of the char at ambient conditions is more relevant *ii)* to decouple the change in char structure from the impact of temperature so we can assess impacts of cycling. Figure 7 illustrates the impact on adsorption capacity as a function of regeneration.

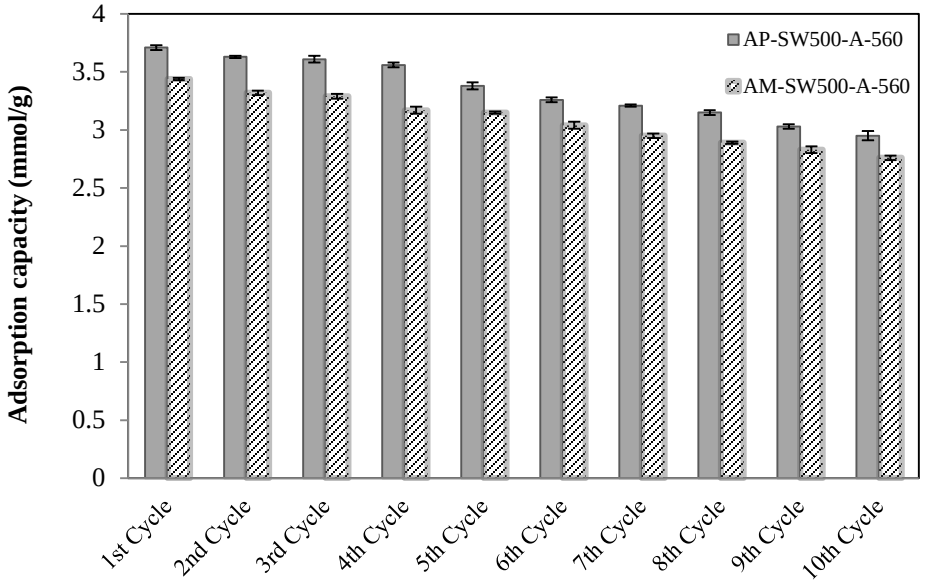


Figure 5-7: $CO_2$ adsorption capacity of cyclic adsorption-desorption experiments

After three cycles, the regeneration capacity is slightly decreased. By five cycles, the adsorption capacity has decreased by 4-8% and by ten cycles, the decrease is 20%. In another study [13], where three cycles were done on nitrogen-enriched carbons for $CO_2$ capture, the decrease in capacity was 5-20% depending on the nature of the nitrogen groups. The regeneration in this case was done under vacuum and 25 ºC. The FTIR analyses of the "regenerated" biochar indicated that a small percentage of $CO_2$ remains on the surface (likely due to chemisorption). This was corroborated by desorption tests in (3Flex surface characterization analyzer -MicroMeritics) which showed some $CO_2$ remains on the structure after regeneration. This could account for the decrease in adsorption capacity as in this experimental system the outlet $CO_2$ is measured. This also observed elsewhere [13]. Our work shows that the modified biochar shows good

regeneration potential however, more studies are required to determine the strength of the $CO_2$ binding (e.g. higher temperatures and/or lower pressures in desorption).

### 5.3. Conclusion

In this work, N-functionalized biochars were prepared and $CO_2$ adsorption experiments were conducted comparing both functionalized and non-functionalized chars. Non-activated functionalized biochars adversely affecting $CO_2$ adsorption. However, moderate thermal activation enhanced the SA and retained enough functionality to generate a material capable of adsorbing $CO_2$ efficiently. After thermal treatment, there was a decrease in the nitrogen content, indicating possible decomposition of some N-containing functional groups and loss of nitrogen. However, thermal activation of the functionalized chars led to higher surface area, pore volume, and lower H:C ratio and ultimately N-enriched biochar followed by moderate physical activation (AP-SW500-A-560) was found to have much higher adsorption capacity compared with commercially available activated carbon (Norit CA1) and recent carbon-based adsorbents in the literature. It appears that retaining some nitrogen functionality enhances adsorption and makes up for a decreased SA limiting the physical adsorption. This study reports the use of moderate, rather than extreme activation temperatures, combined with tailored functionalization of readily available and sustainably sourced biochar as an alternative to more costly adsorbents. Further investigations should focus on optimization of activation conditions, nitrogen loading, and desorption conditions to evaluate the impact of the thermal treatment on the nature of functional groups responsible for chemical adsorption.

**Acknowledgment**

This work was carried out with the support of NSERC (Natural Science and Engineering Research Council of Canada), SGS (School of Graduate Studies of Memorial University), and BioFuelNet Canada. The authors sincerely acknowledge the valuable assistance provided by Dr. MacQuarrie's group (Cape Breton University) in functionalizing studies conducted during this work and Dr. Sadegh Papari (Memorial University) for producing the biochar samples.

## References


(1) Papari, S.; Hawboldt, K.; Helleur, R. Pyrolysis: A Theoretical and Experimental Study on the Conversion of Softwood Sawmill Residues to Biooil. Ind. Eng. Chem. Res. 2015, 54 (2), 605–611.

(2) Papari, S.; Hawboldt, K.; Helleur, R. Production and Characterization of Pyrolysis Oil from Sawmill Residues in an Auger Reactor. Ind. Eng. Chem. Res. 2017.

(3) Rao, M. A.; Di Rauso Simeone, G.; Scelza, R.; Conte, P. Biochar Based Remediation of Water and Soil Contaminated by Phenanthrene and Pentachlorophenol. Chemosphere 2017, 186, 193–201.

(4) Plaza, M. G.; Durán, I.; Querejeta, N.; Rubiera, F.; Pevida, C. Experimental and Simulation Study of Adsorption in Postcombustion Conditions Using a Microporous Biochar. 1. CO 2 and N 2 Adsorption. Ind. Eng. Chem. Res. 2016, 55 (11), 3097–3112.

(5) Cai, W.; Zhang, S.; Hu, X.; Jaroniec, M. In Situ Synthesis of Nitrogen-Enriched Activated Carbons from Procambarus Clarkii Shells with Enhanced CO2 Adsorption Performance. Energy & Fuels 2018.

(6) Bamdad, H.; Hawboldt, K.; MacQuarrie, S. A Review on Common Adsorbents for Acid Gases Removal: Focus on Biochar. Renewable and Sustainable Energy Reviews. 2016.

(7) Xue, B.; Yu, Y.; Chen, J.; Luo, X.; Wang, M. A Comparative Study of MEA and DEA for Post-Combustion CO2capture with Different Process Configurations. Int. J. Coal Sci. Technol. 2017, 4 (1), 15–24.

(8) Shafeeyan, M. S.; Daud, W. M. A. W.; Houshmand, A.; Shamiri, A. A Review on Surface Modification of Activated Carbon for Carbon Dioxide Adsorption. Journal of Analytical and Applied Pyrolysis. 2010, pp 143–151.

(9) Ahmad, M.; Rajapaksha, A. U.; Lim, J. E.; Zhang, M.; Bolan, N.; Mohan, D.; Vithanage, M.; Lee, S. S.; Ok, Y. S. Biochar as a Sorbent for Contaminant Management in Soil and Water: A Review. Chemosphere. 2014, pp 19–23.

(10) Sevilla, M.; Valle-Vigõn, P.; Fuertes, A. B. N-Doped Polypyrrole-Based Porous Carbons for CO 2 Capture. Adv. Funct. Mater. 2011, 21 (14), 2781–2787.

(11) Zhang, X.; Wu, J.; Yang, H.; Shao, J.; Wang, X.; Chen, Y.; Zhang, S.; Chen, H. Preparation of Nitrogen-Doped Microporous Modified Biochar by High Temperature CO 2 –NH 3 Treatment for CO 2 Adsorption: Effects of Temperature. RSC Adv. 2016, 6 (100), 98157–98166.

(12) Thote, J. A.; Iyer, K. S.; Chatti, R.; Labhsetwar, N. K.; Biniwale, R. B.; Rayalu, S. S. In Situ Nitrogen Enriched Carbon for Carbon Dioxide Capture. Carbon N. Y. 2010, 48 (2), 396–402.

(13) Plaza, M. G.; Pevida, C.; Arenillas, A.; Rubiera, F.; Pis, J. J. CO2 Capture by

Adsorption with Nitrogen Enriched Carbons. Fuel 2007, 86 (14 SPEC. ISS.), 2204–2212.

(14) Bamdad, H.; Hawboldt, K. Comparative Study between Physicochemical Characterization of Biochar and Metal Organic Frameworks (MOFs) as Gas Adsorbents. Can. J. Chem. Eng. 2016, 9999, 1–7.

(15) Yang, G. X.; Jiang, H. Amino Modification of Biochar for Enhanced Adsorption of Copper Ions from Synthetic Wastewater. Water Res. 2014.

(16) Tran, V. T.; Kim, J. H.; Jeong, K. J.; Kwon, J.; Kim, S. H.; Lee, J. Highly Stable Functionalized Aluminum Nanoparticles for Magneto-Energetic Composite Fabrication. Combust. Flame 2018, 187, 96–104.

(17) Gautam, S.; Guria, C.; Rajak, D. K.; Pathak, A. K. Functionalization of Fly Ash for the Substitution of Bentonite in Drilling Fluid. J. Pet. Sci. Eng. 2018, 166, 63–72.

(18) Zhi, X.; Mao, Y.; Yu, Z.; Wen, S.; Li, Y.; Zhang, L.; Chan, T. W.; Liu, L. γ-Aminopropyl Triethoxysilane Functionalized Graphene Oxide for Composites with High Dielectric Constant and Low Dielectric Loss. Compos. Part A Appl. Sci. Manuf. 2015, 76, 194–202.

(19) Liu, H.; Cai, X.; Wang, Y.; Chen, J. Adsorption Mechanism-Based Screening of Cyclodextrin Polymers for Adsorption and Separation of Pesticides from Water. Water Res. 2011, 45 (11), 3499–3511.

(20) Przepiórski, J.; Skrodzewicz, M.; Morawski, A. W. High Temperature Ammonia Treatment of Activated Carbon for Enhancement of CO2 Adsorption. Appl. Surf. Sci. 2004, 225 (1–4), 235–242.

(21) Chai, S. H.; Liu, Z. M.; Huang, K.; Tan, S.; Dai, S. Amine Functionalization of Microsized and Nanosized Mesoporous Carbons for Carbon Dioxide Capture. Ind. Eng. Chem. Res. 2016, 55 (27), 7355–7361.

(22) Liu, Q. S.; Zheng, T.; Wang, P.; Guo, L. Preparation and Characterization of Activated Carbon from Bamboo by Microwave-Induced Phosphoric Acid Activation. Ind. Crops Prod. 2010, 31 (2), 233–238.

(23) Lee, S. H.; Choi, C. S. Chemical Activation of High Sulfur Petroleum Cokes by Alkali Metal Compounds. Fuel Process. Technol. 2000, 64 (1), 141–153.

(24) Irani, M.; Gasem, K. A. M.; Dutcher, B.; Fan, M. CO2 Capture Using Nanoporous TiO(OH)2/tetraethylenepentamine. Fuel 2016, 183, 601–608.

(25) Zhang, C.; Song, W.; Ma, Q.; Xie, L.; Zhang, X.; Guo, H. Enhancement of CO2 Capture on Biomass-Based Carbon from Black Locust by KOH Activation and Ammonia Modification. Energy and Fuels 2016, 30 (5), 4181–4190.

(26) Arenillas, A.; Smith, K. M.; Drage, T. C.; Snape, C. E. CO2 Capture Using Some Fly Ash-Derived Carbon Materials. In Fuel; 2005; Vol. 84, pp 2204–2210.

(27) Maroto-Valer, M. M.; Tang, Z.; Zhang, Y. CO2 Capture by Activated and

Impregnated Anthracites. In Fuel Processing Technology; 2005; Vol. 86, pp 1487–1502.

(28) Heydari-Gorji, A.; Belmabkhout, Y.; Sayari, A. Polyethylenimine-Impregnated Mesoporous Silica: Effect of Amine Loading and Surface Alkyl Chains on CO 2 Adsorption. Langmuir 2011, 27 (20), 12411–12416.

(29) Dutcher, B.; Fan, M.; Russell, A. G. Amine-Based CO2capture Technology Development from the Beginning of 2013-A Review. ACS Appl. Mater. Interfaces 2015, 7 (4), 2137–2148.

(30) Zhao, Y.; Liu, X.; Yao, K. X.; Zhao, L.; Han, Y. Superior Capture of CO2 Achieved by Introducing Extra-Framework Cations into N-Doped Microporous Carbon. Chem. Mater. 2012, 24 (24), 4725–4734.

(31) Papari, S.; Hawboldt, K. A Review on the Pyrolysis of Woody Biomass to Bio-Oil: Focus on Kinetic Models. Renewable and Sustainable Energy Reviews. 2015, pp 1580–1595.

(32) Chatterjee, R.; Sajjadi, B.; Mattern, D. L.; Chen, W. Y.; Zubatiuk, T.; Leszczynska, D.; Leszczynski, J.; Egiebor, N. O.; Hammer, N. Ultrasound Cavitation Intensified Amine Functionalization: A Feasible Strategy for Enhancing CO2capture Capacity of Biochar. Fuel 2018, 225, 287–298.

# 6. CHAPTER SIX

## Molecular Modeling as a Tool for Study of Surface Heterogeneity and Nitrogen Functionalizing of Biochars

This chapter has been proofread and edited by Dr. Kelly Hawboldt and Dr. Stephanie MacQuarrie.

**Graphical Abstract**

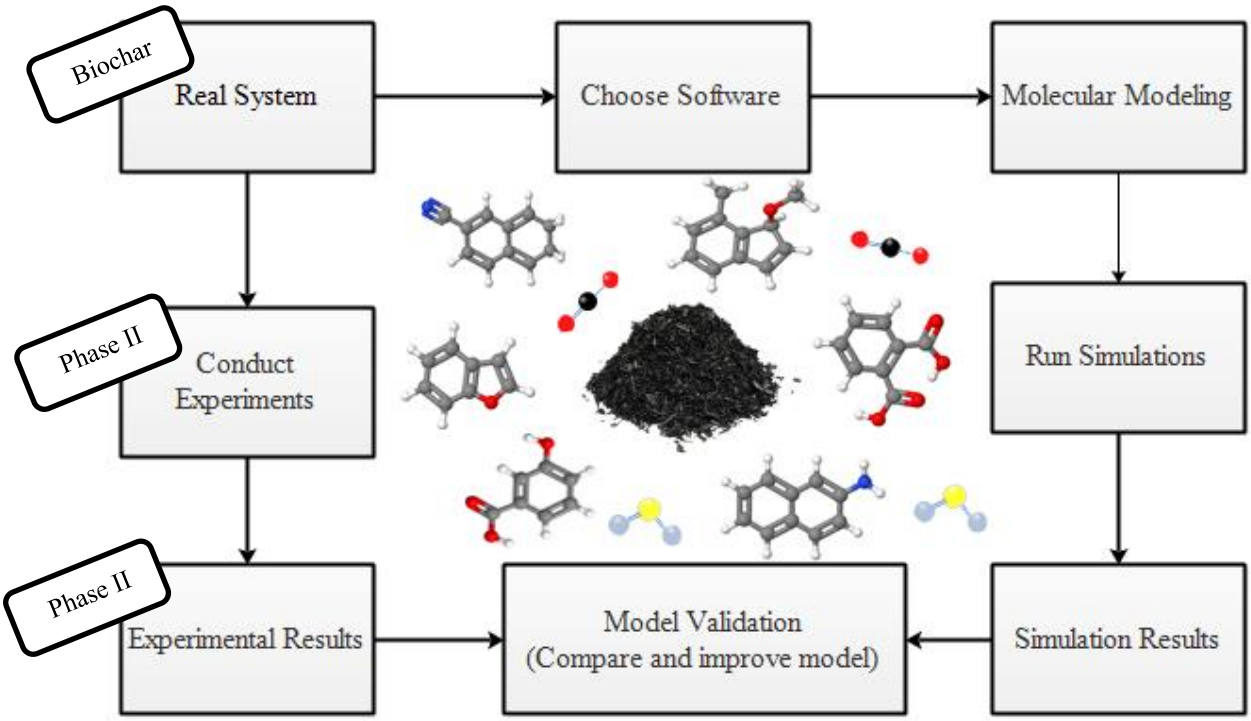


**Abstract**

The adsorption of $CO_2$ onto different original and modified biochars was investigated in chapter four and five, respectively. The obtained results from previous chapters were used in this chapter for validation of molecular modeling outcomes. The functionality of biochar surfaces depends on the nature of the feedstock, pyrolysis temperature, and residence time. In this chapter, molecular modeling was used as a tool to determine the types of functionalization that could enhance adsorption and to pre-screen the target adsorbate for the sake of minimizing experimental time. The impact of single functional group and interaction between them (including nitrile, methyl, ether, furan, carboxyl, hydroxyl, amine, and amide) on the adsorption of target adsorbate onto biochar was

investigated. Among biochar inherent functional groups simulated, the lowest heat of adsorption occurred with carboxyl and hydroxyl for $CO_2$ adsorption due to hydrogen bonding, which demonstrates these two functional groups are the best candidates for interacting with $CO_2$. The simulations showed amine/amide functional groups enhanced $CO_2$ adsorption with more exothermic adsorption, possibly because of stronger bonding compared to other functional groups. The interaction of $H_2S$ with biochar released higher heat of adsorption in comparison to $CO_2$, but approximately equal Gibbs free energy, indicating $CO_2$ can be used as a surrogate to $H_2S$. The simulation results were compared against experimental results and the thermodynamic properties were satisfactorily matched.

**Introduction**

Biochar sourced from forestry residues is potentially more environmentally sustainable and cost-effective alternative to adsorbents used in removing acid gases ($CO_2$/$H_2S$) from gas streams when compared to traditional methods. Biochar surface properties are a function of production conditions (*i.e.* temperature and residence time) and feedstock; therefore, biochars produced at different conditions may vary structurally, however they maintain interesting and applicable functionalities. In fact, these surface functional groups formed during production, enhance the ability of biochar to adsorb certain chemicals including small gases, compared to commercially available, expensive activated charcoals. The heterogeneous nature of the surface has led to much of the research in this area using a process of experimental trial and error to determine the best target molecules. We have implemented molecular modeling paired with experimental results to better

design adsorption experiments by modeling interactions between target gas and the adsorbent surface to get an idea of the propensity for adsorption and comparing to bench top experiments.

Some researchers [1–3] have modeled the molecular structure of biochar produced from fast pyrolysis, slow pyrolysis, and gasification systems quantitatively using $^{13}C$ nuclear magnetic resonance spectroscopy ($^{13}C$-NMR). In this work, we have employed molecular modeling as a tool to pre-screen the adsorbates minimizing the experimental time, reducing waste, energy, risk concerns of handling chemicals, etc. Further, it can be used to determine the types of functionalization that could enhance adsorption of target adsorbates. Acid gases are common contaminants in oil and gas operations, landfill gases, and other industrial effluents. One of the methods for removal of acid gases ($CO_2$/$H_2S$) is adsorption, which can solve the practical limitations of conventional techniques (*e.g.* absorption). Absorption processes are space and cost intensive; however, common adsorbents (*e.g.* metal oxide based, carbon based, and silica based) represent a potentially more sustainable approach for removal of acid gases. Simulations of $CO_2$/$H_2S$ adsorption on carbon materials have been done by a number of researchers [5-7]. Dang et al. [4] studied $CO_2$ adsorption on brown coal using GCMC (grand canonical Monte Carlo) computational approach. The adsorption energy ($E_{ads}$) of $CO_2$ on brown coal surfaces calculated using DFT indicated the basicity of the oxygen- and nitrogen-containing groups controls the adsorption strength of $CO_2$. Lim et al. [5] carried out calculations based on the Vienna ab initio simulation package (VASP, version 5.2.12) on carbon structures with N-functional groups (such as cyanide, pyrrole, pyridone, pyridine, amine, and quaternary amines). A model of carbon material with 9 aromatic rings consisting of

32 C atoms and 16 H atoms was constructed. They showed that pyridone and pyridine groups showed the most enhancements on adsorption of $CO_2$ compared to other functional groups (such as cyanide, pyrrole, *etc*.). The adsorption of pure $SO_2$ and $H_2S$ and their selective adsorption from various gas mixtures by porous aromatic frameworks (PAFs) were investigated by Zhang et al. [6] using GCMC simulations. A periodic PAF unit cell was constructed and the influence of functional groups including -$CH_3$, -CN, -COOH, -$COOCH_3$, -OH, -$OCH_3$, -$NH_2$ and -$NO_2$ on the adsorption was investigated. The binding energy calculations showed inclusion of any of the functional groups enhanced adsorption but the electron withdrawing groups such as -CN, -COOH, -$COOCH_3$ and -$NO_2$ were more effective.

The bulk of publications used a simplified char structure with one functional group as a model [8–10]. In this work, we constructed a biochar structure with multiple functionalities in order to approximate actual biochar. In this study, a surface composition/structure of biochar was selected from published char structure as a basis compound and built in software. The model was compared with analyses of char generated in our labs to ensure the model was an accurate representation of the actual biochar. The model was then used to test the char's affinity for $CO_2$/$H_2S$ as a function of the functional group. The impact of modifying the surface with nitrogen functional groups on adsorption was compared with unmodified biochar.

## 6.1. Theoretical and experimental details

### 6.1.1. Surface construction and validation

The first step is to construct the biochar surface. A limited number of molecular representations of biochar have been proposed in the literature [7–9]. For this study, the most comprehensively characterized molecular structure was selected from literature in order to study the adsorption of $CO_2$ onto biochar [3]. The selected surface was constructed by Zhao et al. [3] based on solid state $^{13}C$ nuclear magnetic resonance (NMR) and pyrolysis-gas chromatography-mass spectrometry (Py-GC-MS) analyses. The 2D and 3D structure of biochar as Gaussian input files were modeled using Marvin Sketch amd 64 and Jmol 14.4.4 software, and are outlined below (Figure 6-1).

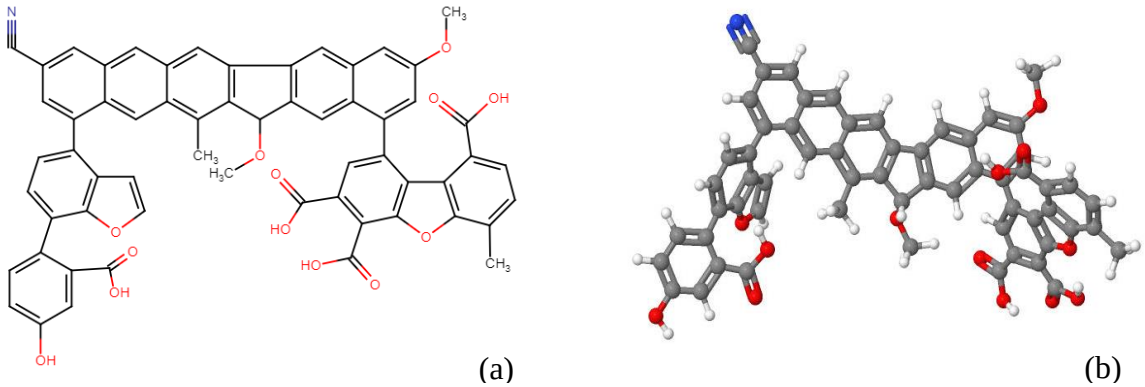


Figure 6-1: (a) 2D model of biochar structure, (b) 3D model of optimized biochar structure, Colors Code: C= gray; N= blue; H= white; O=red

To assess the ability of the model to simulate our actual biochar, the infrared spectra and elemental compositions of prepared biochar produced in our lab [10] were compared with that of the simulated surface. The structure has 111 atoms, 508 electrons, and a

neutral surface. This was further divided into seven carbon surfaces with different functionality: 1) nitrile, 2) methyl, 3) ether, 4) furan, 5) carboxyl, and 6) hydroxyl. Sections were compared to determine effect of functional group on $CO_2$ adsorption (Figure 6-2a-g).

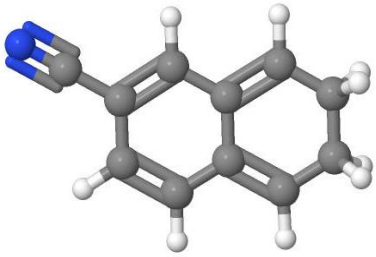

**a) Portion 1**
**nitrile**

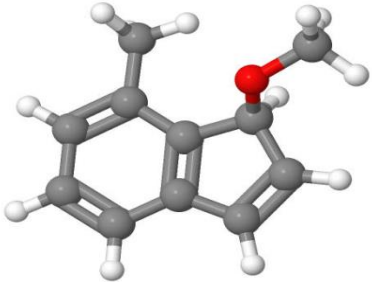

**b) Portion 2**
**methyl, ether**

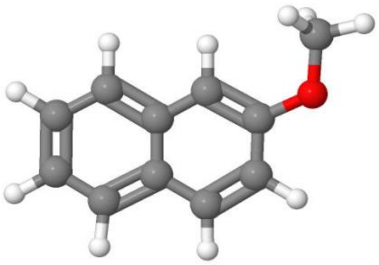

**c) Portion 3**
**ether**

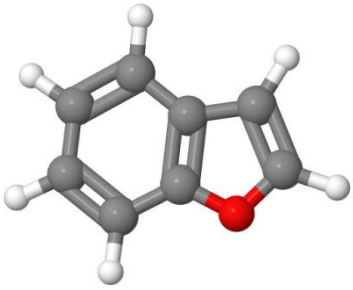

**d) Portion 4**
**furan**

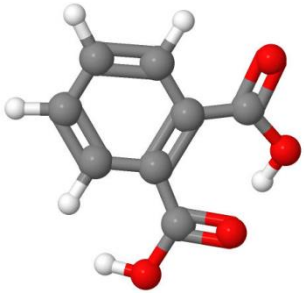

**e) Portion 5**
**carboxyl**

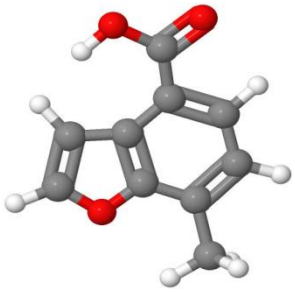

**f) Portion 6**
**carboxyl, furan**

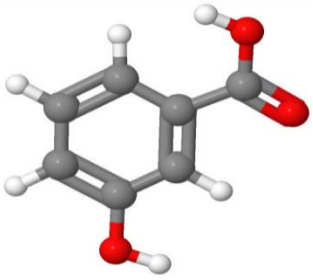

**g) Portion 7**
**carboxyl, hydroxyl**

Figure 6-2: Structure of different functionalized biochar portions (a-g)

Amine functionalized of carbonaceous surfaces can improve the adsorption capacity based on previous studies [23-25]. To study the impact of these groups, in separate simulations the functional groups of all 7 portions were replaced with amine groups, nitrile and ether were replaced with amine functional groups (Figure 6-3 a and b).

**a) Portion 1 amine**

**b) Portion 3 amine**

Figure 6-3: Structure of two portions of amine functionalized biochar as an example

### 6.1.2. Computational methodology and simulation

After constructing the structure, the electronic interaction between target and the surface was performed using Gaussian 09 [11] software (on ACENET consortium at Memorial University). Initially, the energy of the simulated surfaces and gas phase adsorbates were reduced (optimization) by fixing the bond length and angles to stabilize the system. The $CO_2$ molecule then introduced to each structure portion with specified distance (outlined in section 2.2). Thermodynamic properties and vibrational frequencies were calculated by density functional theory (DFT). DFT is a computational method simulates the molecules

based on electron density [12]. Figure 6-4 illustrates the algorithm of DFT for computing the molecule properties.

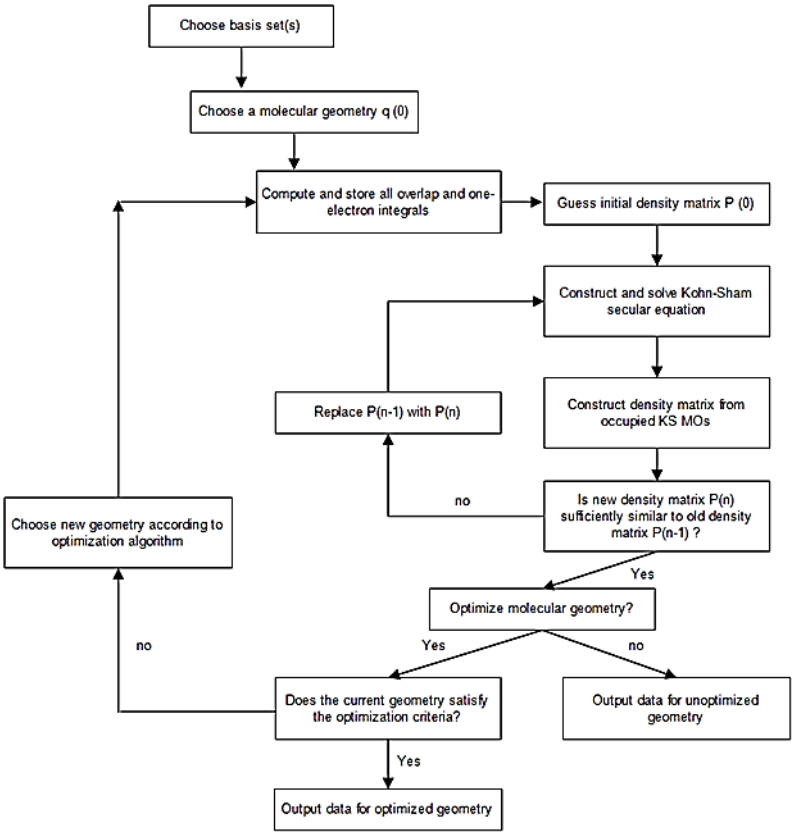


Figure 6-4: Algorithm of density functional theory (DFT) [13]

The basis set (6-31G(d) in our study) and molecular geometry are first specified by user. The software then suggests the density matrix ($\rho(r,t)$) at time zero ($t=0$) and the density matrix elements (Equation 1) are updated accordingly. Gaussian software uses as default initial estimate from the extended Hückel theory. The total electron density is expanded in terms of the molecular orbitals (Equation 1) and then each orbital can be expanded in terms of a set of atomic orbitals or the basis set (Equation 2).

$$\rho(r,t) = \sum n_i \, f_n |\psi_i(r,t)|^2 \quad (1)$$

$$\psi_i(r,t) = \sum c_i \, \chi \quad (2)$$

where $n_i$ is number of occupied orbitals, r is the position of particles in the system, t is the time, $\psi_i(r,t)$ is the molecular orbitals (square root of electrons/(atomic unit)$^3$) at distance r and time t, $\chi$ is the atomic orbitals (square root of electrons/(atomic unit)$^3$), and $c_i$ is constant.

Once convergence of the density matrix is achieved, the final energy of the system is computed by inserting the calculated final density matrix (ρ(r)) as below [10]:

$$E_{KS}[\rho(r)] = T_{ni}[\rho(r)] + V_{ne}[\rho(r)] + V_{ee}[\rho(r)] + \Delta T[\rho(r)] + \Delta V_{ee}[\rho(r)] \quad (3)$$

where $T_{ni}$ is the kinetic energy of non-interacting electrons, $V_{ne}$ is the nuclear-electron interaction energy, $V_{ee}$ is the electron-electron repulsion energy, ΔT is the correction to the kinetic energy deriving from the interacting of the electrons, $\Delta V_{ee}$ is the correction to the electron-electron repulsion energy. The atomic unit of all terms in equation 3 is in Hartree.

DFT simulations were based on the B3LYP/6-31G(d) level of theory. The B3LYP theory is a hybrid method for doing DFT calculations, comprising parts of ab initio (such as Hartree-Fock) with improvement on DFT mathematics (faster with better accuracy). The selected level of theory (B3LYP/6-31G(d)) provides reliable vibrational frequencies with high accuracy, low cost, and shorter running time in comparison with the other DFT calculation methods (such as Local Density Approximation [LDA] and Gradient Correct

[GC]) [14]. The B3LYP/6-31G(d) method has shown good performance in describing the $CO_2$ adsorption on the microporous carbon materials [4]. Although the DFT methods underestimate weak interactions such as Van der Waals forces [15,16], they still provide a valuable assessment of interaction energies for relative comparison.

### 6.1.3. Adsorption energy calculation

After running simulations with Gaussian software, the output energies were obtained. The bonding energy was calculated by subtracting the summation of the output energy of optimized target gas ($CO_2$/$H_2S$) and adsorbent surface (biochar) from the optimized adsorbate-adsorbent complex. All the products and reactants should be at the same temperature and pressure.

$$\Delta E_{ads}(adsorbent - adsorbate) = E_{adsorbent-adsorbate} - (E_{adsorbent} + E_{adsorbate}) \quad (6)$$

where $E_{adsorbent}$, $E_{adsorbate}$, and $E_{adsorbent\text{-}adsorbate}$ is the energy of isolated biochar, $CO_2$/$H_2S$, and biochar-$CO_2$/$H_2S$ system, respectively. Lower (negative) adsorption energy indicates stronger bonding between adsorbate and surface [17]. Frequency calculations were performed to obtain a minimum energy and IR vibrations. The energy minima for all optimized geometries of reactants and products allowed us to estimate Enthalpy and Gibbs free energy for the system based on Equation 3.

To gain better insight into adsorption process, the Mulliken population analysis was performed using GaussView 5.0.8 software to calculate the amount of charge transferred to/from surface/$CO_2$ molecules. The most favourable adsorption regions are determined by the interaction between the electrostatic potential of the surface and that of the guest

molecule [18]. Population analysis shows the charge distribution in the system and determines partial charge amount and location within the molecule. The Mulliken charge distribution is the most common population analysis and is highly dependent on the basis set function. This analysis is applicable for comparing partial charge of atoms between two different geometries with the same basis set. The charge distribution of each atom ($\Delta q_i$) of the biochar surface was calculated with and without the adsorbate ($CO_2$ molecule) to determine the amount of charge transferred during adsorption [19] using the following equations:

$$\Delta q_i = q_{i,biochar\ after\ adsorption} - q_{i,biochar\ before\ adsorption} \quad (4)$$

$$\Delta q_j = q_{j,CO2\ after\ adsorption} - q_{j,CO2\ before\ adsorption} \quad (5)$$

where *i* is a biochar surface atom, and *j* is a $CO_2$ atom.

### 6.1.4. Preparation and characterization of biochar

The actual biochar was prepared via fast pyrolysis in a 4 kg/h capacity auger reactor, details of this system are reported in [10] from softwood (balsam fir). The elemental analysis of the biochar was performed using a CHN/O Analyzer (Perkin Elmer Series II 2400) and the oxygen content was determined by the difference of total elements and wt.% of C, H, and N. Infrared spectra were obtained using a FTIR (Bruker Alpha FTIR spectrometer) with a range of 400 to 4000 $cm^{-1}$, a resolution of 4 $cm^{-1}$, and a total of 24 scans for both background and sample measurement.

## 6.2. Results and discussion

### 6.2.1. Validation of the surface model

To obtain a reliable picture of the surface of the biochar samples in terms of functional groups and to compare with simulated spectra, a calculated IR spectrum for the whole biochar surface model and functionalized one were produced and compared to the experimental analysis (Figure 6-5).

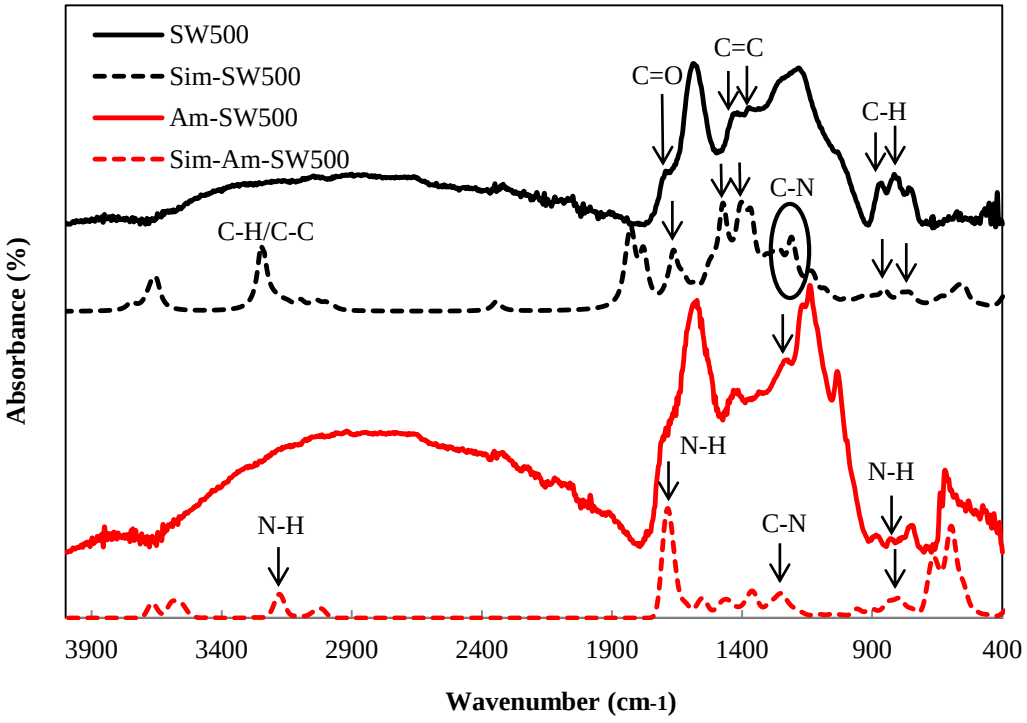


Figure 6-5: Experimental and simulated IR frequencies for original and functionalized biochar (SW500: sawdust produced at 500 °C, Am-SW500: amine functionalized sawdust produced at 500 °C)

The absorption peak at 900-700 $cm^{-1}$ correspond to aromatic C-H stretch and 1600-1500 $cm^{-1}$ ,to C=C in aromatics, respectively [20]. The peak at 1700-1600 $cm^{-1}$ could be related to C=O stretching in the carbonyl group [21]. The small peak in the 3000-2700 $cm^{-1}$ region is the aliphatic C-H stretch vibration and/or C-C chains and only presented in the simulated biochar spectrum [22]. C-N groups were more pronounced in the simulated biochar at 1250-1000 $cm^{-1}$, due to higher amount of nitrogen in simulated biochar compared to the prepared biochar. The peaks are quite visible for the simulated functionalized biochar since amine groups are the only functionality on the surface. However, in practice most of the amine functional groups are usually in the same zone as other groups and subsequently masked by them. The N-H peaks were found at 780-730, 3500-3200, and around 1600 $cm^{-1}$. A qualitative comparison suggests that many simulated spectra correspond well with the experimental one and few peaks are unmatched. As expected, the IR frequencies of simulated char were more transparent with nice sharp peaks. The reason could be due to using a single carbon surface with defined functional groups in the simulation study, while in each experimental runs, the complex sample structure interacts with infrared radiation more and correspondingly shows spectra that are more vibrational. Table 6-1 shows that the empirical formula of the simulated biochar is very close to that of the actual biochar.

Table 6-1: Elemental analysis of actual and simulated biochar

| Sample | Elemental composition (%) | | | | Empirical Formula |
|---|---|---|---|---|---|
| | C | H | N | O | |
| Actual Biochar | 73.25 | 3.64 | 0.16 | 22.15 | $C_{60}\ H_{36}\ N_{0.1}\ O_{14}$ |
| Simulated Biochar | - | - | - | - | $C_{60}\ H_{37}\ N\ O_{13}$ |

Slight differences between the two IR frequencies and empirical formulas are due to using different sources. The biochar was pyrolyzed from woody biomass (Sawdust) at 500 ºC; while, the simulated biochar was sourced from crop straw at 500 ºC. In general, these two methods demonstrate that the biochar surface model could represent properties of the actual biochar well and can be used as an alternative to actual biochar in order to investigate the effect of functional groups.

### 6.2.2. $CO_2$ adsorption on biochar surface

Given the heterogeneous nature of the biochar, it is challenging to determine experimentally which functional groups can enhance or potentially inhibit the adsorption of target adsorbate. In this section, molecular modeling was used to assess the adsorption potential. The first set of $CO_2$ adsorption simulations were performed on the surface with the functional groups outlined in Figure 6-2. The $CO_2$ molecule was introduced to each functional group with specified distance. This distance was determined by summation of the van der walls radius of each atom (Table 6-2), for instance this distance is 1.54A°+1.85A° in portion 1.

Table 6-2: Van der Waals radii of selected atoms (in A°) [23]

| Element | $R_0$ |
|---|---|
| C | 1.85 |
| H | 1.20 |
| N | 1.54 |
| O | 1.40 |

It is worth mentioning that the $CO_2$ molecule remained in linear conformation even after energy minimization of the system that shows weak adsorption, deviation from linearity indicates stronger adsorption. The calculated $CO_2$ heat of adsorption for each portion is outlined in Figure 6-6(a-g).

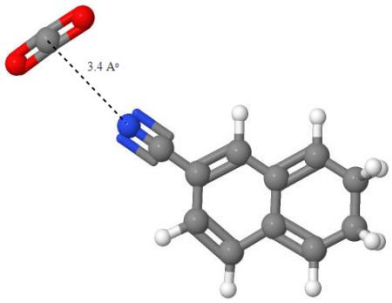


**a) Portion 1**
**$\Delta H_{ads}$= -5.2 kJ/mol**

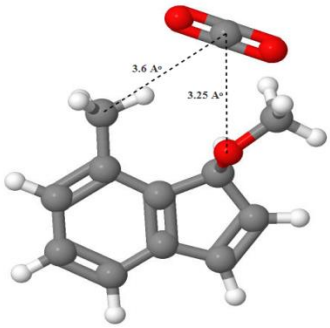


**b) Portion 2**
**$\Delta H_{ads}$= -0.4 kJ/mol**

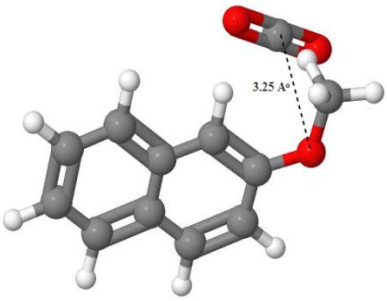


**c) Portion 3**
**$\Delta H_{ads}$= -4.5 kJ/mol**

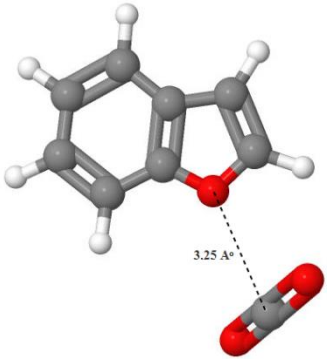


**d) Portion 4**
**$\Delta H_{ads}$= -7.3 kJ/mol**

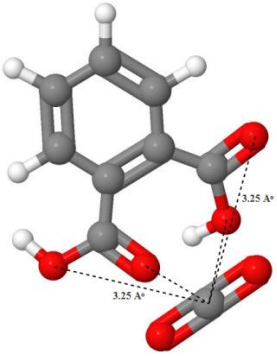


**e) Portion 5**
**$\Delta H_{ads}$= -2.1 kJ/mol**

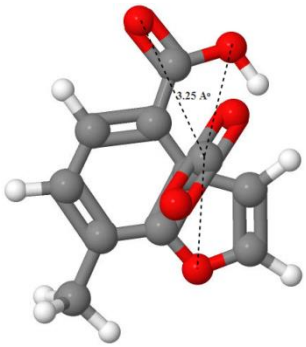


**f) Portion 6**
**$\Delta H_{ads}$= -4.2 kJ/mol**

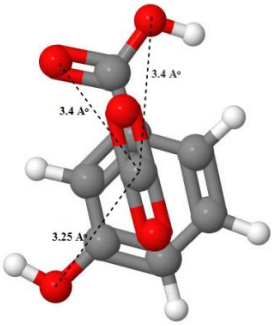

**g) Portion 7**
**$\Delta H_{ads}$= -10.6 kJ/mol**

Figure 6-6: Interaction configurations and adsorption energies (in kJ/mol) for $CO_2$ and surface functional groups at 25 °C and 1 atm

The minimum and maximum enthalpy of adsorption was -0.4 kJ/mol (portion 2 and -10.6 kJ/mol (portion 7) as outlined in Figure 6-6 b,g. The results suggested carboxyl and hydroxyl in portion 7 have higher affinity for $CO_2$ adsorption when compared to methyl and ether in portion 2. This is due to the hydrogen bonding between O-H (hydroxyl) and the nearest O of $CO_2$ (O-H$\cdots$O=C). The proton in H atom and electronegative O in the $CO_2$ molecule enhances electrostatic attraction between adsorbate and surface. Figure 6-7 illustrates the electrostatic potential map (EPM) or Mulliken population analysis on the electron density of the sample.

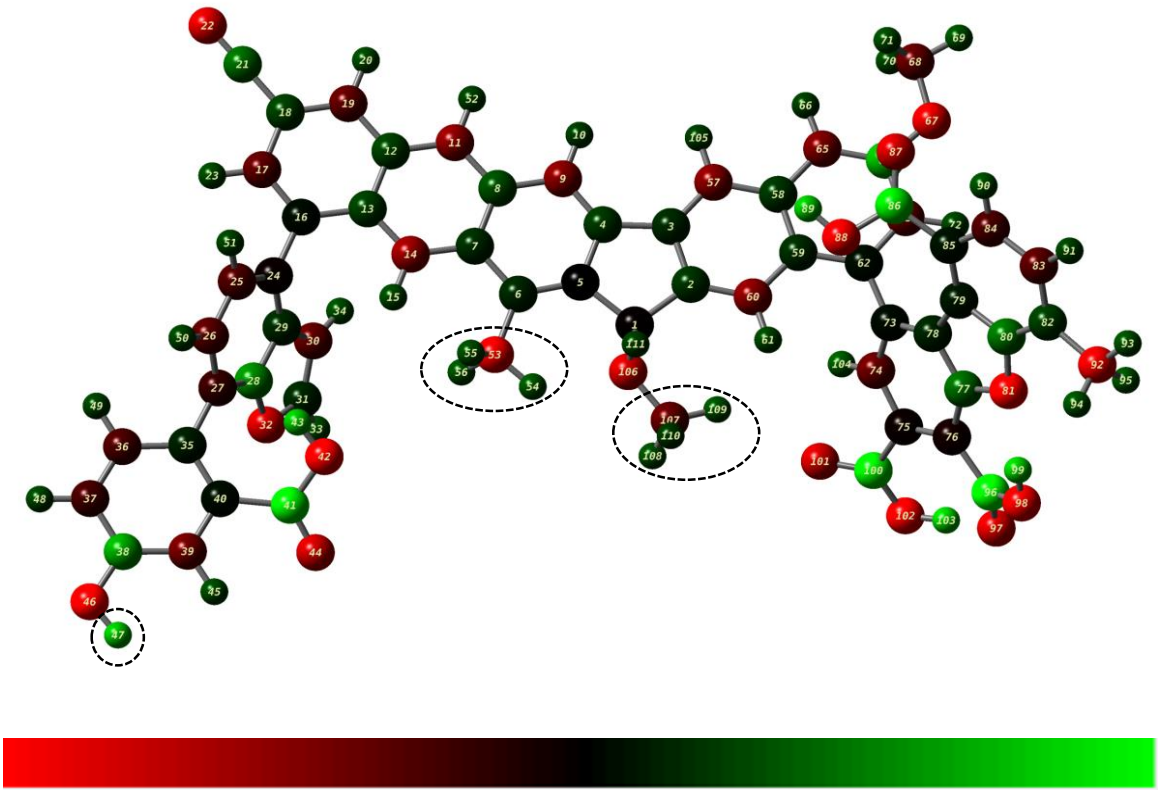

Figure 6-7: Mulliken charge distribution of biochar surface, Colour range: -0.64 e (red) to 0.64 e (green)

The EPM is a useful tool for understanding electrophilic and nucleophilic sites for different reactions [24]. In the figure, green represents a positive potential, red represents a negative potential, and black indicates neutrality. For instance, the charge of $H_{47}$ (Light green, hydroxyl) of portion 7 are higher than the $H_{54\text{-}56,108\text{-}110}$ (Dark green, methyl (53) and ether (107) functional groups) in portion 2 (Figure 6-7). This validates the weaker interaction of $C_{53/107}$-$H_{54\text{-}56/108\text{-}110}$ ···O (portion 2) than typical hydrogen bond of $O_{46}$-$H_{47}$···O (portion 7) observed in adsorption energy [25,26]. The charge distribution of electrostatic interactions of $CO_2$ by biochar surface in each portion is represented in Figure 6-8.

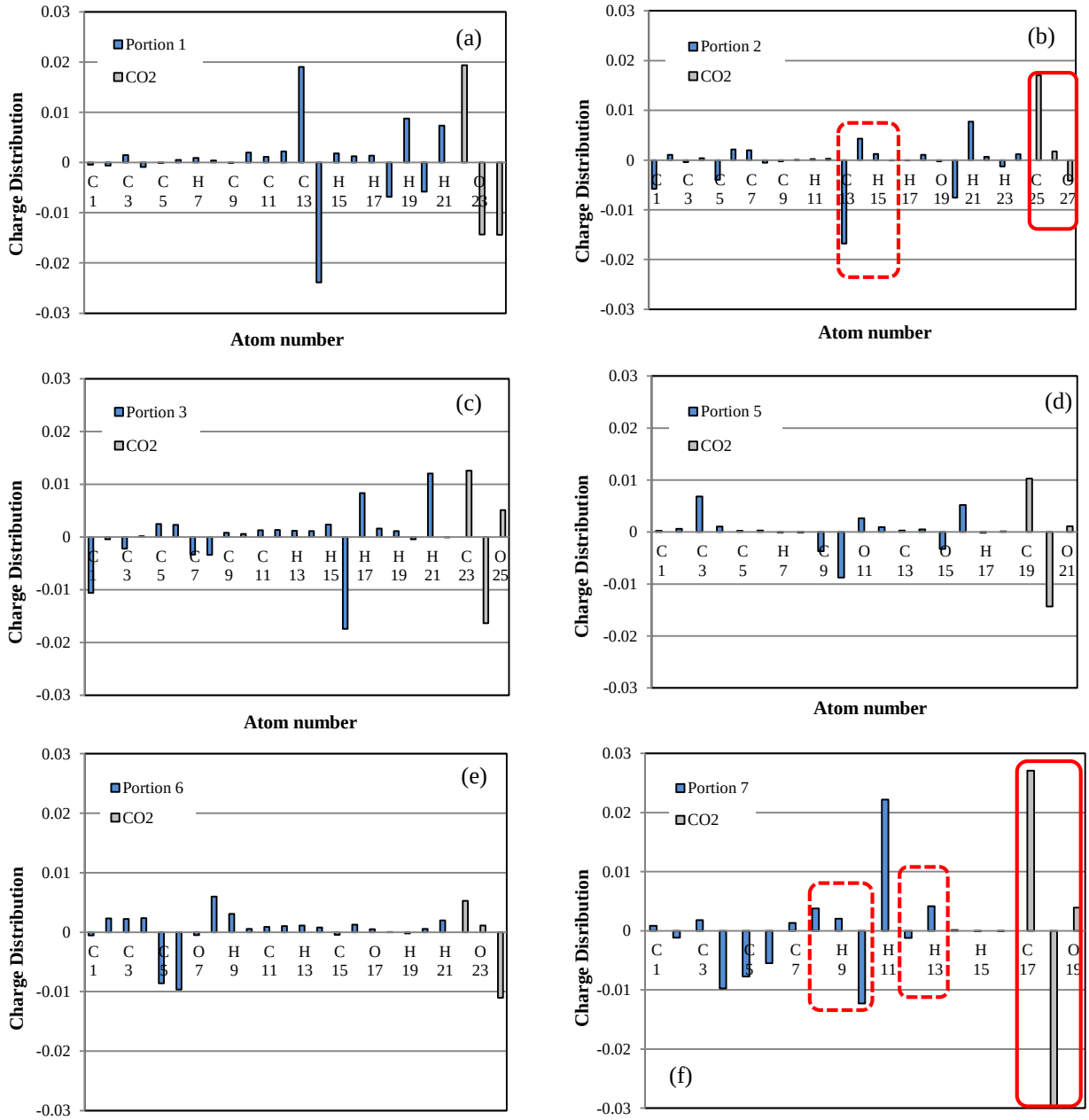


Figure 6-8: Distribution of electrons among the elements according to the Mulliken molecular orbital population analysis in different portions

Figures 6-8 (a) to (f) were used to analyze the adsorption of $CO_2$ in terms of biochar surface charges below. The charge of each atom will be changed through adsorption. Although the absolute values of these charges are typically not accurate, the focus here is on relative changes before and after adsorption [27].

The impacts of different functional groups on $CO_2$ adsorption are shown in Figure 6-9.

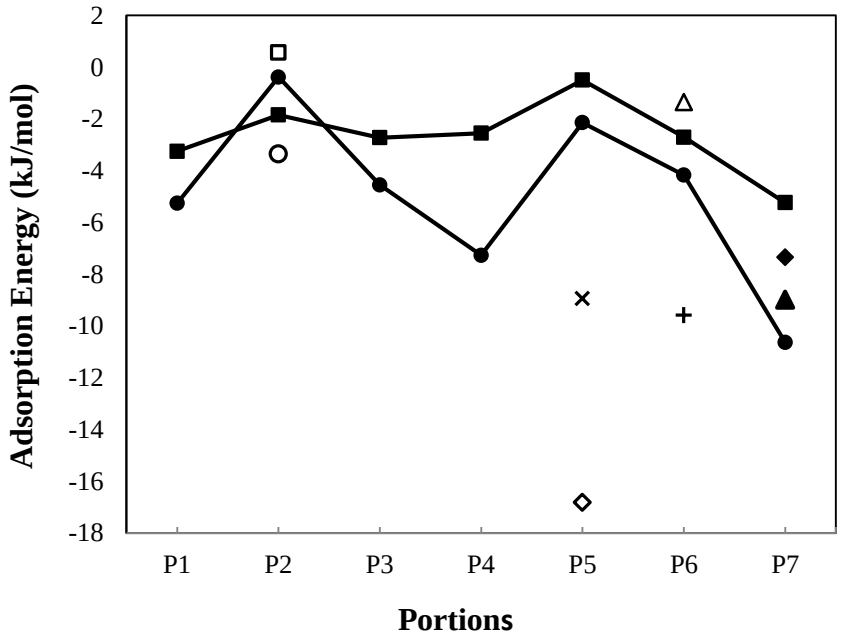


Figure 6-9: The effect of different functional groups on heat of adsorption at 25 °C and 1 atm, –●– Portions with functional groups, –■– Portions with functional groups removed, □ Portion 2- methyl, ○ Portion 2 - ether, ◊ Portion 5 - two carboxyl by distance, × Portion 5 - one carboxyl, + Portion 6 - carboxyl and methyl, Δ Portion 6 - furan and methyl, ▲ Portion 7 - carboxyl, ♦ Portion 7 – hydroxyl

The line "–■–" are the simulation results using a pure carbon surface, with no functionality, while line "–●–" is the original surface with portions as outlined in Figure 6-2. The points on the graph are the results of simulations where different functional groups are removed or added depending on portions. In general, functional groups (–●–)

improved the $CO_2$ adsorption in all portions (lower adsorption energies) excluding portion 2 compared to the pure carbon surface. In portion 2, the single ether (○) shows better adsorption when compared to the original structure (Figure 6-2) with methyl and ether present (■). When only the methyl group (□) is included the adsorption is the weakest. This could be due to the very low charge transfer (*i.e.* weak bond) from hydrogen in methyl groups (dashed boundary) to oxygen in $CO_2$ (red boundary in Figure 8) compared to other functional groups. For portion 5, in the original structure (Figure 6-2), the two carboxyl groups are attached at adjacent carbons (–●–). There is potential for the carboxyl groups to bind through hydrogen bonding and therefore hinder $CO_2$ adsorption. As such, two cases were studied, one where only one carboxyl group was present (×) and the second where the one carboxyl group was moved to a non-adjacent carbon (◊). When one carboxyl group was removed, the energy of adsorption decreased approximately four times (~-9 kJ/mol). For the second case, the energy of adsorption reduced significantly (~9 times) indicating hydrogen bonding was likely occurring between adjacent carboxyl groups. Carboxyl, methyl, and furan are present in portion 6. The energy of adsorption decreased by removing furan (+) and increased when removing the carboxyl group (Δ). The reason behind this fact could be due to the weak bonding occurring between methyl and furan (C-H…O), increasing the adsorption enthalpy. The lowest adsorption enthalpy in portion 7 was with the original structure (Figure 6-2) with both functional groups (carboxyl and hydroxyl) attached to non-adjacent carbon (–●–). In contrast to portion 5, there was no hydrogen bonding to interfere with adsorption. In Figure 6-8, both functional group (dashed boundary) and target adsorbate charges were shown by red boundary, indicating the highest charge distribution among portions and

subsequently lowest adsorption energy. Portion 7 with carboxyl (▲) showed better adsorption compared to the hydroxyl group (♦). This sequence suggest that the polarity (COOH > OH > C=O > $C_2O$) determines the adsorption strength of $CO_2$ on the oxygen-containing functional groups [4].

### 6.2.3. $CO_2$ adsorption on functionalized biochar surface

In this set of simulations, all 7 portions were replaced with primary amine groups, as demonstrated below (Figure 6-10) in portions 1 and 3 where nitrile and ether was replaced by amine, respectively.


**a) Portion 1**
**$\Delta H_{ads}$= -9 kJ/mol**

**b) Portion 3**
**$\Delta H_{ads}$= -6.4 kJ/mol**

Figure 6-10: Interaction configurations and adsorption energies (in kJ/mol) for $CO_2$ and amine functionalized biochar as an example (a,b) at 25 °C and 1 atm

A second set of simulations were performed where only portions 5,6, and 7 were replaced with amide groups. The carboxyl functional groups, located in portion 5, 6, and 7 could be converted to amide groups while functionalizing with nitrogen (Figure 6-11).

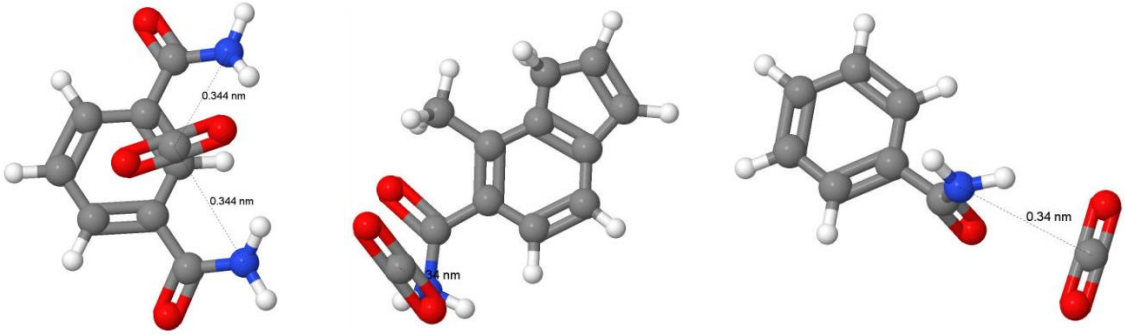


**a) Portion 5 amide** **b) Portion 6 amide** **c) Portion 7 amide**

Figure 6-11: Optimized interaction configurations of $CO_2$ with amide functionalized surface

The amine and amide functional groups interact with $CO_2$ through stronger bonding. The proposed mechanism in this section is physisorption interaction. In all portions (other than portion 7) the amine groups showed lower heat of adsorption and consequently bonded more strongly in comparison to other functional groups (Figure 6-12).

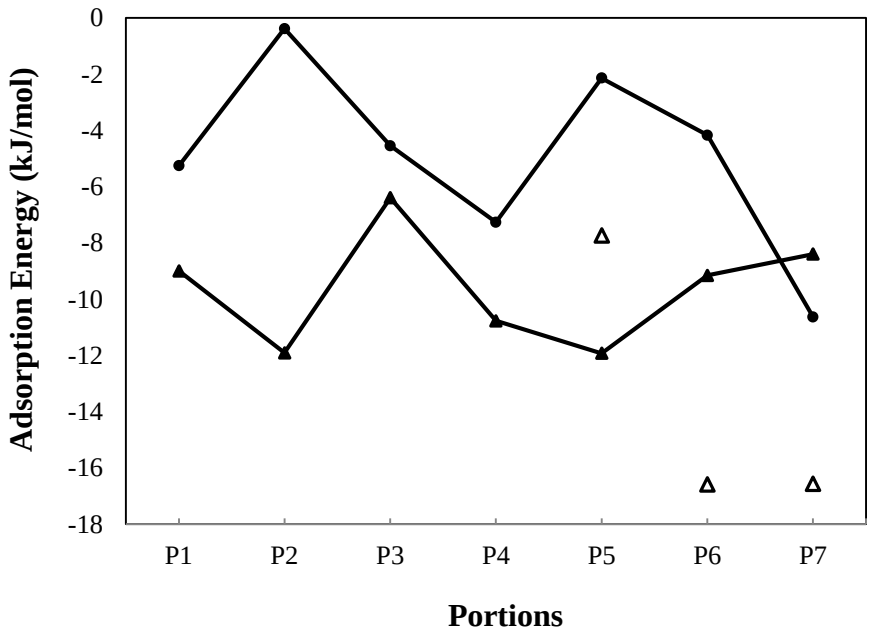

Figure 6-12: The impact of amine and amide functional groups vs. the other functional groups at 25 °C and 1 atm, -▲- amine functional groups, Δ amide functional group, -●- original functional groups

For portion 1, the π-π interaction could be between the orbitals of C≡N (nitrile) and C=O ($CO_2$). The π bonds are non-covalent bonds, which interact weaker with $CO_2$ compared to hydrogen bonding in this portion. Figure 6-6 indicates two hydrogen bonds (O-H···O) in portion 7 (carboxyl and hydroxyl groups) which shows stronger bonding than the single hydrogen bond between amine and $CO_2$ (N-H···O). The reason is because oxygen is more electronegative (tendency to attract a shared pair of electrons) than nitrogen. The Mulliken charge distribution (Figure 6-8 and Table 6-3) back this up as the charge transfer from hydrogen to oxygen in O-H···O is higher than N-H···O in portion 7. Among all portions functionalized with amine groups, portion 2 and 5 have the lowest heat of adsorption (~-12kJ/mol). The reason is that more electrons were transferred to N and from C in $CO_2$ molecule, resulting in a stronger bonding with $CO_2$ in comparison to other portions (Table 6-3).

Table 6-3: Charge distribution of $CO_2$, N, and H in amine and amide groups

| | $O_1^*$ | C | $O_2^*$ | Functional group | N | H (avg.) |
|---|---|---|---|---|---|---|
| Portion 1 | -0.008 | 0.023 | -0.025 | amine | -0.012 | 0.006 |
| Portion 2 | -0.010 | 0.025 | -0.036 | amine | -0.015 | 0.01 |
| Portion 3 | -0.026 | 0.022 | -0.005 | amine | -0.012 | 0.01 |
| Portion 4 | -0.011 | 0.024 | -0.016 | amine | -0.015 | 0.009 |
| Portion 5 | -0.025 | 0.030 | -0.008 | amine | -0.014 | 0.004 |
| | -0.022 | 0.023 | 0.025 | amide | -0.016 | 0.005 |
| Portion 6 | -0.017 | 0.023 | -0.016 | amine | -0.013 | 0.006 |
| | 0.002 | 0.028 | -0.039 | amide | -1.103 | 0.437 |

| | | | | | | |
|---|---|---|---|---|---|---|
| Portion 7 | -0.026 | 0.022 | -0.006 | amine | 0.038 | -0.004 |
| | 0.004 | 0.029 | -0.040 | amide | -0.020 | 0.015 |

*Oxygen atoms of $CO_2$ molecule

The amide functional groups (portion 5, 6, and 7) produced the lowest heat of adsorption due to high polarity of amide groups (Figure 6-11). As Table 6-3 illustrates, the amount of charge gained by nitrogen in amide groups is higher than amine, leading the hydrogen with higher fractional positive charge and stronger bonding with $CO_2$. Portion 6 and 7 with the highest fractional charge distribution (Table 6-3) released the lowest adsorption enthalpy (~-17 kJ/mol) among portions (Figure 6-12). In general, amide functional groups can have better performance in $CO_2$ adsorption but the position of functionalizing is another factor affecting the process.

### 6.2.4. $H_2S$ adsorption vs. $CO_2$ adsorption on biochar surface

The adsorption of $H_2S$ on the biochar surface at 20 ºC and 1 atm was evaluated via the same method as described above for $CO_2$. It should be noted, it was assumed that the molecule does not disassociate, but adsorbs as $H_2S$ (in the absence of water). This is in line with the physical adsorption proposed by other work [28]. Figure 6-13 compares the enthalpy and free energy of $H_2S$ and $CO_2$ adsorption on biochar at the same condition.

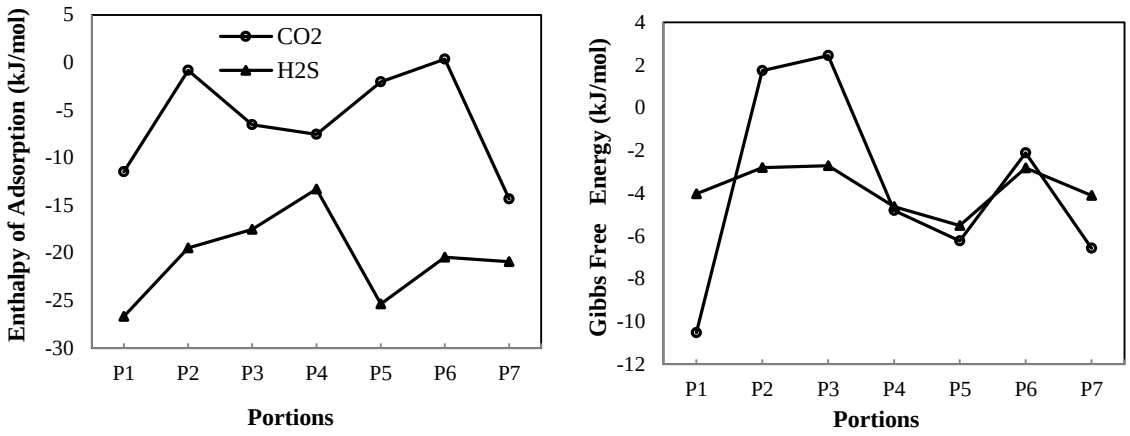


Figure 6-13: Thermodynamic information for $CO_2$/$H_2S$ systems

The enthalpy of the $H_2S$ interaction with biochar ranged from -13.3 to -26.7 kJ/mol. The mean of these values is between physisorption and chemisorption [29]. The average Gibbs free energy of $CO_2$/$H_2S$-biochar systems were approximately the same (-3.73 and -3.81 kJ/mol), indicating both processes are spontaneous (favourable) and potentially $CO_2$ could be used as a surrogate for $H_2S$ in initial screening experiments of this biochar. This is important, as there are significant costs and safety issues when working with $H_2S$. Molecular modeling allows one to screen modified and unmodified chars with a surrogate such as $CO_2$ and should the char show potential the more elaborate lab set up for $H_2S$ can be created.

### 6.2.5. Comparison of theoretical results with experimental data

In this section, the obtained thermodynamic properties from DFT calculations and experiments were compared. Table 6-4 summarizes the interaction energy, enthalpy, and free energy of the adsorption system at 20 °C and 1 atm.

Table 6-4: Calculated and experimental values of adsorption energy, enthalpy, and free energy for unaltered biochar

| System | $\Delta E_{noC}$ | $\Delta(ZPE)^{\dagger}$ | $\Delta(TE)^{\ddagger}$ | $\Delta E_C$ | $\Delta H^{\circ}_{Cal}$ | $\Delta H^{\circ}_{exp}$ | $\Delta G^{\circ}_{Cal}$ | $\Delta G^{\circ}_{exp}$ |
|---|---|---|---|---|---|---|---|---|
| Portion 1 | -10.39 | 1.23 | 0.21 | -8.95 | -11.48 | | -10.53 | |
| Portion 2 | -4.30 | 1.52 | 0.36 | -2.42 | -0.82 | | 1.73 | |
| Portion 3 | -6.76 | 0.95 | -2.33 | -8.13 | -6.54 | | 2.43 | |
| Portion 4 | -12.26 | 1.74 | 0.30 | -10.22 | -7.54 | | -4.81 | |
| Portion 5 | -6.09 | 0.91 | 0.15 | -5.03 | -2.03 | | -6.24 | |
| Portion 6 | -4.34 | 0.85 | 0.03 | -3.46 | 0.34 | | -2.12 | |
| Portion 7 | -14.70 | 1.96 | 0.50 | -12.25 | -14.33 | | -6.57 | |
| $CO_2$/biochar* Avg. | -8.41 | 1.31 | -0.11 | -7.21 | -6.06 | -8.17 | -3.73 | -2.90 |

*****All results are reported in kJ/mol, $^{\dagger}$ZPE: zero-point energy, $^{\ddagger}$TE: thermal contribution to energy

Regarding energetics, the B3LYP contribution to the interaction energy is not corrected ($\Delta E_{noc}$); therefore, the thermal contribution to energy, Δ(TE), and zero-point energy, Δ(ZPE), should be added up to give the final corrected interaction energy ($\Delta E_C$). Zero-point energy (ZPE) is the lowest possible energy that a quantum mechanical system may have and is the energy of the ground state [30]. Calculated results for the zero-point energy, Δ(ZPE), and the thermal contribution to energy and enthalpy, including Δ(TE), Δ(TG), and Δ(TH), were also reported by the software (some results not presented here for the sake of brevity). It should be noted that Δ(TG) and Δ(TH) included the correction terms, Δ(ZPE) and Δ(TE). $\Delta E_{noc}$ and Δ(TH) were added up to give the adsorption enthalpy, $\Delta H^0_{Cal}$, to be compared with the corresponding experimentally determined value, $\Delta H^0_{exp}$ [31]. The average heat of adsorption ($\Delta H^0_{exp}$) was calculated experimentally to reflect the realistic thermodynamic property [32]. $\Delta G^0_{Cal}$ was determined by summation of $\Delta E_{noc}$ and Δ(TG) and compared with $\Delta G^0_{exp}$ [31]. In Table 6-4, calculated

values of thermodynamic parameters, $\Delta H^0$ and $\Delta G^0$, showed reasonable agreements with those experimentally found (~20% deviation). In addition, both thermodynamic parameters demonstrate the adsorption is favourable. The difference between theoretical and experimental results could be due to several reasons: the experiments were conducted in dynamic mode, but the simulation runs were static; the DFT simulations underestimate weak interaction energies [15]; and the thermodynamic parameters were calculated experimentally based on the degree of filling of the adsorbent; however, all the degree of filling or surface loading cannot be covered in practice.

The thermodynamic properties were not determined experimentally for the functionalized biochar. As such, the comparison between simulation and experiments was conducted qualitatively in this case. The experimental outcomes obtained in our lab showed that the $CO_2$ adsorption capacity for aminated char is higher than the unaltered one, similar to the absolute value of heat of adsorption in simulation results (Figure 6-12).

**Conclusion**

In this study, we have highlighted the role of surface functional sites of biochar in the $CO_2/H_2S$ adsorption. The biochar surface model was validated by two methods: comparison of IR analysis and empirical formula. The optimized interaction between different portions of pristine biochar and $CO_2$ as an adsorbate illustrated that the minimum and maximum heat of adsorption (*i.e.* -10.6 and -0.4 kJ/mol) attributed to carboxyl-hydroxyl and methyl-ether groups, respectively. The more exothermic $CO_2$ adsorption was due to hydrogen bonding interaction (O-H···O) which is stronger than C-H···O bonding. The carboxyl functional groups showed lower enthalpy of adsorption

compared to hydroxyl due to higher polarity. To confirm the impact of functional groups on $CO_2$ adsorption, all of the functional groups were removed and consequently the adsorption enthalpy was increased in most of the portions. The amine functional groups replaced with all other functional groups, improved $CO_2$ adsorption due to stronger bonding. The investigation of $H_2S$ adsorption on the biochar surface showed the mean enthalpy of the reaction was ~-20 kJ/mol and accordingly chemisorption was accompanied by physisorption in this case. $CO_2$ can be used as an effective substitute for $H_2S$ since the Gibbs free energy for adsorption of both on biochar were roughly the same. Further, the thermodynamic parameters were computed and they were in reasonable accordance with experimental results. In this study, molecular modeling was employed as a tool to pre-screen the types of functionality that could improve or impede adsorption onto heterogeneous structure of biochar in addition to determining the target adsorbate gas in shorter time without doing experiments. Further investigations are still required to develop molecular modeling with regard to realistic conditions of adsorption process (*i.e.* temperature and pressure) and adsorbate mixtures such as natural or produced gas.

**Acknowledgment**

This research was supported by Compute Canada team, Ace-net consortium, and Gaussian Inc. The authors acknowledged Mr. Oliver Stueker (Memorial University) and Mr. Ross Dickson (Dalhousie University) for their great support during this project.

## References


[1] Keiluweit M, Nico PS, Johnson M, Kleber M. Dynamic molecular structure of plant biomass-derived black carbon (biochar). Environ Sci Technol 2010;44:1247–53. doi:10.1021/es9031419.

[2] Brewer CE, Schmidt-Rohr K, Satrio JA, Brown RC. Characterization of biochar from fast pyrolysis and gasification systems. Environ Prog Sustain Energy 2009;28:386–96. doi:10.1002/ep.10378.

[3] Zhao N, Lv Y, Yang X. A new 3D conceptual structure modeling of biochars by molecular mechanic and molecular dynamic simulation. J Soils Sediments 2017;17:641–55. doi:10.1007/s11368-015-1308-y.

[4] Dang Y, Zhao L, Lu X, Xu J, Sang P, Guo S, et al. Molecular simulation of CO2/CH4 adsorption in brown coal: Effect of oxygen-, nitrogen-, and sulfur-containing functional groups. Appl Surf Sci 2017;423:33–42. doi:http://dx.doi.org/10.1016/j.apsusc.2017.06.143.

[5] Lim G, Lee KB, Ham HC. Effect of N-Containing Functional Groups on CO 2 Adsorption of Carbonaceous Materials: A Density Functional Theory Approach. J Phys Chem C 2016;120:8087–95. doi:10.1021/acs.jpcc.5b12090.

[6] Zhang D, Jing X, Sholl DS, Sinnott SB. Molecular Simulation of Capture of Sulfur-Containing Gases by Porous Aromatic Frameworks. J Phys Chem C 2018. doi:10.1021/acs.jpcc.8b03767.

[7] Xiao X, Chen B. A Direct Observation of the Fine Aromatic Clusters and Molecular Structures of Biochars. Environ Sci Technol 2017;51:5473–82. doi:10.1021/acs.est.6b06300.

[8] Zhao N, Lü Y, Li G. Characterization and three-dimensional structural modeling of humic acid via molecular mechanics and molecular dynamic simulation. Chem Res Chinese Univ 2013;29:1180–4. doi:10.1007/s40242-013-3156-x.

[9] Kaal J, Martínez Cortizas A, Reyes O, Soliño M. Molecular characterization of Ulex europaeus biochar obtained from laboratory heat treatment experiments - A pyrolysis-GC/MS study. J Anal Appl Pyrolysis 2012;95:205–12. doi:10.1016/j.jaap.2012.02.008.

[10] Bamdad H, Hawboldt K. Comparative study between physicochemical characterization of biochar and metal organic frameworks (MOFs) as gas adsorbents. Can J Chem Eng 2016;9999:1–7. doi:10.1002/cjce.22595.

[11] Frisch, M. J.; Trucks, G.W.; Schlegel, H. B.; Scuseria, G. E.; Robb, M. A.; Cheeseman, J. R.; Scalmani, G.; Barone, V.;Mennucci, B.; Petersson, G. A.; Nakatsuji, H.; Caricato, M.; Li, X.; Hratchian, H. P.; Izmaylov, A. F.; Bloino, J.; Zheng, G.; Sonnenber DJ. Gaussian 09. Gaussian, Inc Wallingford CT 2009:2–3. doi:111.

[12] Chapter 9: Density Functional Theory (DFT) Methods n.d.:1–6.

[13] Cramer CJ. Essentials of Computational Chemistry Theories and Models. vol. 42.

2004. doi:10.1021/ci010445m.

[14] Bytheway I, Wong MW. The prediction of vibrational frequencies of inorganic molecules using density functional theory. Chem Phys Lett 1998;282:219–26. doi:10.1016/S0009-2614(97)01281-5.

[15] Zhao Y, Truhlar DG. Density functionals for noncovalent interaction energies of biological importance. J Chem Theory Comput 2007;3:289–300. doi:10.1021/ct6002719.

[16] Dunbar RC. Complexation of Na+ and K+ to aromatic amino acids: A density functional computational study of cation-pi interactions. J Phys Chem A 2000;104:8067–74. doi:10.1021/jp000524l.

[17] Pettersson LGM, Nilsson A. A molecular perspective on the d-band model: Synergy between experiment and theory. Top Catal 2014;57:2–13. doi:10.1007/s11244-013-0157-4.

[18] Delle Piane M, Corno M, Pedone A, Dovesi R, Ugliengo P. Large-scale B3LYP simulations of ibuprofen adsorbed in MCM-41 mesoporous silica as drug delivery system. J Phys Chem C 2014;118:26737–49. doi:10.1021/jp507364h.

[19] Kwon S, Choi J Il, Lee SG, Jang SS. A density functional theory (DFT) study of CO2 adsorption on Mg-rich minerals by enhanced charge distribution. Comput Mater Sci 2014;95:181–6. doi:10.1016/j.commatsci.2014.07.042.

[20] Wang L, Butterly CR, Wang Y, Herath HMSK, Xi YG, Xiao XJ. Effect of crop

residue biochar on soil acidity amelioration in strongly acidic tea garden soils. Soil Use Manag 2014;30:119–28. doi:10.1111/sum.12096.

[21] Gunes A, Inal A, Sahin O, Taskin MB, Atakol O, Yilmaz N. Variations in mineral element concentrations of poultry manure biochar obtained at different pyrolysis temperatures, and their effects on crop growth and mineral nutrition. Soil Use Manag 2015;31:429–37.

[22] Chen WY, Mattern DL, Okinedo E, Senter JC, Mattei AA, Redwine CW. Photochemical and acoustic interactions of biochar with CO2 and H2O: Applications in power generation and CO2 capture. AIChE J 2014;60:1054–65. doi:10.1002/aic.14347.

[23] Bondi A. van der Waals Volumes and Radii. J Phys Chem 1964;68:441–51. doi:10.1021/j100785a001.

[24] Tanak H, Yavuz M. Density functional computational studies on (E)-2-[(2-Hydroxy-5-nitrophenyl)-iminiomethyl]-4-nitrophenolate. J Mol Model 2010;16:235–41. doi:10.1007/s00894-009-0539-5.

[25] Kim KH, Kim Y. Theoretical studies for lewis acid-base interactions and C-H···O weak hydrogen bonding in various CO2 complexes. J Phys Chem A 2008;112:1596–603. doi:10.1021/jp709648q.

[26] Matsuura H, Yoshida H, Hieda M, Yamanaka SY, Harada T, Shin-Ya K, et al. Experimental Evidence for Intramolecular Blue-Shifting C-H···O Hydrogen

Bonding by Matrix-Isolation Infrared Spectroscopy. J Am Chem Soc 2003;125:13910–1. doi:10.1021/ja030538f.

[27] Radovic LR. The mechanism of CO2 chemisorption on zigzag carbon active sites: A computational chemistry study. Carbon N Y 2005;43:907–15. doi:10.1016/j.carbon.2004.11.011.

[28] Shang G, Li Q, Liu L, Chen P, Huang X. Adsorption of hydrogen sulfide by biochars derived from pyrolysis of different agricultural/forestry wastes. J Air Waste Manag Assoc 2016;66:8–16. doi:10.1080/10962247.2015.1094429.

[29] Çalişkan E, Göktürk S. Adsorption characteristics of sulfamethoxazole and metronidazole on activated carbon. Sep Sci Technol 2010;45:244–55. doi:10.1080/01496390903409419.

[30] Müller U. Inorganic Structural Chemistry: Second Edition. 2007. doi:10.1002/9780470057278.

[31] Ochterski JW, Ph D. Thermochemistry in Gaussian. Gaussian Inc Pittsburgh PA 2000;264:1–19. doi:10.1016/j.ijms.2007.04.005.

[32] Huang L, Ning Z, Wang Q, Qi R, Zeng Y, Qin H, et al. Molecular simulation of adsorption behaviors of methane, carbon dioxide and their mixtures on kerogen: Effect of kerogen maturity and moisture content. Fuel 2018;211:159–72. doi:10.1016/j.fuel.2017.09.060.

# 7. CHAPTER SEVEN

## Summary and Recommendations for Future Work

The research presented in this thesis contributes new information and observations with respect to how operating conditions, feedstock properties, functional groups, and modification impacts on $CO_2$ adsorption by specific type of biochar. The overall conclusion was that biochar can be used as an alternative to commercial adsorbent as it is more environmentally-friendly, a low cost adsorbnet, and showed better adsorption. The biochar was produced through the lab-scale tube furnace reactor and the pilot 2-4 kg/h auger reactor and the adsorption experiments were conducted in the designed fixed bed reactor. Several analytical techniques were employed to characterize the biochar samples. In addition, the biochar surface was simulated in order to investigate the effect of various functional groups on adsorption of $CO_2$/$H_2S$. This thesis was comprised of five sections: literature review (chapter two), characterization of biochar (chapter three), biochar adsorption via theoretical and experimental study (chapter four), modification of biochar structure (chapter five), and molecular modeling of biochar surface (chapter six).

### 7.1. Literature Review

The purpose of the first phase of this study was to investigate biochar production methods, isotherms, molecular modeling, and different adsorption units to use this information further. The literature was reviewed to compare biochar with commercial adsorbents and the results indicated biochar could be used as a feasible alternative to activated carbon as it is an environmentally friendly and low-cost adsorbent. The results showed the properties of biochar such as carbon, hydrogen content, and surface area was profoundly affected by pyrolytic temperature. The adsorption of $H_2S$ on plain carbon surfaces is proposed to occur by the mechanism proposed by Adib et al. Two different

process systems, including dynamic and static, were used in the literature to determine adsorption capacities and rates. The application of molecular modeling to describe adsorption process and different simulation methods were studied.

### 7.2. Characterization of biochar

The aim of this phase of the thesis was to evaluate the biochar properties produced from three different woody biomasses: softwood (sawdust and bark (Balsam fir)) and hardwood (Ash wood) through fast pyrolysis at 400-500 ºC and then to compare them in terms of chemical, physical, and morphological properties with those of MOFs reported in the literature. MOFs are one of the effective adsorbents for removal of $H_2S$ from natural gas and $CO_2$ capture. The experimental results of the pH tests illustrated that the biochar samples were basic, which may indicate possible better acidic gas adsorption. The FTIR and TGA results showed biochar had higher carbon content and more aromatic functional groups in comparison with MOFs. However, the thermal stability and surface area of MOFs was found to be higher than the biochars. The SEM and XRD results showed structural differences in the morphology, pore size, mineral content of biochar and MOF-5. The MOF-5 had uniform micropore structure while biochars had honeycomb structure with variable pore diameters. Although all the biochar samples had almost the same physiochemical properties, sawdust biochar produced at 500 °C had the highest surface area, which can be chosen as the best option for adsorption experiments.

### 7.3. Biochar Adsorption

This phase of the study investigated the impact of operating parameters and their interactions on adsorption capacity of the biochar. A fixed bed rector was designed and validated in order to study biochars sourced from different types of feedstock. A series of adsorption experiments on biochar were carried out to determine the impact of temperature (°C), total inlet flow rate (mL $min^{-1}$), and carbon dioxide concentration (%V/V) on adsorption capacity (mmol $g^{-1}$) of char. The operating conditions which maximized adsorption were 20 °C, 60 mL $min^{-1}$ flow rate, and pure $CO_2$. The $CO_2$ inlet concentration was the most influential variable and the interactions between temperature–total flow rate and temperature–%$CO_2$ were significant in the adsorbent capacity of the biochar. The highest adsorption capacity (2.4 mmol $g^{-1}$) was found for softwood biochar produced at 500 °C (F-P-SW500) compared to the other studied chars while a commercial Zeolite-13X had 1.7 mmol $g^{-1}$ $CO_2$ uptake capacity. The isotherm study indicated the Freundlich model was a better fit because of the non-homogeneous nature of the surface of the biochar and possible multilayer adsorption. The thermodynamic properties results showed $CO_2$ adsorption was a spontaneous process ($\Delta G<0$), involving physical adsorption ($\Delta H<20$ kJ $mol^{-1}$), and was exothermic in nature ($\Delta H<0$). Through kinetic analysis, a pseudo first-order model showed an excellent fit with the data, because the pseudo-first order model applied to processes that involve physical adsorption or reversible interaction between adsorbent and adsorbate, such as $CO_2$ adsorption on activated carbon or zeolite sorbents. The results of this chapter suggested that biochar derived from "waste" materials could be used as a sustainable alternative to existing

adsorbents for contaminant removal from acid gases. However, it should be noted this work is limited to 100% $CO_2$ more extensive studies where $CO_2$ composition is varied and inhibiting/competing gases are added must be studied.

### 7.4. Modification of biochar structure

This phase of the study focused on modification of biochar structure in order to improve adsorption capability of the biochar. In this chapter, unmodified, thermally activated, and chemically modified biochars were compared based on the ability to adsorb carbon dioxide. Two novel methods, 1. Nitration followed by reduction and 2. Condensation of condensable siloxanes, were used to functionalize the biochar surface. The results indicated the $CO_2$ capture capacity decreased due to reducing the surface area and pore blockage. The biochars (unmodified and chemically modified) were thermally activated via air diluted with nitrogen at a moderate 560 ºC to enhance the capacities. The presence of nitrogen in functionalized samples was confirmed by elemental analysis. However, after thermal treatment the intensity of nitrogen group peaks decreased, indicating possible decomposition of the functional groups. Based on characterization results, the activated functionalized samples had a higher surface area, pore volume, and lower H:C ratio compared to unmodified ones, which could enhance the adsorption capability of biochars. The synthesized N-functionalized biochar followed by physical activation (AP-SW500-A-560) showed much higher adsorption capacity compared to commercial activated carbon (Norit CA1) and recent carbon-based adsorbents. The activated N-loaded biochar had an overall lower surface area than chemically activated

commercial carbon (Norit CA1) but higher adsorption due to retaining some nitrogen functionality enhances adsorption and makes up for a decreased surface area.

### 7.5. Molecular modeling of biochar surface

The purpose of this phase of the study was to use molecular modeling to determine the "best" target adsorbate for adsorption onto biochar and to screen the type of functional groups, which could enhance adsorption. The impact of each functional group (including nitrile, methyl, ether, furan, carboxyl, hydroxyl, amine, and amide) and interactions were investigated through molecular simulation and experiment. The surface composition/structure of biochar was selected from published char structure as a basis compound and built in the software. The model was validated with analyses of char generated in our labs to ensure the model was an accurate representation of the actual biochar. The electronic interaction between target gases ($CO_2$/$H_2S$) and the surface was performed using Gaussian 09 software. The results illustrate the minimum and maximum heat of adsorption (*i.e.* -10.6 and -0.4 kJ/mol) obtained for carboxyl-hydroxyl and methyl-ether groups, respectively. The interaction between $CO_2$ and carboxyl-hydroxyl of biochar occurred with hydrogen bonding (O-H…O), while methyl-ether groups interact weaker with $CO_2$ by C-H…O bonding. By removing all of the functional groups, the adsorption enthalpy was increased in most of the portions. The simulations of nitrogen functionalized biochar showed amine/amide functional groups enhanced $CO_2$ adsorption with more exothermic adsorption. The investigation of $H_2S$ adsorption on the biochar surface showed the heat of adsorption released was higher in comparison to $CO_2$, but approximately equal Gibbs free energy, indicating $CO_2$ can be used as a surrogate to $H_2S$.

The simulation results were compared against experimental results and the thermodynamic properties were reasonably in agreement.

### 7.6. Recommendations for Future Work

The application of biochar as gas adsorbent with efficient removal of acid gases were investigated through this study; however, further efforts are still required to modify and/or design the biochar structure at a molecular-level, improve the adsorption capacity, regenerate the biochar, and sequester the adsorbate. The recommendations for future work based on the results of this dissertation are summarized below:

- The inlet gas used in this study was pure $CO_2$ or mixed with $N_2$. However, in actual conditions, such as natural gas or produced gas from industries, the mixture fractions are different and associated with some impurities. As such, it is recommended to introduce feed gas similar to the actual condition at the same operating temperature and pressure to evaluate interference/competition effects.
- From a safety point of view, working with $H_2S$ in the lab environment poses an exceptionally high risk due to toxicity. Therefore, it is suggested if all the on-site risks (engineering controls *e.g.* ventilation systems) and proper protections (*e.g.* PPE) were identified, the adsorption capacity of $H_2S$ can be experimentally determined separately or with $CO_2$.
- In chapter three, the biochar characterizations including physical, chemical, and morphological were determined and compared with MOFs as one of the adsorbents for purification of natural/produced gas. The author suggests to

experimentally measuring the $CO_2/H_2S$ or $CO_2$-$H_2S$ mixture adsorption capacity of the MOFs and other commercial acid gas adsorbents along with biochars in chapter four to have better comparison of these adsorbents. The selectivity can be calculated as well when using $CO_2$-$H_2S$ mixture.

- The water content typically combined with natural/produced gas and it can have impact on the adsorption. The effect of $H_2O$ on $CO_2/H_2S$ adsorption should hence be taken into consideration.
- In chapter four, the optimum temperature, $CO_2$ concentration, and total inlet flow rate were obtained according to a series of lab-scale experiments in the fixed bed reactor in order to maximize adsorption capacity. The developed model via response surface methodology is specific to the designed system and type of biochar. The author recommends adding the type of biochar to independent variables in the CCD model to demonstrate the impact of this parameter and the interactions on adsorption capacity of biochars. Further, the breakthrough time can be added to response parameters.
- In addition to co-pyrolysis of different types of sawmill residues, co-pyrolysis of these residues with other waste materials (*e.g.* aquatic waste or coffee waste) or catalyst (*e.g.* HZSM-5) could change/modify biochar structure. This change might be in favour of better adsorption for the application of biochar.
- Based on the current study and the literature review, the thermal modification was conducted at 560 °C using air flow diluted with nitrogen (5% oxygen) for two hours to activate biochar samples in chapter five. The author suggests designing a

set of experiments to find the optimum condition(s) for activating. The independent parameters for developing the CCD model could be activation temperature, time, and activating agent.

- In chapter five, two methods were used for amine functionalizing of biochars. The amount of nitrogen loading was determined by elemental analysis before and after functionalizing. The obtained results indicated an optimum amount of nitrogen functionalizing can enhance the adsorption capacity compared to pristine biochar. As a result, it is suggested to use a technique to control the nitrogen loading in order to maximize the adsorption capacity (optimization of loading condition). In addition, the activation process could be done before functionalizing to compare with the current results.
- The desorption characteristics study was limited in this work due to time restrictions. Further investigations regarding regeneration of biochar and $CO_2$ sequestration are still required. The impact of different parameters including temperature, time duration, cycle numbers, and purging gas on regeneration of biochar could be an interesting topic in future work.
- The adsorption process of $CO_2$ and $H_2S$ on biochar was simulated individually in this study and the thermodynamic parameters and FTIR results were validated with experimental data obtained from adsorption of $CO_2$ on unmodified biochar. This simulation can also be done by $CO_2$ and $H_2S$ simultaneously and/or with other gases in natural/produces gases, then validate with experimental data adsorption on modified/unmodified biochar.

- The molecular dynamic (MD) software is usually used as a tool to simulate sophisticated systems with considering position of atoms over time. The author suggests applying MD in order to consider space and time evolution of a system and running millions of atoms in each job.
- Based on the results found from statistical analysis (chapter four), the operating parameters interaction and trends were identified. Using this information would be very helpful for scaling-up the fixed bed reactor in future work.